



# Optimal Control of Boundary Layer Transition

Markus Högberg

Doctoral Thesis Stockholm, 2001

Royal Institute of Technology Department of Mechanics Optimal Control of Boundary Layer Transition by Markus Högberg

> November 2001 Technical Reports from Royal Institute of Technology Department of Mechanics SE-100 44 Stockholm, Sweden

Typsatt i  $\mathcal{A}_{\mathcal{M}}\mathcal{S}\text{-}\mathbb{I}^{\!\!A}T_{\!\!E}X.$ 

Akademisk avhandling som med tillstånd av Kungliga Tekniska Högskolan i Stockholm framlägges till offentlig granskning för avläggande av teknologie doktorsexamen fredagen den 9 november 2001 kl. 10.15 i Kollegiesalen, Administrationsbyggnaden, Kungliga Tekniska Högskolan, Valhallavägen 79, Stockholm.

© Markus Högberg 2001 Norstedts Tryckeri AB, Stockholm 2001

#### Optimal control of boundary layer transition.

Markus Högberg Department of Mechanics, Royal Institute of Technology S-100 44 Stockholm, Sweden

#### Abstract

Methods for optimal control of transition in boundary layers are investigated and developed in this thesis. A model problem is studied in order to investigate an approximative method for objective function gradient computations. The approximation is to use the continuous formulation of the equations, instead of the discrete counterpart, to derive the optimization problem. The conclusion is that the approximative method is sufficiently accurate for the purpose of transition control. A nonlinear control approach using the Navier–Stokes equations and the associated adjoint equations to minimize an objective function measuring the energy of the perturbation to a laminar flow is developed and tested using direct numerical simulations.

A similar optimization problem is posed, using the Orr–Sommerfeld–Squire equations, which can be solved directly to obtain localized physical space feedback control laws. The performance of these control laws is quantified in direct numerical simulations by computing transition thresholds. It is shown that the threshold values can be increased by about 500% for a random perturbation. By using a physically motivated modification of the objective function it is shown that these linear controllers are also able to relaminarize a low Reynolds number turbulent flow.

In this linear framework an estimator in the form of an extended Kalman filter is developed and shown to have exponential convergence using the normal derivative of the normal vorticity as a wall measurement. The estimator and controller are combined into a compensator for which transition thresholds are computed. In this case the threshold value for the random perturbation is only increased by about 48%.

The linear control approach is then applied in direct numerical simulations of spatially developing boundary layer flows with successful reduction of perturbation energies for Tollmien–Schlichting waves and optimal perturbations in the Blasius boundary layer. In a Falkner–Skan–Cooke flow the control strategy also reduces the energy of traveling and stationary, saturated cross-flow vortices.

**Descriptors:** laminar-turbulent transition, transition control, turbulence control, flow control, boundary layer flow, channel flow, optimal control, adjoint equations, Riccati equations, Orr–Sommerfeld–Squire equations, secondary instability, transient growth, DNS, oblique waves, Falkner–Skan–Cooke flow, cross-flow vortices.

# **Preface**

This thesis is about optimal control of transition and turbulence in channel and boundary layer flow. The first part is a summary of the research presented in the papers included in the second part. An effort has been made to make the summary available to a general audience, and short sections describing methods and equations are included to make the thesis more self-contained. The summary also includes presentation of, and discussions about, the main results obtained. References to the papers in part 2 are made in order to clarify where to find more detailed information. Related research is reviewed and referred in order to put the present work into context and to help identify original contributions. A guide to the papers and the different authors respective contributions is also included in the last chapter of the thesis.

The seven papers in part 2 are adjusted to comply with the present thesis format for consistency, but their contents have not been altered compared to published or submitted versions except for minor corrections. The presentation is streamlined for clarity, and the discussion and the papers are for this reason not organized in chronological order.

Stockholm, 20011002  $Markus\ H\ddot{o}gberg$ 

# Contents

Preface	iv	
Part 1. Summary	1	
Tate 1. Summary	1	
Chapter 1. Overview	3	
1.1. Introduction	3	
1.2. Objectives		
1.3. Problem formulation issues	5	
1.4. Optimization methods	6	
1.4.1. Nonlinear equations	6	
1.4.2. Linear equations	7	
1.5. Governing equations	8	
1.6. Flow control background	11	
1.6.1. Laminar flow control	11	
1.6.2. Wave cancellation	11	
1.6.3. Opposition control	12	
1.6.4. Suboptimal control	13	
1.6.5. Nonlinear control	13	
1.6.6. Linear control	14	
1.7. Thesis outline	16	
Chapter 2. Nonlinear control	17	
2.1. Control problem	17	
2.2. Model problem	19	
2.2.1. Continuous formulation	20	
2.2.2. Discrete formulation	20	
2.2.3. Comparing the formulations	20	
2.3. Derivation and Implementation	21	
2.3.1. Optimization	23	
2.4. Control of oblique waves	23	

# vi CONTENTS

2.4.1. Transition scenario	23
2.4.2. Control	24
Chapter 3. Linear control and estimation	25
3.1. Controller	26
3.1.1. Properties of $\hat{X}$	28
3.2. Estimator	29
3.3. Compensator	31
3.4. Spatial localization	31
3.5. Performance of controller	32
3.5.1. Direct numerical simulation code	32
3.5.2. Transition thresholds	33
3.5.3. Turbulence control	34
3.5.4. Linear v.s Nonlinear optimal control	37
3.6. Performance of estimator	37
3.7. Performance of compensator	38
Chapter 4. Control of spatial boundary layer flows	41
4.1. Linear control methodology	41
4.2. Application of Linear Controller	42
4.3. Numerical simulations	43
4.4. Control of TS waves	43
4.5. Control of streamwise streaks	44
4.6. Falkner–Skan–Cooke flow	45
4.7. Control of cross-flow vortices	46
4.7.1. Traveling vortices	46
4.7.2. Stationary vortices	47
4.8. Implications for the transition process	48
Chapter 5. Discussion	51
Chapter 6. Quick guide to papers and authors contribut	tions 53
Acknowledgment	56
Bibliography	57
Part 2. Papers	63
Paper 1. Numerical approaches to optimal control of a model equation for shear flow instabilities	a 67

	CONTENTS	vii
Paper 2.	Optimal control of wall bounded flows	91
Paper 3.	Spatially localized convolution kernels for decentralized control and estimation of plane channel flow	123
Paper 4.	Decentralized feedback control and estimation of transition in plane channel flow	149
Paper 5.	Optimal control of transition initiated by oblique waves in channel flow	183
Paper 6.	Secondary instability of cross-flow vortices in Falkner-Skan-Cooke boundary layers	195
Paper 7.	Linear optimal control applied to instabilities in spatial boundary layers	221

# Part 1 Summary

#### CHAPTER 1

# Overview

#### 1.1. Introduction

The desire to control processes governed by the laws of nature has been a driving force for mankind ever since we were unable to control fire. The potential benefits from such abilities has attracted researchers in many areas such as biology, chemistry, combustion, aerodynamics, physics and fluid mechanics. In these areas many processes with complex dynamics occur, and the gains from being able to control these processes can be substantial from economic as well as environmental perspectives. Within the field of fluid mechanics there are many challenging control problems to consider. The ability to prevent turbulence could have a large impact on the performance of air and water vehicles since the drag, and thereby also the fuel consumption, can be decreased. Enhancing or stimulating turbulence can also be of interest where efficient mixing or heat transfer is desired. In other applications the main concern is to suppress or trigger separation in a controlled manner. Flow control can take many different forms and some kind of classification of different strategies is useful. The term passive control is used when the flow is affected without requiring an input of energy. The swimsuits developed to decrease the drag of a swimmer uses a passive strategy where the manufacturers claim to have imitated the skin of a shark. Apparently it is a successful design since so many new world records have been set by people wearing those suits. Another sport where passive flow control has had an impact is golf. The small dimples in the surface the ball trigger turbulence and thereby separation is delayed and drag is reduced. As opposed to passive control, active control requires an energy input to the flow. This is done either according to a predetermined scheme in an open loop or determined from measured data in a closed loop. An example of an active, open loop, approach to flow control is used in the process of continuous casting of metals. Magnetic fields are applied to affect the flow in the mold during the casting process to improve the quality of the solid metal. Another example is the application of suction on the wing or fin of an airplane to stabilize the flow and decrease drag. Closed loop active control is also known as reactive control which means that information about the state of the process measured and used in feedback to the controller that acts based on this information. This kind of controller is used in large scale flow systems e.g. to get the optimal mixture of gas and air in a combustion engine to maximize the efficiency and minimize pollution. It is not as commonly used to affect the flow itself on a

#### 4 1. OVERVIEW

small scale as it is for these larger systems. In the last decade there has been rapid development of mechanical sensors and actuators for small scale flow measurement and actuation through the MEMS technology, and these devices are being used in laboratory experiments around the world. The development of this new technology could mean that we in the near future will see more active and reactive flow control in practical use. In this thesis the topic of flow control is approached from a numerical perspective. Tools from optimization and control theory are applied to fluid mechanical systems in order to evaluate different strategies. The focus is on active and reactive control of flows in simple geometries. Such model problems are used to evaluate new methods and to establish what is doable and what is not, which provides important information for future research in this field.

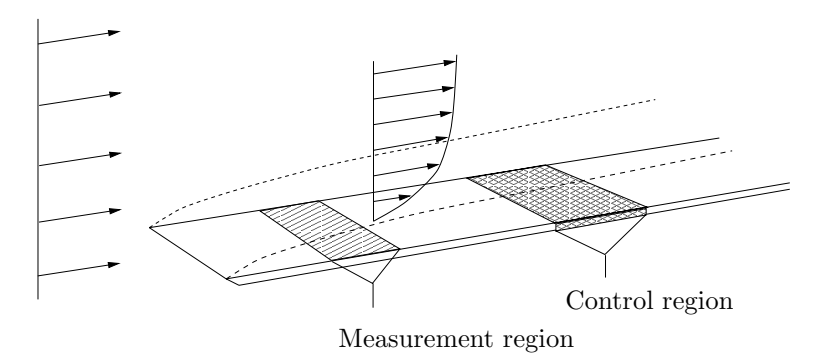


FIGURE 1.1. Schematic picture of measurement based control of boundary layer transition.

#### 1.2. Objectives

In figure 1.1 a hypothetical flow control situation is sketched. A homogeneous flow from the left flows past a flat plate on which a thin boundary layer develops. On the surface of the flat plate the fluid is at rest and at a short distance above the surface it has the speed of the freestream, the region in between where there is a rapid change in fluid velocity is the boundary layer. If the flow is perturbed in the boundary layer, for example by a surface roughness or free stream turbulence, these perturbations can grow and cause transition to turbulence. One goal of transition control is to be able to prevent this from happening. In an experiment this could mean that at some region of the surface of the plate measurements are made to obtain information about the state of the flow. This information is then used to compute an optimal normal velocity distribution to be applied in the control region and hopefully transition can be avoided or at least delayed.

The process of transition from laminar to turbulent flow is an area of intensive research and many of the secrets of the dynamics of this nonlinear process are yet to be revealed. Complicated processes leading to transition

such as the bypass transition scenarios with nonlinear effects are non-intuitive and can therefore be difficult to control. The goal of the current work is to determine how to control such processes in the optimal way given the method of controlling the flow, and an objective function describing the features of the flow to be controlled. In other words the problems studied can be viewed as the formulation and solution of an optimization problem. Exploring the many possibilities for flow control within this framework is necessary in order to identify efficient and feasible flow control schemes for practical use. One can also speculate that by doing this, it is possible study the results to gain insight into the physics of transition and perhaps identify key mechanisms of this complex process. The studies are limited to low Reynolds numbers and simple geometries where the bypass transition scenarios are dominating, and exponential primary instabilities are absent unless the mean flow profile has an inflection point. These flows are suitable to study in numerical experiments, and numerical methods as well as reliable simulation codes have been developed for these purposes. The transition scenarios considered in this work have been subject to intensive studies and the recent book by Schmid & Henningson (2001) covers many aspects of transition and contains most of the present knowledge in this field.

#### 1.3. Problem formulation issues

The complicated physics of a transitional flow makes it difficult to identify the key mechanisms to be targeted by an effective control scheme. Different physical properties of the flow can be affected by the controller through the choice of objective function, which therefore is an important part of the formulation of the optimization problem. In the present thesis a measure of the energy of flow perturbations is often used in the objective functions, but this is not in any way suggested to be the best choice for all cases. Other possibilities are e.g. drag, mass flux, vorticity or something that is not a quantity of the flow itself such as the transition point.

There are several possibilities to affect the flow of a fluid. Heating and cooling can be used to affect the viscosity of the fluid, application of magnetic and electrodynamic forces can be used when the fluid is conducting and blowing and suction through small holes can be used if the flow in bounded by a solid surface. Different methods are applicable to different situations and flow characteristics. The method of actuation chosen here is blowing and suction at solid walls since it is a fairly simple way of acting on the flow, and also because it is a technique that is widely used both in experimental and numerical studies. The blowing and suction is also restricted to have zero net mass flux, and this will limit the ability of the control to affect the mean flow but is suitable for controlling perturbations.

When the objective and the actuation technique is chosen the formulation of the optimization problem is basically done. The next step is to choose the equations to use for description of the flow that the optimal controller is to be designed for. The properties of the governing equations will also implicitly determine what methods can be used to solve the optimization problem. When the Navier–Stokes equations are used, an iterative optimization technique must be used due to the nonlinearities of the equations. If the governing equations are the linearized Navier–Stokes equations, the optimal solution can be found directly through the solution of Riccati equations. Once all choices have been made, the framework in which the control is developed is determined and it is also known in what sense the control will be optimal. It is important to remember in the nonlinear control case that the resulting control obtained is far from general, and only optimal with respect to the particular perturbation, and the discretization of the control. In the linear control case we can compute controllers that are independent of the initial perturbation and time, which makes this approach more general.

#### 1.4. Optimization methods

The optimization methods used in the present work are very general, and instead of giving a detailed description for the particular problems considered here a more general form is used to illustrate the methods. In particular one can look at a general real system of equations to get a picture of how the nonlinear and the linear optimization approaches are connected. There are many equivalent ways of formulating these problems, and a common method not discussed here is to use a Lagrangian multiplier technique, whereas an *adjoint* equation approach is used in this work. The papers in the second part of the thesis give more detailed information on these methods.

Consider a dynamical system described by the evolution equation,

$$\dot{\mathbf{x}} = \mathcal{A}(\mathbf{x}) + \mathcal{B}(\mathbf{x}, \mathbf{u}), \quad \mathbf{x}(t=0) = \mathbf{x}_0,$$

where the dot denotes a time derivative,  $\mathbf{x}$  is the state variable and  $\mathbf{u}$  represents a forcing. The operators  $\mathcal{A}$ , describing the dynamics, and  $\mathcal{B}$ , describing how the forcing affects the dynamics, can be dependent of the state corresponding to a nonlinear case or independent of the state in a linear case. The problem is now to find the function  $\mathbf{u}$  that minimizes an objective function,

$$\mathcal{J} = \frac{1}{2} \int_{0}^{T} \mathbf{x}^* \mathcal{C}_1^* \mathcal{C}_1 \mathbf{x} + \ell^2 \mathbf{u}^* \mathbf{u} \, \mathrm{d}t,$$

where the T denotes the time interval and an asterisk (\*) indicates a transpose. The quantity of the state to be minimized is measured through  $C_1$ . Assuming that  $\mathcal{B}(\mathbf{x})$  is given, the problem is to find  $\mathbf{u} = \mathbf{u}_+$  such that  $\mathcal{J}(\mathbf{u}_+) \leq \mathcal{J}(\mathbf{u})$  for all possible functions  $\mathbf{u}$ . We wish to find an expression for the gradient of  $\mathcal{J}$  with respect to  $\mathbf{u}$  in order to use gradient based optimization techniques to find  $\mathbf{u}_+$ . By defining the operator,

$$\mathcal{L}(\mathbf{x}) = \dot{\mathbf{x}} - \mathcal{A}(\mathbf{x}),$$

we can write the state equation as,

$$\mathcal{L}(\mathbf{x}) = \mathcal{B}(\mathbf{x}, \mathbf{u}), \quad \mathbf{x}(t=0) = \mathbf{x}_0.$$

To find the gradient with respect to  $\mathbf{u}$  we need to look at first variation of  $\mathcal{J}$ ,

$$\delta \mathcal{J} = \int_{0}^{T} \mathbf{x}^{*} \mathcal{C}_{1}^{*} \mathcal{C}_{1} \delta \mathbf{x} + \ell^{2} \mathbf{u}^{*} \delta \mathbf{u} \, dt \stackrel{\triangle}{=} \int_{0}^{T} \left( \frac{\mathrm{D} \mathcal{J}}{\mathrm{D} \mathbf{u}} \right)^{*} \delta \mathbf{u} \, dt,$$

and of the state equation,

$$\left(\nabla_{\mathbf{x}} \mathcal{L}(\mathbf{x}) - \nabla_{\mathbf{x}} \mathcal{B}(\mathbf{x}, \mathbf{u})\right) \delta \mathbf{x} = \nabla_{\mathbf{u}} \mathcal{B}(\mathbf{x}, \mathbf{u}) \delta \mathbf{u}, \quad \delta \mathbf{x}(t = 0) = 0.$$

Defining the inner product,

$$\langle \mathbf{p}, \delta \mathbf{u} \rangle = \int_{0}^{T} \mathbf{p}^* \cdot \delta \mathbf{u} \, \mathrm{d}t,$$

and using the adjoint identity,

$$\langle \mathbf{p}, \mathcal{N} \delta \mathbf{u} \rangle = \langle \mathcal{N}^* \mathbf{p}, \delta \mathbf{u} \rangle + \text{boundary terms},$$

allows us to define the adjoint equation,

$$\left(\nabla_{\mathbf{x}} \mathcal{L}(\mathbf{x}) - \nabla_{\mathbf{x}} \mathcal{B}(\mathbf{x}, \mathbf{u})\right)^* \mathbf{p} = \mathcal{C}_1^* \mathcal{C}_1 \mathbf{x}, \quad \mathbf{p}(t = T) = 0,$$

where  $\mathbf{p}$  denotes the adjoint state variables with properly defined boundary conditions. Combining the adjoint equation and the variational form of the objective-function gives us the gradient,

$$\frac{\mathrm{D}\mathcal{J}}{\mathrm{D}\mathbf{u}} = \left(\nabla_{\mathbf{u}}\,\mathcal{B}(\mathbf{x},\mathbf{u})\right)^{\star}\mathbf{p} + \ell^{2}\mathbf{u}.$$

Since the operators are nonlinear we need to iterate by updating the control in the opposite direction of the gradient and then compute the new gradient until a minima is reached.

#### $1.4.2.\ Linear\ equations$

If the operators in the previous section are linear we can use a direct technique to solve the optimization problem. This is because we can directly identify what the solution should be from the equations and compute it numerically. In the following the derivation is summarized and for mathematical details of this problem see e.g. Ito & Morris (1998). It is assumed that  $\mathcal{A}$  is a linear closed operator and that  $\mathcal{B}$  is linear and bounded. The equation can now be written,

$$\dot{\mathbf{x}} = A\mathbf{x} + B\mathbf{u}, \quad \mathbf{x}(t=0) = \mathbf{x}_0,$$

and the gradient expression becomes,

$$\frac{\mathrm{D}\mathcal{J}}{\mathrm{D}\mathbf{u}} = \mathcal{B}^{\star}\mathbf{p} + \ell^2\mathbf{u}.$$

By introducing a linear mapping such that,

$$\mathbf{p} = X(t) \mathbf{x}$$

where X self-adjoint and non-negative we can find the optimal solution by setting the gradient to zero. This gives a feedback law for  $\mathbf{u}$ ,

$$\mathbf{u} = \underbrace{-\frac{1}{\ell^2} \mathcal{B}^* X(t)}_{K(t)} \mathbf{x}.$$

Substituting the linear mapping and the feedback law into the adjoint equation and combining it with the state equation leads to an operator Riccati equation for X that has to be satisfied for any admissible  $\mathbf{x}$ ,

$$\left(\dot{X} + \mathcal{A}^*X + X\mathcal{A} - X\frac{1}{\ell^2}\mathcal{B}\mathcal{B}^*X + \mathcal{C}_1^*\mathcal{C}_1\right)\mathbf{x} = 0, \quad X(t = T) = 0.$$

If  $T \to \infty$  in the objective function we need to find the stationary solution to the Riccati equation to get the optimal time-independent feedback law.

A related problem is that of state estimation when only a noisy measurement of the state is assumed to be known. The objective is then to reconstruct the state from these measurements in an optimal fashion. Formulating this problem in the linear setting also leads to a Riccati equation similar to the one for the control problem. This optimal estimator is also known as a Kalman filter.

### 1.5. Governing equations

For the reader not familiar with the governing equations and the basic stability results forming the foundation for analysis of transition a short summary is given in this section. The flow of an incompressible Newtonian fluid is governed by the Navier–Stokes equations. In their dimensionless form they can be written using Cartesian tensor notation,

$$\frac{\partial u_i}{\partial t} + u_j \frac{\partial u_i}{\partial x_j} = -\frac{\partial \pi}{\partial x_i} + \frac{1}{Re} \frac{\partial^2 u_i}{\partial x_j^2},$$

$$\frac{\partial u_i}{\partial x_i} = 0,$$
(1.1)

where  $\{u_i\}_{i=1}^3$  are the velocity components and  $\pi$  is the pressure. The Reynolds number Re is composed of a length scale L, a velocity scale U and a viscosity scale  $\nu$  such that,

$$Re = \frac{UL}{\nu}$$
.

The choice of length scales and velocity scales depend on the particular flow considered. The centerline Reynolds number  $Re_{cl} = U_c h/\nu$  is often used for the laminar channel flow. It is based on the centerline velocity  $U_c$  and half the height of the channel h. For turbulent flows the skin-friction Reynolds number  $Re_{\tau} = \bar{u}_{\tau} h/\nu$  is commonly used. The velocity scale is here the mean

skin-friction velocity  $\bar{u}_{\tau} = \sqrt{\bar{\tau}_w/\rho}$ , where  $\bar{\tau}_w = \mu(\partial \bar{u}/\partial y)_{\text{wall}}$  is the mean skin friction on the walls. For boundary layer flows the displacement thickness  $\delta^*$  is used as the characteristic length scale and the freestream velocity  $U_{\infty}$  as velocity scale. This gives the displacement thickness Reynolds number  $Re_{\delta^*} = U_{\infty}\delta^*/\nu$ . The Navier-Stokes equations are also accompanied by boundary conditions, depending on the geometry, and initial conditions. On a solid surface it is common to apply a no-slip condition meaning that the fluid is at rest. In the case of control the boundary conditions can also be used to describe the actuation. If a fluid is flowing past a wall the velocity of the flow rapidly increases as we move away from the surface. This region where the velocity changes is known as the boundary layer and its thickness depends on the Reynolds number. In the boundary layer the flow is sensitive to perturbations and under certain conditions these can be unstable. By multiplying the Navier-Stokes equations (1.1) with  $u_i$  and integrating over a volume V with homogeneous boundary conditions we obtain the Reynolds-Orr equation describing the evolution of the perturbation energy  $E_V$ ,

$$\frac{\mathrm{d}E_V}{\mathrm{d}t} = -\int\limits_V u_i \, u_j \frac{\partial U_i}{\partial x_j} \, \mathrm{d}V - \frac{1}{Re} \int\limits_V \frac{\partial u_i}{\partial x_j} \frac{\partial u_i}{\partial x_j} \, \mathrm{d}V, \tag{1.2}$$

where  $U_i$  is used to denote the base flow. In the derivation of this equation the nonlinear terms have dropped out showing that the governing mechanism for energy growth is linear. The first integral on the right hand side represents the exchange of energy between the base flow and the perturbations and the second integral represent the viscous dissipation. If the energy of a perturbation reaches a sufficiently large amplitude, nonlinear effects become important and redistribute energy between different modes and there is a possibility for transition to turbulence. The importance of linear mechanisms for energy growth (see e.g. Henningson (1996)), motivates the use of the linearized Navier–Stokes equations.

A particular form of the linearized Navier–Stokes equations is obtained by linearizing around a base flow and then projecting the two dimensional equations on a divergence free manifold eliminating the pressure. The equation obtained through this procedure is,

$$\frac{\partial}{\partial t} \Delta v = -U \frac{\partial}{\partial x} \Delta v + U'' \frac{\partial v}{\partial x} + \frac{1}{Re} \Delta^2 v$$

$$v = v' = 0 \quad \text{at solid walls and in the far field,}$$
(1.3)

where v is the normal velocity and a prime (') is used to denote a normal derivative. When wave like perturbations are considered, equation (1.3) is known as the Orr–Sommerfeld equation. The drawback of the linearized equations is that they are only valid if the flow is spatially invariant, meaning that it has exactly the same characteristics no matter at what location it is considered. If the base flow changes, e.g. in the streamwise direction of a flat plate, the linear analysis only provides an approximation of the dynamics of the flow. Neglecting the effects of viscosity in the Orr–Sommerfeld equation, the Rayleigh

equation is obtained. Lord Rayleigh (1880) showed using this equation that the base flow must have an inflection point to support exponential instabilities. Fjørtoft (1950) strengthened this necessary criterion by showing that the inflection point must also be associated with a maximum of the spanwise mean vorticity. Under these conditions the flow can experience what is known as an inviscid instability. The Orr–Sommerfeld equation has for a long time been used to analyze wave like perturbations in a viscous flow in terms of eigenvalues and eigenvectors. If an eigenvalue is unstable, a perturbation exciting the corresponding eigenmode will grow at an exponential rate. These unstable eigenvalues can only be found for certain velocity profiles and if the Reynolds number is larger than a critical value.

The early focus in transition research was on growth and breakdown caused by so called Tollmien-Schlichting (TS) waves corresponding to unstable eigenvalues of the Orr-Sommerfeld equation. The critical value of the Reynolds number, above which unstable eigenvalues exist, has been determined for many flows, and in some cases they were found to be infinite even though the flow can indeed be turbulent. More conservative critical Reynolds numbers can be computed from the Reynolds-Orr equation but the most reliable values are those obtained from experiments. Morkovin (1969) noted that other mechanisms for transition were observed in experiments and that the TS-mechanism could be bypassed. The term bypass transition originates from this statement and basically includes all transition scenarios with perturbation growth not originating from a two dimensional exponential instability. In experiments investigating the turbulent bursting process, Kim, Kline & Reynolds (1971) noted that prior to a turbulent burst, low velocity fluid was lifted up from the wall. The underlying inviscid linear mechanism was analyzed by Landahl (1975) in order to explain burst regeneration. Landahl (1980) also studied this mechanism in the context of inviscid growth of localized disturbances, and the reported findings are referred to as the *lift-up* effect in the literature. The lift-up effect is the physical mechanism responsible for e.g. the generation and algebraic growth of streamwise streaks in a boundary layer.

When three dimensional perturbations are considered an additional equation is needed to describe the perturbations,

$$\frac{\partial \omega}{\partial t} = -U' \frac{\partial v}{\partial z} - U \frac{\partial \omega}{\partial x} + \frac{1}{Re} \Delta^2 \omega,$$

$$\omega = 0 \quad \text{at solid walls and in the far field.}$$
(1.4)

where  $\omega(=(\nabla \times \mathbf{u}) \cdot \mathbf{e}_2)$  is the normal vorticity. This equation is known as the Squire equation when wave like perturbations are considered. The eigenmodes of the combined Orr–Sommerfeld–Squire equations are not orthogonal and therefore a perturbation can experience transient growth even if all eigenvalues of the system are stable. The non-orthogonality allows destructive interference between different eigenmodes possibly resulting in an initial perturbation with low energy. If the modes then decay at different rates, the total energy of the perturbation will increase. Once the maximum distance between

the modes, measured in an energy like metric, has been reached the perturbation energy will start to decay. In the last decade this mechanism for energy growth has received much attention, see e.g. Gustavsson (1991); Butler & Farrell (1992); Reddy & Henningson (1993) and Trefethen *et al.* (1993).

#### 1.6. Flow control background

A complete review of all aspects of flow control would extend hundreds of years back in time but here only an attempt to cover the last decade or so is made. An extensive amount of work has been done in flow control in the past, and reviews of experimental and numerical work have been written on the subject by for example Moin & Bewley (1994), Joslin, Erlebacher & Hussaini (1996), Gad-el-Hak (1996), Lumley & Blossey (1998) and Bewley (2001). Articles mainly concerning the mathematical aspects of the optimization methods used for flow control can be found in the books edited by e.g. Gunzburger (1995) and Sritharan (1998). The focus in this section is on computational transition and turbulence control in boundary layer and channel flow. A nice recent review of computational efforts in flow control is also given by Hinze & Kunisch (2000) in an issue of Flow, Turbulence & Combustion devoted to adjoint methods and their applications.

#### 1.6.1. Laminar flow control

The most straightforward method to eliminate growth of perturbations is to stabilize the boundary layer by modifying the mean flow profile. This is one of few active flow control methods that has actually been attempted in flight experiments. The mean flow is then altered by applying distributed suction on the wing. A review of the efforts on laminar flow control can be found in Joslin (1998). Recently more advanced schemes using an optimized profile for the suction distribution have been developed. In Pralits, Hanifi & Henningson (2001) the parabolized stability equations (PSE) are used coupled with the boundary layer equations to minimize the perturbation energy through modification of the mean flow. Balakumar & Hall (1999) performed similar optimization to move the transition point as far downstream as possible given certain restrictions. Similar methods can also be used to optimize the geometry of e.g. a wing to get the desired properties.

#### 1.6.2. Wave cancellation

The paper by Thomas (1990) reviews the early efforts on the control of TS waves using an anti-phase control strategy. A brief review is given also by Metcalfe (1994). It is reported that experimental attempts to cancel TS waves have resulted in delay of transition but complete cancellation of the perturbations has never been obtained. One important issue in experiments is precise actuation, and many papers on experimental flow control are focused on determining the properties of a particular actuator and its effect for specific perturbations. Actuation is no problem numerically since it is just a matter of altering the

boundary conditions. It is difficult to find comparisons between experimental data and computational results since an experimental actuation device is not always properly modeled in the computations. Using direct numerical simulations, Laurien & Kleiser (1989) studied the possibilities of delaying and accelerating transition due to TS waves in a parallel Blasius boundary layer by local two dimensional blowing and suction. The report that the control is only effective if applied at an early stage of transition when the perturbations are still two dimensional, but even then complete cancellation is not obtained. A three dimensional base flow with localized perturbations was considered in the recent paper by Wassermann & Kloker (2000). They investigated control of crossflow vortex packets using a phase shifted modal control scheme with actuation through blowing and suction. They found that the phase shift needed to be individually adjusted for the different modes in order to achieve substantial reduction of perturbation energy.

#### 1.6.3. Opposition control

One of the most popular control strategies for numerical control of turbulence is opposition control. The term comes from the numerical investigation of Choi, Moin & Kim (1994) where a detection plane for the velocity was introduced in the flow at a distance  $y^+ \approx 10$  from the walls in a channel. The detected velocity was then phase shifted by 180° and applied as a boundary condition on the wall. With this method the drag in a turbulent channel at  $Re_{\tau} = 100$ was reduced by as much as 25% using the normal velocity and by 30% using the spanwise velocity. These results have inspired further research on similar methods, and the drag reduction obtained through this simple method has become somewhat of a benchmark for other schemes to be compared with. The dependence on the location of the detection plane was explored by e.g. Hammond, Bewley & Moin (1998). They investigated the control action and its effects, explaining why the control fails when the detection plane is to close or to far from the surface. The control strategy was also evaluated by Farrel & Ioannou (1996) by application to a linear system with the possibility to change the phase shift as well as the location of the detection plane. This approach enabled them to study the linear dynamics of the closed loop system with opposition control finding that the variance of their parameterized turbulence could be reduced as much as by 70% near the wall. Wind tunnel experiments were recently performed by Rebbeck & Choi (2001) using opposition control showing the possibility for drag reduction also in practice.

The physical mechanism behind the success of opposition control is related to manipulation of near-wall streamwise vortices. The scheme effectively moves the regions of high shear related to these vortices away from the wall and thereby reduces drag. An alternative way of treating the near wall vortices was reported by Koumoutsakos (1997) who applied control by prescribing the vorticity flux at the wall. An in phase control increases the vorticity flux and and out of phase control reduces it through cancellation of near wall vortices.

This idea was applied to a turbulent channel flow at  $Re_{\tau} = 180$  by Koumoutsakos (1999) resulting in a drag reduction of about 40% for the out of phase control. It should also be noted that this feedback control scheme only relies on measurements of the instantaneous pressure at the wall. In a recent paper Gmelin & Rist (2001) evaluates the direct feedback of wall vorticity flux for control of transition in boundary layers using direct numerical simulations and linear stability theory.

#### 1.6.4. Suboptimal control

Possible applications of gradient based optimal control techniques were identified and analyzed by Abergel & Temam (1990) and much of the current efforts on optimal flow control can be traced back to the ideas in this particular paper. Choi et al. (1993) introduced the concept of suboptimal control of a fluid system and applied it to the Burgers equation. The basic idea of suboptimal control is to avoid the large memory and computational time requirements for optimal control by using an objective function over one time step only. The methodology was applied to a turbulent channel flow at  $Re_{\tau} = 100$  by Bewley & Moin (1994) resulting in a 17% drag reduction. Even though this was less than what was obtained with opposition control this method was based on optimal control theory, which is a firm foundation, and has a potential for improvements. In practice a control scheme can only rely on measurable information that can be used to impose certain boundary conditions to the flow. Through analysis of the governing equation one can come up with boundary conditions that will minimize the instantaneous value of a specific objective function. The suboptimal control of Lee, Kim & Choi (1998) uses this idea to derive the optimal boundary conditions for minimizing a carefully designed objective function based on wall pressure fluctuations or wall shear stress, resulting in a skin friction drag reduction of up to 22%.

Lee et al. (1997) used a neural network to adaptively find a feedback law for the local wall shear stress to control turbulence using direct numerical simulations. They achieved about 20% drag reduction using this strategy, and also with a simple control scheme deduced from the optimized neural network drag reduction of the same order was achieved.

#### 1.6.5. Nonlinear control

The body of literature on this subject is huge and only work on channel and boundary layer flow is considered here, noting that investigations for other geometries and problem formulations can be very similar, see e.g. Gunzburger & Manservisi (2000) or Berggren (1998). The step from the suboptimal scheme to an optimal scheme is taken by extending the time interval over which optimization is performed. A particular type of objective function is the one used for receding horizon optimization, which means that a large time interval is divided into smaller parts, and then the control is optimized over these parts successively with only a penalty on the final state in each interval. It is possible

with this method to completely relaminarize a flow with turbulent initial conditions and this has been done using direct numerical simulations by Bewley, Moin & Temam (2001) and using large eddy simulations by Collis et al. (2000). In the investigations of Bewley, Moin & Temam (2001) it was found that the performance of the resulting control can differ widely depending on the choice of flow properties included in the objective function, which was also indicated by Lee, Kim & Choi (1998). A terminal measure of turbulent kinetic energy was found to be the most suitable one to use to obtain relaminarization. Hinze & Kunisch (2000) prefers the term sub-optimal also for the receding horizon control, but in theory it should be possible to use a long enough time interval to obtain relaminarization without the receding horizon technique. The increase in memory requirement can be avoided by using a check-pointing technique (see e.g. Berggren, Glowinski & Lions (1996)) at the expense of increased computational cost. In paper 2 in this thesis a direct numerical simulation code for solving the nonlinear optimal control problem in channel flow is developed and tested for controlling oblique wave perturbations. The code is developed do have a simple structure and to be suitable for extension to the spatial boundary layer flow. The approximative method of using the continuous equations to derive the control problem is also evaluated for a simple model problem in paper 1.

A problem setup similar to the one in figure 1.1 was studied for a two dimensional flow using direct numerical simulations by Joslin *et al.* (1997). The measurement region was located downstream of the actuation and they considered both a spatial boundary layer flow and a channel flow. The objective was to match the shear stress in the perturbed flow to that in a laminar flow on a portion of the wall. They reported that actuation through blowing and suction resulted in successful delay of transition due to TS waves in both channel flow and in the Blasius boundary layer.

#### 1.6.6. Linear control

The focus of flow control has to a large extent been on the problems of drag reduction and turbulence control. In many applications turbulence can be avoided initially but eventually there is transition to turbulence. If the control is applied during the transition process the need for turbulence control can perhaps be avoided. Since energy growth in a fluid flow is a linear process it makes sense that linear equations could be used to control transition. The findings reported by e.g. Henningson (1996); Farrel & Ioannou (1996); Kim & Lim (2000) about the importance of linear mechanisms for sustaining turbulence indicate that linear controllers could also be used to control turbulence.

Using the linearized equations for flow control is a fairly new concept. One early study was that of Bower *et al.* (1987) where the superposition control concept was evaluated using the Orr–Sommerfeld equations with periodic blowing and suction as boundary condition. A simple proportional control scheme based on measurements of wall shear was used by Hu & Bau (1994). They used

heating and cooling at the wall to modify the viscosity of the flow in order to suppress instabilities. In the aforementioned paper by Farrel & Ioannou (1996) the linear equations are used to evaluate the opposition control strategy. In Gmelin & Rist (2001) the performance of a wall vorticity flux feedback scheme is quantified e.g. by computations of neutral curves for the controlled linear system.

Classical control theory was applied to two dimensional perturbations in a laminar channel flow by Joshi, Speyer & Kim (1997). The control problem is based on a stream function formulation of the Orr–Sommerfeld equations. Blowing and suction actuation was computed using feedback of wall shear. By using a constant gain feedback integral compensator they could stabilize the flow and modify its properties. Modern control theory was used to compute optimal ( $\mathcal{H}_2$ ) controllers using this stream function formulation in Joshi, Speyer, & Kim (1999). The same formulation has also been used to develop reduced order robust controllers for the multi wavenumber case in Cortelezzi & Speyer (1998) and Cortelezzi *et al.* (1998). Recently Baramov, Tutty & Rogers (2000) used a similar approach to develop robust ( $\mathcal{H}_{\infty}$ ) controllers, accounting for effects of localized actuation. The two dimensional controllers were extended for application to three dimensional flows by augmenting an *ad hoc* scheme in the third dimension in Lee *et al.* (2001). For a turbulent channel flow at  $Re_{\tau} = 100$  this scheme resulted in a drag reduction of 17%.

Three dimensional perturbations were considered by Bewley & Liu (1998) where both optimal and robust control strategies were evaluated for both suband supercritical Reynolds numbers at isolated wavenumbers in a linearized channel flow. A problem formulation for three dimensional perturbations is also discussed in Kang et al. (1999) and for multiple wavenumbers in Kang, Cortelezzi & Speyer (1999). The key property utilized in these three papers is the decoupling of different wave number pairs when the Orr-Sommerfeld-Squire equations are used. It was suggested in Bewley & Liu (1998) that the optimal control for the full physical system could be obtained through an inverse Fourier transform of optimal controllers computed for an array of wave number pairs. Bamieh, Paganini, & Dahleh (2000) reports that such optimal control laws, computed for a spatially invariant distributed system, should be spatially localized with exponentially decaying tails. In paper 3 in the present thesis, localized feedback laws for both control and estimation are computed using a slightly modified version of the problem formulation in Bewley & Liu (1998). The performance of these controllers and estimators is quantified in terms of their ability to prevent transition in paper 4. A simple nonlinear extension through gain scheduling is introduced together with a modification of the objective function in paper 3 and shown to be sufficient in order to relaminarize a low Reynolds number (  $Re_{\tau} = 100$  ) turbulent channel flow. Section 3.5.3 in this thesis, contains recent results showing that relaminarization of the same turbulent flow can also be obtained without gain scheduling using a fully linear

state feedback controller. A comparison with the nonlinear optimal control is performed in paper 5 to demonstrate consistency between the two methods.

The advantage of using control theory is that the optimization problem can be solved off-line independently of the particular perturbation to the flow. Unfortunately the control tools are developed for dynamical systems that can be written in the standard form  $\dot{\mathbf{x}} = A\mathbf{x}$  and this is, today, only manageable for simple flows and geometries. For spatially developing flows the iterative, adjoint based optimization technique is more suitable even when the governing equations used are linear. Cathalifaud & Luchini (2000) considered control of the spatially developing laminar flow over a flat-, as well as a concavewall with optimal perturbations using the the boundary layer equations. They computed distributions of blowing and suction that successfully minimized the objective functions penalizing terminal values, or an integral over time, of the perturbation energy. In Walter, Airiau & Bottaro (2001) a similar problem is studied using the linear PSE focusing on TS wave perturbations. A possible advantage of using PSE is that non-parallel effects are accounted for, and it is also easy to extend to include weak nonlinear effects. In paper 7 the linear controllers developed in the present work for parallel flows are shown to be applicable also in the spatial setting. Successful suppression of exponential instabilities as well as transiently growing perturbations is obtained even when the perturbation amplitude is large.

#### 1.7. Thesis outline

The main focus of the work in this thesis is the second part of the measurement based control strategy where the information about the state of the flow is assumed to be available. The question is then how to use this information in the optimal way. The optimization techniques described in section 1.4 can be applied to these flow control problems using either linear or nonlinear equations. In order to test different strategies a simpler flow than the one depicted in figure 1.1 is studied initially, namely the flow in a channel between two parallel infinite walls. The results from this simple flow case is then extended to more complicated situations. The application of nonlinear adjoint based optimization technique to control of the Navier-Stokes equations for flow in a channel is described briefly in chapter 2 based on the work in papers 1 and 2. The linear control theory and its application to flow control and estimation in papers 3, 4 and 5 is discussed in chapter 3. In chapter 4 the work from paper 7 about application of the linear controller to spatially evolving flows is discussed for different flow situations and perturbations. Implications for the secondary instabilities studied in paper 6 are also discussed. Finally a brief discussion of the main results and suggestions for future work is presented in chapter 5, and quick guide to the papers included in this thesis and the contribution of the respective authors is given in chapter 6.

#### CHAPTER 2

# Nonlinear control

When applying the nonlinear approach to compute optimal controls an iterative optimization technique must be used due to the nonlinearities in the state equation. These nonlinearities prevent direct solution of the optimization problem since the solution cannot be identified directly from the equations. To do iterative optimization, information about the gradient of the objective function can be used. The alternative to use an optimization approach that is not based on gradient information is not feasible due to the high dimensionality of the problem. An efficient method for obtaining gradient information is the adjoint equation approach. Only two numerical simulations are then required independently of the number of degrees of freedom. The drawback of this approach compared to other ways to compute the gradient is that information must be saved about the whole solution of the equations in space and time. This requires a lot of computer memory. From a practical point of view this type of control is not very useful since it will only work for exactly the flow perturbation that has been studied. On the other hand important details about the nonlinear mechanisms involved could be revealed since these are accounted for by the resulting optimal control. The approach is also easily extended to a robust formulation accounting for the worst case disturbance as described by Bewley, Temam & Ziane (2000). A control that is robust in this sense can be applied in more general situations.

#### 2.1. Control problem

Considering nonlinear control, the governing equations are the incompressible Navier–Stokes equations in dimensionless form,

$$\frac{\partial \mathbf{u}}{\partial t} + (\mathbf{u} \cdot \nabla)\mathbf{u} = -\nabla \pi + \frac{1}{Re_{cl}} \nabla^2 \mathbf{u},$$

$$\nabla \cdot \mathbf{u} = 0,$$
(2.1)

where  $\mathbf{u}$  is the velocity vector,  $\pi$  is the pressure and  $Re_{cl}$  denotes the Reynolds number of the flow. The equations are complemented by boundary and initial conditions. Consider the flow in a channel that is periodic in x and z, illustrated in figure 2.1, driven by a condition that keeps the mass-flux constant. The alternative of using a constant pressure gradient to force the flow would explicitly determine the mean drag in the channel and applying boundary control would

Upper control surface  $\Gamma_U$  U(y) z Lower control surface  $\Gamma_L$ 

Figure 2.1. Geometry of flow domain  $\Omega$  for channel flow simulations.

not change that. The flow is laminar and has an initial perturbation of some kind that will cause energy growth and perhaps also transition to turbulence.

Control is applied through blowing and suction normal to the channel walls  $\Gamma_U$  and  $\Gamma_L$  and is restricted to have a zero net mass flux. The control has a continuous distribution over the wall and is represented by number of sinusoidal modes. The velocity components in the horizontal directions are subject to a no-slip condition on the walls.

The objective function describing what will be minimized by the control contains a measure of the energy of the perturbation to the laminar flow. A measure of the control input is also included to regularize the optimization problem and bound the control energy used. It is also useful to allow the time interval which the objective function covers be variable in order to be able to modify the optimization problem. Using  $\varphi$  to denote the control the objective function is,

$$J(\varphi) = \frac{\varepsilon}{2} \int_{T_1^c}^{T_2^c} \int_{\Gamma} |v|^2 d\Gamma dt + \frac{1}{2} \int_{T_1^o}^{T_2^o} \int_{\Omega} (\mathbf{u} - \mathbf{u}_T)^2 d\Omega dt, \qquad (2.2)$$

where  $v = \mathbf{e_2} \cdot \mathbf{u}$ ,  $(T_1^c, T_2^c)$  is the control time period and  $(T_1^o, T_2^o)$  is the observation time period. The target velocity profile is denoted  $u_T$  and  $\varepsilon$  is the regularization parameter. The optimization problem is then: find  $\varphi^*$  which satisfies,

$$J(\varphi^*) \le J(\varphi) \quad \forall \ v(\varphi)|_{\Gamma} \in \mathcal{U}_{ad},$$

where  $\mathcal{U}_{\mathrm{ad}}$  denotes the set of admissible controls.

#### 2.2. Model problem

The proper way of deriving the adjoint equations is to use the discretized version of the equations and objective function and derive the discrete adjoint equation from them. This can however be a much more difficult derivation than starting from the continuous equations. By studying a model problem for shear flow instabilities the effect of the approximation of using the continuous equations could be investigated. By solving the same optimization problem using a spectral method for the approximative formulation and a finite element method (FEM) with an exact formulation, the differences could be evaluated. The details of this study is reported in paper 1 in this thesis. Considering the

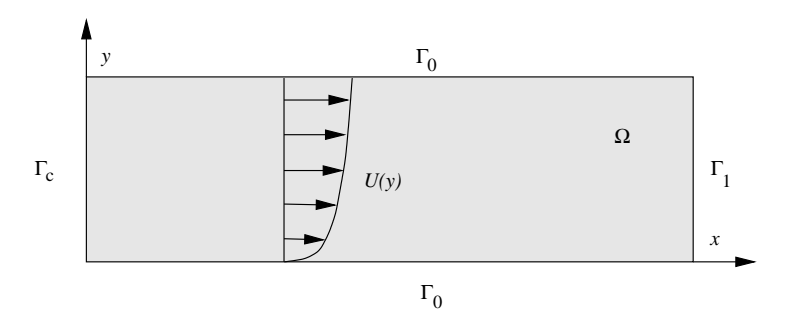


FIGURE 2.2. The computational domain studied in the model problem.

scalar advection diffusion equation,

$$u_t + U(y) u_x - \alpha u - \frac{1}{R} \Delta u = f \qquad \text{in } Q = \Omega \times (0, T),$$

$$u = 0 \qquad \text{on } \Sigma_0 = \Gamma_0 \times (0, T),$$

$$u = \varphi \qquad \text{on } \Sigma_c = \Gamma_c \times (0, T),$$

$$\frac{R}{2} U(y) u - u_x = 0 \qquad \text{on } \Sigma_1 = \Gamma_1 \times (0, T),$$

$$u(t = 0) = u_0,$$

in a two dimensional domain  $\Omega$  with the boundary  $\Gamma$  depicted in figure 2.2. The indices t or x denote a derivative in time or space and the velocity profile,

$$U(y) = (1 - e^{-y})/(1 - e^{-y_{\text{max}}}),$$

is chosen to mimic a boundary layer profile. Control is applied through the boundary condition for u on the inflow boundary  $\Gamma_c$  and the boundary condition on the outflow boundary  $\Gamma_1$  is non-reflecting. For the optimization problem the objective function is,

$$J(\varphi) = \frac{\varepsilon}{2} \int_{\Sigma_c} \varphi^2 \, d\Sigma + \frac{1}{2} \int_{Q} u^2 \, dQ,$$

where  $\varepsilon$  is the regularization parameter. Optimization using information about the gradient of the objective function is then performed using a standard conjugate gradient method.

#### 2.2.1. Continuous formulation

A solver for the optimization problem derived from the continuous equations was implemented using a Chebyshev collocation method to give good accuracy. The gradient of the objective function in the continuous formulation is,

$$\nabla J(\varphi) = \varepsilon \varphi + \frac{1}{R} p_x \Big|_{\Gamma_c}, \tag{2.3}$$

where p is the solution to the associated adjoint equation.

#### 2.2.2. Discrete formulation

A finite element discretization was made of both the state equation and the objective function. Then the associated discrete adjoint equation was derived based on the discrete equations. This results in an optimization problem where the gradient is obtained to machine precision of the computer. In the fully discrete case, the gradient is a vector  $\nabla J_h^{\Delta t}$  of dimension  $N \times M$ , where N is the number of time steps and M is the number of mesh points on the  $\Gamma_c$  boundary, excluding the corner points. Each component of this vector is evaluated by computing,

$$(\nabla J_h^{\Delta t})_{i,n} = \varepsilon \int_{\Gamma_c} w^i \varphi_n \, d\Gamma + \int_{\Omega} u^n w^i \, d\Omega$$
$$- \int_{\Omega} w^i \left[ \left( \frac{1}{\Delta t} - \alpha \right) p^n - p^{n+1} \right] d\Omega$$
$$- \frac{1}{R} \int_{\Omega} \nabla p^n \cdot \nabla w^i \, d\Omega - \int_{\Omega} U p^{n+1} w_x^i \, d\Omega,$$
 (2.4)

where n = 1, ..., N, i = 1, ..., M, and where  $w^i$  are the base functions of the FEM discretization such that it is 1 at node i on  $\Gamma_c$  and zero at all other nodes of the triangulation. In expression (2.4), the fully discrete co-states  $\{p^n\}_{n=1}^N$  are obtained by solving the corresponding discrete adjoint equation.

It is clear that the gradient expression (2.4) would not be obtained by simply discretizing the continuous expression (2.3). Also the discrete adjoint equation differs substantially from what is obtained by discretizing the continuous counterpart.

#### 2.2.3. Comparing the formulations

Comparing the two methods was mainly performed in terms of convergence rate. In particular the dependence on the different numbers of degrees of freedom, or resolution, and the parameters  $\alpha$  and R was studied. A typical plot of

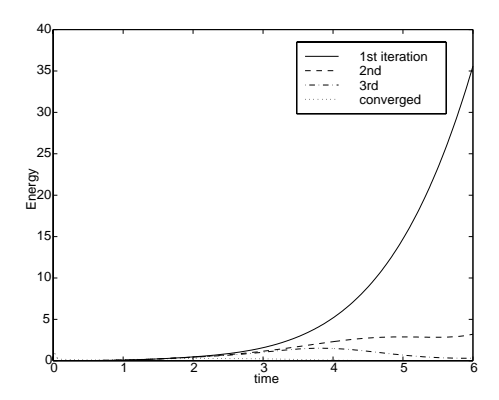


FIGURE 2.3. Energy growth in box at different stages of optimization. R=50 and  $\alpha=1.5$ 

the reduction in the gradient norm shows a large drop for the first iterations using either method. The curve then flattens out and from the slope of the curve in this region the convergence rate is computed. The fully discrete formulation was found to have faster convergence in general, and the dependence on the parameters and the resolution was larger for the continuous formulation. The conclusion from this study was that using the adjoint equations derived from the continuous formulation was sufficient to get close to the optimal solution of the control problem. Especially when focusing on controlling strong instabilities the approximate formulation was found to be sufficient. In figure 2.3 it is shown that the strong instability is taken care of in the first few iterations of the optimization, and the additional iterations required to reach the optimal solution is merely a fine tuning of the control. Despite the differences in convergence rate, the performance in the initial steps of the optimization was found to be similar for both formulations. It was also observed that convergence rate for the later iterations decreased rapidly with increasing R. This indicates that the computational cost will increase when applying this methodology to high Reynolds number flows since a larger number of iterations will required to find the optimal solution.

#### 2.3. Derivation and Implementation

Motivated by the findings from the model problem, the continuous equations are used to derive the adjoint equations for the nonlinear optimization problem. The drawback is that only an approximation of the true optimal solution will be obtained. In order to decrease the sensitivity to changes in the number of degrees of freedom in time of the control a parameterization of the control in time was found to be useful. The full derivation of the adjoint equation and gradient expression is given in paper 2 in this thesis.

To facilitate efficient implementation and solution of the optimization problem the existing spectral channel flow code of Lundbladh, Henningson & Johansson (1992) was used as a template for the optimization code. The code uses Fourier modes in the periodic directions and Chebyshev polynomials in the wall normal direction with either a collocation or tau method. The time stepping scheme is a four step Runge–Kutta method for the advective terms and a Crank-Nicholson method for the viscous terms. The solver is based on a velocity-vorticity  $(v - \omega)$  formulation of the Navier–Stokes equations, and therefore the adjoint equations need to be put in that form prior to implementation as well. The Navier–Stokes equations (2.1) in  $v - \omega$  form are (Benney & Gustavsson (1981)),

$$\begin{split} \frac{\partial \Delta v}{\partial t} &= \left(\frac{\partial^2}{\partial x^2} + \frac{\partial^2}{\partial z^2}\right) H_2 - \frac{\partial}{\partial y} \left(\frac{\partial H_1}{\partial x} + \frac{\partial H_1}{\partial z}\right) + \frac{1}{Re_{cl}} \Delta^2 v, \\ \frac{\partial \omega}{\partial t} &= \frac{\partial H_1}{\partial z} - \frac{\partial H_3}{\partial x} + \frac{1}{Re_{cl}} \Delta \omega, \end{split} \tag{2.5}$$

where  $H = \mathbf{u} \times (\nabla \times \mathbf{u})$ . Using the objective function 2.2 the gradient is,

$$\frac{\partial J}{\partial \varphi_L} = \int_{\Gamma_L} \psi_L \left( \varepsilon \varphi_L^T \psi_L - \sigma \right) d\Gamma, \tag{2.6}$$

and

$$\frac{\partial J}{\partial \varphi_U} = \int_{\Gamma_U} \psi_L \left( \varepsilon \varphi_U^T \psi_L + \sigma \right) d\Gamma. \tag{2.7}$$

where  $\psi$  denotes the base functions for the control, the index L and U denotes the lower and upper wall respectively, and  $\sigma$  denotes the adjoint pressure. The adjoint equation in the form corresponding to  $v - \omega$  for the adjoint states is

$$-\frac{\partial \Delta p_{2}}{\partial t} = \left(\frac{\partial^{2}}{\partial x^{2}} + \frac{\partial^{2}}{\partial z^{2}}\right) \tilde{H}_{2} - \frac{\partial}{\partial y} \left(\frac{\partial \tilde{H}_{1}}{\partial x} + \frac{\partial \tilde{H}_{1}}{\partial z}\right) + \frac{1}{Re_{cl}} \Delta^{2} p_{2},$$

$$-\frac{\partial \left(\nabla \times \mathbf{p}\right)_{2}}{\partial t} = \frac{\partial \tilde{H}_{1}}{\partial z} - \frac{\partial \tilde{H}_{3}}{\partial x} + \frac{1}{Re_{cl}} \Delta \left(\nabla \times \mathbf{p}\right)_{2},$$
(2.8)

where  $\mathbf{p} = (p_1, p_2, p_3)$  denotes the adjoint states and,

$$\tilde{H} = -\mathbf{u} \times (\nabla \times \mathbf{p}) + 2(\nabla \mathbf{p})^T \mathbf{u} + \chi[T_1^o, T_2^o](\mathbf{u} - \mathbf{u}_T).$$

The function  $\chi[t_1, t_2]$  is such that it is one if  $t \in [t_1, t_2]$  and zero otherwise. The adjoint equations are solved backwards in time. Considering this, equations (2.5) and (2.8) are identical except for the expressions for H and  $\tilde{H}$ , and the same solver can be used for both equations with only small modifications.

Since the advantage of the  $v-\omega$  formulation is that pressure is eliminated the adjoint pressure is not solved for explicitly. Fortunately its gradients can

easily be evaluated on the walls through the expression,

$$\sigma_{x}\Big|_{W} = \frac{1}{Re_{cl}} \frac{\partial^{2} p_{1}}{\partial y^{2}}\Big|_{W} + v \frac{\partial p_{1}}{\partial y}\Big|_{W},$$

$$\sigma_{z}\Big|_{W} = \frac{1}{Re_{cl}} \frac{\partial^{2} p_{3}}{\partial y^{2}}\Big|_{W} + v \frac{\partial p_{3}}{\partial y}\Big|_{W},$$

where W denotes either wall. From this information we can then compute the objective function gradient by integrating to get the adjoint pressure on the walls. Note that we cannot get the constant part of the adjoint pressure but it is not needed since zero mass flux control is considered. A check of how accurately the gradients of the objective function are computed can be done by comparison with a finite difference computation. By perturbing the control at every degree of freedom we can compute the finite difference gradient and then it can be compared to the one computed using the adjoint equations. Testing this for a few difference sets shows that the error obtained by computing the norm of the difference between the normalized gradients obtained from the finite difference and adjoint computations respectively is less than 1% in the initial iterations.

#### 2.3.1. Optimization

When the gradient has been determined, and standard gradient based optimization algorithm can be applied to solve the problem. A steepest descent approach is not so efficient, and a conjugate gradient algorithm is not well suited for non-linear problems. Instead a limited memory quasi Newton approach called L-BFGS-B described in Byrd et al. (1994) is used for the nonlinear optimal control problem. This algorithm was downloaded from the Internet and included in the code without modifications.

#### 2.4. Control of oblique waves

Optimal control of transition initiated by oblique waves applying the methodology outlined in this chapter is attempted to evaluate the code before further development.

#### 2.4.1. Transition scenario

The transition scenario involving oblique waves as initial perturbation is a four-stage process. Oblique waves force streamwise vortices that through the *lift-up* mechanism creates streamwise streaks that can breakdown to turbulence through secondary instabilities. From the linearized equations the transient energy growth associated with the formation of the streaks is found to be due to the non-orthogonality of the eigenmodes of the system. This mechanism for energy growth is thoroughly studied and explained in e.g. Gustavsson (1991); Butler & Farrell (1992); Reddy & Henningson (1993) and Trefethen *et al.* (1993). The breakdown process of the streaks due to the secondary instability is under active investigation, the recent experimental work of e.g. Westin *et al.* (1994),

Matsubara & Alfredsson (2001) and Elofsson (1998) has increased the physical understanding and so has numerical studies by e.g. Berlin *et al.* (1999).

#### 2.4.2. Control

Control is applied at the different stages of the transition scenario to investigate how sensitive the control is to different initial conditions.

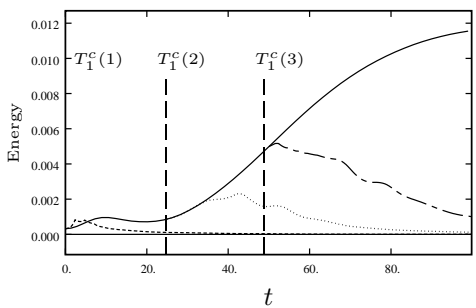


FIGURE 2.4. solid: The energy growth without control; dashed: case 1; dotted: case 2; dash-dot: case 3.

Figure 2.4 shows the energy evolution of controlled flow in a channel where the initial condition is a pair of oblique waves and  $Re_{cl} = 2000$ . The control is allowed to act in all Fourier modes of the simulation and is distributed with 20 degrees of freedom in time. In all cases the observation starts at t = 50 and continues until the end of the simulation, and once the control has been turned on it remains so until the end of the simulation.

First control is applied from t=0, denoted case 1, and the energy growth is initially slightly larger than in the uncontrolled case, but thereafter the energy rapidly decays. In this case the control acts on the oblique waves directly preventing them from inducing strong streamwise vortices. In case 2 the streamwise vortices have already formed and control is applied at t=25. Initially the energy follows the curve for the uncontrolled case but then at approximately t=35 it starts decaying. Finally in case 3 the control is applied at t=50 to the growing streaks. In this case the energy also follows the curve for the uncontrolled case until t=55 before it starts decaying. It should be noted that there is a difference between the cases in terms of how large fraction of the control interval that is overlapping the observation interval which makes it hard to draw specific conclusions. At least we can conclude that the control can handle the different stages of the transition process.

In all cases about 10-15 iterations of the optimization algorithm was needed to reach a converged solution with the criterion that the reduction of the objective function was close to zero in the last iteration. The reduction of the gradient norm was about three orders of magnitude. These results indicate that using the continuous formulation of the optimization problem is feasible for this type of scenario.

#### CHAPTER 3

# Linear control and estimation

Using the linear equations opens up for the use of modern control theory techniques. With an objective function over infinite time, we can get a time independent solution of the optimal control problem. We can then apply this control online in direct numerical simulations of different transition scenarios, and using a gain scheduling technique also to turbulence. The need for gain scheduling is due to that the change in the mean flow profile, which we have used to linearize the equations, is large from a laminar to a turbulent flow. The main drawbacks of this approach is that is neither considers the nonlinear terms of the equations governing the flow nor the evolution of the mean flow profile and non-parallel effects.

When designing linear controllers and estimators the starting point is the linearized Navier–Stokes equations known as the Orr–Sommerfeld–Squire equations governing the evolution of small perturbations  $\{v,\omega\}$  to a laminar flow U(y). These equations may be written using a Fourier representation at each wavenumber pair  $\{k_x, k_z\}$  as

$$\dot{\hat{v}} = \underbrace{\hat{\Delta}^{-1} \left\{ -i \, k_x \, U \, \hat{\Delta} + i \, k_x \, U'' + \hat{\Delta} (\hat{\Delta} / Re_{cl}) \right\}}_{\mathcal{L}_{OS}} \, \hat{v}, \tag{3.1a}$$

$$\dot{\hat{\omega}} = \underbrace{\{-i \, k_z \, U'\}}_{\mathcal{L}_C} \, \hat{v} + \underbrace{\{-i \, k_x \, U + \hat{\Delta}/Re_{cl}\}}_{\mathcal{L}_{SQ}} \, \hat{\omega}, \tag{3.1b}$$

where  $\hat{\Delta} \equiv \partial^2/\partial y^2 - k_x^2 - k_z^2$  and hat (^) denotes Fourier coefficients and a prime (') denotes a derivative with respect to y. Note that  $\hat{\Delta}$  is invertible only if the boundary conditions are included. The Reynolds number  $Re_{cl} = U_c h/\nu$  parameterizes the problem, where h is the half-width of the channel,  $U_c$  is the centerline velocity, and  $\nu$  is the kinematic viscosity of the fluid. The boundary conditions are  $\hat{\omega}(y=\pm 1)=\partial \hat{v}/\partial y(y=\pm 1)=0$  and  $\hat{v}(y=\pm 1)=\hat{\phi}_{\pm 1}$  where  $\hat{\phi}_{\pm 1}$  is the control signal on the upper and lower wall. Since these equations are linear and decoupled for different wavenumber pairs it is possible to develop controllers and estimators using optimal control theory for each wavenumber separately. These can then be combined into a physical space controller or estimator through an inverse Fourier transform. Paper 3 contains a detailed description of how this is done and the key points are summarized in the following sections.

#### 3.1. Controller

To be able to apply modern optimal control theory to a dynamical system it is first put in a standard form. In order to obtain this standard form the control needs to be parameterized and expressed as a forcing term instead of a boundary condition to the equations. Since the system is linear the superposition principle can be utilized to lift the boundary conditions and give the desired form. In principle this lifting can be done using any continuous function satisfying the boundary conditions of the problem. One possible choice, used here, is the stationary solution to the inhomogeneous problem with the boundary conditions to be parameterized set to unity. The system can then be written,

$$\dot{\hat{x}} = \hat{A}\,\hat{x} + \hat{B}\,\hat{u},\tag{3.2}$$

where,

$$\hat{x} = \begin{bmatrix} \hat{x}_h \\ \hat{\phi}_{\pm 1} \end{bmatrix}, \quad \hat{A} = \begin{bmatrix} \hat{N} & \hat{N}\hat{Z} \\ 0 & 0 \end{bmatrix}, \quad \hat{B} = \begin{bmatrix} -\hat{Z} \\ I \end{bmatrix}, \quad \hat{u} = \dot{\hat{\phi}}_{\pm 1}, \tag{3.3}$$

and,

$$\hat{N} = \begin{bmatrix} \mathcal{L}_{OS} & 0 \\ \mathcal{L}_{C} & \mathcal{L}_{SQ} \end{bmatrix}, \quad \begin{bmatrix} \hat{v} \\ \hat{\omega} \end{bmatrix} = \begin{bmatrix} \hat{v}_h \\ \hat{\omega}_h \end{bmatrix} + \begin{bmatrix} \hat{v}_p \\ \hat{\omega}_p \end{bmatrix} = \hat{x}_h + \hat{Z}\hat{\phi}_{\pm 1}, \tag{3.4}$$

where the index h denotes the homogeneous part of the solution and p denotes the particular solution used for lifting the boundary condition. In order to formulate the optimization problem an energy measure is introduced such that,

$$\hat{E} = \frac{1}{8 k^2} \int_{-1}^{1} f(y) \left( k^2 |\hat{v}|^2 + \left| \frac{\partial \hat{v}}{\partial y} \right|^2 + |\hat{\omega}|^2 \right) dy = \begin{bmatrix} \hat{v}^* & \hat{\omega}^* \end{bmatrix} \hat{Q} \begin{bmatrix} \hat{v} \\ \hat{\omega} \end{bmatrix}, \quad (3.5)$$

where  $k^2 = k_x^2 + k_z^2$  and f(y) is a weighting function that allows modification of the energy measure and that is equal to one unless otherwise stated. For the case when the flow is divided into a homogeneous and a particular part the energy measure becomes,

$$\hat{E} = \hat{x}^* \begin{bmatrix} \hat{Q} & \hat{Q}\hat{Z} \\ \hat{Z}^*\hat{Q} & \hat{Z}^*\hat{Q}\hat{Z} \end{bmatrix} \hat{x} = \hat{x}^*\hat{Q}\hat{x}.$$

From modern control theory we know that the feedback law  $\hat{K}$  in,

$$\hat{u} = \hat{K}\hat{x},\tag{3.6}$$

minimizing the objective function,

$$\hat{J} = \int_{0}^{\infty} \left( \hat{x}^* \hat{\mathcal{Q}} \hat{x} + \ell^2 \, \hat{u}^* \hat{u} \right) dt, \tag{3.7}$$

is given by the non-negative self-adjoint solution  $\hat{X}$  of the Riccati equation,

$$\left(\hat{X}\hat{A} + \hat{A}^*\hat{X} - \frac{1}{\ell^2}\hat{X}\hat{B}\hat{B}^*\hat{X} + \hat{Q}\right)\hat{x} = 0, \quad \forall \text{ admissible } \hat{x}, \tag{3.8}$$

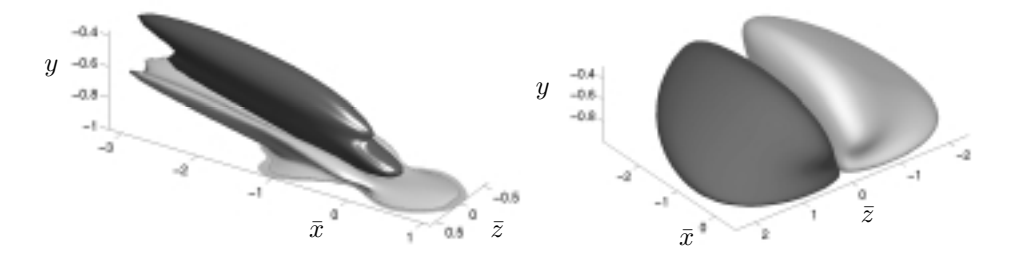


FIGURE 3.1. Localized controller gains for  $Re_{cl}=2000$  with  $\ell^2=0.01$  relating the state x inside the domain to the control forcing u at the point  $\{x=0,y=-1,z=0\}$  on the wall: visualized are a positive and negative isosurface at of the convolution kernels for (left) the wall-normal component of velocity at  $\pm 100$  and (right) the wall-normal component of vorticity at  $\pm 1$ .

through the relation,

$$\hat{K} = -\frac{1}{\ell^2} \hat{B}^* \hat{X}. \tag{3.9}$$

Notice that this feedback law uses only the homogeneous part of the flow inside the channel. It can easily be modified to be a feedback law for the full flow field by subtracting the contribution from the (known) inhomogeneous part. Optimal feedback laws can then be computed for a large number of wave number pairs that sufficiently resolves the dynamics of the system and combined in an inverse Fourier transform to yield a physical space control law described by convolution kernels. The control signal in physical space can then be computed through the convolution integral,

$$\dot{\phi}_{\pm 1}(x,z,t) = \int_{\Omega} \left( k_{\pm 1,v}(x-\bar{x},\bar{y},z-\bar{z}) \ v(\bar{x},\bar{y},\bar{z},t) + k_{\pm 1,\omega}(x-\bar{x},\bar{y},z-\bar{z}) \ \omega(\bar{x},\bar{y},\bar{z},t) \right) d\bar{x} \, d\bar{y} \, d\bar{z},$$

$$(3.10)$$

where  $k_{\pm 1,v}$  and  $k_{\pm 1,\omega}$  are the v and  $\omega$  components of the feedback law for the upper and lower wall. In figure 3.1 feedback kernels for the control are depicted as isosurfaces to illustrate their structure. Both the kernel for the normal velocity and the one for normal vorticity are elongated in the upstream direction and they also angle away from the wall. This makes sense from a physical point of view since the kernels then account for the convective time delay of the perturbations due to the change in the base flow velocity profile in the normal direction. The controller then "knows" that perturbations near the wall move slower than they do closer to the center of the channel.

# 3.1.1. Properties of $\hat{X}$

We have already seen that the Riccati equation provides the optimal solution in section 1.4, where  $\hat{X}$  was introduced as the linear mapping between the state and the adjoint state. To get a feeling for what the solution to the Riccati equation (3.8) represents one can look at the problem from a different perspective. Consider the closed loop system obtained by inserting (3.9) via (3.6) into (3.2),

$$\dot{\hat{x}} = \left(\hat{A} - \frac{1}{\ell^2}\hat{B}\hat{B}^*\hat{X}\right)\hat{x}.\tag{3.11}$$

Introduce a scalar measure V of the perturbations such that,

$$V = \hat{x}^* \hat{X} \hat{x}.$$

where  $\hat{X}$  is self-adjoint, positive and independent of time. By taking the time derivative of this measure an expression for the evolution of this scalar quantity is obtained. This can be written as,

$$\dot{V} = \dot{\hat{x}}^* \hat{X} \hat{x} + \hat{x}^* \hat{X} \dot{\hat{x}}.$$

Inserting (3.11) and performing some algebra results in,

$$\dot{V} = \hat{x}^* \left( \hat{X} \hat{A} + \hat{A}^* \hat{X} - \frac{2}{\ell^2} \hat{X} \hat{B} \hat{B}^* \hat{X} \right) \hat{x}. \tag{3.12}$$

If  $\hat{X} = \hat{Q}$  this would correspond to the Reynolds–Orr equation (1.2) with control, neglecting nonlinear terms. Notice that any self-adjoint, positive  $\hat{X}$  satisfying,

$$\left(\hat{X}\hat{A}+\hat{A}^*\hat{X}-\frac{2}{\ell^2}\hat{X}\hat{B}\hat{B}^*\hat{X}\right)\hat{x}<0,\quad\forall\,\hat{x}\neq0,$$

would guarantee stability, in the sense of Lyapunov, of the system (3.11) since  $V \geq 0$  and  $\dot{V} < 0$ . If the energy measure operator  $\hat{\mathcal{Q}}$  would satisfy this inequality, the resulting closed loop system would not experience any transient growth. If  $\hat{X}$  is chosen to be the solution of the Riccati equation (3.8) expression (3.12) can be rewritten such that,

$$\dot{V} = \hat{x}^* \left( -\hat{\mathcal{Q}} - \frac{1}{\ell^2} \hat{X} \hat{B} \hat{B}^* \hat{X} \right) \hat{x}.$$

Inserting (3.6) we obtain,

$$\dot{V} = -\bigg(\hat{x}^*\hat{\mathcal{Q}}\hat{x} + \ell^2\hat{u}^*\hat{u}\bigg),$$

and one can conclude that V is uniformly decaying. The optimal control obtained is thus such that the objective function (3.7) can be written,

$$\hat{J} = \int_{0}^{\infty} \left( \hat{x}^* \hat{\mathcal{Q}} \hat{x} + \ell^2 \, \hat{u}^* \hat{u} \right) dt = \int_{0}^{\infty} -\dot{V} \, dt = V(t=0) = \hat{x}_0^* \hat{X} \hat{x}_0, \tag{3.13}$$

where  $\hat{x}_0$  denotes the initial perturbation since  $V \to 0$  as  $t \to \infty$ . It can also be shown that any other stabilizing controller will give a larger value of this objective function.

## 3.2. Estimator

To be able to apply these control techniques in real life situations, we must use a method that only requires a limited amount of information about the flow. In the nonlinear control case this would require that we knew the initial conditions exactly and could compute the optimal control off-line and then apply this control to the system. In most cases this is not possible and we need to rely on measurements of different flow quantities. In the linear control framework we can develop an estimator that can be used to reconstruct the state of the flow at the same time as it evolves. We can then use that information to compute the control online. The estimator is based on a model of the actual system, and through control theory we can determine how to force this model in the optimal way given measurements of the flow. The action of the control due to the inhomogeneous boundary condition need not be accounted for since it is assumed to be known, and only an estimator for the homogeneous problem is needed. Consider the system,

$$\dot{\hat{x}}_h = \hat{N}\hat{x}_h + [\hat{G}_1, 0]\hat{w}, 
\hat{y} = \hat{C}\hat{x}_h + [0, \alpha I]\hat{w},$$
(3.14)

where  $\hat{y}$  is a measurement of the state disturbed by a random (zero-mean white Gaussian) process  $\hat{w}$ . In the state equation the disturbance enters through the matrix  $\hat{G}_1$  which should be the square root of the expected covariance of the state disturbances. Since this is a nontrivial quantity to find, the normalized energy measure operator  $\hat{Q}$  as well as the identity I has been used as expected covariance. The parameter  $\alpha$  allows for some flexibility in the estimator design. The measured quantity is the wall normal derivative of the normal vorticity at the channel walls divided by the Reynolds number,

$$\hat{C}\hat{x}_h = \frac{1}{Re_{cl}} \begin{bmatrix} \frac{\partial \omega}{\partial y} \big|_{y=+1} \\ \frac{\partial \omega}{\partial y} \big|_{y=-1} \end{bmatrix}.$$

An estimator of this system can then be described by,

$$\dot{\hat{x}}_e = \hat{N}\hat{x}_e - \hat{\psi},$$

$$\dot{\hat{y}}_e = \hat{C}\hat{x}_e,$$

$$\dot{\hat{y}} = \hat{L}(\hat{y} - \hat{y}_e) = \hat{L}\Delta\hat{y},$$
(3.15)

where  $\hat{\psi}$  is a forcing term driving the estimator state  $\hat{x}_e$  towards the measured

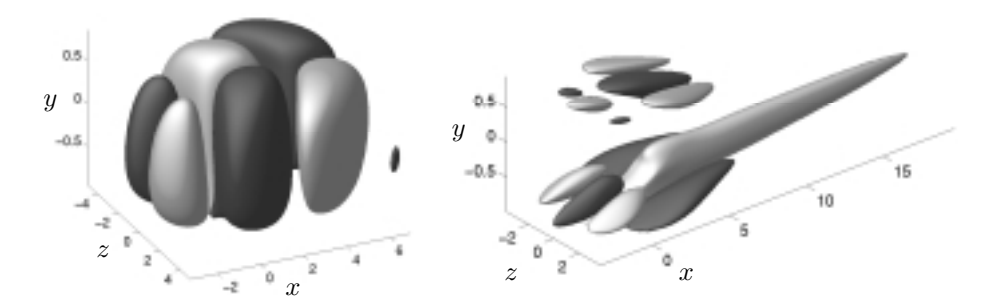


FIGURE 3.2. Localized estimator gains relating the measurement error  $(\hat{y} - \hat{y}_e)$  at the point  $\{x = 0, y = -1, z = 0\}$  on the wall to the estimator forcing terms v inside the domain: visualized are a positive and negative isosurface of the convolution kernels for (left) the wall-normal component of velocity at  $\pm 0.002$  and (right) the wall-normal component of vorticity at  $\pm 0.035$ . The kernels are computed using  $\hat{G}_1\hat{G}_1^* = \hat{Q}$ ,  $Re_{cl} = 2000$  and  $\alpha = 100$ .

state  $\hat{x}_h$  through the feedback law  $\hat{L}$  for the difference between the measurements. When the measurement noise in the system is white, the optimal estimator forcing is the Kalman filter, which is computed by solving a Riccati equation similar to the one for the control problem. From the non-negative self-adjoint solution  $\hat{Y}$  of,

$$\left(\hat{Y}\hat{N}^* + \hat{N}\hat{Y} - \frac{1}{\alpha^2}\hat{Y}\hat{C}^*\hat{C}\hat{Y} + \hat{G}_1\hat{G}_1^*\right)\hat{x}_e = 0, \quad \forall \text{ admissible } \hat{x}_e, \qquad (3.16)$$

the optimal estimator forcing  $\hat{L}$  is obtained through the relation,

$$\hat{L} = -\frac{1}{\alpha^2} \hat{Y} \hat{C}^*.$$

Using the same strategy as in the control case and computing the optimal estimator forcing for a large number of wavenumber pairs we can obtain an estimator forcing in physical space through an inverse Fourier transform. The physical space forcing can then be computed through the convolution integrals,

$$\psi_{v}(x, y, z, t) = \int_{\bar{x}, \bar{z}} \left[ L_{v,+1}(x - \bar{x}, y, z - \bar{z}) \, \Delta y(\bar{x}, y = +1, \bar{z}, t) + L_{v,-1}(x - \bar{x}, y, z - \bar{z}) \, \Delta y(\bar{x}, y = -1, \bar{z}, t) \right] d\bar{x} d\bar{z},$$
(3.17)

and,

$$\psi_{\omega}(x, y, z, t) = \int_{\bar{x}, \bar{z}} \left[ L_{\omega, +1}(x - \bar{x}, y, z - \bar{z}) \, \Delta y(\bar{x}, y = +1, \bar{z}, t) + L_{\omega, -1}(x - \bar{x}, y, z - \bar{z}) \, \Delta y(\bar{x}, y = -1, \bar{z}, t) \right] \, d\bar{x} \, d\bar{z},$$
(3.18)

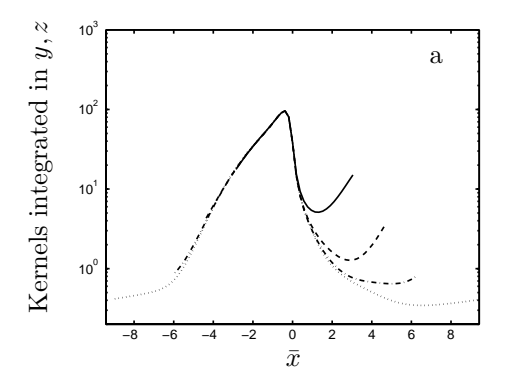
where  $L_{v,\pm 1}$  and  $L_{\omega,\pm 1}$  are the physical space convolution kernels for the estimator forcing exemplified in figure 3.2. The estimator forcing kernels are elongated mainly in the downstream direction and the one for the normal vorticity angles away from the wall. In a similar way as in the control case the kernels thus account for the convective time delay due to the shape of the base flow profile. The effect on the measurement error from perturbations closer to the center of the channel result in a forcing further downstream than for perturbations near the wall. In the simulations an extended Kalman filter is used. This means that a forcing computed from the linear equations is used to force the full nonlinear Navier–Stokes system.

## 3.3. Compensator

Combining the estimator and the controller gives us a compensator. We use the measurements to reconstruct the state, and then we use the reconstructed state to compute the control and apply it to the system we whish to control. Since optimal ( $\mathcal{H}_2$ ) control is considered rather than robust control the separation principle ( see e.g. Skelton (1988) p. 411 ) applies and the estimator and controller can be computed separately. If instead robust ( $\mathcal{H}_{\infty}$ ) control is desired a coupled system of two Riccati equations must be solved with additional requirements on the solutions. The initial condition in the estimator used is usually an unperturbed laminar flow, but if the measured state is partially known a better initial guess could be provided as illustrated in paper 5.

#### 3.4. Spatial localization

One important feature of the convolution kernels obtained is their spatial localization. This property of the optimal controllers computed for a spatially invariant system was predicted theoretically by Bamieh, Paganini, & Dahleh (2000), and in the present work it is demonstrated in practice. This means that the assumption of spatial periodicity becomes redundant since only local information is utilized. The kernels decay exponentially at a distance from the origin and can be truncated to have truly compact support. It has been verified in simulations that this operation does not significantly degrade the performance as reported in paper 4. An illustration of the exponential decay is provided in figure 3.3 where four control kernels for v have been computed with the same parameters but for different box sizes with maintained resolution. The square value of the kernel is integrated in y onto an x-z plane, and this plane



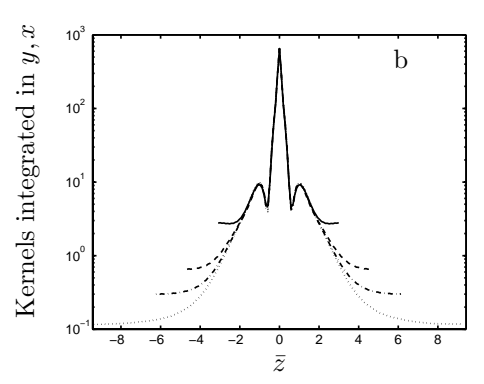


FIGURE 3.3. Illustration of exponential decay of control convolution kernel for normal velocity. a: As a function of  $\bar{x}$  b: As a function of  $\bar{z}$ . Solid lines: box size  $2\pi \times 2\pi$  with resolution  $32 \times 64$  in  $x \times z$ , dashed lines: box size  $3\pi \times 3\pi$  with resolution  $48 \times 96$  in  $x \times z$ , dashed-dotted lines: box size  $4\pi \times 4\pi$  with resolution  $64 \times 128$  in  $x \times z$  and dotted lines: box size  $6\pi \times 6\pi$  with resolution  $96 \times 192$  in  $x \times z$ . In all cases  $\ell = 1$ ,  $Re_{cl} = 2000$  and the number of gridpoints in y was 70.

is than integrated in z or x to obtain a one dimensional representation of the kernel as a function of x or z. It is clear that if the box size is increased, the kernels continue to decay. This property of the kernels facilitates a physical implementation of the system where the need for communication between arrays of sensors and actuators is small compared to a global feedback system. For more discussion about this issue see paper 3 or Bewley (2001).

#### 3.5. Performance of controller

#### 3.5.1. Direct numerical simulation code

The direct numerical simulations with linear control and estimation in temporal channel flow have been performed using the code described and used in Bewley, Moin & Temam (2001) with necessary modifications. The code uses a discretization with Fourier modes in the directions parallel to the walls and an energy-conserving second-order finite difference scheme on a stretched staggered mesh for the wall normal direction. The components with derivatives in the directions parallel to the walls are marched in time using a low-storage third-order Runge–Kutta method. An implicit Crank–Nicholson method is used for each sub-step of the Runge–Kutta method for all terms containing a wall normal derivative to allow strong blowing and suction without imposing restriction on the time step to maintain numerical stability. The control laws are computed using the same resolution as in the simulations i all cases. The computation of the feedback convolution integrals for both control and estimation was implemented both in physical space and in Fourier space. The

Full-state feedback $\ell = 0.1$								
Scenario	$Re_{cl}$	Grid	Lower	Upper	Factor			
(SV)	2000 3000 5000	$16 \times 128 \times 64$ $16 \times 128 \times 64$ $16 \times 128 \times 64$	$1.50 \times 10^{-5}$	$6.55 \times 10^{-5}$ $1.55 \times 10^{-5}$ $3.10 \times 10^{-6}$	10 9.6 11.5			
( OW )		$16 \times 128 \times 64$ $16 \times 128 \times 64$ $16 \times 128 \times 64$	$6.50\times10^{-5}$	$2.50 \times 10^{-4}$ $7.00 \times 10^{-5}$ $1.70 \times 10^{-5}$	102 109 122			
( N )	2000 3000 5000	$32 \times 128 \times 64$ $32 \times 128 \times 64$ $32 \times 128 \times 64$	$5.00 \times 10^{-4}$ $1.80 \times 10^{-4}$ $5.00 \times 10^{-5}$	$5.01 \times 10^{-4}$ $1.90 \times 10^{-4}$ $5.05 \times 10^{-5}$	7 6.8 5.7			

Table 3.1. Full information controlled transition thresholds for the initial perturbations: (SV)–Streamwise vortex, (OW)–Oblique wave and (N)– Random perturbation.

two methods are equivalent and result in identical control signals providing a confirmation that implementation was correct. For the sake of computational efficiency, the Fourier implementation was used in all simulations presented here.

## 3.5.2. Transition thresholds

In order to quantify the performance of the linear controller, simulations have been performed to determine the threshold energy for transition for certain perturbations. The uncontrolled thresholds were determined by Reddy et al. (1998) and the same initial conditions have been used in this study reported in paper 4. To the streamwise vortices and oblique wave perturbations a component of the random noise is also added, corresponding to 1% of the perturbation energy, in order to break symmetries and trigger secondary instabilities. In table 3.1 the resulting thresholds for the controlled system are tabulated with a comparison to the uncontrolled threshold values in the "Factor" column. The factor is computed by dividing the mean threshold value from the controlled case with the one for the corresponding uncontrolled case. In summary the threshold values indicate that the oblique wave perturbation is easy to control compared to the random noise and streamwise vortex perturbations. One can expect roughly about one half order of magnitude higher perturbation energies required for transition in the controlled case with random noise.

#### 3.5.3. Turbulence control

During transition to turbulence there is a substantial change in the mean velocity profile and the same is true for relaminarization. The linear controller is computed for a specific mean flow profile and does not take its evolution into account. Application of feedback control kernels computed for the turbulent mean flow profile, using f(y) = 1 in (3.5), to a three dimensional turbulent channel flow at  $Re_{\tau} = 100$  results in a drag reduction of about 15%. By introducing a simple gain scheduling technique, where controllers have been computed for the seven different velocity profiles shown in figure 3.4 ranging from the laminar to the turbulent one, the controller can be allowed to adapt to the current mean flow during a simulation. This gain scheduling can be viewed as a nonlinear extension of the linear control law. The scheduling is done by computing the energy of the difference between the current mean flow in the simulation and the profiles used to compute feedback laws at each time-step. The kernels corresponding to the profile with the smallest difference from the mean flow are then used to compute the control. In addition to the gain scheduling, the objective function had to be modified to make the controller work. This was discovered when testing to use the identity matrix instead of  $\mathcal{Q}$  in the objective function when computing the kernels. The idea was to make the controller focus on the perturbations near the channel walls. Using the identity matrix has this effect due to that the stretched grid obtained from using the Gauss-Lobatto collocation points is finer near the walls. Unfortunately the resulting control is then grid dependent, and to avoid the grid dependency f(y)was introduced in the energy measure (3.5) to get a similar effect.

The direct numerical simulations were performed in a box with the dimensions  $4\pi \times 2 \times 4/3\pi$  and with a resolution of  $64 \times 64 \times 64$  using a Fourier, Finite difference, Fourier discretization in  $x \times y \times z$  respectively. The control kernels were computed in the same box with a resolution of  $64 \times 70 \times 64$  Fourier, Chebyshev, Fourier modes.

In figure 3.4 the energy, normalized drag and control effort is plotted for three different realizations of the turbulence control. To verify some robustness of this control strategy using  $f(y) = (1-y^2)^{-1/2}$  two different initial conditions have been used. Notice that there is rapid decay of energy as well as drag in all three cases. The drag has an initial transient increase of about 10% before it decays when the controllers using the weighted energy measure are used. Using the control computed using the identity matrix produces an increase of up to 60% in drag initially. In the plot of the control effort one can clearly see transient jumps when the gain-scheduling has decided to switch control kernel. Relaminarization of a three dimensional turbulent channel flow at  $Re_{\tau} = 100$  using zero mass flux blowing and suction control has previously only been achieved using nonlinear optimal control, see e.g. Bewley, Moin & Temam (2001) and Collis *et al.* (2000). They used a receding horizon optimization strategy in direct numerical simulations and large eddy simulations respectively.

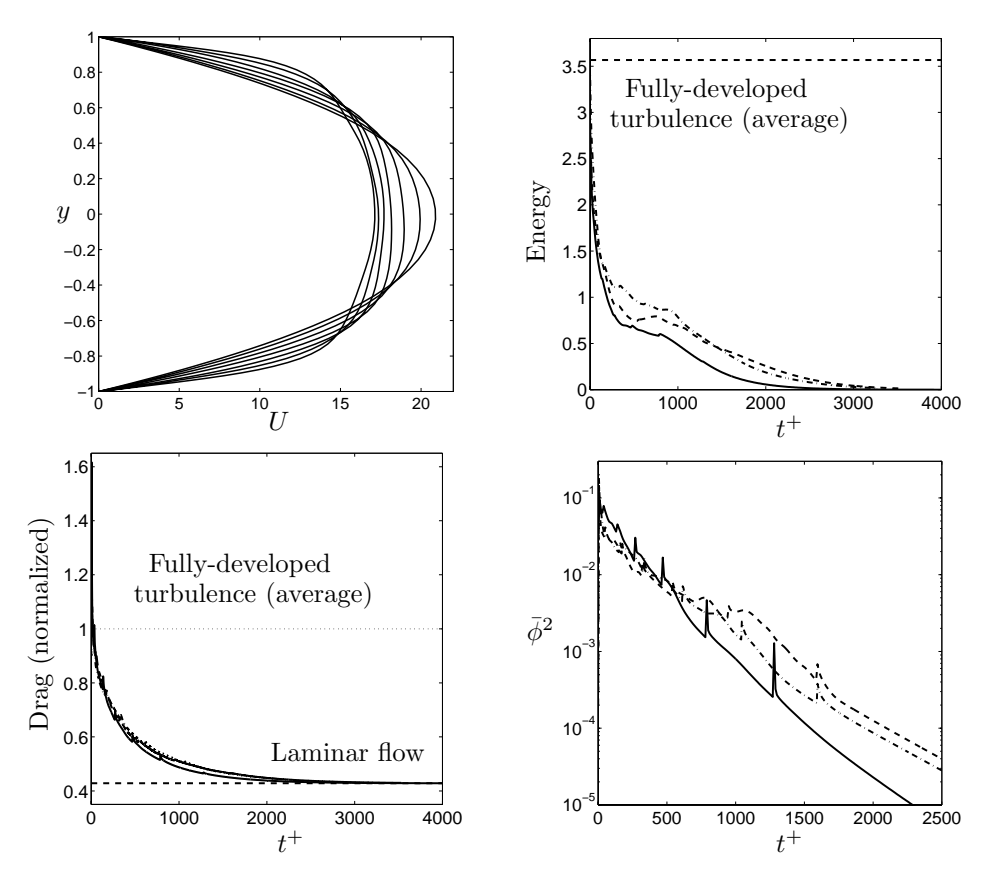


FIGURE 3.4. Evolution of initially fully-developed turbulence at  $Re_{\tau}=100$  with three different controller realizations. Topleft: mean velocity profiles used to compute kernels for the gain scheduling. Top-right: energy of flow perturbation. Down-left: normalized mean drag. Down-right: mean-square value of the control  $\phi$ . Solid is from using the identity matrix in the objective function dotted and dashed are with a weighted energy measure using  $f(y)=(1-y^2)^{-1/2}$  for two different initial conditions. Note that application of the gain-scheduled linear feedback causes the fully turbulent 3D flows to relaminarize in all three cases.

The need for a modification of the energy measure in order to obtain relaminarization indicates that there exists a better physical quantity than total perturbation energy to use in the objective function. Kim & Lim (2000) performed direct numerical simulations where they showed that the coupling term  $\mathcal{L}_C$  in (3.1b) is crucial for the maintenance of the turbulent process near the wall. They suggested that an objective function targeting the effect of this

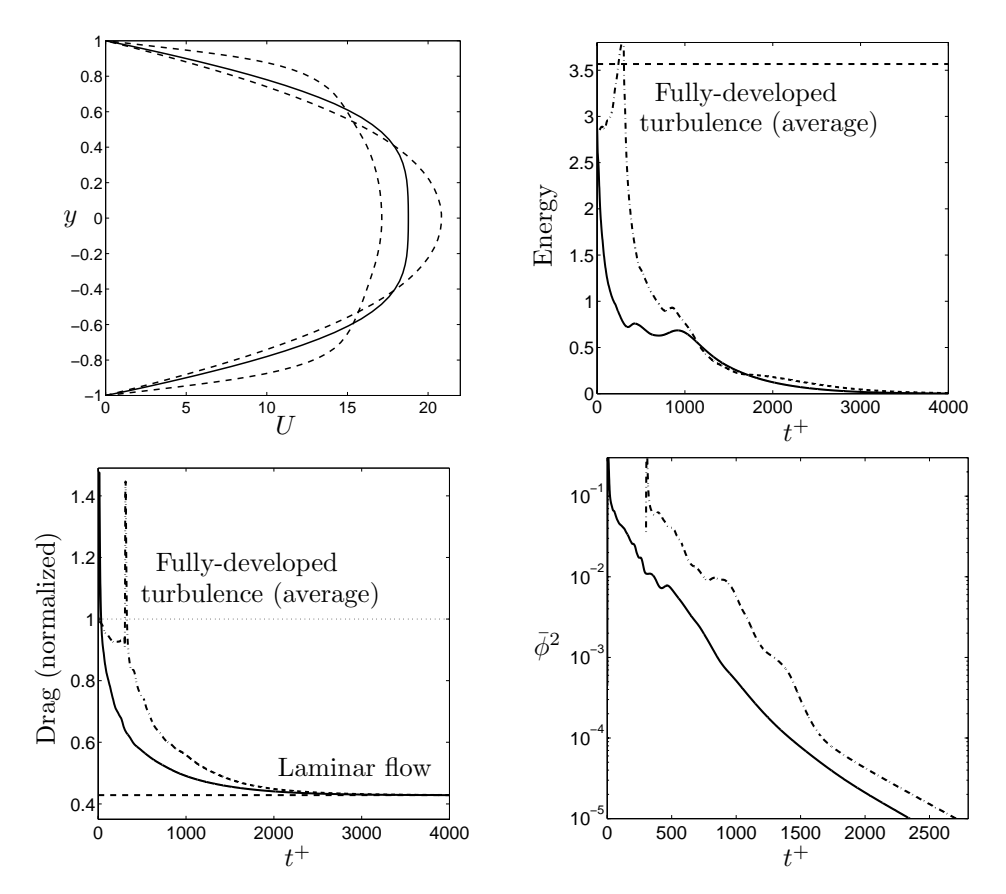


FIGURE 3.5. Evolution of initially fully-developed turbulence at  $Re_{\tau}=100$  when a linear controller computed using  $\ell=1$  and  $f(y)=1+U'(y)^2$  in (3.5) is applied at  $t^+=0$  (solid) and at  $t^+=300$  (dot-dashed). Top-left: The velocity profile used to compute the control kernels (solid), laminar and turbulent profiles (dashed). Top-right: energy of flow perturbation. Down-left: normalized mean drag. Down-right: mean-square value of the control  $\phi$ . Note that application of the completely linear feedback causes the fully turbulent 3D flow to relaminarize in both simulations.

coupling term could result in a effective controller. Inspired by this an energy weighting of the form  $f(y) = 1 + U'(y)^2$  was introduced. Control kernels were then computed using only one of the intermediate velocity profiles used for the gain scheduling described earlier. The velocity profile U(y) used to compute the kernels can be compared to the fully turbulent and the laminar mean velocity profiles in the upper left plot in figure 3.5. The control kernels computed for this profile were then tested in two simulations. The evolution of energy

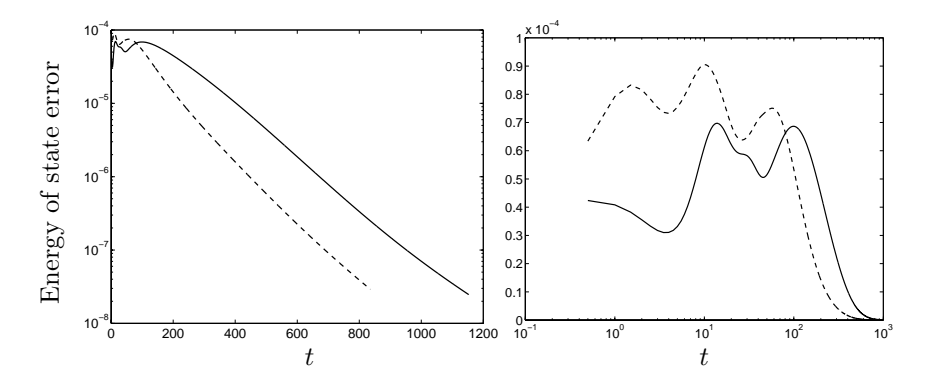


FIGURE 3.6. Convergence of estimator for a random perturbation at  $Re_{cl} = 3000$ . Solid with  $\hat{G}_1\hat{G}_1^* = \hat{Q}$  and dashed with  $\hat{G}_1\hat{G}_1^* = I$ . Left: logarithmic in vertical axis, right: logarithmic in horizontal axis.

and drag in these simulations are shown together with the mean square value of the control in figure 3.5. In these cases the transient increase in drag is about 50% when the control is applied but then there is rapid decrease. These recently obtained results show that it is possible to relaminarize low Reynolds number turbulence with zero mass flux blowing and suction using a completely linear control approach.

#### 3.5.4. Linear v.s Nonlinear optimal control

Comparing the resulting control from the linear and nonlinear methods is interesting from a consistency point of view. With the linear approach the control is computed online whereas the nonlinear method requires many optimization iterations to obtain the control. Adjusting the objective functions and the parameters of the problems to make them comparable should result in practically the same control signal.

In paper 5 this is verified by computing the optimal control for an oblique wave perturbation with small amplitude using the linear approach. The resulting control signal is then inserted into the nonlinear code. Computing the gradient of the objective function using the nonlinear optimal control method shows that the gradient norm is very small for the linear control solution. In a case where strong nonlinearities are present the methods should differ and such a study could provide information about the key nonlinear effects in the transition process.

#### 3.6. Performance of estimator

An estimator is tested by running two direct numerical simulations simultaneously. One simulation has an 'unknown' initial perturbation and the other one is the estimator. The normal derivative of the normal vorticity at the walls is measured in both simulations and the difference is used to force the estimator

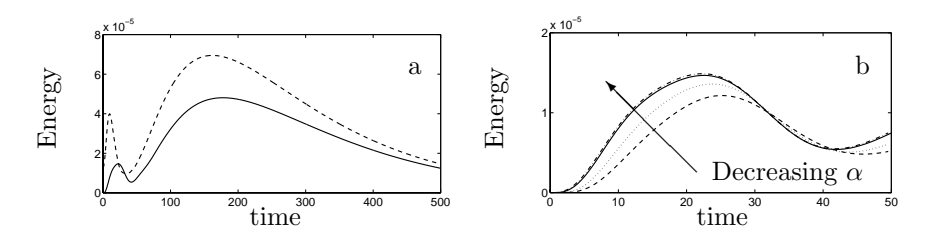


FIGURE 3.7. Energy evolution in estimator with  $\hat{G}_1\hat{G}_1^* = \hat{Q}$  for an oblique wave perturbation with different values on the penalty parameter: a) Dashed– measured state. Solid– estimator state with  $\alpha = 0.01$ . b) Estimator state for  $\alpha = 0.001$ , 0.01, 0.05, 0.1, as dash-dot, solid, dotted, dashed respectively.

using the linear forcing kernels. The initial state in the unknown flow is a random perturbation at an energy level below the transition threshold and the initial guess in the estimator is an unperturbed laminar flow at  $Re_{cl} = 3000$ . Figure 3.6 shows that the state in the estimator converges exponentially to the unknown state after an initial transient. Using  $\hat{G}_1\hat{G}_1^* = \hat{Q}$  gives a small transient during a long time whereas using  $\hat{G}_1\hat{G}_1^* = I$  gives a larger transient for a shorter time. Since both the initial behavior and the convergence are important issues there is no obvious reason why one would be better than the other for the compensator.

In figure 3.7a the energy evolution of the unknown state (dashed) and the estimator state (solid) is plotted. In this case an oblique wave at  $Re_{cl} = 2000$  is the initial perturbation. The dependence on the parameter  $\alpha$  for this case is illustrated in figure 3.7b. It is shown that decreasing the penalty on the measurements gives a more rapid reaction in the estimator up to a limit. The convergence can be improved by providing a better initial guess or perhaps by using additional measurements of the flow at the walls.

## 3.7. Performance of compensator

The combination of the controller and estimator where the state estimate is used to compute the control is called a compensator. In figure 3.8 an oblique wave is controlled at  $Re_{cl}=2000$  using both full information control (dashed) and the compensator (solid). In terms of energy reduction the compensator works almost as well as the full information controller in this case as reported in paper 5.

To quantify the performance of the compensator with  $\hat{G}_1\hat{G}_1^* = \hat{Q}$ , transition thresholds are computed through direct numerical simulations for random noise initial perturbations at  $Re_{cl} = 2000, 3000, 5000$  and for oblique waves and streamwise vortices at  $Re_{cl} = 2000$ . With  $\hat{G}_1\hat{G}_1^* = I$  only one case at  $Re_{cl} = 2000$  with random noise is tested. In some sense this is a worst case

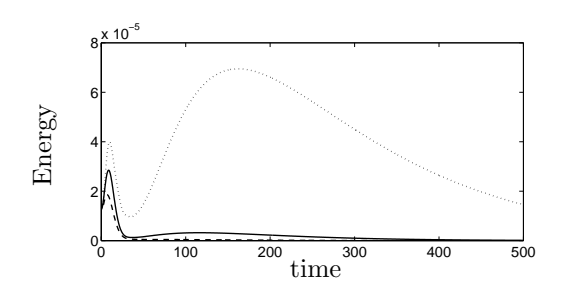


FIGURE 3.8. Performance of full information linear controller (dashed) and compensator using  $\hat{G}_1\hat{G}_1^* = \hat{Q}$  (solid) compared to the uncontrolled (dotted) energy evolution.

Measurement feedback $\alpha = 0.1,  \ell = 0.1$								
Scenario	$Re_{cl}$	Grid	Lower	Upper	Factor			
$\hat{G}_1\hat{G}_1^*=\hat{Q}$								
(SV)	2000	$16\times128\times64$	$1.75\times10^{-5}$	$2.00\times10^{-5}$	2.9			
( OW )	2000	$16\times128\times64$	$1.25\times10^{-5}$	$1.50\times10^{-5}$	5.8			
( N )	3000	$16 \times 128 \times 64$ $16 \times 128 \times 32$ $16 \times 128 \times 32$	$3.25\times10^{-5}$	$3.50\times10^{-5}$	1.28			
$\hat{G}_1\hat{G}_1^*=I$								
( N )	2000	$16 \times 128 \times 64$	$1.05\times10^{-4}$	$1.10\times10^{-4}$	1.48			

Table 3.2. Compensator controlled transition thresholds for the initial perturbations: (SV)–Streamwise vortex, (OW)–Oblique wave and (N)– Random perturbation. Upper part of table with  $\hat{G}_1\hat{G}_1^*=\hat{Q}$  and lower part with  $\hat{G}_1\hat{G}_1^*=I$ .

study since the initial state in the estimator is a laminar flow without perturbations. The performance is not as good as in the full information case, probably due to that the estimator convergence is slow and has an initial transient. In table 3.2 the results are tabulated in the same way as for the full information control case. Again oblique waves appear to be the easiest to control and random noise the most difficult. The increase in transition threshold for the random noise case is only about 30% using  $\hat{G}_1\hat{G}_1^* = \hat{Q}$  which is a lot less than

# 40 3. LINEAR CONTROL AND ESTIMATION

in the full information case. For the case with  $\hat{G}_1\hat{G}_1^*=I$  the initial transient in the estimator is larger. The threshold value is increased by 48% with the compensator showing that this is a slightly better strategy. The choice of  $\hat{G}_1$  is a delicate issue and further research is needed to find the optimal choice for transition control.

#### CHAPTER 4

# Control of spatial boundary layer flows

Spatially evolving flows, such as the boundary layer on a flat plate, have different stability properties than the parallel flows such as the flow in a channel. The methodology for computing linear controllers developed in this thesis summarized in section 3.1 assumes that the flow is parallel and can be described as periodic in the spatial directions. With small modifications to this approach by including a two component base flow and using the Falkner-Skan-Cooke boundary layer profiles we can apply it to boundary layer flows as well. Assuming that the control laws developed are insensitive to small changes in the Reynolds number and that non-parallel effects are small, we can also apply these controllers to the spatially evolving flow to test what kind of performance we can get. The assumption about the non-parallel effects is not true since we can see clearly that they are significant by comparing direct numerical simulations and local stability analysis. From a controls perspective the individual eigenvalues of the system may be less important than the total dynamics. The Reynolds number insensitivity is perhaps also not a good assumption from the stability perspective but might be valid for the controlled system.

# 4.1. Linear control methodology

In the boundary layer case we still use the Orr–Sommerfeld–Squire equations but with a freestream boundary condition in one end instead of a wall as in the channel flow case. Also the equations are formulated for a two component base flow, and become,

$$\frac{\mathrm{d}\hat{v}}{\mathrm{d}t} = \underbrace{\hat{\Delta}^{-1}[-(ik_x U + ik_z W)\hat{\Delta} + ik_x U'' + ik_z W'' + \frac{1}{Re_{\delta^*}}\hat{\Delta}^2]}_{\mathcal{L}_{OS}} \hat{v}$$

$$\frac{\mathrm{d}\hat{\omega}}{\mathrm{d}t} = \underbrace{[ik_x W' - ik_z U']}_{\mathcal{L}_{C}} \hat{v} + \underbrace{[-i(k_x U + k_z W) + \frac{1}{Re_{\delta^*}}\hat{\Delta}]}_{\mathcal{L}_{C}} \hat{\omega}$$
(4.1)

where  $\hat{v}$  and  $\hat{\omega} = i(k_z\hat{u} - k_x\hat{w})$  are the amplitude functions for the normal velocity and the normal verticity, respectively. A prime (') denotes a derivative in the wall-normal direction and U and W are the meanflow components in the

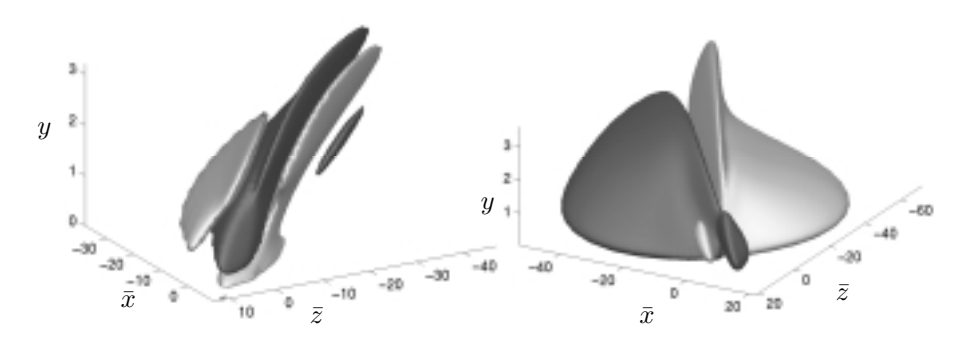


FIGURE 4.1. Left: Isosurfaces at 25 (light) and -25 (dark) of convolution kernel for v. Right: Isosurfaces at 0.5 (light) and -0.5 (dark) of convolution kernel for  $\omega$ .

chordwise and spanwise directions respectively. The boundary conditions are

$$\hat{v}(0) = \phi , \frac{\partial \hat{v}}{\partial u}(0) = 0 , \hat{\omega}(0) = 0, \tag{4.2}$$

$$\hat{v}(y) \to 0, \ \frac{\partial \hat{v}}{\partial y}(y) \to 0, \ \hat{\omega}(y) \to 0 \text{ as } y \to \infty.$$
 (4.3)

Here  $Re_{\delta^*}$  is the Reynolds number based on the velocity scale  $U_{\infty}$  and the displacement thickness  $\delta^*$ , both taken at the stream-wise location  $x_0$ . The procedure to compute the optimal control is then the same as described in section 3.1, with the addition of a penalty parameter  $r^2$  on the control velocity itself, for details see paper 7. Feedback convolution kernels computed for a Falkner–Skan–Cooke base flow are shown in figure 4.1. The spatial localization properties are also obtained for the boundary layer profiles and this is a key property for the extension to a spatial flow. Testing the kernels in a parallel boundary layer shows that their characteristics are similar to those observed in the channel flow.

## 4.2. Application of Linear Controller

The linear controller cannot be expected to be the optimal one for a spatial boundary layer since it is using a parallel flow assumption. Also the kernels are based on one particular mean flow profile, so it will not be able to perform as well when the mean flow is changing in the spatial directions. By only applying the control in a small neighborhood of where the control kernel is computed it should perform fairly well. Considering a Falkner–Skan-Cooke flow we have a mean flow that changes both direction and length scale in the downstream direction. Since the effect of these variation cannot be accounted for with the present control method this flow serves as a good test case for the robustness to variation in the mean flow of the controller. The success in relaminarizing low Reynolds number turbulence in the channel using gain scheduling indicates that there is some robustness of this type. Application of the control is limited in the chordwise direction to be only in a strip on the

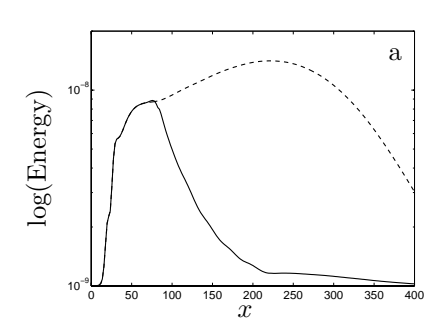
wall. The control kernel is then computed for the position in the center of this strip. The kernels are computed to act on perturbations to the mean flow and in the parallel flow this means excluding only the  $\alpha=\beta=0$  mode. In the spatial flow all  $\beta=0$  modes are used to describe the mean flow and these components must be subtracted before computing the control. To obtain the control signal, the convolution integral for the time derivative of the control velocity is computed for the entire wall. The control velocity is then updated for the next time step and filtered to remain within the specified region with zero net mass flux.

#### 4.3. Numerical simulations

The direct numerical simulations are performed using the spectral code for spatial boundary layer flow described in Lundbladh et al. (1999). The code uses a Fourier discretization in the spanwise and chordwise directions and a Chebyshev collocation- or tau-method can be used in the wall-normal direction. Time marching is performed using a three or four stage, third order, Runge-Kutta method for the advective terms and a second order Crank-Nicholson method for the viscous terms. The simulation of a spatial flow with periodic boundary conditions is possible through a fringe region technique where a volume force that is nonzero only in a small part of the simulation box is added to the Navier-Stokes equations. This forcing makes the simulated flow periodic and thus the Fourier discretization is feasible. Note that the flow in the fringe region is non-physical, but the upstream influence is small. The fringe region technique was thoroughly investigated in Nordström, Nordin & Henningson (1999). The computation of the control convolution integrals is implemented in Fourier space since this is more efficient numerically, and this is equivalent to a physical space implementation as verified in the code used for the channel flow simulations in chapter 3. For details about box size and resolution used in the simulations see paper 7.

#### 4.4. Control of TS waves

One simple test case for control of spatial flows is the Blasius boundary layer perturbed by a two dimensional TS wave. The perturbation is introduced through an oscillating volume force just upstream of the position where it becomes unstable (branch I). In the uncontrolled case it then grows until it reaches the position where it becomes stable again (branch II). When control is applied in the unstable interval the perturbation decays exponentially and the control signal looks just like a TS wave with decaying amplitude. Figure 4.2a shows the energy evolution in the box for the uncontrolled case (dashed) and for the case with control (solid). In figure 4.2b, the control signal as a function of x is plotted for a few different times covering one time period of the TS wave.



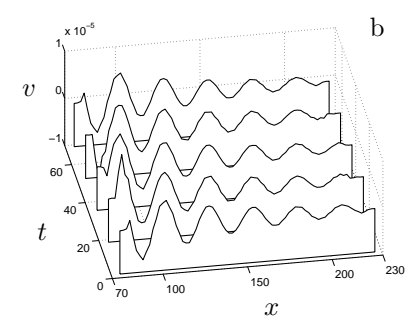
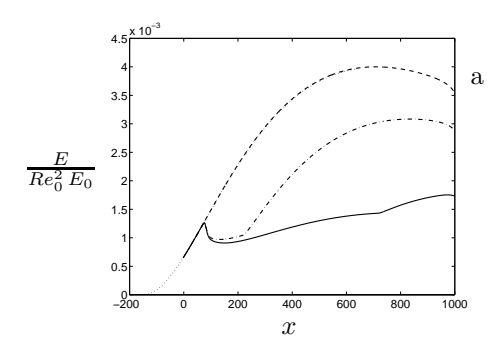


FIGURE 4.2. a: The spatial energy growth of a TS wave perturbation in a Blasius boundary layer with (solid) and without (dashed) control. The non-dimensional frequency of the perturbation is F=200. Control is applied in  $x\in[75,225]$ . b: Control signal during one time period of the TS wave.



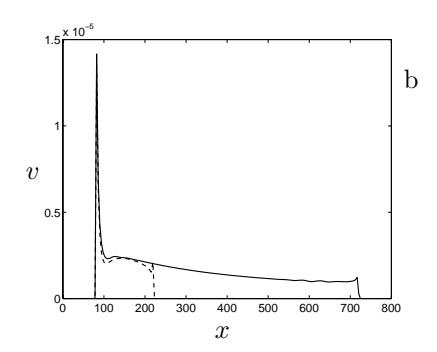


FIGURE 4.3. a: The spatial energy growth of the optimal spatial perturbation at x=237.24 with  $Re_{\delta^*}=468.34$  in the Blasius boundary layer. Dotted: computed from the boundary layer equations. Dashed: computed with DNS. Dash-Dotted: With control applied in  $x\in[75,225]$ . Solid: With control applied in  $x\in[75,725]$ . b: The control (v) distribution at y=z=0 for the streak mode in the case with control in  $x\in[75,725]$  (solid) and  $x\in[75,225]$  (dashed).

## 4.5. Control of streamwise streaks

A more complicated perturbation in the Blasius boundary layer is the optimal perturbation for forcing streamwise streaks. The spatial optimal perturbation (Andersson, Berggren & Henningson (1999); Luchini (2000)) with maximum growth at x=237 is marched using the linear equations to the beginning of the computational box. Control is then applied downstream in two different intervals, one short  $(x \in [75, 225])$  and one longer  $(x \in [75, 725])$ . The control kernels are computed for the position in the center of these intervals and then

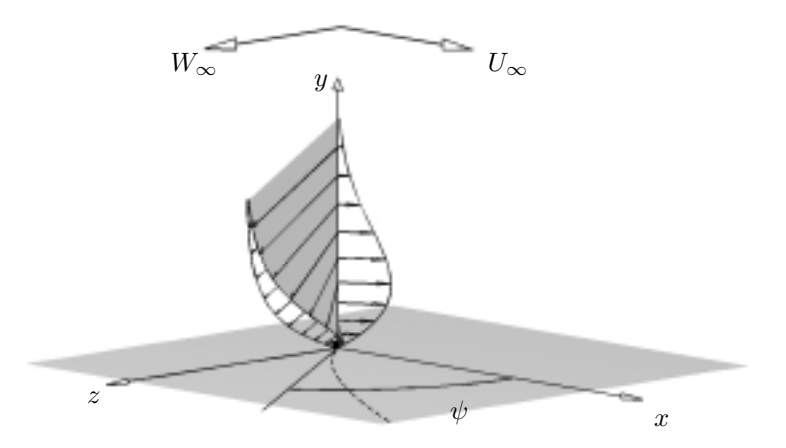


FIGURE 4.4. Falkner–Skan–Cooke base flow and coordinate system used.  $\psi$  is the angle to the streamline of the flow in the free-stream,  $U_{\infty}$  is the chord-wise free-stream component and  $W_{\infty}$  is the spanwise freestream component. The dashed line is the streamline of the flow in the freestream over a flat plate with a pressure gradient in the x direction

applied in direct numerical simulations. The energy evolution of the uncontrolled and the two controlled flows is plotted if figure 4.3a. Uniform decay of the energy is not obtained in any of the two cases but the growth is efficiently lowered by the control within the control interval. Downstream of the control region the perturbation grows again, but does not reach the same energy as in the uncontrolled case. The control signals are shown in figure 4.3b showing an initial peak of the control velocity initially and then a region of slow decrease until the end of the control interval. During the long control interval there is a substantial evolution of the mean flow not accounted for by the control strategy, but still the energy growth is lowered in the whole interval.

## 4.6. Falkner-Skan-Cooke flow

A Falkner–Skan–Cooke (FSC) flow is the solution of the boundary layer equations for the flow over a swept wedge. This flow is similar to what can be found on a part of the wing of a commercial aircraft. Figure 4.4 shows the profiles of the base flow in a coordinate system aligned to the direction of the freestream. The particular base flow considered has a Reynolds number of of  $Re_{\delta^*}=337.9$  based on the local displacement thickness and chordwise freestream velocity at the beginning of the computational box. The chordwise dependence of the base flow is described by the relation

$$U_{\infty} = \left(\frac{x}{x_0} + 1\right)^m$$

where m=0.34207 and  $x_0=354.0$  is used here. The normalized spanwise freestream velocity is  $W_{\infty}=1.442$ . The Blasius flow used earlier is a special

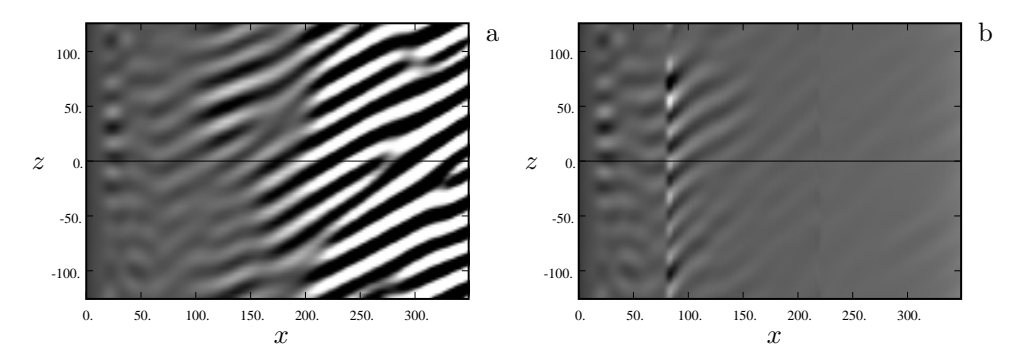


FIGURE 4.5. Snapshots of the normal velocity v in an xz-plane at y=0.5 without control (a) and with control (b). Black is  $v \le -4.5 \times 10^{-5}$  and white is  $v \ge 5.5 \times 10^{-5}$ . The control is applied in  $x \in [75, 225]$ .

case of this flow with m=0 and  $W_{\infty}=0$ . The velocity profiles are then computed numerically using the equations described in e.g. paper 6. Notice that this base flow is only used as an initial condition and to compute boundary conditions on the upper part of the domain in the simulations. The base flow was first used in simulations of control of linear instabilities in a parallel flow to test the control kernels in the flow they are developed for, and also to verify the implementation of the control.

## 4.7. Control of cross-flow vortices

#### 4.7.1. Traveling vortices

If a perturbation with a random distribution in the spanwise direction, changes randomly in time, traveling cross-flow vortices develop downstream. The amplitude of the perturbation is low enough to ensure linear development of the vortices within the computational box. A snapshot of the normal velocity in an x-z plane is shown in figure 4.5a. The linear feedback control is then applied in a strip centered at x = 150 with a width of 150 inlet boundary layer thicknesses. The kernels used are computed with  $\ell^2 = 10^2$  and  $r^2 = 0$ . The simulation is then run again, starting with an unperturbed flow, but now with control. A snapshot at the same time as for the uncontrolled case is shown in figure 4.5b and it shows that there is a significant reduction of the amplitude of the normal velocity within and downstream of the control region. Looking closely at figure 4.5b one can see that a light shade, indicating a positive normal velocity leads to a dark spot in the control region, and vice versa for darker shades, suggesting that the control is of opposition type initially. The time averaged evolution of the perturbation energy integrated in z for the uncontrolled and controlled cases is plotted in figure 4.6. The positive effect of the applied control is clearly shown and also that the decay of energy continues even downstream of the control region. The difference between the controlled

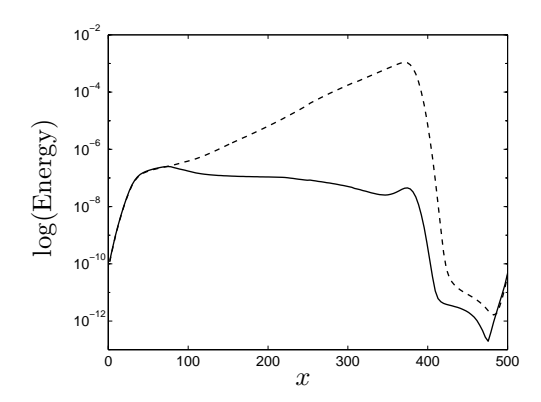


FIGURE 4.6. Time average of energy integrated in the z direction for uncontrolled (dashed) and controlled (solid) simulations of traveling crossflow vortices.

and uncontrolled perturbation energy where the fringe region starts is about four decades.

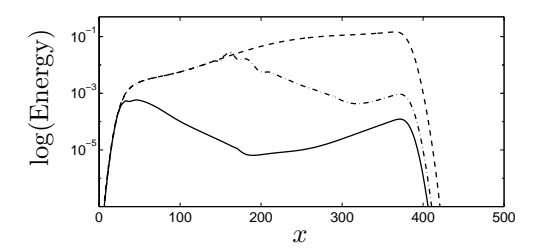


FIGURE 4.7. Energy growth of uncontrolled perturbation and effect of applied control in spatial DNS for  $\beta=0.25$ . Dashed: uncontrolled. Solid: controlled with  $l^2=10^2$  and  $r^2=0$  in the interval  $x\in[25,175]$  centered at x=100. Dash-dot: controlled with  $l^2=10^2$  and  $r^2=0$  in the interval  $x\in[145,295]$  centered at x=220.

## 4.7.2. Stationary vortices

Using a stationary perturbation in the beginning of the computational box, the crossflow vortices generated are also stationary. Given that the amplitude of the perturbation is sufficiently large the vortices will reach an amplitude where they saturate through non-linear interactions. The energy in the  $\beta=1$  mode for the uncontrolled flow, plotted as the dashed line in figure 4.7, grows exponentially initially. Nonlinear saturation causes the growth rate to decrease and close to the fringe it is close to zero. Studying the energy of the five lowest beta modes shows that all the modes have similar behavior but the  $\beta=1$  mode dominates. The linear control is applied to the stationary cross-flow

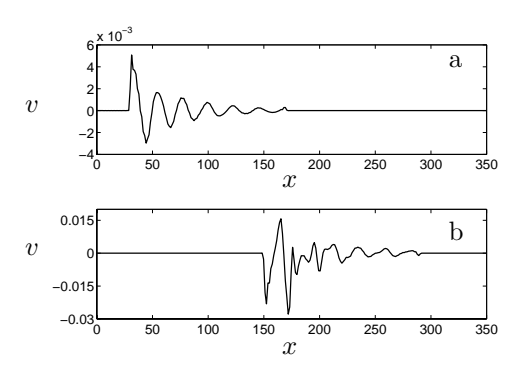


FIGURE 4.8. The normal velocity on the wall at z = 0 in the controlled cases with stationary perturbations. a: Control at  $x \in [75, 225]$ , b: Control at  $x \in [145, 295]$ .

vortices in two different strips and the resulting energy evolution is plotted in figure 4.7. First the control is applied at a position close to where the perturbation is generated and the amplitude of the vortices is low. The energy of the controlled perturbation is plotted as the solid line in figure 4.7. The perturbation energy decays in the region of the control strip, and then starts growing again downstream. The control signal in this case, plotted in figure 4.8a for one spanwise location at z=0, shows a regular oscillatory behavior as expected in this linear case. Then the control strip is moved downstream to a position, centered at x=220, where the vortices have reached an amplitude large enough for nonlinear effects to become apparent. The energy decay is not as smooth as in the previous case illustrated by the dash-dotted line in figure 4.7, but there is still a large reduction of the perturbation energy by the control within the control strip. The control signal, plotted in figure 4.8b for one spanwise position at z=0, is not as regular in this case probably due to the nonlinear effects.

# 4.8. Implications for the transition process

Transition in a spatially evolving boundary layer in a complicated process to study both numerically and experimentally. It was observed in experiments by Kohama, Saric & Hoos (1991); Malik, Li & Chang (1994) and Deyhle & Bippes (1996) that in a FSC flow with stationary cross-flow vortices, secondary instabilities appeared before transition. Both high frequency and low frequency secondary oscillations were observed, but the low frequency was observed early in the breakdown process whereas the high frequency one appeared just prior to breakdown. According to Malik, Li & Chang (1994) the strong, saturated, cross flow vortices give rise to strong shear layers that appear to be inflectionally unstable. Direct numerical simulations of this transition scenario were then performed to try to investigate the structure and the properties of these secondary instabilities by Högberg & Henningson (1998), (included as paper 6)

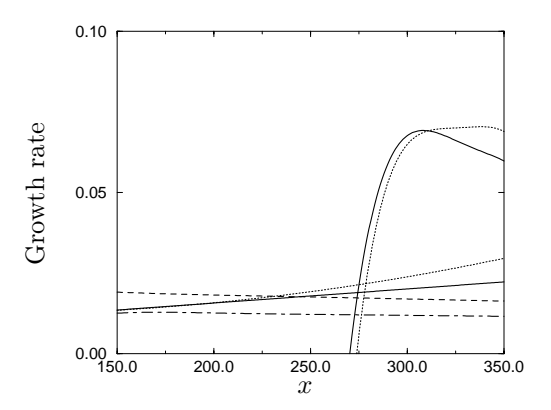


FIGURE 4.9. Growth rates. Solid: Modes with  $\beta=1$ , high and low frequency. Dotted: Based on  $\max(u_{rms})$ , high and low frequency. Dashed: Most unstable linear mode. Dot-Dashed: Most unstable zero-frequency disturbance.

in this thesis), and also by Malik *et al.* (1999) and Bonfigli & Kloker (2000). Results from experiments reported by Lerche (1997) and Kawakami, Kohama & Okutsu (1999) agree well with the findings from the numerical studies.

It was found in Högberg & Henningson (1998) that a low frequency mode grows on weaker vortices whereas a high frequency instability appears to require at least a partially saturated vortex. The two instabilities are also located at different positions on the vortex, the low frequency one in the lower shear layer of the vortex and the high frequency on the upper one. The growth rate of the high frequency secondary instability is found to be much larger than the one for the low frequency mode. For the high frequency instability it is shown in figure 4.9 that the  $\beta = 1$  mode has the most rapid growth initially, but it is later exceeded by the growth rate of the maximum  $u_{rms}$  in the spanwise direction. The location of the secondary instabilities on the saturated vortex from the direct numerical simulations is shown to the right in figure 4.10 and the location of the high frequency instability is also shown on the right in figure 4.11. Qualitative agreement with experiments regarding the location and properties of the secondary instability is observed. These comparisons were presented at the poster session of IUTAM 99 in Sedona, AZ, USA 1999. The location of the high and low frequency secondary oscillations is found to be the same in the experiment as in the direct numerical simulations in figures 4.10 and 4.11.

Since the linear controller is able to reduce the strength of the cross-flow vortices, even when they have started to saturate, the necessary condition, at least for the high frequency secondary instability, has been removed. The linear controller thereby implicitly controls the secondary instability through the primary one. One possible problem with the linear controller is that it could actually excite secondary instabilities in a highly nonlinear flow. The reason

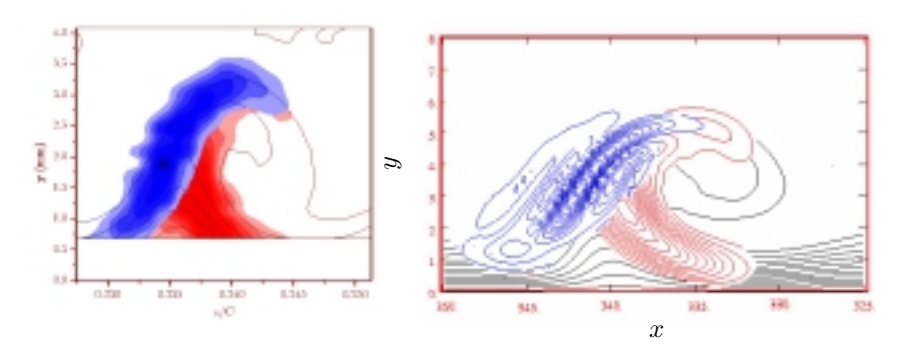


FIGURE 4.10. Left: Adapted from Kawakami et al. (1999) Top layer: Shaded contours of  $u_{rms}$  of High-frequency instability. Middle layer: Shaded contours of  $u_{rms}$  of Low-frequency instability. Bottom layer: Contours of  $u_{rms}$  of cross-flow vortex. Right: From DNS by Högberg and Henningson. Top layer: Contours of  $u_{rms}$  of High-frequency instability. Middle layer: Contours of  $u_{rms}$  of Low-frequency instability. Bottom layer: Contours of  $u_{rms}$  of cross-flow vortex.

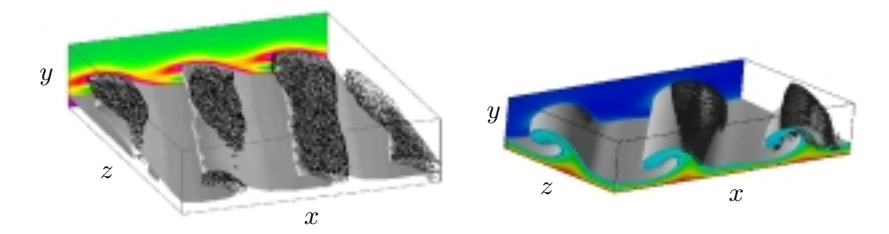


FIGURE 4.11. Left: From Lerche (1997). Gray: Iso-surface of  $\frac{\partial U_s}{\partial y} = 4.0$ . (1,1) mode. Black-mesh: Regions of high-frequency secondary instability. Right: From DNS by Högberg and Henningson. Gray: Iso-volume of mean  $u_{rms}$ . Black: Regions of high-frequency secondary instability.

is that effects from the modification of the mean flow by strong perturbations is not accounted for. Also the effect of the control on the mean flow could be of importance if the control amplitude is sufficiently large. Many of these issues need to be studied in more detail, but the present results are sufficiently encouraging to motivate further research.

#### CHAPTER 5

# Discussion

In this thesis two different approaches to optimal control of transition are studied. The nonlinear, iterative, optimization procedure is widely used within the flow control community and is indeed a powerful tool to use when computing optimal controls. A debated issue is whether it is sufficient to solve the approximative problem by discretizing a continuous formulation of the optimization problem or if the exact optimization problem should be derived for the discretized equations. It was found in the present work that the approximate method of discretizing the continuous optimization problem is sufficient to use for control of strong instabilities but that the convergence rate can be lower that when using an exact approach. The strength of the nonlinear method is that there is a possibility to optimize basically any properties of the flow or the geometry just by specifying the correct objective. Another strength of this nonlinear method is that it can be used for exploring possibilities of controlling separation or manipulation of a turbulent flow where nonlinear effects are important. For active flow control the method has the drawback that it cannot be used online and that it requires powerful computers, but methods like the checkpointing technique can be used together with efficient algorithms for parallelization to overcome these problems.

The second approach tested, and partially developed in this thesis is based on the linear Orr–Sommerfeld–Squire equations which can be used in an optimization problem that can be solved off-line providing a feedback control law. It is shown that in a comparable case the linear approach yields approximately the same optimal control signal as the nonlinear scheme. It is also demonstrated that such linear feedback controllers are able to increase the transition threshold for a random perturbation in channel flow by more than 500%. A physically motivated modification of the objective function was sufficient to obtain relaminarization of a low Reynolds number turbulent flow. The need for a change of the objective function indicates that the fundamental mechanism of turbulence to be targeted by an efficient control strategy remains to be identified, and the idea to focus on the near wall region and the effect of the linear coupling term between normal velocity and vorticity is a step in this direction.

The transition scenario in a Falkner–Skan–Cooke flow is complicated when secondary instabilities are considered but the successful extension of the linear controller to this spatially developing flow is very promising. The amplitude

of the cross-flow vortices can be lowered by application of control, and thus transition through secondary instability growth can be avoided or delayed. The use of the linear Orr–Sommerfeld–Squire equations appear to be sufficient for transition control in many flows, even though nonlinear and spatial effects are neglected.

The linear framework also facilitates the development of state estimators that can be used to reconstruct a flow field from measurements in online simulations with exponential convergence. The convergence with the current formulation was found to be a bit slow, but still exponential. The main problem is the initial transient in the estimator, which exists for all cases tested, since the combination of an estimator and a controller relies on the performance of the estimator. The transition thresholds could only be increased by about 48% for random noise perturbation in a channel flow which is much less than for the full information controller. The fact that the controller mainly relies on information close to the walls could be utilized in the estimator design in future studies. If the flow field near the wall can be estimated with faster convergence the compensator performance could be improved. Also further development by incorporation of more measurements and knowledge about flow properties could improve the present result. Testing and evaluating linear estimation and compensation also in the spatial flow is suggested for a future study.

Once the estimation problem has been solved resulting in good performance of the compensator, these controllers could be tested experimentally. It should be noted that for practical implementation an extension of all aspects of the present work towards robust schemes is necessary. The idealized setting considered here is not likely to exist in practice even in a laboratory. This extension is however straightforward in terms of formulating the problem both in the linear and nonlinear setting, as outlined by Bewley, Moin & Temam (1997) and Bewley, Temam & Ziane (2000). The price of this extension is additional complexity in the solution of the optimization problem. Also discrete actuation and sensing needs to be considered and modeled in order to take the step into the experimental setting in order to assure that this does not substantially affect the performance of the scheme. Both the estimator and the controller can work online given that a sufficiently fast computer is available. This means that they could probably be used in an experimental setup with only minor modifications.

Utilizing the tools from control theory is a very promising approach to flow control that has a large undeveloped potential, and the work in this thesis provides merely a few of the initial steps in the development towards practical implementation. In this work we have only exploited the optimal  $(\mathcal{H}_2)$  controllers so there is plenty of work still to be done in the intersection of fluid mechanics and control theory.

#### CHAPTER 6

# Quick guide to papers and authors contributions

## Paper 1

Numerical approaches to optimal control of a model equation for shear flow instabilities.

M. HÖGBERG (MH) & M. BERGGREN (MB)

A model equation for shear flow instabilities is used to study the effects of using an approximate approach of the adjoint based optimization technique. The problem formulation and derivations were performed jointly by the authors. Coding and numerical simulations and also post-processing of data was performed by MH. The report was written in close cooperation between both authors, where MB has written the more mathematical discussions. An early version of this paper was published as a technical report (Högberg, Berggren & Henningson (1999)). Published in *Journal of Flow, Turbulence and Combustion.* **65** (3/4), 2000.

## Paper 2

Optimal control in wall bounded flows.

M. Högberg, M. Chevalier (MC), M. Berggren & D. S. Henningson (DH) In this paper a solver for the nonlinear optimization problem, using the adjoint equations for gradient computations, is developed and tested for both channel and boundary layer flow. The channel flow problem has been explored by MH and the extension to boundary layer flow was performed by MC. Derivations of adjoint equations and gradient expressions were done by MH and MC in close cooperation with MB. Implementation for solving the channel flow problem was performed by MH and for the boundary layer flow by MC. The report was written jointly by MH and MC with feedback from MB and DH. The results presented for the channel flow case were previously published in the proceedings of ETC8, Barcelona (Högberg, Henningson & Berggren (2000)). Published as a technical report of the Swedish Defence Research Agency (FOI-R-0182-SE), 2001.

## Paper 3

Spatially localized convolution kernels for decentralized control and estimation of plane channel flow.

M. HÖGBERG & T. R. BEWLEY (TB)

The derivation of the linear controllers and estimators is described and results from application to both transition and turbulence are presented. The derivations of the optimization problems was done by MH under the supervision of TB. Implementations and simulations as well as kernel computations were performed by MH and the paper was written by TB and MH jointly. In particular, the discussion about spatial localization and its implications was written by TB. An early, shorter version of this paper was published in the proceedings of the 39th IEEE Conference on Decision and Control (Högberg & Bewley (2000)). Submitted to Automatica.

## Paper 4

Decentralized feedback control and estimation of transition in plane channel flow.

M. HÖGBERG, T. R. BEWLEY & D. S. HENNINGSON

In this work the performance of the linear controller, estimator and compensator is studied and quantified. Implementation and simulations as well as kernel computations was performed by MH. The introduction was written by DH and pictures were produced by MH. The implementation details and results sections were written by MH with feedback from TB and all authors participated in writing the discussion. Submitted to *Journal of Fluid Mechanics*.

#### Paper 5

Optimal control of transition initiated by oblique waves in channel flow. M. Högberg, T. R. Bewley, M. Berggren & D. S. Henningson

This paper compares the performance of the nonlinear and linear control approaches applied to the growth of oblique waves in channel flow. Parametric studies and comparisons are presented. Simulations were performed by MH who also wrote the paper. TB, MB and DH all contributed to this paper with suggestions for improvements and through underlying work. Published in *Proc. Turbulence and Shear Flow Phenomena 2*, vol. I, Stockholm, Sweden, 2001.

#### Paper 6

Secondary instability of cross-flow vortices in Falkner-Skan-Cooke boundary layers.

M. HÖGBERG & D. S. HENNINGSON

In this paper the secondary instabilities of cross-flow-vortices in Falkner–Skan–Cooke boundary layers is studied. Much of the work was performed for the MSc of MH (Högberg & Henningson (1996)), but post processing of data, pictures and discussions as well as writing the journal paper was as a part of the doctoral studies of MH. The idea for the project came from DH and simulations were performed by MH with guidance from DH. The paper was written by MH and DH jointly. Published in *Journal of Fluid Mechanics*, **368** 1998.

## Paper 7

Linear optimal control applied to instabilities in spatial boundary layers. M. Högberg & D. S. Henningson

The application of linear optimal control to spatially developing flows is presented in this paper. TS-waves, optimal perturbations and traveling as well as stationary cross-flow vortices are considered. Kernel computations implementation and simulations were performed by MH. The paper was written by MH with feedback from DH. Submitted to *Journal of Fluid Mechanics*.

# Acknowledgment

First of all I would like to thank my advisor Professor Dan Henningson. He is truly a guru to turn to with queries about the mysteries of fluid mechanics, and his enthusiasm has inspired me to dig deeply into the problems I have faced during my research. The door to his office is always open for a quick question as well as for longer discussions, and I'm very grateful for that.

My assistant advisor Doctor Martin Berggren has been invaluable for my work on adjoint methods. Without his help, it would have taken me a long time to get through all the tricky derivations and obtain insight into the mathematical aspects of these problems.

Professor Thomas Bewley gave me the opportunity to learn about linear control theory and has been a great inspiration. He was also kind enough to arrange for my stay at UCSD for seven months where I had a good time both on and off campus.

Many thanks also to everyone at the department of Mechanics for being part in creating the inspiring atmosphere that we all enjoy. In particular I wish to thank Martin, Janne, Stellan, Luca, Casper, Paul and Mattias for many stimulating and sometimes productive discussions on a wide variety of topics, not always within the scope of fluid mechanics.

Finally I want to thank my friends and my family for supporting me throughout my studies.

Tack Elisabeth för din kärlek och ditt stöd i alla lägen ♡

# **Bibliography**

- Abergel, F. & Temam, R. 1990 On some control problems in fluid mechanics. *Theoret. Comput. Fluid Dyn.* 1, 303–325.
- Andersson, P., Berggren, M. & Henningson, D. S. 1999 Optimal disturbances and bypass transition in boundary layers. *Phys. Fluids* 11, 134–150.
- BALAKUMAR, P. & HALL, P. 1999 Optimum suction distribution for transition control. *Theoret. Comput. Fluid Dynamics* 13 1–19.
- Bamieh, B., Paganini, F., & Dahleh, M. 2000 Distributed Control of Spatially-Invariant Systems. *IEEE Trans. Automat. Contr.*, to appear.
- BARAMOV, L., TUTTY, O. R. & ROGERS, E. 2000 Robust control of plane Poiseuille flow. AIAA paper 2000-2684.
- Benney, D. J. & Gustavsson, L. H. 1981 A new mechanism for linear and nonlinear hydrodynamic instability. *Stud. Appl. Maths* **64**, 185–209.
- Berggren, M., Glowinski, R. & Lions, J. L. 1996 A computational approach to controllability issues for flow-related models. (I): Pointwise control of the viscous Burgers equation. *Int. J. Comput. Fluid Dyn.* 7, 237–252.
- Berggren, M. 1998 Numerical Solution of a Flow-Control Problem: Vorticity Reduction by Dynamic Boundary Action. *SIAM Journal on Scientific Computing* 19(3), 829–860.
- Bewley, T. R. 2001 Flow control: new challenges for a new Renaissance *Prog. Aero. Sci.* 37, 21–58.
- Bewley, T.R., & Liu, S. 1998 Optimal and robust control and estimation of linear paths to transition. *J. Fluid Mech.* **365**, 305-349.
- Bewley, T. R. & Moin, P. 1994 Optimal control of turbulent channel flows In *Active Control of Vibration and Noise* (K. W. Wang *et al.* eds. ) ASME DE, **75**, 221–227.
- Bewley, T. R., Moin, P. & Temam, R. 1997 Optimal and robust approaches for linear and nonlinear regulation problems in fluid mechanics. *AIAA paper* 97-1872.
- Bewley, T. R., Moin, P. & Temam, R. 2001 DNS-based predictive control of turbulence: an optimal benchmark for feedback algorithms. *J. Fluid Mech.* 477, 179–225.
- Bewley, T. R., Temam, R. & Ziane, M. 2000 A general framework for robust control in fluid mechanics. *Physica D* **138**, 360–392.

- Berlin, S., Wiegel, M. & Henningson, D. S. 1999 Numerical and experimental investigation of oblique boundary layer transition *J. Fluid Mech.* **393**, 23–57.
- Bonfigli, G & Kloker, M. 2000 Three-dimensional boundary-layer transition phenomena investigated by spatial direct numerical simulation. In *Laminar-Turbulent Transition*, *Proc. IUTAM Symposium*, *Sedona, Arizona*, *USA* (1999) (Fasel, H. & Saric, W., eds.) 619–624. *Springer-Verlag*.
- Bower, W. W., Kegelman, J. T., Pal, A. & Meyer. G. H. 1987 A numerical study of two-dimensional instability-wave control based on the Orr-Sommerfeld equation *Phys. Fluids* **30**, (4), 998–1004.
- Butler, K.M., & Farrell, B.F. 1992 Three-dimensional optimal perturbations in viscous shear flows. *Phys. Fluids* A 4, 1637-1650.
- Byrd, R. H., Peihuang, L., Nocedal, J. & Zhu, C. 1994 A limited memory algorithm for bound constrained optimization *Technical Report NAM-08* Northwestern University.
- Cathalifaud, P. & Luchini, P. 2000 Algebraic growth in boundary layers: optimal control by blowing an suction at the wall Eur. J. Mech. B Fluids 19, 469–490.
- Collis, S. S., Chang, Y., Kellogg, S. & Prabhu, R. D. 2000 Large eddy simulation and turbulence control AIAA-paper 2000–2564.
- CORTELEZZI, L. & SPEYER, J. L. 1998 Robust reduced-order controller of laminar boundary layer transitions. *Phys. Rev. E* 58,(2) 1906–1910.
- CORTELEZZI, L., SPEYER, J. L., LEE, K. H. & KIM, J. 1998 Robust reduced-order control of turbulent channel flows via distributed sensors and actuators. *Proc.* 37th IEEE Conf. on Decision and Control 2, 1906–1911.
- CHOI, H., MOIN, P. & KIM, J. 1994 Active turbulence control for drag reduction in wall-bounded flows. J. Fluid Mech. 262, 75–110.
- Choi, H., Temam, R., Moin, P. & Kim, J. 1993 Feedback control for unsteady flow and its application to the stochastic Burgers equation. *J. Fluid Mech.* **253**, 509–543.
- Deyhle, H. & Bippes H. 1996 Disturbance growth in an unstable three-dimensional boundary layer and its dependence on environmental conditions. *J. Fluid Mech.* **316**, 73–113.
- ELOFSSON, P. A. 1998 Experiments on oblique transition in wall bounded shear flows TRITA-MEK 1998-5, PhD thesis, Department of Mechanics, KTH, Sweden
- FARREL, B. F. & IOANNOU, P. J. 1996 Turbulence suppression by active control *Phys. Fluids* **8** (5), 1257–1268.
- FJØRTOFT, R. 1950 Application of integral theorems in deriving criteria for instability for laminar flows and the baroclinic circular vortex. *Geofys. Publ., Oslo.* 17 (6), 1–52.
- Gad-el-Hak, M. 1996 Modern developments in flow control. *Appl. Mech. Rev.* 49 (7), 364–379.
- GMELIN, C. & RIST, U. 2001 Active control of laminar-turbulent transition using instantaneous vorticity signals at the wall. *Phys. Fluids* **13** (2), 513–519.
- Gunzburger, M. D. 1995 Flow control. (M. D. Gunzburger ed.) Springer, Berlin.
- Gunzburger, M. D. & Manservisi, S. 2000 Analysis and approximation of the velocity tracking problem for Navier–Stokes flow with distributed control. *SIAM J. Numer. Anal.* **37**, (5), 1481–1512.

- Gustavsson, L. H. 1991 Energy growth of three-dimensional disturbances in plane Poiseuille flow. J. Fluid Mech. 224, 241–260.
- HAMMOND, E. P., BEWLEY, T. R. & MOIN, P. 1998 Observed mechanisms for turbulence attenuation and enhancement in opposition-controlled wall bounded flows. *Phys. Fluids* 10, 2421–2423.
- HENNINGSON, D. S. 1996 Comment on "Transition in shear flows. Nonlinear normality versus non-normal linearity" [Phys. Fluids 7, 3060 (1995)] Phys. Fluids 8, (8), 2257–2258.
- HINZE, M. & KUNISCH, K. 2000 Three control methods for time dependent fluid flow. Flow, Turbulence and Combustion 65, (3/4), 273–298.
- Hu, H. H. & Bau, H. H. 1994 Feedback control to delay or advance linear loss of stability in planar Poiseuille flow. Proc. Royal Soc. London Ser. A 447, (1930), 299–312.
- HÖGBERG, M., BERGGREN, M. & HENNINGSON, D. S. 1999 Numerical Investigation of Different Discretization Approaches for Optimal Control. Technical Report TN 1999-74, FFA, the Aeronautical Research Institute of Sweden, P. O. Box 11021, S-161 11 Bromma, Sweden.
- HÖGBERG, M. & BERGGREN, M. 2000 Numerical approaches to optimal control of a model equation for shear flow instabilities. Flow, Turbulence and Combustion 65, (3/4), 299–320.
- HÖGBERG, M. & BEWLEY, T. R. 2000 Spatially localized convolution kernels for feedback control of transitional flows. In Proc. 39th IEEE Conf. on Decision and Control 4, 3278–3283.
- HÖGBERG, M., BEWLEY, T. R., BERGGREN, M. & HENNINGSON, D. S. 2001 Optimal control of transition initiated by oblique waves in channel flow. In *Proc. Turbulence and Shear Flow Phenomena 2*, vol. I, Stockholm, Sweden (E. LINDBORG *et al.* eds.), 157–161.
- HÖGBERG, M. & HENNINGSON, D. S. 1996 Cross-flow vortices and their secondary instability in Falkner-Skan-Cooke boundary layers. Technical Report TN 1996-60, FFA, the Aeronautical Research Institute of Sweden, P. O. Box 11021, S-161 11 Bromma, Sweden.
- HÖGBERG, M. & HENNINGSON, D. S. 1998 Secondary instability of cross-flow vortices in Falkner-Skan-Cooke boundary layers. *J. Fluid Mech.* **368**, 339–357.
- HÖGBERG, M., HENNINGSON, D. S. & BERGGREN, M. 2000 Numerical Investigation of Different Discretization Approaches for Optimal Control. In *Advances in Turbulence* VIII, Proceedings of the Eighth European Turbulence Conference, (C. DOPAZO *et al.* eds.), CIMNE, Barcelona, Spain, 205–208.
- ITO, K. & MORRIS, K. A. 1998 An approximation theory of solutions to operator Riccati equations for  $\mathcal{H}^{\infty}$  control. SIAM J. Control optim. **36** (1), 82–99.
- JOSHI, S.S., SPEYER, J.L., & KIM, J. 1997 A systems theory approach to the feedback stabilization of infinitesimal and finite-amplitude disturbances in plane Poiseuille flow. J. Fluid Mech. 332, 157–184.
- JOSHI, S.S., SPEYER, J.L., & KIM, J. 1999 Finite-dimensional optimal control of Poiseuille flow. J. Guidance, Control, and Dynamics 22 No. 2, 340–348.
- Joslin, R. D. 1998. Aircraft laminar flow control. Ann. Rev. Fluid Mech. 30, 1–29.

- JOSLIN, R. D., ERLEBACHER, G. & HUSSAINI, M. Y. 1996 Active Control of Instabilities in Laminar Boundary Layers-Overview and Concept Validation *Journal* of Fluids Engineering 118, (3), 494-497.
- JOSLIN, R. D., GUNZBURGER, M. D. & NICOLAIDES, R. A. 1997. Self-Contained Automated Methodology for Optimal Flow Control. AIAA Journal, 35, No. 5, 816-824.
- Kang, S. M., Ryder, V., Cortelezzi, L.& Speyer, J. L. 1999 State-space formulation and controller design for three-dimensional channel flows *Proc. American Control Conference* **3**, 1627–1631.
- KANG, S. M., CORTELEZZI, L.& SPEYER, J. L. 1999 Performance of a linear controller for laminar boundary layer transition in three dimensional channel flow *Private communication*, Luca Cortelezzi.
- KAWAKAMI M., KOHAMA Y. & OKUTSU M. 1999. Stability Characteristics of Stationary Crossflow Vortices in Three-Dimensional Boundary Layer. *AIAA paper* 99-0811.
- KIM, H. T., KLINE, S. J. & REYNOLDS, W. C. 1971 The production of turbulence near a smooth wall in a turbulent boundary layer. *J. Fluid Mech.* **50**, 133–160.
- KIM, J. & LIM, J. 2000 A linear process in wall-bounded turbulent shear flows Phys. Fluids 12 (8), 1885–1888.
- Kohama, Y., Saric W. S. & Hoos J. A. 1991 A high frequency, secondary instability of crossflow vortices that leads to transition. *Proc. R.A.S. Conf. on: Boundary-Layer Transition and Control, Cambridge University April 8-12.*
- KOUMOUTSAKOS, P. 1997 Active control of vortex-wall interactions. *Phys. Fluids* **9** (12), 3808–3816.
- KOUMOUTSAKOS, P. 1999 Vorticity flux control for a turbulent channel flow. *Phys. Fluids* **11** (2), 248–250.
- LANDAHL, M. T. 1975 Wave breakdown and turbulence SIAM J. Appl. Math. 28, (4), 735–756.
- Landahl, M. T. 1980 A note on an algebraic instability of inviscid parallel shear flows. *J. Fluid Mech.* **98**, 243–251.
- LAURIEN, E. & KLEISER, L. 1989 Numerical simulation of boundary-layer transition and transition control. J. Fluid Mech. 199, 403–440.
- Lee, K. H., Cortelezzi, L., Kim, J. & Speyer, J. L. 2001 Application of Robust Reduced-Order Controller to Turbulent Flows for Drag Reduction. *Phys. Fluids* 13 (5), 1321–1330.
- LEE, C., KIM, J., BABCOCK, D., & GOODMAN, R. 1997 Application of neural network to turbulence control for drag reduction. *Phys. Fluids* 9 (6), 1740-1747.
- Lee, C., Kim, J. & Choi, H. 1998 Suboptimal control of turbulent channel flow for drag reduction. J. Fluid Mech. 358, 245–258.
- LERCHE, T. 1997 Experimentelle Untersuchung nichtlinearen Strukturbildung im Transitionsprozeß einer instabilen Grenzschicht. Fortscrittberichte, VDI, Reihe 7: Strömungstechnik, Nr. 310.
- Luchini, P. 2000 Reynolds-number-independent instability of the boundary layer over a flat surface: optimal perturbations. *J. Fluid Mech.* **404** 289–309.
- Lumely, J. & Blossey, P. 1998 Control of turbulence. Ann. Rev. Fluid Mech. 30, 311–327.

- Lundbladh, A., Berlin, S., Skote, M., Hildings, C., Choi, J., Kim, J. & Henningson, D. S. 1999 An efficient spectral method for simulation of incompressible flow over a flat plate. Technical report, Department of Mechanics, KTH, *TRITA-MEK* 1999:11.
- LUNDBLADH, A., HENNINGSON, D. S. & JOHANSSON A. V. 1992. An Efficient Spectral Integration Method for the Solution of the Navier-Stokes Equations *FFA TN* 1992-28
- Malik, M.R., Li, F. & Chang, C.-L. 1994 Crossflow disturbances in three-dimensional boundary layers: nonlinear development, wave interaction and secondary instability. *J. Fluid Mech.* **268**, 1–36.
- Malik M. R., Li, F., Choudhari M. M. & Chang, C-L 1999 Secondary instability of crossflow vortices and swept-wing boundary-layer transition *J. Fluid Mech.* **399**, 86–115.
- MATSUBARA, M. & ALFREDSSON, P. H. 2001 Disturbance growth in boundary layers subjected to free-stream turbulence. J. Fluid Mech. 430, 149–168.
- METCALFE, R. W. 1994 Boundary layer control: A brief review. In Computational Fluid Dynamics '94, Invited lectures of the Second European CFD Conference; Stuttgart, Germany. (S. Wagner, J. Periaux & E. Hirschel. eds.), 52–60, John Wiley & Sons.
- Moin, P. & Bewley, T. R. 1994 Feedback control of turbulence. *Appl. Mech. Rev.* 47 (6), part 2, S3-S13.
- MORKOVIN, M. V. 1969 On the many faces of transition. In *Viscous Drag Reduction*, (C. S. Wells ed.), 1–31. Plenum Press.
- NORDSTRÖM, J., NORDIN, N. & HENNINGSON, D. S. 1999 The fringe region technique and the Fourier method used in the direct numerical simulation of spatially evolving viscous flows. SIAM J. Sci. Comp. 20 (4), 1365–1393.
- Pralits J. O., Hanifi, A. & Henningson D. S. 2001 Adjoint-based optimization of steady suction for disturbance control. Part 1. Incompressible flows. In *Towards optimal design of vehicles with low drag: Applications to sensitivity analysis and optimal control*. Licentiate thesis of Jan Pralits, Department of Mechanics, Royal Institute of Technology, Stockholm, Sweden *TRITA-MEK* 2001:07.
- RAYLEIGH, J. W. S. 1880 On the stability, or instability, of certain fluid motions. *Proc. Math. Soc. London* 11, 57–70.
- REBBECK, H. & CHOI, K.-S. 2001 Opposition control of near-wall turbulence with a piston type actuator. *Phys. Fluids* **13** (8), 2142–2145.
- Reddy, S. C., & Henningson, D. S. 1993 Energy growth in viscous channel flows. J. Fluid Mech. 252, 209-238.
- Reddy, S. C., Schmid, P. J., Baggett, J. S. & Henningson, D. S. 1998 On stability of streamwise streaks and transition thresholds in plane channel flows. *J. Fluid Mech.* **365**, 269-303.
- Schmid, P. J., & Henningson, D. S. 2001 Stability and transition in shear flows. Springer.
- Skelton, R. E. 1988 Dynamic Systems Control, Linear Systems Analysis and Synthesis. John Wiley & Sons.
- SRITHARAN, S. S. 1998 Optimal control of viscous flows. (S. S. SRITHARAN ed. ) SIAM.
- THOMAS, A. S. W. 1990 Active wave control of boundary-layer transition. In Viscous

- Drag Reduction in Boundary Layers (Bushnell, D. M. & Hefner, J. N., eds.. American Institute of Aeronautics and Astronautics, Washington, D.C. Vol. 123 in Progress in Astronautics and Aeronautics.
- Trefethen, L.N., Trefethen, A.E., Reddy, S.C., & Driscoll, T.A. 1993 Hydrodynamic stability without eigenvalues. *Science* **261**, 578-584.
- Walther, S., Airiau, C. & Bottaro, A. 2001 Optimal control of Tollmien—Schlichting waves in a developing boundary layer. *Phys. Fluids*, **13** (7), 2087—2096.
- Wassermann, P., Kloker, M. 2000 DNS-Investigations of the Development and Control of Crossflow Vortices in a 3D Boundary-Layer Flow. In *Laminar-Turbulent Transition, Proc. IUTAM Symposium, Sedona, Arizona, USA* (1999) (Fasel, H. & Saric, W., eds.), 565–570. *Springer-Verlag*.
- Westin, K. J. A., Boiko, A. V., Klingmann, B. G. B, Kozlov, V. V. & Alfredsson, P. H. 1994 Experiments in a boundary layer subjected to free-stream turbulence. Part I. Boundary layer structure and receptivity. *J. Fluid Mech.*, **281**, 193–218.

Part 2

Papers

# Paper 1

# Numerical approaches to optimal control of a model equation for shear flow instabilities

By Markus Högberg\* and Martin Berggren<sup>†‡</sup>

We investigate two different discretization approaches of a model optimalcontrol problem, chosen to be relevant for control of instabilities in shear flows. In the first method, a fully discrete approach has been used, together with a finite-element spatial discretization, to obtain the objective function gradient in terms of a discretely-derived adjoint equation. In the second method, Chebyshev collocation is used for spatial discretization, and the gradient is approximated by discretizing the continuously-derived adjoint equation. The discrete approach always results in a faster convergence of the conjugate-gradient optimization algorithm. Due to the shear in the convective velocity, a low diffusivity in the problem complicates the structure of the computed optimal control, resulting in particularly noticeable differences in convergence rate between the methods. When the diffusivity is higher, the control becomes less complicated, and the difference in convergence rate reduces. The use of approximate gradients results in a higher sensitivity to the degrees of freedom in time. When the system contains a strong instability, it only takes a few iteration to obtain an effective control for both methods, even if there are differences in the formal convergence rate. This indicates that it is possible to use the approximative gradients of the objective function in cases where the control problem mainly consists of controlling strong instabilities.

# 1. Introduction

In some fluid-mechanics systems, like boundary layers undergoing transition to turbulence, dramatic effect on global flow parameters may be achieved by minute local perturbations. Whereas such a fundamental instability property is a problem in many applications, it is the basis for the vision of dramatic performance improvements of fluid-mechanics systems using devices sensing and acting only on small parts of the flow with minute energy. This is somewhat parallel to the strategy among modern fighter-jet manufacturers to obtain superior performance by intentionally designing an unstable configuration that are stabilized by active means. Such control devices could be used to obtain drag

<sup>\*</sup>Department of Mechanics, Royal Institute of Technology (KTH), SE-100 44 Stockholm, Sweden

<sup>&</sup>lt;sup>†</sup>The Swedish Defence Research Agency (FOI), SE-172 90 Stockholm, Sweden

<sup>&</sup>lt;sup>‡</sup>Department of Scientific Computing, Uppsala University

reduction on bodies, increased lift on wings, increased propulsion efficiency, heat- and mass-transfer reduction or enhancement, control of combustion instabilities, and control of aeroacoustic pressure fluctuations. Overviews of the area of flow control, with emphasis on transition control, can be found in the articles of Metcalfe (1994), Reshotko (1994), and Gad-el-Hak (1996).

Optimal control is when one selects a set of parameters of the problem, the state equation, to be controlled. A numerical quantity, the objective function is introduced, defining the objective of the control. Optimization methods are then used to find parameter values that minimizes the objective function. This off-line way of computing the optimal control for a specific flow situation can give results that can be analyzed and used to construct control laws to be used in on-line feedback systems.

An efficient way of computing gradients of the objective function, to be used in the optimization process, is the adjoint-equation approach. Using this approach, the computational cost of the gradient calculation will be independent of the degrees of freedom for the control. The adjoint-equation approach is therefore particularly attractive when the parameter space is large. For a rapid convergence of the optimization algorithm, the gradient directions need to be accurate, and discretization effects may significantly affect the accuracy. Deriving the gradient on the discrete level yields exact gradients up to round off. In this approach, the state equation (the governing equation for the phenomenon under consideration) and the objective function are first discretized. Then, an expression for the gradient of the discrete objective function is derived. The gradient will be expressed in terms of an adjoint equation which will be the exact transpose of the discrete linearized state equation. The word "transpose" means that an inner-product is involved: the discrete adjoint equation will be a transpose to the linearized state equation with respect to some particular inner products, usually the ones that are used to define the norms in the objective function. This approach to obtain gradient expressions is followed for the semi-discrete case in section 3 below and for the fully discrete case using finite elements for the spatial discretization in section 4.1.

The derivation of a fully discrete gradient is often straightforward in principle, although it can be tedious; an example for the unsteady Navier–Stokes equation is given by Berggren (1998). For complicated numerical schemes, it can be difficult, or even impossible, to obtain exact, discrete adjoint equations. For instance, when using spectral collocation, it is not clear that the discrete approach is meaningful. A simpler approach is to discretize directly the expressions for the "continuous" adjoint equation and the gradient, as is done in section 4.2 below. This will in general introduce errors in the gradient directions. How much this will affect the convergence of the optimization algorithm is not clear a priori; it will most certainly depend on the application. Glowinski & He (1998) discuss this issue and argue that state equations that are relatively insensitive to changes in the control parameters are particularly sensitive to discretization errors in gradients.

The current work is a case study in which we compare the performance of the "discrete" and "continuous" approach. The model problem, presented in section 2, is chosen to resemble the behavior of exponential disturbance growth in shear flows. We have chosen this as a platform to compare these approaches before applying optimal control to transition phenomena in channel and boundary-layer flows. In particular, we would like to evaluate under which conditions we can get a decent performance of the continuous approach, since the Navier–Stokes solver we are considering uses spectral collocation. Gradient expressions in the semi-discrete case—discretized in time only—are given in section 3. Two different spatial discretizations, using finite-element and spectral methods, are presented in section 4. Expressions for the exact, discrete gradient and adjoint equation, associated with the finite-element discretization, are presented in section 4.1.1. Expressions for the approximate gradient, based on discretization, using spectral methods, of corresponding semi-discrete expressions are presented in section 4.2. For brevity, we have chosen not to include any derivations of gradients and adjoint equations in this article; full details are contained in an accompanying technical report (Högberg, Berggren & Henningson (1999)). The optimization procedure is presented in section 5, the numerical studies is reported in section 6, which leads to conclusions presented in section 7.

#### 2. The control problem

The equation considered here is a linear model problem, with advection and diffusion plus a single exponential instability term. Our main interest in this work is to control the exponential instability; the current equation is suitable for this purpose. The computational domain  $\Omega$  is depicted in figure 1, and the state equation is

$$u_{t} + U(y) u_{x} - \alpha u - \frac{1}{Re} \Delta u = f \qquad \text{in } Q = \Omega \times (0, T),$$

$$u = 0 \qquad \text{on } \Sigma_{0} = \Gamma_{0} \times (0, T),$$

$$u = \varphi \qquad \text{on } \Sigma_{c} = \Gamma_{c} \times (0, T),$$

$$\frac{Re}{2} U(y) u - u_{x} = 0 \qquad \text{on } \Sigma_{1} = \Gamma_{1} \times (0, T),$$

$$u(t = 0) = u_{0} \qquad (1)$$

The velocity profile,  $U(y) = (1 - e^{-y})/(1 - e^{-y_{\text{max}}})$ , is chosen to mimic a boundary layer profile. An energy analysis of this equation shows that it is stable when

$$\alpha \le \frac{\pi^2}{Re} \left( \frac{1}{4l^2} + \frac{1}{h^2} \right),\tag{2}$$

where l and h are the length and the height of the box  $\Omega$ , respectively. For large values of  $\alpha$ , the equation will be unstable with an exponential disturbance growth. This is the case when it is interesting to apply a control to prevent disturbances from growing.

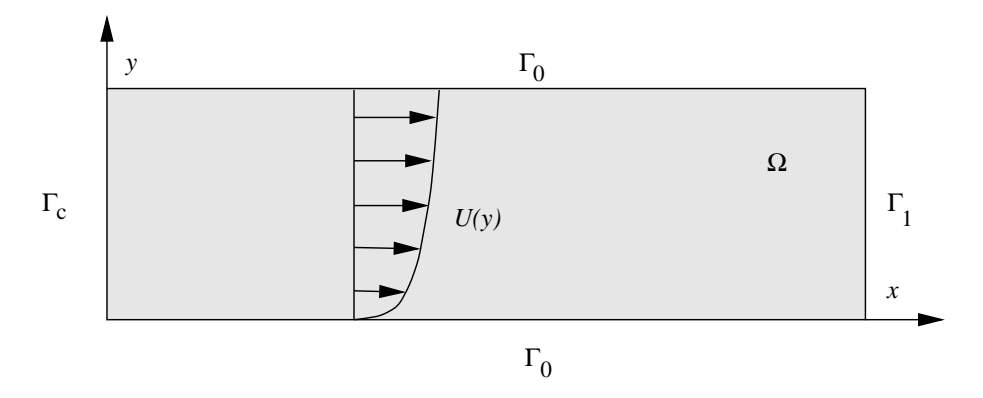


FIGURE 1. The computational domain studied.

The control problem consists of using the boundary condition  $\varphi$  to damp out the disturbance u as much as possible in the domain, still keeping the "size" of the control within reasonable limits. We therefore define an objective function (or cost function)  $J(\varphi)$  that quantifies our aim. The objective function used for the present study is the functional

$$J(\varphi) = \frac{\varepsilon}{2} \int_{\Sigma_c} \varphi^2 \, d\Sigma + \frac{1}{2} \int_{Q} u^2 \, dQ, \tag{3}$$

where u is calculated from  $\varphi$  by solving equation (1); the regularization parameter  $\varepsilon > 0$  serves the purpose of controlling the "size" of the control.

Our control problem may be formulated mathematically as:

find 
$$\varphi^* \in L^2(\Sigma_c)$$
 such that  $J(\varphi^*) \le J(\varphi) \ \forall \ \varphi \in L^2(\Sigma_c).$  (4)

Thus, the admissible controls is in our case the space  $L^2(\Sigma_c)$ , that is, functions that are square integrable in  $\Sigma_c$ .

# 2.1. Well-posedness

The choice of admissible controls as well as the choice of measure of the disturbances  $(L^2(Q))$  in our case) is indeed a *choice*. There are many other possibilities. Choosing the admissible controls to be merely square integrable is a quite weak requirement; it is also possible, for instance, to limit norms on derivatives in space and/or time. We have chosen  $L^2(\Gamma_c)$  for two main reasons. First,  $L^2$ -like norms are the the most-used measure of disturbances in the transition community. Second, it is easier to evaluate gradients of J if the norm on the control does not involve derivatives. Some choices of admissible controls that are "natural" from a mathematical point of view would complicate the gradient evaluation considerably, requiring the evaluation of fractional powers

of operators on the manifold  $\Gamma_c$ , or the solution of a boundary-value problem in time on  $\Sigma_c$  just to compute the derivative.

Whatever choice is made, it is clearly desirable that state equation (1) is a well-posed problem for each admissible control. Within the standard (" $H^1$ ") theory for parabolic initial-boundary-value problems (Dautray & Lions (1992)), it is not sufficient that inhomogeneous Dirichlet boundary conditions, such as the one on  $\Gamma_c$ , is merely in  $L^2(\Gamma_c)$ . However, by the Lions & Magenes (1972) technique of transposition, one can weaken the requirement on the boundary data and obtain a continuous dependence of  $u \in L^2(Q)$  on controls  $\varphi \in L^2(\Sigma_c)$ . It has to be stressed that the solution  $\varphi^*$  to problem (4), as well as corresponding solution u to state equation (1) may be smooth anyway, even if this is not required a priory. In fact, the solutions we compute in section 6 turn out to be quite smooth. Also note that the terminal control case raises additional concerns. For instance, if the objective function involves the term

$$\int_{\Omega} u(x,T)^2 \,\mathrm{d}\Omega,\tag{5}$$

it is not sufficient to work with admissible controls within  $L^2(Q)$ , since the mapping  $\varphi \mapsto u|_{t=T}$  is not continuous from  $L^2(Q)$  into  $L^2(\Omega)$ . To obtain a well-posed terminal control problem, the norm on the control can be strengthened, or the  $L^2(\Omega)$  norm on the observation in (5) can be weakened. For an example of the latter, we refer to Berggren, Glowinski & Lions (1996). Other options could be to average the observation over a narrow time interval  $(T - \tau, T + \tau)$ , or to exclude a portion around the control boundary from the observation, that is, replace the region  $\Omega$  in expression (5) with  $\omega \subset \Omega$ , where distance  $(\overline{\omega}, \Gamma_c) > 0$ . The last approach uses the fact that a nonsmooth control only can produce nonsmooth states locally in the vicinity of the control boundary due to the parabolic nature of the state equation.

# 2.2. Gradient expression

The conjugate-gradient algorithm, which will be used to solve the discrete version of problem (4), requires the gradient of the objective function. We compute the gradient by the adjoint-equation approach. This section states relevant expressions for the "continuous" case, that is, before discretization.

The gradient of the objective function (3) is defined through the directional derivative

$$\delta J = \langle \nabla J(\varphi), \delta \varphi \rangle = \lim_{s \to 0} \left| \frac{J(\varphi + s \, \delta \varphi) - J(\varphi)}{s} \right|,$$

where  $\delta \varphi$  is a variation of the control.

A perturbation technique together with integration by parts in space and time yields

$$\nabla J(\varphi) = \varepsilon \varphi + \frac{1}{Re} p_x \Big|_{\Gamma_c},\tag{6}$$

where the co-state p = p(x, t) is the solution to the adjoint equation

$$-p_t - U(y)p_x - \alpha p - \frac{1}{Re}\Delta p = u \quad \text{in } Q,$$

$$p = 0 \quad \text{on } \Sigma_0 \cup \Sigma_c,$$

$$\frac{Re}{2}U(y)p + p_x = 0 \quad \text{on } \Sigma_1,$$

$$p(t = T) = 0 \quad (7)$$

Thus, the gradient of J is computed as follows. Given  $\varphi$ , obtain corresponding state u by solving equation (1). From this u, compute corresponding co-state p by solving the adjoint equation (7). The gradient is then obtained by expression (6).

### 3. Temporal discretization and the semi-discrete gradient

We start by discretizing in time and obtain expressions for the gradient that corresponds to the ones given in section 2.2.

For the temporal discretization of state equation (1), we use  $u_t \approx (u^{n+1} - u^n)/\Delta t$ , implicit treatment of diffusion term, and explicit advection. This gives, for  $n = 0, \ldots, N-1$ , the time discrete equations,

$$\frac{u^{n+1} - u^n}{\Delta t} + U(y)u_x^n - \alpha u^{n+1} - \frac{1}{Re}\Delta u^{n+1} = f^{n+1} \quad \text{in} \quad \Omega, 
u^{n+1} = 0 \quad \text{on} \quad \Gamma_0, 
u^{n+1} = \varphi^{n+1} \quad \text{on} \quad \Gamma_c, \qquad (8) 
\frac{Re}{2}U(y)u^n - u_x^{n+1} = 0 \quad \text{on} \quad \Gamma_1, 
u^0 = u_0.$$

We approximate the objective function J in (3) with

$$J^{\Delta t} = \frac{\varepsilon}{2} \Delta t \sum_{n=1}^{N} \int_{\Gamma_c} |\varphi^n|^2 d\Gamma + \frac{1}{2} \Delta t \sum_{n=1}^{N} \int_{\Omega} |u^n|^2 d\Omega.$$
 (9)

Note that the gradient expression (6) is a function defined in  $\Sigma_c = \Gamma_c \times (0, T)$ . The gradient of the time discrete functional (9), derived by integration by parts in time and partial summation in time, is an N-vector with each component being a function on  $\Gamma_c$ ,

$$\nabla J^{\Delta t} = \left\{ \varepsilon \varphi^n + \frac{1}{Re} p_x^n \Big|_{\Gamma_c} \right\}_{n=1}^N, \tag{10}$$

where  $p^N$  is the solution to the problem

$$-\frac{p^{N+1} - p^N}{\Delta t} - \alpha p^N - \frac{1}{Re} \Delta p^N = u^N \quad \text{in} \quad \Omega,$$

$$p^N = 0 \quad \text{on} \quad \Gamma_0 \cup \Gamma_c,$$

$$p_x^N = 0 \quad \text{on} \quad \Gamma_1,$$

$$p^{N+1} = 0 \quad \text{in} \quad \Omega,$$

$$(11)$$

whereas  $p^n$ , for  $n = N - 1, \ldots, 1$ , solves problem

$$-\frac{p^{n+1}-p^n}{\Delta t} - Up_x^{n+1} - \alpha p^n - \frac{1}{Re}\Delta p^n = u^n \quad \text{in} \quad \Omega,$$

$$p^n = 0 \quad \text{on} \quad \Gamma_0 \cup \Gamma_c,$$

$$-\frac{Re}{2}U(y)p^{n+1} - p_x^n = 0 \quad \text{on} \quad \Gamma_1.$$
(12)

Note that the semi-discrete adjoint equations (11) and (12) are *not* obtained by a discretization of equation (7). Once the time-discrete state equation (8) and the objective function (9) are introduced, the gradient of the time-discrete objective function is *uniquely* defined; it is just a matter of deriving an expression for it. Also note that the first step of the semi-discrete adjoint (11) is different than the rest; this is a consequence of the explicit treatment of the advection term in state equation (8).

#### 4. Spatial discretizations

#### 4.1. Finite-element discretization

First we consider the discretization of the semi-discrete state equation (8). We use the standard uniform triangulation K of  $\Omega$  depicted in figure 2. Let  $V^h$  denote the space of continuous, piecewise linear functions, that is,

$$V^h = \{ w \mid w \in C^0(\Omega), w|_{T_h} \in P_1 \quad \forall T_h \in K \}.$$

Let  $V_{00}^h$  denote the subspace of  $V^h$  consisting of functions with zero trace on  $\Gamma_c \cup \Gamma_0$ ,

$$V_{00}^h = \{ w \mid w \in V^h, w|_{\Gamma_c \cup \Gamma_0} = 0 \}$$

The space of traces on  $\Gamma_c$  of functions in  $V^h$  will be denoted  $\gamma_c V^h$ , that is,

$$\gamma_c V^h = \{ \mu \mid \mu = w |_{\Gamma_c}, \text{ for some } w \in V^h \}.$$

Given  $\mu \in \gamma_c V^h$ , we also define,

$$V_0^h(\mu) = \{ w \mid w \in V^h, w|_{\Gamma_c} = \mu \text{ and } w|_{\Gamma_1} = 0 \}.$$

At each time step, the discrete controls will belong to  $\gamma_c V^h$ , the discrete states to  $V_0^h(\mu)$ , and the test functions to  $V_{00}^h$ .

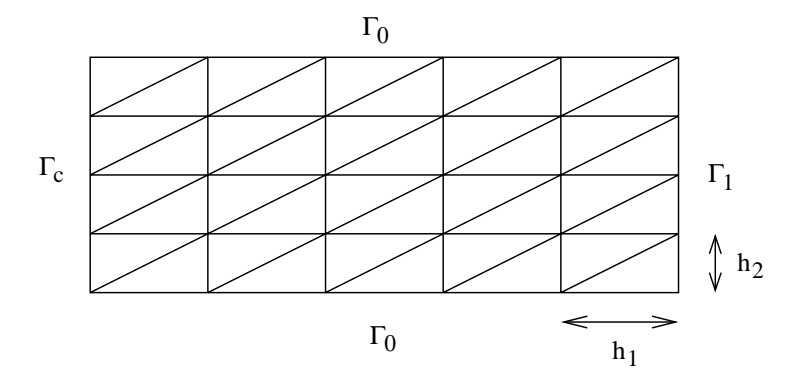


FIGURE 2. Schematic triangulation of the domain  $\Omega$ .

From the weak formulation of equation (8), we obtain the following fully discrete approximation to the state equation (1),

$$u_{h}^{0} \in V_{00}^{h} \text{ such that}$$

$$\int_{\Omega} u_{h}^{0} w \, d\Omega = \int_{\Omega} u^{0} w \, d\Omega \quad \forall w \in V_{00}^{h};$$
for  $n = 0, \ldots, N - 1$ ,  $u_{h}^{n+1} \in V_{0}^{h}(\varphi_{h}^{n})$  such that,
$$(1 - \alpha \Delta t) \int_{\Omega} u_{h}^{n+1} w \, d\Omega + \frac{\Delta t}{Re} \int_{\Omega} \nabla u_{h}^{n+1} \cdot \nabla w \, d\Omega$$

$$= \int_{\Omega} u_{h}^{n} w \, d\Omega + \Delta t \int_{\Omega} U u_{h}^{n} w_{x} \, d\Omega - \frac{\Delta t}{2} \int_{\Gamma_{1}} U u_{h}^{n} w \, d\Gamma$$

$$+ \int_{\Omega} f_{h}^{n+1} w \, d\Omega, \quad \forall w \in V_{00}^{h},$$

$$(13)$$

where  $\varphi_h^n \in \gamma_c V^h$ ,  $n = 1, \ldots, N$  are given.

We use the following discrete objective function:

$$J_h^{\Delta t}(\varphi_h) = \frac{\varepsilon}{2} \Delta t \sum_{n=1}^N \int_{\Gamma_n} |\varphi_h^n|^2 d\Gamma + \frac{1}{2} \Delta t \sum_{n=1}^N \int_{\Omega} |u_h^n|^2 d\Omega,$$
 (14)

and the fully discrete optimal control problem is:

find 
$$\varphi_{h*}^n \in \gamma_c V^h$$
,  $n = 1, \ldots, N$ , such that  $J(\{\varphi_{h*}^n\}_{n=1}^N) \leq J(\{\varphi_h^n\}_{n=1}^N)$ ,  $\forall \varphi_h^n \in \gamma_c V^h$ .

#### 4.1.1. Gradient expression

For the finite-element discretization, we follow the same route as in section 3. That is, we do not directly discretize the expressions for the adjoint equation

and the gradient given in section 3. Rather, we observe that once we have defined the discrete state equation (13) and the objective function (14), the gradient is uniquely defined, and we *derive* an expression for the gradient.

Recall that the gradient (10) of the time-discrete objective function is an N-vector with each component being a function on  $\Gamma_c$ . In the fully discrete case, the gradient is a vector of dimension  $NM_2$ , where  $M_2$  is the number of mesh points on the  $\Gamma_c$  boundary, excluding the corner points. Each component of this vector is evaluated by computing

$$(\nabla J_h^{\Delta t})_{i,n} = \varepsilon \int_{\Gamma_c} w^i \varphi_n \, d\Gamma + \int_{\Omega} u^n w^i \, d\Omega$$
$$- \int_{\Omega} w^i \left[ \left( \frac{1}{\Delta t} - \alpha \right) p^n - p^{n+1} \right] \, d\Omega$$
$$- \frac{1}{Re} \int_{\Omega} \nabla p^n \cdot \nabla w^i \, d\Omega - \int_{\Omega} U p^{n+1} w_x^i \, d\Omega,$$
 (15)

where n = 1, ..., N,  $i = 1, ..., M_2$ , and where  $w^i \in V^h$  such that it is 1 at node i on  $\Gamma_c$  and zero at all other nodes of the triangulation. In expression (15), the fully discrete co-states  $\{p^n\}_{n=1}^N$  are computed as follows. First,  $p^N \in V_{00}^h$  is the computed as the solution to

$$\begin{split} p^{N+1} &= 0, \\ \int\limits_{\Omega} [(1 - \alpha \Delta t) p^N - p^{N+1}] w \, \mathrm{d}\Omega + \frac{\Delta t}{Re} \int\limits_{\Omega} \nabla p^N \nabla w \, \mathrm{d}\Omega = \Delta t \int\limits_{\Omega} u^N w \, \mathrm{d}\Omega \\ \forall w \in V_{00}^h, \end{split}$$

then, for  $n=N-1,\,\dots,\,1,\,p^n\in V^h_{00}$  is the solution to \*

$$\int_{\Omega} [(1 - \alpha \Delta t)p^{n} - p^{n+1}]w \, d\Omega + \frac{\Delta t}{Re} \int_{\Omega} \nabla p^{n} \cdot \nabla w \, d\Omega 
+ \Delta t \int_{\Omega} p^{n+1}Uw_{x} \, d\Omega - \frac{\Delta t}{2} \int_{\Gamma_{1}} Up^{n+1}w \, d\Gamma = \Delta t \int_{\Omega} u^{n}w \, d\Omega 
\forall w \in V_{00}^{h}.$$
(16)

# 4.2. Spectral discretization

When applying the finite-element discretization in section 4.1, we defined the discrete objective function (14) and the discrete state equation (13). Then we derived a discrete adjoint equation that yields the exact gradient of the

<sup>\*</sup>Expression (15) is not derived directly as an approximation to expressions (6) or (10), and the relation between these expressions might appear non-obvious. However, expression (15) is indeed the correct variational approximation of the gradient (10); see the discussion by (Glowinski 1984, App. I A 5) or Berggren, Glowinski & Lions (1996).

objective function (in exact arithmetics). We consider an alternative approach for the spectral Chebyshev discretization. The semi-discrete state equation (8) and corresponding adjoint equation (11)–(12) are discretized similarly using Chebyshev collocation in both the x and y direction. Using this discretized adjoint in the gradient expression (10), we expect, even in exact arithmetic, to obtain an error in the gradient direction. The question is how much this will affect the performance of the optimization algorithm.

We consider approximations to solutions of the semi-discrete state equation (8), which at each time level will be of the form

$$u_c(x,y) = \sum_{n=0}^{N_x} \sum_{m=0}^{M_y} \widehat{u}_c^{nm} T^n(x) T^m(y),$$

where  $T^n$  is the Chebyshev polynomial of degree n. We use spectral collocation at the Gauss–Lobatto points

$$x_{j} = \cos \frac{j\pi}{N_{x}}, \qquad j = 0, \dots N_{x},$$

$$y_{k} = \cos \frac{k\pi}{N_{y}}, \qquad k = 0, \dots N_{y},$$

$$(17)$$

to compute the coefficients  $\widehat{u}_c^{nm}$ , or, equivalently, the the value of  $u_c$  at the collocation points. (For simplicity, we assume here that the domain is  $\Omega = (-1,1) \times (-1,1)$ .) The semi-discrete state equation (8) is enforced exactly at the collocation points for  $j=1,\ldots,N_x-1$  and  $k=1,\ldots,N_y-1$ , whereas the boundary conditions are enforced for  $j=0,\ N_x$  and  $k=0,\ N_y$ . This yields a system of the type  $\mathcal{A}u^{n+1}=b(u^n)$  which is solved using Gaussian elimination. The elements of the matrix  $\mathcal{A}$  are computed using simple recursion formulas for the derivatives. Consult the book by Canuto et al. (1988) for a full account on the implementation of pseudo-spectral methods. Note that the matrix  $\mathcal{A}$  will be dense, as opposed to the sparse, block-diagonal matrices obtained in the FEM case; the accuracy is on the other hand much higher. The same approach is used to approximate the semi-discrete adjoint equation (11)–(12). The co-state approximations  $p_c(x,y)^n$  for time level  $n=1,\ldots,N$ , are used to obtain the spectral approximation of the objective-function gradient,

$$\nabla J_c^{\Delta t} = \left\{ \varepsilon \varphi^n(y) + \frac{1}{Re} \frac{\partial p_c^n}{\partial x}(0, y) \right\}_{n=1}^N, \tag{18}$$

for  $y \in \Gamma_c$ .

In the optimization algorithm described in section 5, we need to evaluate inner-products and norms in the form of integrals over the control boundary  $\Gamma_c$ . From the values of a function at the collocation points, we can evaluate the integral of the function through the quadrature formula

$$\int_{-1}^{1} u(y) \, \mathrm{d}y \approx \sum_{j=0}^{N_y} u(y_j) w_j,$$

where the following weights (Hanifi, Schmid & Henningson (1996)) are used:

$$w_j = \frac{b_j}{N_y} \left\{ 2 + \sum_{n=2}^{N_y} c_n \frac{(1 + (-1)^n)}{(1 - n^2)} \cos \frac{nj\pi}{N_y} \right\},$$

$$b_j = \begin{cases} 1/2 & j = 0, N_y \\ 1 & 1 \le j \le N_y - 1 \end{cases} c_n = \begin{cases} 1 & n = 0, N_y \\ 2 & 1 \le n \le N_y - 1. \end{cases}$$

The value of the objective function is also evaluated using the same quadrature formula,

$$J_c^{\Delta t}(\varphi) = \frac{\varepsilon}{2} \Delta t \sum_{n=1}^N \sum_{k=0}^{M_y} |\varphi^n(y_k)|^2 w_{y_k} + \frac{1}{2} \Delta t \sum_{n=1}^N \sum_{j=0,k=0}^{N_x, M_y} |u^n(x_j, y_k)|^2 w_{x_j} w_{y_k},$$
(19)

where  $x_i$  and  $y_k$  are the Gauss-Lobatto points (17).

#### 5. Solving the control problem

For a problem, such as the one studied here, with a quadratic objective function and a linear state equation, a well-suited minimization algorithm is an adaptation to the current context of the conjugate gradient method of Hestenes & Stiefel (1952). This algorithm was originally developed to solve a system of linear equations Ax = b with a symmetric and positive definite matrix A. The algorithm is stated in Golub & Van Loan (1989), for instance. To simplify the notation, we here discuss the algorithm as if it was applied at the differential-equation level. In practice, we of course use approximations: finite differences for the temporal discretization, as described in section 3, and either a finite-element (section 4.1) or a spectral discretization (section 4.2) in space.

We apply the conjugate-gradient algorithm to solve minimization problem (4). As in the linear-algebra case, this means that a "linear system" is solved, namely the equation

$$(\varepsilon \mathcal{I} + \mathcal{A}^* \mathcal{A}) \varphi^* = b, \tag{20}$$

where  $\mathcal{A}$  is the mapping  $\varphi \mapsto u$  obtained by solving a homogeneous version of state equation (1) (that is, with f = 0 and  $u_0 = 0$ ; the inhomogeneities are all collected in the right-hand side b). Moreover,  $\mathcal{A}^*$  denotes the adjoint (or transpose) of operator  $\mathcal{A}$ . The operator  $\mathcal{A}^*$  is the mapping

$$u \mapsto \frac{\partial p}{\partial x}\Big|_{\Gamma_c},$$

where p is obtained from u by solving the adjoint equation (7).

The conjugate-gradient algorithm requires symmetry of the operator

$$\tilde{\mathcal{A}} \stackrel{def}{=} (\varepsilon \mathcal{I} + \mathcal{A}^* \mathcal{A}) \tag{21}$$

which occurs in the left-hand side of (20), otherwise the algorithm cannot be expected to converge. In the discrete case, corresponding operator will be symmetric when using exact gradients, as we do for the finite-element discretization in section 4.1.1. Approximating the gradient, as we do for the spectral discretization in section 4.2, does *not* yield a symmetric operator in general. Thus, there is no guarantee that the algorithm converges in the latter case.

#### 5.2. Convergence properties

The conjugate-gradient algorithm has linear convergence properties except for the first few iterations (and the last few ones, for problems with a small number of degrees of freedom). This motivates the model  $\|\nabla J(\varphi^n)\| \approx CK^n$  for studying the convergence properties. The classical estimate (Axelsson (1996)) of K is

$$K = \frac{\sqrt{\kappa} - 1}{\sqrt{\kappa} + 1},$$

where  $\kappa = \|\tilde{\mathcal{A}}\| \|\tilde{\mathcal{A}}^{-1}\|$  is the condition number of the operator  $\tilde{\mathcal{A}}$  as defined in expression (21). In our case  $\kappa = \tilde{\lambda}_n \varepsilon^{-1}$ , where  $\tilde{\lambda}_n$  is the largest eigenvalue of  $\tilde{\mathcal{A}}$ . Equivalently,  $\kappa = 1 + \sigma_n^2 \varepsilon^{-1}$  where  $\sigma_n = \|\mathcal{A}\|$  is the largest singular value associated with the mapping  $\mathcal{A}$ , see Glowinski & Lions (1994). If  $\sigma_n$  is well separated from the other singular values, this estimate can be improved. In this case, the "effective" condition number is  $\kappa_{\text{eff}} \approx 1 + \sigma_{n-1}^2 \varepsilon^{-1}$  where  $\sigma_{n-1}$  is the next-largest singular value of  $\mathcal{A}$ . The number of iterations will depend on  $\kappa_{\text{eff}}$  plus one extra iteration for the separated singular value. This is of interest in our case, since it is expected that the exponential instability associated with  $\alpha$  will result in a well separated, large singular value of  $\mathcal{A}$ .

The conjugate gradient algorithm offers a simple way of estimating the extremal eigenvalues of  $\tilde{\mathcal{A}}$  by computing the eigenvalues of the matrix

$$T_{n} = \begin{pmatrix} \frac{1}{\rho_{0}} & -\frac{\gamma_{0}}{\rho_{0}} \\ -\frac{\gamma_{0}}{\rho_{0}} & \frac{1}{\rho_{1}} + \frac{\gamma_{0}}{\rho_{0}} & -\frac{\gamma_{1}}{\rho_{1}} \\ & -\frac{\gamma_{1}}{\rho_{1}} & \frac{1}{\rho_{2}} + \frac{\gamma_{1}}{\rho_{1}} & -\frac{\gamma_{2}}{\rho_{2}} \\ & & \cdot & \cdot \\ & & \cdot & \cdot \end{pmatrix}, \tag{22}$$

where  $\gamma_n = ||\nabla J(\varphi_n)||/||\nabla J(\varphi_{n-1})||$  is the coefficient which is used to blend the old search direction with the new gradient to compute the new search direction, and where  $\rho_n$  is the step length, used to update the control, the state, and the gradient at each iterate. Consult chapter 10 of Golub & Van Loan (1989) for more details.

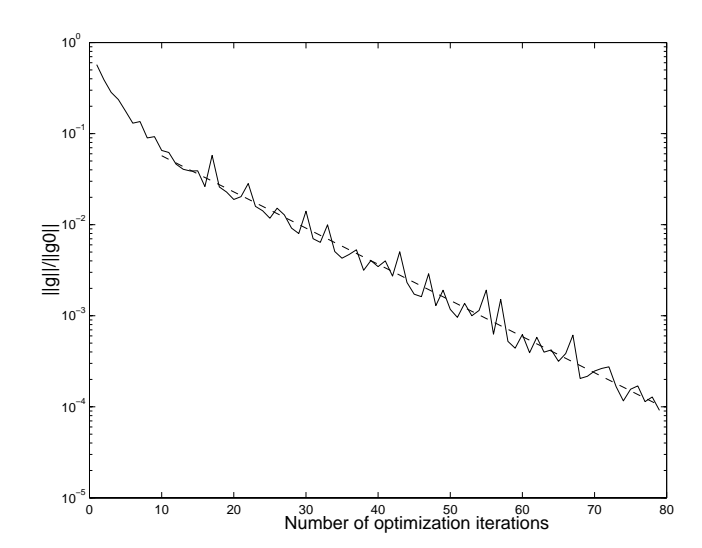


FIGURE 3. Convergence behavior with a least-squares estimate of the linear convergence rate.

For comparison of convergence properties of the conjugate gradient algorithm, the K factor describes the convergence rate. After the initial steps of optimization the convergence rate is linear. A least-squares fit of a straight line in a logarithmic scale gives the slope of the convergence curve. Figure 3 shows the approximation of the linear part of the convergence curve. The slope of this line is equal to  $\log K$ . A low value of K indicates fast convergence whereas a high value corresponds to slow convergence. A K value of 1 implies no convergence.

To obtain comparable results for the two discretization methods, we must use comparable resolutions as well. The spectral method uses a discretization in space that is not uniform, whereas we use a uniform mesh for the FEM discretization. In the discrete objective functions  $J(\varphi)$ , expressions (14) and (19), the control boundary is accounted for twice, since it is a part of second integral as well as of the first. This means that we for coarse discretization get an extra, implicit regularization of the optimization problem. This regularization is greater for the FEM case, since the cells at the control boundary typically are coarser. As the number of grid points increases, the effect of this implicit regularization decreases.

#### 6. Numerical studies

#### 6.1. Test problem

As an initial condition for the computation, consider a disturbance in the domain of the form  $u(x,y) = 0.1(y^2 - 2y)(x^2 - 2x)$  (figure 4). This disturbance will develop in different ways depending on the parameters  $\alpha$  and Re. High

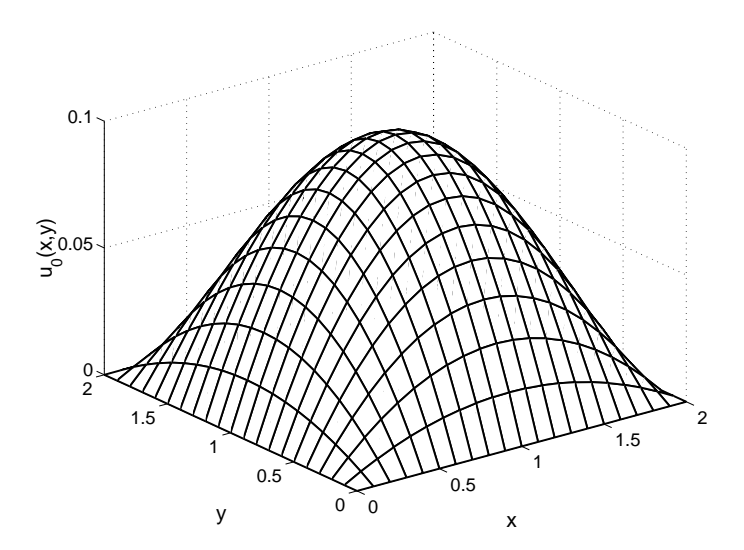


FIGURE 4. Typical initial disturbance used in computations presented.

values of  $\alpha$  give a strong instability, and the value of Re decides the diffusivity of the problem. The convective velocity profile  $U(y) = (1 - e^{-y})/(1 - e^{-y_{\text{max}}})$  is used, and the domain is  $\Omega = (0, 2) \times (0, 2)$  for most simulations.

#### 6.2. Critical value of $\alpha$

To investigate for which values of  $\alpha$  there is an instability, we choose a value of Re and compute the evolution of an initial disturbance using the discrete versions of state equation (1). The results from the FEM code and from the spectral code were practically identical, and the critical value of  $\alpha$  agreed with the estimate (2), plotted as a crossed circle in figure 5. The growth rate of the disturbance is the logarithm of the time derivative for the disturbance energy. The exponential growth rate is proportional to  $\alpha$  as can be seen in figure 5. For other values of Re than Re = 1 (as in this case) this curve is shifted up or down.

# 6.3. Convergence dependence on $\alpha$

To study if the map  $\mathcal{A}$  in (21) actually has a well separated singular value we calculate the eigenvalues of the matrix  $T_n$  in (22). For different values of  $\alpha$  we noted that there are a few eigenvalues that are separated from the others. Ideally we would get only one separated eigenvalue, but probably due to round-off errors in the conjugate-gradient algorithm we get a few extra large eigenvalues. Figure 6 shows the eigenvalues for different values of  $\alpha$ .

If we study the K dependence on  $\alpha$ , we expect it to be approximately constant. In figure 7, we see that there is a small increase in K as  $\alpha$  increases. This increase is small compared to what would be obtained if the condition

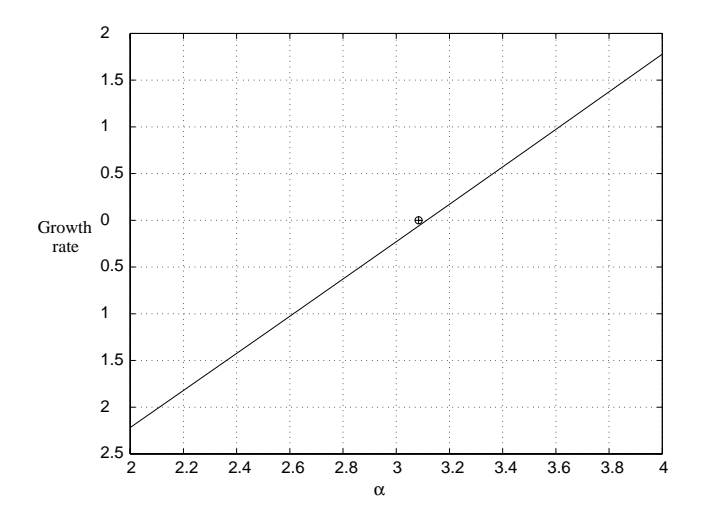


FIGURE 5. Growth rate of disturbance versus  $\alpha$ . Here Re=1. Crossed circle is from estimate (2).

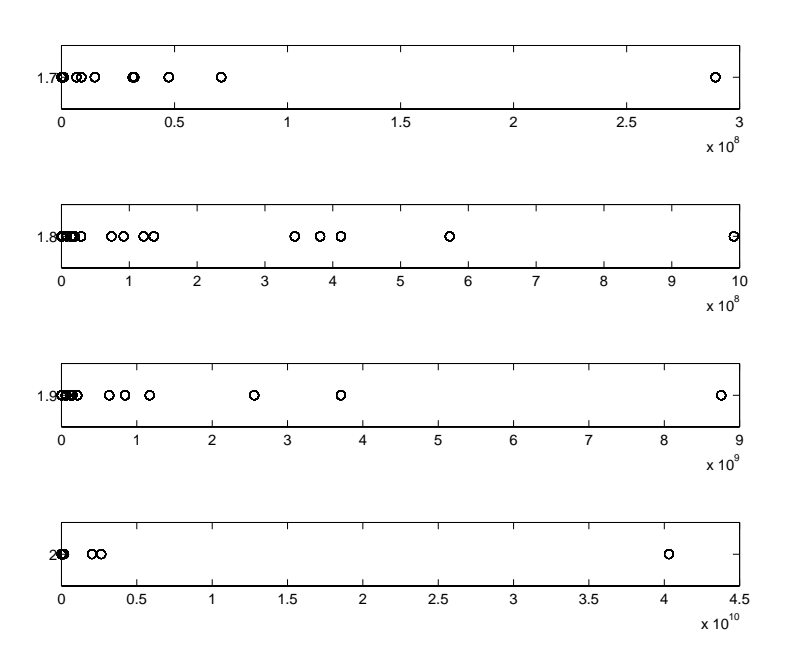


FIGURE 6. Spectra of  $T_n$ , n = 20 for  $\alpha = \{1.7, 1.8, 1.9, 2.0\}$ , Re = 30, and  $\varepsilon = 10^{-10}$ .

number grew as fast as the largest singular value for increasing  $\alpha$ . This verifies the expected behavior of the algorithm, discussed in section 5.2, for a well-separated largest singular value of  $\mathcal{A}$ . The small increase in K can be explained

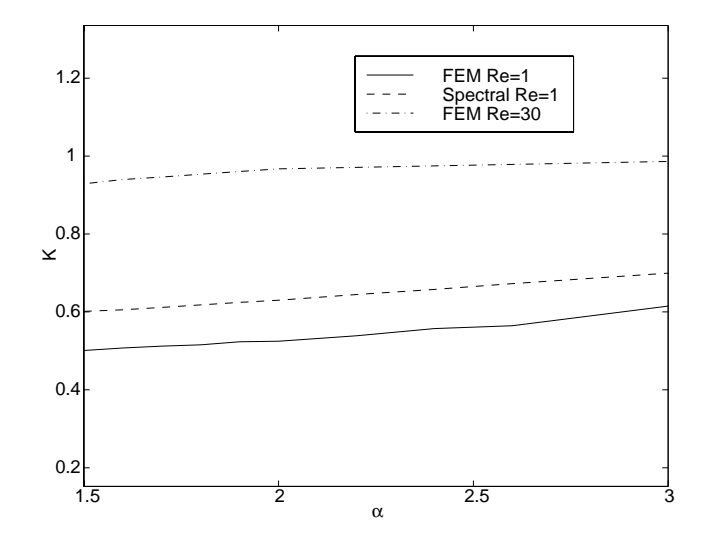


FIGURE 7. K dependence on  $\alpha$ . Solid: FEM, Re=1 and  $\varepsilon=10^{-6}$ . Dashed: Spectral, Re=1 and  $\varepsilon=10^{-6}$ . Dash-dotted: FEM Re=30 and  $\varepsilon=10^{-10}$ .

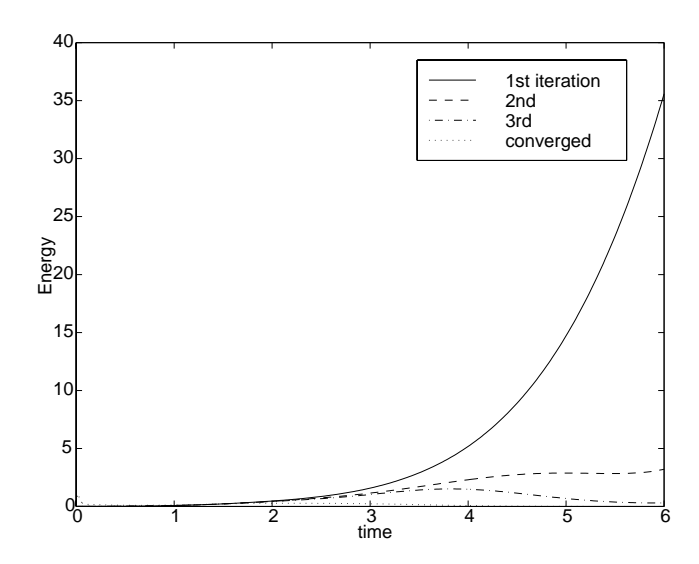


FIGURE 8. Energy growth in box at different stages of optimization. Re=50 and  $\alpha=1.5$ 

by contamination due to accumulation of round-off errors in the conjugate-gradient algorithm.  $\,$ 

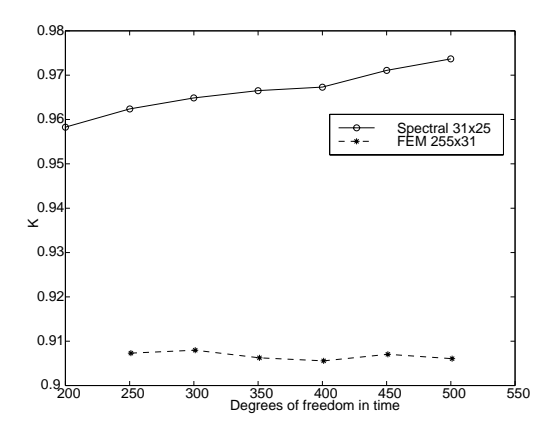


FIGURE 9. Convergence factor vs. degrees of freedom in time. Unstable case with  $\alpha = 1.5$  and Re = 100.

Most of the decrease of the objective function is obtained in the first few steps of the optimization; additional iterations only slightly improves the results. Figure 8 shows the energy growth in the box at different stages of optimization. The exponential growth of the disturbance is gone already after one iteration and the energy decays after two.

#### 6.4. Dependence of problem size on convergence

If the degrees of freedom of the problem are increased, the convergence rate of the conjugate-gradient algorithm usually decreases. However, the dependence on the degrees of freedom differs between the two methods. Since the spectral method is based on a derivation of the gradient for the semi-discrete problem, it is not expected to perform as well as the FE method, which is based on an exact derivation of the discrete objective-function gradient.

In figure 9 we see the dependence for the convergence factor K on degrees of freedom in time for an unstable case with Re=100 and  $\alpha=1.5$ . The difference between the methods is large, and performance of the spectral method degrades with increasing number of time steps whereas it does not for the FE method. If the number of degrees of freedom of the control is increased in space rather than in time, figure 10, both methods seem rather independent in terms of convergence rate. However, if the resolution is much too small, the spectral method actually did not converge at all.

A stable case is studied in figure 11. Here  $\alpha=0$  and Re=10. Convergence here is fairly good for both methods. As the number of degrees of freedom is increased, K grows for both methods, but faster for the spectral method.

#### 6.5. Diffusivity dependence

There is also a dependence on the diffusivity of the state equation. A high Re yields a problem that is dominated by convection in the upper part of the

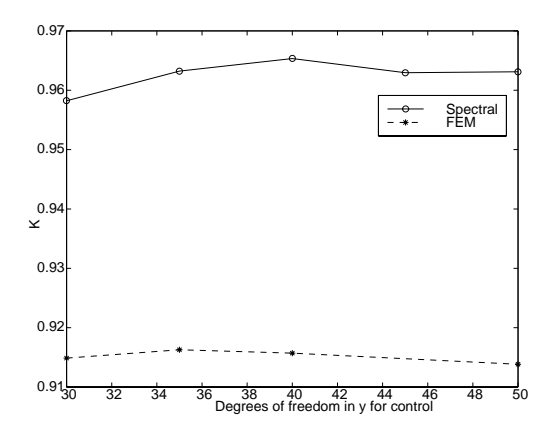


FIGURE 10. Convergence factor vs. degrees of freedom in y. Unstable case with  $\alpha=1.0$  and Re=100.

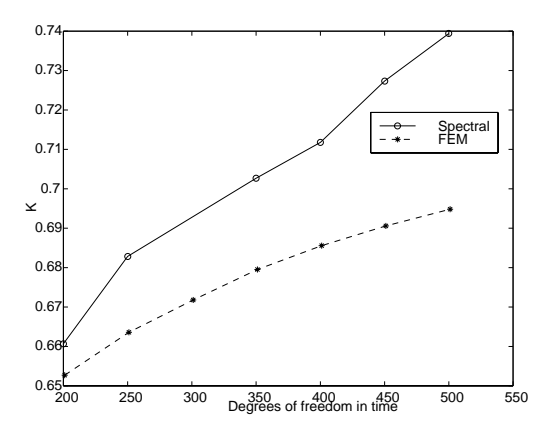


FIGURE 11. Convergence factor vs. degrees of freedom in time. Stable case with  $\alpha=0$  and Re=10.

domain and by diffusion close to the lower boundary; this follows from the shape of the convection velocity U(y). If the final time T is sufficiently large, this means that the control is very effective throughout the domain, except close to the lower boundary. This yields a complicated control with strong gradients in both the wall-normal coordinate y and in time, which requires many iterations to fully resolve by the conjugate-gradient algorithm. At low values of Re this effect is less clear, since the control is obtained mainly through the diffusion term. Note also that if the final time T is not long enough for a disturbance to propagate through the domain, we obtain a control that does not have much effect close to the outflow.

Figure 12 shows K for different values of Re with  $\alpha=1$  kept constant. The problem is unstable for all values of Re used. For low values of Re both methods

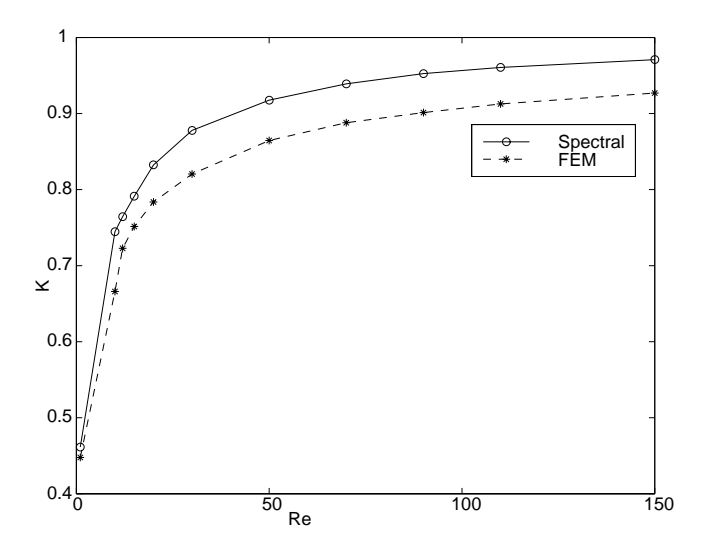


FIGURE 12. Convergence factor vs. Re. Diffusivity of control problem increases with decreasing Re. Unstable case with  $\alpha = 1$  and 200 degrees of freedom in time.

perform well. As Re is increased both methods have slower convergence rate, and the spectral method is more sensitive to this decrease in diffusivity. The methods appear to approach a high K value as Re is increased. This value is close to 1 for the spectral code. Finally, for Re=150, the conjugate-gradient algorithm fails to converge when using the spectral approximations, see figure 13.

#### 6.6. Objective function

The value of the objective function after optimization is a measure of how well the optimization method performed. Since the same initial disturbance and the same parameters have been used for both methods the values are comparable. The objective function is minimized to approximately the same value for both methods, and the resulting controls are almost identical. As long as the conjugate-gradient algorithm converges, and the resolution is not too crude, we find that the higher accuracy of the spectral code gives lower values of the discrete objective function than is obtained for the same number of points with the FEM code, see table 1. The values of the objective function in the table are taken after 20 optimization steps. This is a case with a strong instability but a high diffusivity, so the control is fairly simple. The reduction in the objective function is computed by comparing with the value obtained without any control.

The conjugate gradient algorithm should produce monotonically decreasing values of the objective function. This is also observed when using exact

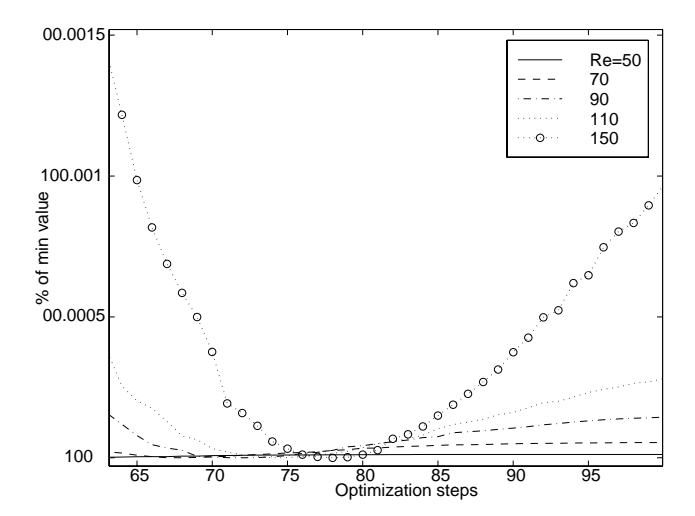


FIGURE 13. Objective Function in % of minimum value vs. optimization steps. Complexity of control problem increases with Re. Unstable case with  $\alpha=1$  and 200 degrees of freedom in time.

FEM			Spectral			
$N_y$	$\operatorname{Cost}$	Red. $\%$	$N_y$	$\operatorname{Cost}$	Red. %	
8	0.2005	99.93	8	0.2149	99.90	
16	0.1892	99.92	16	0.1900	99.91	
24	0.1871	99.92	24	0.1864	99.92	
32	0.1867	99.92	32	0.1855	99.92	

TABLE 1. Values of the objective function and objective function reduction for the two different methods at a number of resolutions. Final time T=5, Re=10, and  $\alpha=2.0.$  The x resolution was 255 for FEM and 31 for the spectral method.

gradients in the FEM discretization. For the most complex cases, there is not a monotonic decrease of the objective function with the spectral method, even when the optimization converges. This is most likely due to the fact that the gradients are not exact, and therefore we do not find the actual minimum of the discretized objective function.

#### 7. Discussion and conclusions

We have compared two different discretization approaches for optimal control of a model problem selected in order to resemble the behavior of instability growth in shear flows. We always obtained a faster convergence of the finite-element version which uses exact gradients than the spectral one using approximate gradients. This is particularly noticeable in demanding cases when convergence can be expected to be slow with any method. For example, when Re is high, the system is dominated by diffusion close to the wall y=0 but by advection in the rest of the domain. This results in a complicated control and requires many iterations to resolve it numerically. The slower convergence when using approximate gradients makes a large difference in this case and the conjugate gradient algorithm may even fail to converge. When reducing the time step, the degrees of freedom for the control increases, and we noted that convergence degraded when using approximate gradients, but convergence degraded to a much lower degree, or not at all, when exact gradients were used.

When a strong instability is present in the system, this increases vastly the value of the objective function. It also increases the condition number of the optimization problem, but the convergence rate of the optimization algorithm is not much affected as explained in section 5.2. This phenomenon was also verified numerically. Only a few iteration were needed to control the strong instability and drastically reduce the value of the objective function. This was observed whether exact or approximate gradients were used. Note that this also holds for cases when the linear convergence is slow, that is, when the value of K, as defined in section 5.2, is close to one. In this case, we can successfully control the instability only after a few iterations, but to obtain full convergence of the optimization algorithm requires many iterations. However, full convergence may not be of much interest for this case.

Our results indicate that it would certainly be desirable to use exact gradients for optimal control of shear flows. However, when adding routines that solve the adjoint equations to a given code that was not designed with this in mind, it will be hard, if not impossible, to obtain exact gradients due to the complexity of the code. The current investigations suggests that approximate gradient can be used at least when controlling a dominating instability. One way of improving the convergence rate could be to parameterize the control, especially the temporal development, in order to reduce the degrees of freedom. Fixing the degrees of freedom, the accuracy of the gradient direction may improve when the numerical resolution of the simulation is increased.

#### References

- Axelsson, O. 1996 Iterative Solution Methods. Cambridge University press.
- Berggren, M. 1998 Numerical Solution of a Flow-Control Problem: Vorticity Reduction by Dynamic Boundary Action. SIAM Journal on Scientific Computing 19(3), 829–860.
- Berggren, M., Glowinski, R. & Lions, J. L. 1996 A Computational Approach to Controllability Issues for Flow-Related Models. (II): Control of Two-Dimensional, Linear Advection-Diffusion and Stokes Models. *International Journal of Computational Fluid Dynamics* 6(4), 253–274.
- CANUTO, C., HUSSAINI, M. Y., QUARTERONI, A. & ZANG, T.A. 1988 Spectral methods in Fluid Dynamics Springer-Verlag, Berlin
- DAUTRAY, R. & J. L. LIONS 1992 Mathematical Analysis and Numerical Methods for Science and Technology, Vol. 5: Evolution Problems I. Springer-Verlag, Berlin
- Gad-el-Hak, M. 1996 Modern developments in flow control. *Appl. Mech. Rev* **49**(7), 365–379.
- GLOWINSKI, R. 1984 Numerical Methods for Nonlinear Variational Problems. Springer-Verlag, New York
- GLOWINSKI, R. & J. HE 1998 On Shape Optimization and Related Issues. In: J. Borggaard, J. Burns, E. Cliff, and S. Schreck (eds.): Computational Methods for Optimal Design and Control, Proceedings of the AFOSR workshop on Optimal Design and Control, Arlington, Virginia. Birkhäuser, Boston pp. 151–179.
- GLOWINSKI, R. & LIONS, J. L. 1994 Exact and approximate controllability for distributed parameter systems (Part I). Acta Numerica. pp.269-378.
- GOLUB, G. H. & VAN LOAN, C. F. 1989 *Matrix computations*. The Johns Hopkins University press, Baltimore, MD.
- Hanifi, A., Schmid P. J. & Henningson D. S. 1996 Transient growth in compressible boundary layer flow. *Phys. Fluids*, 8 (3), 826–837.
- Hestenes, M. R. & Stiefel E. 1952 Methods of conjugate gradient for solving linear systems. *Journal Research National Bureau of Standards* **45**, 409-436.
- HÖGBERG, M., BERGGREN, M. & HENNINGSON, D. S. 1999 Numerical Investigation of Different Discretization Approaches for Optimal Control. Technical Report TN 1999-74, FFA, the Aeronautical Research Institute of Sweden, P. O. Box 11021, S-161 11 Bromma, Sweden.
- LIONS, J. L. & MAGENES, E. 1972 Non-Homogeneous Boundary Value Problems and Applications, Vol. 2. Springer-Verlag, Berlin.
- METCALFE, R. W. 1994 Boundary Layer Control: A Brief Review. In: S. WAGNER, J. PERIAUX & E. HIRSCHEL (eds.): Computational Fluid Dynamics '94, Invited Lectures of the Second European CFD Conference; Stuttgart, Germany, John Wiley & Sons, New York pp. 52–60.
- Reshotko, E. 1994 Boundary Layer Instability, Transition and Control. AIAA Paper 94-0001.

Paper 2

2

# Optimal control of wall bounded flows

By Markus Högberg\*, Mattias Chevalier\*†, Martin Berggren†‡ and Dan S. Henningson\*†

Optimal control of transition in channel flow and boundary layer flow is attempted. First the optimization problem is stated and the corresponding adjoint equations used to compute the gradient of the objective function are derived for both the channel flow and boundary layer flow problems. Implementation and numerical issues are discussed, and some details of the implementation are explained. The governing equations used are the incompressible Navier-Stokes equations with appropriate boundary conditions for the two cases. The boundary condition on the wall normal velocity at the walls of the channel, or at the single wall in the boundary layer case, is used as control and is determined in the iterative optimization procedure. The objective function used for the optimization problem contains the perturbation energy and a regularization term on the applied control. The optimization problem is formulated using a continuous formulation in space and time using the primitive variables, velocity and pressure, and is then rewritten in a formulation containing only the wall normal velocity and the wall normal vorticity. An existing solver for the incompressible Navier-Stokes equations using this formulation can then also be used to solve the associated adjoint problem. Implementation is straightforward using this formulation and the efficiency of the original solver is maintained. To test the performance of the solver of the optimization problem, the derived formulation is applied on different stages of the oblique transition scenario in the channel flow case. In a parallel Falkner-Skan-Cooke flow successful control of an inviscid instability is reported, and in the spatial Blasius flow the energy growth of a Tollmien-Schlichting wave is efficiently inhibited.

#### 1. Introduction

In the last decade, one topic in fluid mechanics that has been subject to an increasing interest is *flow control*. The explosive development in computer technology has made it possible to approach these problems from a numerical point of view, and also to construct small devices to be used for measurements and actuation in experiments. The numerical approach to flow control can for

<sup>\*</sup>Department of Mechanics, Royal Institute of Technology (KTH), SE-100 44 Stockholm, Sweden

 $<sup>^{\</sup>dagger} \text{The Swedish Defence Research Agency (FOI), SE-172 90 Stockholm, Sweden$ 

<sup>&</sup>lt;sup>‡</sup>Department of Scientific Computing, Uppsala University

example be used to design the shape of a wing to minimize drag or to solve some other optimization problem. Mathematical aspects of the flow control problem is the topic of the books edited by Gunzburger (1995) and Sritharan (1998). Computational approaches to flow control are reviewed in the paper by Hinze & Kunisch (2000). Optimal control of channel flow using direct numerical simulations was previously considered using by Bewley, Moin & Temam (2001) and using large eddy simulations by Collis *et al.* (2000). In addition to channel flow Joslin *et al.* (1997) also considered the boundary layer case with a two dimensional flow in direct numerical simulations.

In this work we consider the problem of control of transition from laminar to turbulent flow in a channel and a boundary layer. In many applications there is a large potential benefit from the ability to prevent transition whereas in other applications the turbulent state is the desired one. Our objective is to delay or prevent transition at low Reynolds numbers, particularly focusing on the bypass transition (Morkovin (1969)) scenarios, not originating from an exponential instability. The problem of bypass transition is important in many practical applications, and considerable amounts of research has been done on this subject see e.g. the recent book by Schmid & Henningson (2001).

#### 2. Optimization problem formulations

The formulation of an optimal control problem is based on three important decisions. The choice of governing equations, determining what means of actuation to use, and what properties of the flow to control. For a particular flow geometry and with given fluid properties, these choices have to be made with care.

In this work the governing equations are the incompressible Navier–Stokes equations. In a recent study, successful application of feedback controllers computed from the linearized Navier–Stokes equations was performed by Högberg & Bewley (2001) in temporal channel flow. Changes in the mean flow is not easily taken into account using this formulation. Thus, a proper treatment of problems where this is important, such as a flow with local separation, requires the use of the full Navier–Stokes equations.

Since no particular quantity is known that establishes where we are on the path to transition the choice of objective function is difficult. The mean skin friction drag could be used as an indicator, since it has a jump at transition, and can be used to define a transition point, as for example in Reddy et al. (1998). On the other hand, Bewley, Moin & Temam (2001) showed that the mean drag was not a good choice for the objective function when the purpose was to relaminarize turbulence in a channel flow, and concluded that the turbulent kinetic energy was a more appropriate choice. Since we are interested in control of transition rather than turbulence, the energy of the deviation from the mean flow appears to be an appropriate quantity to minimize. An increased physical understanding of the transition process and the crucial mechanisms

of turbulence could provide a guide to the best choice of objective function as pointed out by Kim & Lim (2000).

It is important to choose the properties of the control in such a way that it is able to do its task in an efficient way. For our study, we have chosen to use blowing and suction at the wall during a specified period in time. The state of the flow is observed during another, possibly overlapping, period in time. When a spatially rather than a temporally evolving flow is considered it is physically meaningful to specify also the spatial extent of the control and observation regions. The control is restricted to have zero mass flux, in order to limit the ability to affect the mean flow and focus the control effort on the perturbations.

The gradient of the objective function may be expressed in terms of the solution of an adjoint equation. Here, we discretize the expressions for the adjoint equations and the gradient that have been derived on the "continuous" level. An alternative is to discretize the Navier–Stokes equations and the objective function and derive the adjoint equations and the gradient expression on the discrete level. The latter approach leads to more accurate gradient directions, but it seems difficult to apply for the present discretizations. Issues related to the errors introduced by the approximative (continuous) formulation are discussed in e.g. Glowinski & He (1998) and Gunzburger (1998). The use of the continuous formulation is motivated by the findings in Högberg & Berggren (2000) where one conclusion was that it is sufficient to use the approximative (continuous) formulation in order to control strong instabilities. It was noted that in such cases most of the reduction of the objective function is achieved in the first few iterations, and additional iterations only result in a fine tuning of the control. The drawback is that it will require more iterations to reach the true optimal solution, if it is even possible, than with the discrete formulation.

#### 2.1. Governing equations

In this section we consider the channel flow problem and the details of the method used to solve the optimization problem. The boundary layer problem is basically an extension of the channel flow case. The differences are outlined in section 2.3, and a full description is provided in Appendix A.

Our computational domain depicted in figure 1 is

$$\Omega = (-x_L/2, x_L/2) \times (-1, 1) \times (-z_L/2, z_L/2),$$

in x, y, z, and we define

$$\Gamma_L = \Omega(y = -1), \quad \Gamma_U = \Omega(y = 1) \quad \text{and} \quad Q = \Omega \times (0, T).$$

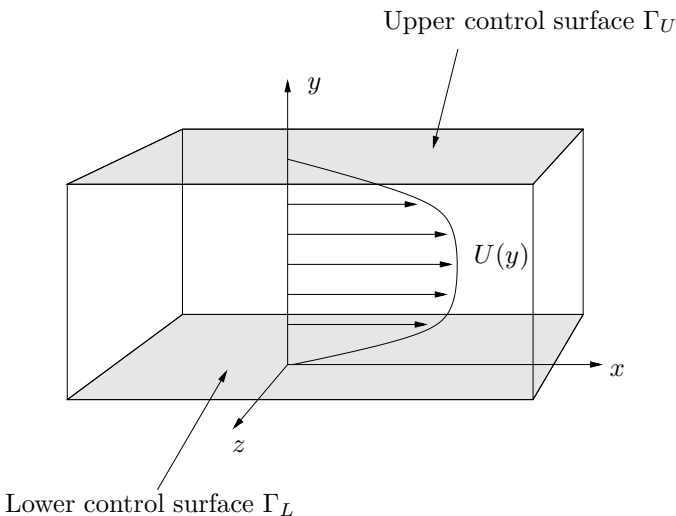


Figure 1. Geometry of flow domain  $\Omega$  for channel flow simulations.

The non-dimensional, incompressible Navier–Stokes equations with a Reynolds number, Re, based on the centerline velocity and half the channel height are,

$$\begin{cases} \frac{\partial u}{\partial t} + (u \cdot \nabla)u - \frac{1}{Re}\Delta u + \nabla \pi = -\nabla P & \text{in } Q, \\ \nabla \cdot u = 0 & \text{in } Q, \\ u|_{t=0} = u_0, \end{cases}$$
 (1)

where  $u = (u_1, v, w)$  is the velocity vector,  $\pi$  is the pressure and  $\nabla P$  represents the pressure gradient driving the flow and can either be constant or used to ensure constant mass flux. Periodic boundary conditions in x and z, and control through blowing and suction together with a no-slip condition for the directions parallel to the wall gives the complete set of boundary conditions,

$$u|_{x=-x_L/2} = u|_{x=x_L/2},$$

$$u|_{z=-z_L/2} = u|_{z=z_L/2},$$

$$e_i \cdot u|_{y=-1} = \begin{cases} \varphi_L^T \psi_L = \sum_{m=1}^{M_L} \varphi_{L,m}(t) \, \psi_{L,m}(x,z) & \text{in } (T_1^c, T_2^c) & \text{for } i = 2, \\ 0 & \text{otherwise,} \end{cases}$$

$$e_i \cdot u|_{y=1} = \begin{cases} \varphi_U^T \psi_U = \sum_{m=1}^{M_U} \varphi_{U,m}(t) \, \psi_{U,m}(x,z) & \text{in } (T_1^c, T_2^c) & \text{for } i = 2, \\ 0 & \text{otherwise,} \end{cases}$$

$$(2)$$

where  $e_i$  are unit basis vectors in the coordinate directions, and  $\psi$  are basis functions for the control designed to have zero net mass flux. We can now

introduce the control variable  $\varphi$  defined as:

$$\varphi = (\varphi_L, \varphi_U)^T, \begin{cases} \varphi_L = (\varphi_{L,1}, \dots, \varphi_{L,M_L})^T, \\ \varphi_U = (\varphi_{U,1}, \dots, \varphi_{U,M_U})^T. \end{cases}$$

To completely specify the optimal control problem we also need an objective function. If we choose to minimize the energy of the deviation from a target velocity distribution, the objective function is:

$$J(\varphi) = \frac{\varepsilon}{2} \int_{T_1^c}^{T_2^c} \int_{\Gamma} |v|^2 d\Gamma dt + \frac{1}{2} \int_{T_1^o}^{T_2^o} \int_{\Omega} |u - u_T|^2 dQ,$$
 (3)

where  $(T_1^c, T_2^c)$  is the control time period and  $(T_1^o, T_2^o)$  is the observation time period. The target velocity profile is denoted  $u_T$ . The optimization problem is then: find  $\varphi^*$  which satisfies

$$J(\varphi^*) \le J(\varphi) \quad \forall \ v(\varphi)|_{\Gamma} \in \mathcal{U}_{\mathrm{ad}}$$

where  $\mathcal{U}_{ad}$  has been used to denote the set of admissible controls which is a subset of  $L^2((T_1^c, T_2^c); \mathbb{R}^{M_L+M_U})$ .

#### 2.2. Derivation of objective function gradient.

The gradient of the objective function  $\nabla J$  is defined by

$$\delta J(\varphi) = \lim_{s \to 0} \frac{J(\varphi + s \,\delta\varphi) - J(\varphi)}{s} = \langle \nabla J, \delta\varphi \rangle$$

$$= \left\langle \frac{\partial J}{\partial \varphi_L}, \delta\varphi \right\rangle + \left\langle \frac{\partial J}{\partial \varphi_U}, \delta\varphi \right\rangle, \tag{4}$$

where  $\delta \varphi$  is the first variation of the control. The functional  $\delta J$  is the first variation of J with respect to  $\delta \varphi$ . To find an expression for  $\nabla J$  we start by differentiating the objective function (3) to get,

$$\delta J(\varphi) = \varepsilon \int_{T_c^c}^{T_2^c} \int_{\Gamma} \delta v \, v \, d\Gamma \, dt + \int_{T_c^o}^{T_2^o} \int_{\Omega} \delta u \cdot (u - u_T) \, dQ, \tag{5}$$

where  $\delta v = e_2 \cdot \delta u$  and  $\delta u$  is the first variation of u with respect to  $\delta \varphi$ . To find an expression for the relation between  $\delta u$  and  $\delta \varphi$  we differentiate state equation (1),

$$\begin{cases}
\frac{\partial \delta u}{\partial t} + (\delta u \cdot \nabla)u + (u \cdot \nabla)\delta u - \frac{1}{Re}\Delta \delta u + \nabla \delta \pi = 0 & \text{in } Q, \\
\nabla \cdot \delta u = 0 & \text{in } Q, \\
\delta u|_{t=0} = 0,
\end{cases} (6)$$

96

and boundary conditions (2),

$$\delta u|_{x=-x_L/2} = \delta u|_{x=x_L/2},$$

$$\delta u|_{z=-z_L/2} = \delta u|_{z=z_L/2},$$

$$e_i \cdot \delta u|_{y=-1} = \begin{cases} \delta \varphi_L^T \psi_L = \sum_{m=1}^{M_L} \delta \varphi_{L,m}(t) \psi_{L,m}(x,z) & \text{in } (T_1^c, T_2^c) \\ 0 & \text{otherwise,} \end{cases}$$

$$e_i \cdot \delta u|_{y=1} = \begin{cases} \delta \varphi_U^T \psi_U = \sum_{m=1}^{M_U} \delta \varphi_{U,m}(t) \psi_{U,m}(x,z) & \text{in } (T_1^c, T_2^c) \\ 0 & \text{otherwise.} \end{cases}$$

$$(7)$$

Now we introduce a vector function p = p(x, y, z, t) such that  $e_i \cdot p = p_i$  and require p to satisfy the boundary conditions:

$$p|_{x=-x_L/2} = p|_{x=x_L/2},$$

$$p|_{z=-z_L/2} = p|_{z=z_L/2},$$

$$p|_{y=-1} = p|_{y=1} = 0.$$
(8)

The boundary conditions may be chosen during the derivation but in order to simplify the presentation they are introduced already at this point. Taking the dot product between p and equation (6) and integrating over Q yields

$$\int_{Q} p \cdot \left( \underbrace{\frac{\partial \delta u}{\partial t}}_{1} + \underbrace{(\delta u \cdot \nabla)u}_{2} + \underbrace{(u \cdot \nabla)\delta u}_{3} - \underbrace{\frac{1}{Re} \Delta \delta u}_{4} + \underbrace{\nabla \delta \pi}_{5} \right) dQ = 0.$$
 (9)

Then, step by step, we apply integration by parts to move derivatives from  $\delta u$  to p. We start with the first term in the integral (9), containing the time derivative:

$$\int_{Q} p \cdot \frac{\partial \delta u}{\partial t} dQ = \int_{\Omega} (p(T) \cdot \delta u(T) - p(0) \cdot \delta u(0)) d\Omega - \int_{Q} \delta u \cdot \frac{\partial p}{\partial t} dQ$$

$$= \int_{\Omega} p(T) \cdot \delta u(T) d\Omega - \int_{Q} \delta u \cdot \frac{\partial p}{\partial t} dQ,$$
(10)

where we have used that  $\delta u(t=0)=0$ . Then consider the fourth and fifth terms in integral (9), involving  $\Delta \delta u$  and  $\delta \pi$ :

$$-\frac{1}{Re} \int_{Q} p \cdot \Delta \delta u \, dQ + \int_{Q} (p \cdot \nabla) \delta \pi \, dQ$$

$$= -\frac{1}{Re} \int_{0}^{T} \left[ \int_{\Gamma} \frac{\partial \delta u}{\partial n} \cdot p \, d\Gamma - \int_{\Omega} \nabla p : \nabla \delta u \, d\Omega \right] dt$$

$$+ \int_{0}^{T} \left[ \int_{\Gamma} n \cdot p \, \delta \pi \, d\Gamma - \int_{\Omega} \delta \pi (\nabla \cdot p) \, d\Omega \right] dt$$

$$= \int_{0}^{T} p \cdot \left( n \, \delta \pi - \frac{1}{Re} \frac{\partial \delta u}{\partial n} \right) \, d\Gamma dt$$

$$+ \frac{1}{Re} \int_{0}^{T} \left[ \int_{\Gamma} \delta u \cdot \frac{\partial p}{\partial n} d\Gamma - \int_{\Omega} \delta u \cdot \Delta p \, d\Omega \right] dt - \int_{Q} \delta \pi (\nabla \cdot p) \, dQ$$

$$= \frac{1}{Re} \int_{T_{\Gamma}^{c}}^{T_{c}^{c}} \left[ \delta \varphi_{L}^{T} \int_{\Gamma_{L}} \psi_{L} \frac{\partial p_{2}}{\partial n} \, d\Gamma + \delta \varphi_{U}^{T} \int_{\Gamma_{U}} \psi_{U} \frac{\partial p_{2}}{\partial n} \, d\Gamma \right] dt$$

$$- \frac{1}{Re} \int_{Q} \delta u \cdot \Delta p \, dQ - \int_{Q} \delta \pi (\nabla \cdot p) \, dQ.$$
(11)

where: denotes a complete contraction; that is,

$$\nabla p : \nabla \delta u = \sum_{i,j=1}^{3} \frac{\partial (e_i \cdot p)}{\partial x_j} \frac{\partial (e_i \cdot \delta u)}{\partial x_j}.$$
 (12)

In the third equality of (11), we use the boundary condition on  $\delta u$  from (7) and on p from (8).

We can simply rewrite the second term in (9):

$$\int_{Q} p \cdot (\delta u \cdot \nabla) u \, dQ = \int_{Q} \delta u \cdot (\nabla u)^{T} p \, dQ.$$
(13)

For the third term in (9), we use Gauss theorem, the boundary condition on p in (8) and the incompressibility condition,

$$\int_{Q} p \cdot (u \cdot \nabla) \delta u \, dQ$$

$$= \int_{0}^{T} \int_{\Gamma} (p \cdot \delta u) (n \cdot u) \, d\Gamma \, dt$$

$$- \int_{Q} (p \cdot \delta u) (\nabla \cdot u) \, dQ - \int_{Q} \delta u \cdot (u \cdot \nabla) p \, dQ$$

$$= -\int_{Q} \delta u \cdot (u \cdot \nabla) p \, dQ,$$
(14)

Then by inserting (10), (11), (13) and (14) into (9) we get:

$$\int_{\Omega} p(T) \, \delta u(T) \, d\Omega 
+ \frac{1}{Re} \int_{T_{1}^{c}}^{T_{2}^{c}} \left[ \delta \varphi_{L}^{T} \int_{\Gamma_{L}} \psi_{L} \frac{\partial p_{2}}{\partial n} \, d\Gamma + \delta \varphi_{U}^{T} \int_{\Gamma_{U}} \psi_{U} \frac{\partial p_{2}}{\partial n} \, d\Gamma \right] dt 
+ \int_{Q} \delta u \cdot \left( -\frac{\partial p}{\partial t} - \frac{1}{Re} \Delta p + (\nabla u)^{T} p - (u \cdot \nabla) p \right) dQ 
- \int_{Q} \delta \pi \left( \nabla \cdot p \right) dQ = 0.$$
(15)

If we then require p to satisfy the adjoint equations:

$$\begin{cases}
-\frac{\partial p}{\partial t} - \frac{1}{Re} \Delta p + (\nabla u)^T p - (u \cdot \nabla) p + \nabla \sigma = \begin{cases} u - u_T & \text{in } (T_1^o, T_2^o) \\ 0 & \text{otherwise} \end{cases} & \text{in } Q, \\
\nabla \cdot p = 0 & \text{in } Q, \\
p|_{t=T} = 0,
\end{cases}$$
(16)

with the boundary conditions from (8) and where  $\sigma$  is a scalar field (the "adjoint pressure"). Then (15) becomes

$$\int_{T_1^o}^{T_2^o} \int_{\Omega} \delta u \cdot (u - u_T) \, dQ - \int_{Q} \delta u \cdot \nabla \sigma \, dQ = 0,$$
 (17)

since  $\partial p_2/\partial n$  is zero at the boundaries  $y=\pm 1$ . This follows from the fact that the no-slip condition implies

$$\frac{\partial p_1}{\partial x} = \frac{\partial p_3}{\partial z} = 0$$

on the walls and from the condition requiring p to be divergence-free. Also, note that the initial condition for the adjoint equations (16) is set at t = T and that the equations are integrated backwards in time.

Integrating the second term in the integral (17) by parts yields

$$-\int_{Q} \delta u \cdot \nabla \sigma \, dQ = -\iint_{0}^{T} n \cdot \delta u \, \sigma \, d\Gamma \, dt + \int_{Q} \sigma \, \nabla \cdot \delta u \, dQ$$

$$= -\iint_{0}^{T} n \cdot \delta u \, \sigma \, d\Gamma \, dt,$$
(18)

since  $\nabla \cdot \delta u = 0$ . Inserting the boundary condition on  $\delta u$  from (7) into (18) we get,

$$- \iint_{0}^{T} n \cdot \delta u \, \sigma \, d\Gamma \, dt$$

$$= \int_{T_{1}^{c}}^{T_{2}^{c}} \int_{\Gamma_{L}} \delta \varphi_{L}^{T} \psi_{L} \sigma \, d\Gamma \, dt - \int_{T_{1}^{c}}^{T_{2}^{c}} \int_{\Gamma_{U}} \delta \varphi_{U}^{T} \psi_{U} \sigma \, d\Gamma \, dt.$$

$$(19)$$

If we now insert (18) and (19) into (17) we get,

$$\int_{T_1^c}^{T_2^c} \left[ \delta \varphi_L^T \int_{\Gamma_L} \psi_L \sigma \, d\Gamma - \delta \varphi_U^T \int_{\Gamma_U} \psi_U \sigma \, d\Gamma \right] dt 
+ \int_{T_2^o}^{T_2^o} \int_{\Omega} \delta u \cdot (u - u_T) \, dQ = 0.$$
(20)

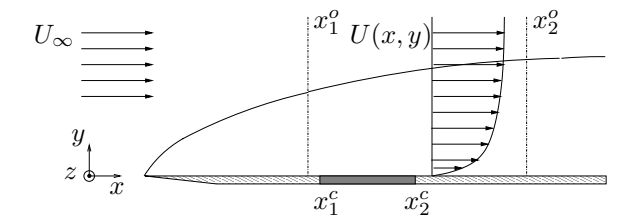


FIGURE 2. Geometry for boundary layer flow simulations.

Finally we can now insert (20) into (5) using (2) to eliminate  $\delta u$ 

$$\delta J(\varphi) = \left\langle \frac{\partial J}{\partial \varphi_L}, \delta \varphi \right\rangle + \left\langle \frac{\partial J}{\partial \varphi_U}, \delta \varphi \right\rangle$$

$$= \int_{T_1^c}^{T_2^c} \left\{ \delta \varphi_L^T \left[ \int_{\Gamma_L} \psi_L \left( \varepsilon \varphi_L^T \psi_L - \sigma \right) d\Gamma \right] \right\}$$

$$+ \delta \varphi_U^T \left[ \int_{\Gamma_U} \psi_U \left( \varepsilon \varphi_U^T \psi_U + \sigma \right) d\Gamma \right] \right\} dt.$$
(21)

From expression (21) we can identify the gradient of the objective function (3),

$$\frac{\partial J}{\partial \varphi_L} = \int_{\Gamma_L} \psi_L \left( \varepsilon \varphi_L^T \psi_L - \sigma \right) d\Gamma, \tag{22}$$

and

$$\frac{\partial J}{\partial \varphi_U} = \int_{\Gamma_U} \psi_U \left( \varepsilon \varphi_U^T \psi_U + \sigma \right) d\Gamma. \tag{23}$$

#### 2.3. Extension to boundary layer

Only minor changes are needed to rephrase the channel flow problem to the boundary layer flow depicted in figure 2. A complete derivation of the boundary layer counterpart of the channel flow optimization problem can be found in Appendix A. In this section only the key differences will be pointed out and commented.

The growing boundary layer is modeled by

$$\begin{cases}
\frac{\partial u}{\partial t} + (u \cdot \nabla)u - \frac{1}{Re}\Delta u + \nabla \pi = \lambda(x)(U - u) & \text{in } Q, \\
\nabla \cdot u = 0 & \text{in } Q, \\
u|_{t=0} = u_0,
\end{cases}$$
(24)

with periodic boundary conditions in the horizontal directions, that is, the xand z-directions,

$$u|_{x=-x_{l}/2} = u|_{x=x_{l}/2},$$
  
 $u|_{z=-z_{l}/2} = u|_{z=z_{l}/2}.$ 
(25)

The term  $\lambda(x)(U-u)$  is a forcing term used to make the flow situation sketched in figure 2 periodic, enabling the use of Fourier discretization in simulations of the physical flow. This is known as a fringe region technique and is described further in Lundbladh et al. (1999) and analyzed by Nordström, Nordin & Henningson (1999). Left to be specified are the conditions on the wall and in the free-stream. On the wall the boundary condition for the horizontal velocities is a no-slip condition and the wall normal velocity  $v_c$  is given by the control. The free-stream boundary condition should be applied at  $y=y_{\rm fst}$  where the flow is not influenced by the existence of the boundary layer, but the simulation box has to be of reasonable height. An artificial boundary condition modeling the existence of the free-stream is thus used to allow truncation of this large domain. Here a Neumann condition is used at the artificial free-stream boundary. This choice requires that the simulation box is high enough for the perturbations in the boundary layer not to influence the flow at the upper boundary.

$$u|_{y=y_{\rm fst}} = U_{\infty}$$
 (which is approximated by  $\frac{\partial u}{\partial n}\Big|_{\Gamma_u} = 0$ ),  
 $u|_{\Gamma_c} = nv_c$ , (26)  
 $u|_{\Gamma_l \setminus \Gamma_c} = 0$ ,

where  $\Gamma_u$  and  $\Gamma_l$  represent the upper and lower part of the boundary respectively. The part of the boundary where control is applied is denoted  $\Gamma_c$ .

As for the channel flow case we expand the control  $v_c$  in basis functions  $\psi_{l,m}$  with zero mass flux, where  $\varphi_{l,m}$  are time dependent coefficients for the basis functions,

$$v_c(x,z,t) = \begin{cases} \varphi_l^T \psi_l = \sum_{m=1}^M \varphi_{l,m}(t) \psi_{l,m}(x,z) & \text{in } (T_1^c, T_2^c), \\ 0 & \text{otherwise.} \end{cases}$$
 (27)

Where we have introduced the control vector  $\varphi_l$  defined as:

$$\varphi_l = (\varphi_{l,1}, \dots, \varphi_{l,M}).$$

Comparing with the corresponding equation for channel flow, equation (1) and the associated boundary conditions, there are two differences. The boundary condition at the upper wall is now replaced by a free-stream velocity condition. Also the aforementioned fringe forcing term which is needed only for spatial simulations is added to the right hand side. The scalar function  $\lambda = \lambda(x)$  is

nonzero only in the fringe region and is defined as follows:

$$\lambda(x) = \lambda_{\text{max}} \left[ S \left( \frac{x - x_{\text{start}}}{\Delta_{\text{rise}}} \right) - S \left( \frac{x - x_{\text{end}}}{\Delta_{\text{fall}}} + 1 \right) \right]$$

where  $\lambda_{\text{max}}$ ,  $x_{\text{start}}$ ,  $x_{\text{end}}$ ,  $\Delta_{\text{rise}}$  and  $\Delta_{\text{fall}}$  are parameters used to specify the strength, extent and shape of the fringe forcing. The S-function is defined as

$$S(r) = \begin{cases} 0 & r \le 0, \\ \frac{1}{1 + \exp(1/(1-r) + 1/r)} & 0 < r < 1, \\ 1 & r > 1. \end{cases}$$

Another difference from the channel flow problem formulation appears in the second term of the objective function J, equation (3), where the observation of state can now be limited in space as well as in time which yields,

$$J(\varphi_l) = \frac{\varepsilon}{2} \int_{T_c^c}^{T_c^c} \int_{\Gamma_c} |v_c|^2 d\Gamma dt + \frac{1}{2} \int_{T_c^o}^{T_c^o} \int_{\Omega_o} |u - u_T|^2 dQ, \qquad (28)$$

where  $(T_1^c, T_2^c)$  is the control time period and  $(T_1^o, T_2^o)$  is the observation time period and  $\Omega_o$  is the part of the spatial domain  $\Omega$  where the state of the flow is observed. This is only used for spatial simulations.

As for the channel flow derivation, we get to the stage where the adjoint equations with the variables p and  $\sigma$  are introduced:

$$\begin{cases}
-\frac{\partial p}{\partial t} + (\nabla u)^T p - (u \cdot \nabla)p \\
-\frac{1}{Re} \Delta p + \lambda(x)p + \nabla \sigma = \begin{cases} u - u_T & \text{in } (T_1^o, T_2^o) \times \Omega_o \\ 0 & \text{otherwise} \end{cases} & \text{in } Q, \\
\nabla \cdot p = 0 & \text{in } Q, \\
p|_{t=T} = 0.
\end{cases}$$

along with the boundary conditions:

$$p|_{x=-x_{l}/2} = p|_{x=x_{l}/2},$$

$$p|_{z=-z_{l}/2} = p|_{z=z_{l}/2},$$

$$p|_{\Gamma_{l}} = 0,$$

$$p|_{y=y_{\text{fst}}} = 0, \quad \left(\text{which is approximated by } \frac{\partial p}{\partial n}\Big|_{\Gamma_{n}} = 0\right).$$
(30)

As with the free-stream boundary condition in (26) we have introduced an artificial boundary, to truncate the adjoint domain, where the adjoint "free-stream" is modeled.

Due to the fringe forcing, the additional term  $\lambda(x)p$  has to be included in the adjoint equations. The forcing  $u-u_T$  is now confined to the spatial domain

 $\Omega_o$  due to the variable spatial extent of the observation. These adjustments lead to following the expression for the gradient:

$$\frac{\partial J}{\partial \varphi_l} = \int_{\Gamma_c} \psi_l \left( \varepsilon \varphi_l^T \psi_l - \sigma \right) d\Gamma. \tag{31}$$

# 3. Adapting to the simulation codes

# 3.1. Reformulation of the adjoint equations

To be able to use existing spectral channel flow and boundary layer flow codes by Lundbladh, Henningson & Johansson (1992) and Lundbladh *et al.* (1999) respectively, we need to reformulate the adjoint equations into a similar form to the one used there. The simulation code for the boundary layer problem is based on the channel flow code and the solution procedure is identical. The Navier–Stokes equations are implemented in a  $v-\omega$  formulation, where linear and nonlinear terms are treated separately. We can write the adjoint equations (16) or (29) as,

$$\begin{cases}
-\frac{\partial p}{\partial t} - \frac{1}{Re}\Delta p - H + \nabla(u \cdot p) + \nabla\sigma = 0, \\
\nabla \cdot p = 0, \\
p|_{t=T} = 0,
\end{cases}$$
(32)

with the boundary conditions (8) or (30), and where H in the following denotes either  $H_{ch}$  or  $H_{bl}$  corresponding to the forcing terms in the channel and boundary layer cases respectively. In order to avoid derivatives of u in the adjoint equations, terms involving such derivatives are reformulated. Using the identity

$$u \times (\nabla \times p) - 2(\nabla p)^T u + \nabla (u \cdot p) = (\nabla u)^T p - (u \cdot \nabla) p$$

the forcing in the channel flow case is given by

$$H_{ch} = -u \times (\nabla \times p) + 2(\nabla p)^T u + \begin{cases} u - u_T & \text{in } (T_1^o, T_2^o), \\ 0 & \text{otherwise,} \end{cases}$$

and in the boundary layer case we use

$$H_{bl} = -u \times (\nabla \times p) + 2(\nabla p)^T u - \lambda(x) p + \begin{cases} u - u_T & \text{in } (T_1^o, T_2^o) \times \Omega_o, \\ 0 & \text{otherwise,} \end{cases}$$

but apart from this, the procedure is the same in both cases. If we take the divergence of equation (32) we get a Poisson equation for the adjoint pressure:

$$\Delta \sigma = \nabla \cdot H - \Delta(u \cdot p). \tag{33}$$

We can then apply the Laplace operator to equation (32), take the second component, and combine with (33) to get:

$$-\frac{\partial \Delta p_2}{\partial t} - \frac{1}{Re} \Delta^2 p_2 - \left(\frac{\partial^2}{\partial x^2} + \frac{\partial^2}{\partial z^2}\right) H_2 + \frac{\partial}{\partial y} \left(\frac{\partial H_1}{\partial x} + \frac{\partial H_3}{\partial z}\right) = 0.$$
 (34)

Then we take the second component of the equation obtained by taking the curl of equation (32) and again making use of (33) to get,

$$-\frac{\partial(\nabla \times p)_2}{\partial t} - \frac{1}{Re}\Delta(\nabla \times p)_2 - \left(\frac{\partial H_1}{\partial z} - \frac{\partial H_3}{\partial x}\right) = 0.$$
 (35)

We can write equation (34) as a system of two second order equations:

$$\begin{cases}
-\frac{\partial \phi}{\partial t} = h_{p_2} + \frac{1}{Re} \Delta \phi, \\
\Delta p_2 = \phi, \\
p_2(y = \pm 1) = \frac{\partial p_2}{\partial y} (y = \pm 1) = 0,
\end{cases} (36)$$

where

104

$$h_{p_2} = \left(\frac{\partial^2}{\partial x^2} + \frac{\partial^2}{\partial z^2}\right) H_2 - \frac{\partial}{\partial y} \left(\frac{\partial H_1}{\partial x} + \frac{\partial H_3}{\partial z}\right). \tag{37}$$

Written on the same form equation (35) reads:

$$\begin{cases}
-\frac{\partial(\nabla \times p)_2}{\partial t} = h_{(\nabla \times p)_2} + \frac{1}{Re} \Delta(\nabla \times p)_2, \\
(\nabla \times p)_2(y = \pm 1) = 0,
\end{cases}$$
(38)

where

$$h_{(\nabla \times p)_2} = \left(\frac{\partial H_1}{\partial z} - \frac{\partial H_3}{\partial x}\right). \tag{39}$$

Equations (36), (37), (38) and (39) are identical to those solved by the spectral channel flow and boundary layer codes with slight changes to H and a negative time derivative. Since the adjoint equations are solved backwards in time, we can in practice use the same solver.

#### 3.2. Gradient evaluation

In the gradient of the objective function we need the adjoint pressure at the wall. This is not available directly since we have eliminated the adjoint pressure term from the equations, and thus the pressure is not computed explicitly. If we evaluate equation (16) or (29) at the walls, we get

$$\sigma_x \Big|_W = \frac{1}{Re} \frac{\partial^2 p_1}{\partial y^2} \Big|_W + v \frac{\partial p_1}{\partial y} \Big|_W,$$

$$\sigma_z \Big|_W = \frac{1}{Re} \frac{\partial^2 p_3}{\partial y^2} \Big|_W + v \frac{\partial p_3}{\partial y} \Big|_W,$$
(40)

where W denotes the value at the wall and v is the wall normal velocity at the wall, or rather the control input. Note that in the channel flow case there are two walls and in the boundary layer flow there is only one. Since the constant part of the adjoint pressure disappears in the integral over the basis functions  $\psi$  in (22) and (23) we can compute the objective function gradient by integration of these adjoint pressure gradients at the wall.

# 4. Implementation issues

#### 4.1. Simulation codes

The implementation of the adjoint solver is based on existing direct numerical simulation codes for channel and boundary layer flow. These codes have been extensively used and are thoroughly verified. The channel flow code is described in Lundbladh, Henningson & Johansson (1992) and the boundary layer code in Lundbladh et al. (1999). The time marching is performed with a Runge–Kutta method for advective terms and a Crank–Nicolson scheme for the viscous terms. A spectral method described in Canuto et al. (1988) is used with a Fourier discretization in x and z, and a Chebyshev method in y. The discretization of, and the solution procedure for, the Navier–Stokes equations is described in Lundbladh, Henningson & Johansson (1992). The adjoint equation is solved in exactly the same way, with the formulation of the equations described in section 3.1. For the boundary layer case the code described in Lundbladh et al. (1999) is used and since it is based on the channel flow code the implementation is similar.

The solution of the adjoint equations require knowledge about the full state in space and time from the solution of the Navier–Stokes system. This is achieved by saving a large number of velocity fields equidistant in time and interpolating linearly in time when the adjoint equations are solved. This introduces an error, but if the time step between saved field is small enough, we expect a sufficiently accurate approximation. The number of saved velocity fields can become large especially if the time domain is long. An efficient way of reducing the memory requirement is to use a check-pointing technique, see for example Berggren (1998). This decreases the memory requirement at the cost of increased computational time. For the simple test cases presented in this paper check-pointing has not been necessary, but for larger cases, especially simulations requiring high spatial resolution, it will be needed.

#### 4.1.1. Implementation of control

The control is implemented as the Fourier coefficients of the v velocity at the wall(s). The control function is discretized in time with a fixed time step that can be used to change the time resolution of the control and there is one set of coefficients for each control time. Linear interpolation is used for the control in times between the discrete control times. The control always starts and ends with zero velocity, and has zero mass flux. The time step in the solution of both the forward and adjoint equations is adjusted to be small enough to at

106

least resolve the control in time, even if the time step allowed for numerical stability is larger.

When simulating a spatial boundary layer the control is applied only on  $\Gamma_c$  which extends over the interval  $(x_1^c, x_2^c)$  in the chordwise direction. In the code a filtering is added to handle this, and to ensure that the zero mass flux condition on the control is enforced,

$$\int_{\Gamma_c} v_c \, \mathrm{d}\Gamma = 0. \tag{41}$$

The control is then modified to have zero velocity outside  $\Gamma_c$ ,

$$\int_{\Gamma_l} \tilde{\varphi}_l^T \psi_l \, d\Gamma = \int_{\Gamma_l} (\varphi_l^T \psi_l + c) \chi(x_1^c, x_2^c) \, d\Gamma = 0$$
(42)

which yields,

$$c = -\frac{\int\limits_{\Gamma_l} \varphi_l^T \psi_l \, \chi(x_1^c, x_2^c) \, d\Gamma}{\int\limits_{\Gamma_l} \chi(x_1^c, x_2^c) \, d\Gamma},$$
(43)

and where  $\chi(r_1, r_2) = \chi[r_1, r_2](r)$  is defined as:

$$\chi[r_1, r_2](r) = \begin{cases} 1 & \text{if } r \in (r_1, r_2), \\ 0 & \text{otherwise.} \end{cases}$$

$$\tag{44}$$

The procedure for modifying the control can be summarized as follows:

$$\hat{\varphi}_l \xrightarrow{\text{inverse FFT}} \varphi_l \xrightarrow{\text{Filtering and mass flux correction}} \tilde{\varphi}_l \xrightarrow{\text{FFT}} \hat{\tilde{\varphi}}_l$$

assuming that we denote the original Fourier space control with  $\hat{\varphi}_l$  and the final control in Fourier space with  $\hat{\varphi}_l$ . This final control constitutes the boundary condition in the simulation when the spatial extent of the control is limited.

# 4.1.2. Computing the objective function gradient

The gradient of the objective function is evaluated from the adjoint pressure on the walls as described in section 3.2. When the adjoint equations are solved, the adjoint pressure on the walls must also be computed simultaneously in the control interval. Since the  $p_1$  and  $p_3$  velocities are available at each time step we can compute the pressure gradients  $\sigma_x$  and  $\sigma_z$  using (40). The corresponding pressure is then computed by integrating these gradients with the constant part of the adjoint pressure set to zero, since it does not enter the gradient computation. The adjoint pressure is then projected onto the basis functions of the control using (22), (23) or (31). In the spatial boundary layer case the gradient (31) is computed in Fourier space, but we should only integrate over  $\Gamma_c$ . The gradient is transformed to physical space and there a step function which cuts out the region  $\Gamma_c$  is applied. This filtering procedure is similar to

that for the control. The resulting gradient is then transformed back to Fourier space.

#### 4.2. Optimization routine

Optimization is performed with a limited memory quasi-Newton method. The algorithm, L-BFGS-B (Byrd et al. (1994)), is available on the Internet (the web-link is given in the reference list next to Byrd et al. (1994)) and was downloaded and compiled without modifications. It is an algorithm well suited for large non-linear optimization problems, with or without bounds on the control variables. The BFGS method uses an approximation of the Hessian matrix of the objective function, instead of the full matrix. The algorithm has been shown to work well for many different types of optimization problems. The flow of the optimization process is described in figure 3. The limited memory BFGS algorithm differs from the standard BFGS algorithm in that it never stores the Hessian matrix. Instead only a certain number of gradient and control updates from earlier optimization iterations are stored. These are then used to build an approximation of the Hessian matrix. Consult Byrd et al.

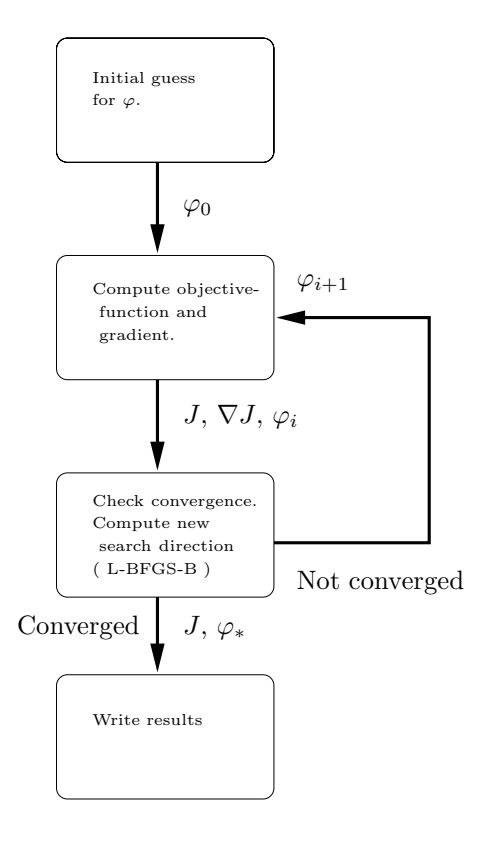


FIGURE 3. The flow in the optimization with L-BFGS-B.

(1994) for details. The inputs to the optimization routine are the control, the gradient of the control and the value of the objective function. A new control is then obtained as output and applied in the next iteration until the convergence criterion has been met. There are a few different convergence criteria that can be used simultaneously or separately such as the norm of the gradient and the relative reduction of the objective function between iterations.

#### 5. Results

# 5.1. Gradient accuracy

To verify that the implementation is correct as well as that the problem has been formulated correctly, one can check the accuracy of the gradient of the objective function. By perturbing one degree of freedom of the control and computing the resulting change in the objective function the gradient with respect to that degree of freedom can be approximated. Performing this procedure for all degrees of freedom gives the complete objective function gradient. The gradient so computed can then be used to verify that the gradient obtained from the adjoint equation approach is correct. This has been done at different stages of the optimization process for a number of different cases, varying the flow perturbation as well as the initial guess for the control. The accuracy of the gradient direction is quantified by normalizing the two gradients and computing the norm of the difference between them. This difference is less than 1% for all channel and boundary layer flow cases tested when the optimization routine is in the initial iterations. When the gradient accuracy is computed for solutions close to the optimal solution, the accuracy is degraded and the error can be as large as 10% - 20%. This degraded accuracy slows down the convergence of the optimization routine and makes it difficult to reach the true optimal solution.

#### 5.2. Control of oblique transition in channel flow

As a first test case, we study the oblique transition scenario. Oblique waves are introduced in the flow, where they grow and induce streamwise vortices. The vortices then produce streamwise streaks that grow until they finally break down and transition occurs. The threshold energies for this type of bypass transition are studied in Reddy et al. (1998). The initial stage of this scenario is the growth of oblique waves. If the amplitude is low, this is all that happens before the flow returns to the laminar state. With a higher amplitude, the oblique waves induce enough streamwise vorticity to generate streaks. The streaks grow to a much higher amplitude than the oblique waves. If the initial disturbance is large enough, we get transition to turbulence.

Testing the optimal control on this scenario is done at three different stages and with different time resolution. First control is applied at the very beginning where only the oblique waves are present, secondly the control is applied in the beginning of the streak growth, where both streaks and oblique waves are present. The last case application of the control to the growing streaks.

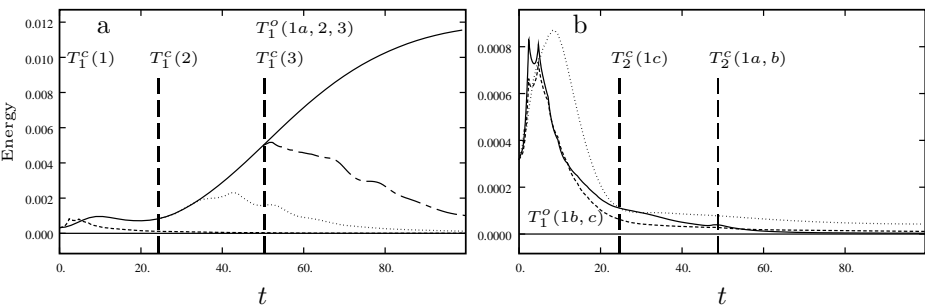


FIGURE 4. [a] Solid: the energy growth without control; dashed: case 1a; dotted: case 2; dash-dot: case 3. [b] solid: case 1a; dashed: case 1b; dotted: case 1c.

The results in this section were previously reported in Högberg, Henningson & Berggren (2000).

Five different simulations are performed using the same initial condition. The objective is to minimize the integral of the deviation from the laminar flow profile from time  $T_1^o$  to  $T_2^o = 100$ . The Reynolds number is 1500 and the box size is  $2\pi \times 2 \times 2\pi$  in x,y,z. In case 1a,b,c the control is applied from time  $T_1^c = 0$  until  $T_2^c = 50$  in a,b and  $T_2^c = 25$  in c. The objective function is measured from  $T_1^o = 50$  in case 1a and from  $T_1^o = 0$  in cases 1b and 1c. For cases 2 and 3 the control is applied from  $T_1^c = 25$  and  $T_1^c = 50$  respectively, and the objective function from  $T_1^o = 50$ . The resulting control velocity in all cases is of the order 2% of the centerline velocity. The reduction of the gradient norm is about three orders of magnitude after 10-15 optimization iterations.

The energy evolution of the controlled flows is shown in figure 4a. The growth of the oblique waves is efficiently hindered by the control formulation in 1a,b,c and the growth of streaks is eliminated also in cases 2 and 3. In case 2 the control is applied during the formation of the streaks. Initially the energy is allowed to grow but then the growth is hindered by the control and energy decays as. In case 3 the streaks have formed and are growing when control is applied.

In figure 4b the differences between the controlled flows in cases 1a,b and c are shown. In case 1a the energy is not penalized by the objective function initially as it is in 1b, and this results in lower energy after t=50 than in case 1b. A higher temporal resolution of the control is applied during a shorter time in case 1c. The result is a smoother energy curve but not as low energy at a later time as in the other two cases.

#### 5.3. Control in a parallel boundary layer flow

In order to evaluate this type of control strategy for a parallel boundary layer flow we consider an inviscid instability. Inviscid instabilities can exist only if the velocity profile has an inflection point. In a boundary layer flow with a three-dimensional velocity profile, there is always a direction in which such an inflection point exists. In this direction an unstable eigenvalue to the linearized problem was found. The corresponding eigenmode is added to an undisturbed base flow, and the sum is then used as the initial velocity field for the simulations. The base flow is chosen as a Falkner–Skan–Cooke (FSC) flow with the same parameters as are used in the investigation by Högberg & Henningson (2001) where the Reynolds number is  $Re_{\delta_0^*} = 337.9$ . The spatial variation of the chordwise mean flow is given through,

$$U_{\infty} = \left(\frac{x}{x_0} + 1\right)^m,$$

where  $x_0 = 354.0$ . Furthermore, the cross-flow velocity was  $W_{\infty} = 1.44232$  and m = 0.34207. The box dimensions for our simulations are  $25.14 \times 20 \times 25.14$  measured in  $\delta^*$  with a resolution of  $4 \times 129 \times 4$  in  $x \times y \times z$  respectively. The resolution in the y-direction is chosen fairly large to ensure high accuracy for the y-derivatives needed in the adjoint computation.

For the temporal simulation we use the Falkner–Skan–Cooke flow at x=0. The eigenvalue of the mode used in the simulation is  $\omega=(-0.15246+i0.0382)$ , for the parameter choice  $\alpha=0.25$ ,  $\beta=-0.25$ . The control is applied from  $T_1^c=0$  to  $T_2^c=150$  and over the entire boundary  $(\Gamma_c=\Gamma_l)$ . The objective function is measured from  $T_1^o=0$  to  $T_2^o=150$  and over the whole spatial domain  $(\Omega_o=\Omega)$ .

Figure 5 shows the disturbance energy growth due to the eigenmode and also the result when the optimal control is applied. As we can see from the figure the exponential energy growth is stopped almost immediately by the control. The first energy peak is mostly due to the energy expenditure to exert control. The maximum magnitude of the control is of the order of 0.02% of the free-stream velocity. The gradient norm is reduced about two orders of

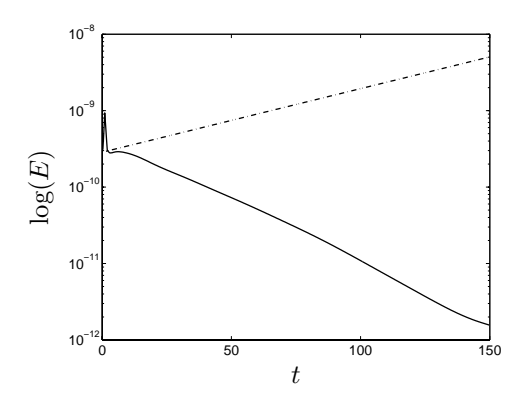


FIGURE 5. Solid: the disturbance energy growth with optimal control; dash-dot: the disturbance energy growth for temporal FSC flow without control.

magnitude after 5-10 optimization iterations.

#### 5.4. Control in a spatial boundary layer flow

A more general flow case to study is when we let the boundary layer grow in the chordwise direction. For this case we have chosen to study a Tollmien-Schlichting (TS) wave in a Blasius boundary layer. The dimensions of the simulation box are  $200\times20\times10$  measured in  $\delta_0^*$  with a resolution of  $96\times129\times4$  in  $x\times y\times z$  respectively. The TS wave is triggered by an oscillating volume force at x=10 which is slightly upstream of branch I, located at  $x\approx40$  where it becomes unstable. The volume forcing does not introduce a pure TS-eigenmode into the flow and this will result in a varying growth of the total energy of the perturbation.

The control is allowed to be active between  $T_1^c = 0$  and  $T_2^c = 400$  and is located on  $\Gamma_c = (20, 70) \times (-5, 5)$ . The control is localized in space to give us a region to observe its action downstream of the control area.

The observation time interval is also limited to give the control enough freedom to act initially since we are more interested in the final results. Thus, the objective function is measured from  $T_1^o = 380$  to  $T_2^o = 400$  over the domain  $\Omega_o = (20, 150) \times (0, 20) \times (-5, 5)$  that includes only the physical solution meaning that the fringe region is omitted.

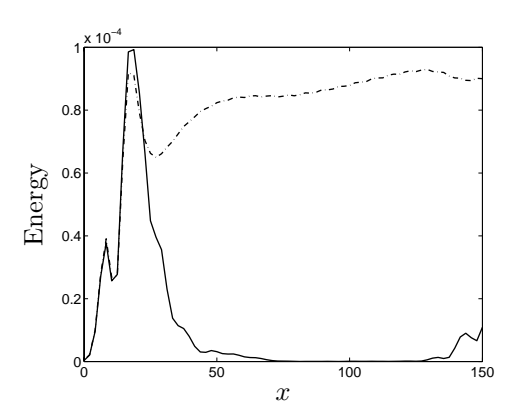


FIGURE 6. Solid: the disturbance energy growth with optimal control; dash-dot: the disturbance energy growth for a spatial Blasius boundary layer flow without control.

Without the control we can see how the disturbance energy grows in figure 6, whereas with the optimal control applied on  $\Gamma_c$  the energy growth is efficiently interrupted.

# 6. Summary and conclusions

First we conclude that optimal control of transition appears to be possible to compute with the approximative discretized adjoint technique used in this work. This was also what the preliminary study by Högberg & Berggren (2000) suggested. In addition, the optimization problem was derived using the primitive

variables velocity and pressure but solved using a velocity–vorticity formulation. This made it easy to implement a solver for the adjoint equations using already developed codes as templates. The adjoint solver thus benefited from the efforts put into making the existing codes computationally efficient.

The optimization routine BFGS by Byrd *et al.* (1994) was found to perform well for the present optimization problems. No modification of the code was necessary.

The test cases for the boundary layer code provide confirmation that we can solve an optimization problem. From the simple parametric study of control of oblique waves in channel flow we can draw a few conclusions.

- The temporal extent of the control appears to be more important than the resolution.
- Allowing a higher energy initially can result in lower energy at a later time.
- It appears that there is enough control authority using blowing and suction on the wall to handle all the different stages of the oblique transition scenario.
- The choice of objective function in terms of time intervals is very important for the performance of the resulting control.

The simple flow cases studied to test the code can now be replaced with more complicated flows. In particular flows where non-linear effects are dominating are of interest, and so are flows with spatial variations in the mean flow profile.

#### Appendix A. Derivation of gradient for boundary layer

Appendix A.1. The governing equations

The domain where we solve the governing equations, given  $0 < T < +\infty$ , is

$$\Omega = (-x_l/2, x_l/2) \times (0, y_l) \times (-z_l/2, z_l/2),$$

$$Q = \Omega \times (0, T).$$
(45)

The boundary of  $\Omega$  is denoted  $\Gamma$ , and

$$\Gamma_l = \Gamma(y=0), \quad \Gamma_u = \Gamma(y=y_l),$$
(46)

and  $\Gamma_c \subset \Gamma_l$  represents the part of the lower boundary where control is applied. For temporal simulations  $\Gamma_c$  coincide with  $\Gamma_l$ .

The governing equations for boundary layer flow are the same as for the channel flow except for an extra term which is added to enforce periodicity of the physical flow in the streamwise direction. This is only needed for spatial simulations.

$$\begin{cases}
\frac{\partial u}{\partial t} + (u \cdot \nabla)u - \frac{1}{Re}\Delta u + \nabla \pi = \lambda(x)(U - u) & \text{in } Q, \\
\nabla \cdot u = 0 & \text{in } Q, \\
u|_{t=0} = u_0,
\end{cases} (24)$$

with periodic boundary conditions in the horizontal directions, that is, the xand z-directions,

$$u|_{x=-x_{l}/2} = u|_{x=x_{l}/2},$$
  
 $u|_{z=-z_{l}/2} = u|_{z=z_{l}/2}.$ 
(25)

Left to be specified are the conditions in the free-stream and on the wall,

$$u|_{y=y_{\rm fst}} = U_{\infty}$$
 (which is approximated by  $\frac{\partial u}{\partial n}\Big|_{\Gamma_u} = 0$ ),  
 $u|_{\Gamma_c} = nv_c$ ,  
 $u|_{\Gamma_l \setminus \Gamma_c} = 0$ . (26)

In equation (24), U = U(x,y) is the velocity field that we force the solution towards in the fringe region. Pressure is denoted  $\pi$  and the Reynolds number Re is defined based on the free-stream velocity and the displacement thickness  $\delta^*$ . The scalar function  $\lambda = \lambda(x)$  is nonzero only in the fringe region and is defined as follows:

$$\lambda(x) = \lambda_{\text{max}} \left[ S\left(\frac{x - x_{\text{start}}}{\Delta_{\text{rise}}}\right) - S\left(\frac{x - x_{\text{end}}}{\Delta_{\text{fall}}} + 1\right) \right],$$

where  $\lambda_{\text{max}}$ ,  $x_{\text{start}}$ ,  $x_{\text{end}}$ ,  $\Delta_{\text{rise}}$  and  $\Delta_{\text{fall}}$  are parameters used to specify the strength, extent and shape of the fringe forcing. The S-function is defined as,

$$S(r) = \begin{cases} 0 & r \le 0, \\ \frac{1}{1 + \exp(1/(1-r) + 1/r)} & 0 < r < 1, \\ 1 & r \ge 1. \end{cases}$$

As for the channel flow case we expand the control  $v_c$  in basis functions  $\psi_{l,m}$  with zero mass flux, and where  $\varphi_{l,m}$  are time dependent coefficients for the basis functions,

$$v_c(x,z,t) = \begin{cases} \varphi_l^T \psi_l = \sum_{m=1}^M \varphi_{l,m}(t)\psi_{l,m}(x,z) & \text{in } (T_1^c, T_2^c), \\ 0 & \text{otherwise.} \end{cases}$$
(27)

Where we have introduced the control vector  $\varphi_l$  defined as:

$$\varphi_l = (\varphi_{l,1}, \dots, \varphi_{l,M}).$$

Appendix A.2. The objective function

We minimize the deviation energy from a given target velocity distribution  $u_T$  and add a regularization term including an  $\varepsilon > 0$ :

$$J(\varphi_l) = \frac{\varepsilon}{2} \int_{T_1^c}^{T_2^c} \int_{\Gamma_c} |v_c|^2 d\Gamma dt + \frac{1}{2} \int_{T_1^o}^{T_2^o} \int_{\Omega_o} |u - u_T|^2 dQ,$$
 (28)

where  $(T_1^c, T_2^c)$  is the control time period and  $(T_1^o, T_2^o)$  is the observation time period and  $\Omega_o$  is the part of the domain  $\Omega$  where the state of the flow is observed. The control problem can now be defined as:

Find 
$$\varphi^* \in \mathcal{U}_{ad}$$
 such that  $J(\varphi^*) \leq J(\varphi_l) \quad \forall \ v_c(\varphi_l) \in \mathcal{U}_{ad},$  (47)

where  $\varphi^*$  is the optimal control. The set of admissible controls is denoted  $\mathcal{U}_{ad}$  and is a subset of  $L^2((T_1^c, T_2^c); \mathbb{R}^M)$ .

Appendix A.3. Derivation of the objective function gradient

We begin by differentiating the objective function (28)

$$\delta J(\varphi_l) = \varepsilon \int_{T_1^c}^{T_2^c} \int_{\Gamma_c} \delta v_c \, v_c \, d\Gamma \, dt + \int_{T_1^o}^{T_2^o} \int_{\Omega_o} \delta u \cdot (u - u_T) \, dQ, \tag{48}$$

where the gradient of J is defined through the directional derivative of J in the  $\delta\varphi_l$ -direction as done in (4). The differentiated Navier–Stokes equations have the form

$$\begin{cases}
\frac{\partial \delta u}{\partial t} + (\delta u \cdot \nabla)u + (u \cdot \nabla)\delta u - \frac{1}{Re}\Delta \delta u + \nabla \delta \pi = -\lambda(x)\delta u & \text{in } Q, \\
\nabla \cdot \delta u = 0 & \text{in } Q, \\
\delta u|_{t=0} = 0,
\end{cases} (49)$$

with the boundary conditions

$$\delta u|_{x=-x_l/2} = \delta u|_{x=x_l/2},$$

$$\delta u|_{z=-z_l/2} = \delta u|_{z=z_l/2},$$

$$\delta u|_{y=y_{\text{fst}}} = 0,$$

$$\delta u|_{\Gamma_c} = n\delta v_c,$$

$$\delta u|_{\Gamma_l \setminus \Gamma_c} = 0,$$
(50)

where

$$\delta v_c(x, z, t) = \begin{cases} \delta \varphi_l^T \psi_l = \sum_{m=1}^M \delta \varphi_{l,m}(t) \psi_{l,m}(x, z) & \text{in } (T_1^c, T_2^c), \\ 0 & \text{otherwise.} \end{cases}$$
(51)

Now, let us consider the adjoint variable p = p(x, y, z, t) and the adjoint pressure  $\sigma = \sigma(x, y, z, t)$  and require p to satisfy the boundary conditions:

$$p|_{x=-x_{l}/2} = p|_{x=x_{l}/2},$$

$$p|_{z=-z_{l}/2} = p|_{z=z_{l}/2},$$

$$p|_{\Gamma_{l}} = 0,$$

$$p|_{y=y_{\text{fst}}} = 0.$$
(52)

The boundary condition at  $y=y_{\rm fst}$  can be approximated with the artificial boundary condition

$$\left. \frac{\partial p}{\partial n} \right|_{\Gamma_u} = 0,$$

in the numerical simulations. With a sufficiently high box not only this condition will hold but also p and  $\sigma$  will approach zero.

By multiplying the first equation in (49) with p and then integrating over Q we obtain

$$\int_{Q} p \cdot \left( \underbrace{\frac{\partial \delta u}{\partial t}}_{1} + \underbrace{(\delta u \cdot \nabla)u}_{2} + \underbrace{(u \cdot \nabla)\delta u}_{3} \right) dQ = 0.$$

$$\underbrace{-\frac{1}{Re} \Delta \delta u + \nabla \delta \pi}_{4} + \underbrace{\lambda(x)\delta u}_{5} dQ = 0.$$
(53)

We apply integration by parts in space and time to move the derivatives from u to the adjoint variable p. For clarity we perform this step by step for each term. The first term gives

$$\int_{Q} p \cdot \frac{\partial \delta u}{\partial t} dQ = \int_{\Omega} (p(T) \cdot \delta u(T) - p(0) \cdot \delta u(0)) d\Omega$$

$$- \int_{Q} \frac{\partial p}{\partial t} \cdot \delta u dQ$$

$$= \int_{\Omega} p(T) \cdot \delta u(T) d\Omega - \int_{\Omega} \frac{\partial p}{\partial t} \cdot \delta u dQ,$$
(54)

where we have used the fact that  $\delta u(t=0)=0$ . Next, we consider the fourth term

$$-\frac{1}{Re} \int_{Q} p \cdot \Delta \delta u \, dQ + \int_{Q} p \cdot \nabla \delta \pi \, dQ$$

$$= -\frac{1}{Re} \int_{0}^{T} \left[ \int_{\Gamma} p \cdot \frac{\partial \delta u}{\partial n} \, d\Gamma + \int_{\Omega} \nabla p : \nabla \delta u \, d\Omega \right] \, dt$$

$$+ \int_{0}^{T} \left[ \int_{\Gamma} p \cdot n \, \delta \pi \, d\Gamma \, dt - \int_{\Omega} \nabla \cdot p \, \delta \pi \, d\Omega \right] \, dt$$

$$= \int_{0}^{T} \int_{\Gamma_{u}} p \cdot \left( n \, \delta \pi - \frac{1}{Re} \frac{\partial \delta u}{\partial n} \right) \, d\Gamma \, dt + \frac{1}{Re} \int_{0}^{T} \int_{\Gamma} \frac{\partial p}{\partial n} \cdot \delta u \, d\Gamma \, dt \qquad (55)$$

$$- \frac{1}{Re} \int_{Q} \Delta p \cdot \delta u \, dQ - \int_{Q} \nabla \cdot p \, \delta \pi \, dQ$$

$$= \frac{1}{Re} \int_{0}^{T} \int_{\Gamma_{u}} \frac{\partial p}{\partial n} \cdot \delta u \, d\Gamma \, dt + \frac{1}{Re} \int_{T_{1}^{c}}^{T_{2}^{c}} \left[ \delta \varphi_{l}^{T} \int_{\Gamma_{l}} \psi_{l} \nabla p_{2} \cdot n \, d\Gamma \right] dt$$

$$- \frac{1}{Re} \int_{Q} \Delta p \cdot \delta u \, dQ - \int_{Q} \nabla \cdot p \, \delta \pi \, dQ,$$

where  $p = (p_1, p_2, p_3)$ . In the second equality we used the boundary condition (30) for p at y = 0 and enforced symmetry. In the third equality the condition for  $\delta u$  at y = 0 in (50) was used. We also assumed that p goes to zero at the artificial boundary  $y = y_l$ . The : denotes a complete contraction defined as in (12).

The next term to rewrite, in relation (53), is the second term

$$\int_{Q} p \cdot (\delta u \cdot \nabla) u \, dQ = \int_{Q} (\nabla u)^{T} p \cdot \delta u \, dQ.$$
(56)

Finally, we rewrite the third term in (53)

$$\int_{Q} p \cdot (u \cdot \nabla) \delta u \, dQ$$

$$= \iint_{0}^{T} (p \cdot \delta u)(n \cdot u) \, d\Gamma \, dt$$

$$- \int_{Q} (p \cdot \delta u)(\nabla \cdot u) \, dQ - \int_{Q} (u \cdot \nabla) p \cdot \delta u \, dQ$$

$$= \iint_{0}^{T} (p \cdot \delta u)(n \cdot u) \, d\Gamma \, dt - \int_{Q} (u \cdot \nabla) p \cdot \delta u \, dQ,$$
(57)

where we have used the continuity condition on u and the boundary conditions (30) for p. The fifth term needs no rewriting.

Substituting (54), (55), (56) and (57) into (53) yields

$$\int_{\Omega} p(T) \cdot \delta u(T) \, d\Omega + \frac{1}{Re} \int_{T_{1}^{c}}^{T_{2}^{c}} \left[ \delta \varphi_{l}^{T} \int_{\Gamma_{l}} \psi_{l} \nabla p_{2} \cdot n \, d\Gamma \right] dt 
+ \int_{Q} \delta u \cdot \left( -\frac{\partial p}{\partial t} + (\nabla u)^{T} p - (u \cdot \nabla) p - \frac{1}{Re} \Delta p + \lambda(x) p \right) dQ 
- \int_{Q} \delta \pi \nabla \cdot p \, dQ + \frac{1}{Re} \int_{0}^{T} \int_{\Gamma_{u}} \frac{\partial p}{\partial n} \cdot \delta u \, d\Gamma \, dt 
+ \int_{0}^{T} \int_{\Gamma_{u}} (n \cdot u) (p \cdot \delta u) \, d\Gamma \, dt = 0.$$
(58)

Now, require p to satisfy the adjoint equations:

$$\begin{cases}
-\frac{\partial p}{\partial t} + (\nabla u)^T p - (u \cdot \nabla)p \\
-\frac{1}{Re} \Delta p + \lambda(x)p + \nabla \sigma = \begin{cases} u - u_T & \text{in } (T_1^o, T_2^o) \times \Omega_o \\ 0 & \text{otherwise} \end{cases} & \text{in } Q, \\
\nabla \cdot p = 0 & \text{in } Q, \\
p|_{t=T} = 0,
\end{cases}$$

118

with the boundary conditions (30). With these assumptions equation (58) becomes

$$\int_{T_1^o \Omega_o}^{T_2^o} \delta u \cdot (u - u_T) \, dQ - \int_{Q} \delta u \cdot \nabla \sigma \, dQ 
+ \frac{1}{Re} \int_{0}^{T} \int_{\Gamma_u}^{dp} \frac{\partial p}{\partial n} \cdot \delta u \, d\Gamma \, dt + \int_{0}^{T} \int_{\Gamma_u}^{T} (n \cdot u)(p \cdot \delta u) \, d\Gamma \, dt = 0,$$
(59)

since p and  $\partial p_2/\partial n$  is zero on the boundary y=0 due to the no-slip and continuity conditions. The second term in (59) can be rewritten

$$-\int_{Q} \delta u \cdot \nabla \sigma \, dQ = -\int_{0}^{T} \int_{\Gamma} \delta u \cdot n \, \sigma \, d\Gamma \, dt + \int_{Q} \nabla \cdot \delta u \, \sigma \, dQ$$

$$= -\int_{0}^{T} \int_{\Gamma} \delta u \cdot n \, \sigma \, d\Gamma \, dt,$$
(60)

since  $\nabla \cdot \delta u = 0$ . The final step is now to substitute the terms involving  $\delta u$ . When that is done the second term in the perturbed objective function (48) can be replaced with terms involving  $\delta \varphi$ . Since  $\delta u$  is known on parts of the boundary we can proceed as follows

$$-\int_{0}^{T} \int_{\Gamma} \delta u \cdot n \, \sigma \, d\Gamma \, dt$$

$$= -\int_{0}^{T} \int_{\Gamma_{u}} \delta u \cdot n \, \sigma \, d\Gamma \, dt + \int_{T_{1}^{c}}^{T_{2}^{c}} \left[ \delta \varphi_{l}^{T} \int_{\Gamma_{c}} \psi_{l} \sigma \, d\Gamma \right] dt.$$
(61)

Combining equation (60) and (61) and inserting that into (59) yield

$$\int_{T_1^o}^{T_2^o} \int_{\Omega_o} \delta u \cdot (u - u_T) \, dQ + \int_{0}^{T} \int_{\Gamma_u} \delta u \cdot \left( \frac{1}{Re} \frac{\partial p}{\partial n} - \sigma n + (n \cdot u) p \right) \, d\Gamma \, dt + \int_{T_2^o}^{T_2^o} \left[ \delta \varphi_l^T \int_{\Gamma_c} \psi_l \sigma \, d\Gamma \right] \, dt = 0.$$
(62)

Applying the fourth boundary condition (30) for p together with the assumption that also p = 0 and  $\sigma = 0$  (see the beginning of the section) at  $y = y_l$  we get

$$\int_{T_1^o}^{T_2^o} \int_{\Omega_o} \delta u \cdot (u - u_T) \, dQ = -\int_{T_1^c}^{T_2^c} \left[ \delta \varphi_l^T \int_{\Gamma_c} \psi_l \sigma \, d\Gamma \right] dt.$$
 (63)

Remains only to substitute (63) into (48) which yields

$$\delta J(\varphi_l) = \int_{T_1^c}^{T_2^c} \delta \varphi_l^T \int_{\Gamma_c} \psi_l \left( \varepsilon \varphi_l^T \psi_l - \sigma \right) d\Gamma dt$$
 (64)

where the gradient of the objective function can be identified as:

$$\frac{\partial J}{\partial \varphi_l} = \int_{\Gamma_c} \psi_l \left( \varepsilon \varphi_l^T \psi_l - \sigma \right) d\Gamma. \tag{31}$$

This is exactly the same expression for the gradient as for the channel flow case, equation (22) and (23), except that this gradient is restricted to information from  $\Gamma_c$ .

#### References

BERGGREN, M. 1998 Numerical solution of a flow-control problem: vorticity reduction by dynamic boundary action SIAM J. Sci. Comput., 19 (3), 829-860

Bewley, T. R., Moin, P., Temam, R. 2001. DNS-based predictive control of turbulence: an optimal target for feedback algorithms. *J. Fluid Mech.* **477**, 179–225.

Byrd, R. H., Peihuang, L., Nocedal, J. & Zhu, C. 1994. A limited memory algorithm for bound constrained optimization *Technical Report NAM-08* Northwestern University. http://www.netlib.org/toms/778

Canuto, C. Hussaini, M. Y., Quarteroni, A. & Zang, T. A. 1988. Spectral methods in Fluid Dynamics Springer

Collis, S. S., Chang, Y., Kellogg, S. & Prabhu, R. D. 2000 Large eddy simulation and turbulence control AIAA-paper 2000–2564.

GLOWINSKI, R. & HE, J. 1998 On shape optimization and related issues *Computational Methods for Optimal Design and Control*, J. BORGGAARD *et al.* (eds), Birkhäuser, Boston, 151-179.

Gunzburger, M. D. 1998 Sensitivities in computational methods for optimal flow control Computational Methods for Optimal Design and Control, J. Borggaard et al. (eds), Birkhä user, Boston, 197-236

Gunzburger, M. D. 1995 Flow control. (M. D. Gunzburger ed.) Springer, Berlin. Hinze, M. & Kunisch, K. 2000 Three control methods for time dependent fluid flow. Flow, Turbulence and Combustion 65, (3/4), 273–298.

HÖGBERG, M. & BERGGREN, M. 2000. Numerical investigation of different discretization approaches for optimal Control. Flow, Turbulence and Combustion 65, (3/4), 273–298.

- HÖGBERG, M. & BEWLEY, T. R. 2001. Spatially localized convolution kernels for decentralized control and estimation of plane channel flow. Submitted to Automatica
- HÖGBERG, M. & Henningson, D. S. 2001. Linear optimal control applied to instabilities in spatial boundary layers. Submitted to *J. Fluid Mech.*
- HÖGBERG, M., HENNINGSON, D. S. & BERGGREN, M. 2000. Optimal control of bypass transition. In *Advances in turbulence VIII*, DOPAZO, C. *et al.*, editors
- JOSLIN, R. D., GUNZBURGER, M. D. & NICOLAIDES, R. A. 1997. Self-Contained Automated Methodology for Optimal Flow Control. AIAA Journal, 35 (5), 816-824
- KIM, J. & LIM, J. 2000 A linear process in wall-bounded turbulent shear flows Phys. Fluids 12 (8), 1885–1888.
- LUNDBLADH, A., HENNINGSON, D. S. & JOHANSSON, A. V. 1992. An Efficient Spectral Integration Method for the Solution of the Navier–Stokes Equations FFA TN 1992-28
- Lundbladh, A., Berlin, S., Skote, M., Hildings, C., Choi, J., Kim, J. & Henningson, D. S. 1999 An efficient spectral method for simulation of incompressible flow over a flat plate. Technical report, Department of Mechanics, KTH, *TRITA-MEK* 1999:11
- MORKOVIN, M. V. 1969. The many faces of transition. In *Viscous Drag Reduction* (Wells, C. S., editor). Plenum Press.
- NORDSTRÖM, J., NORDIN, N. & HENNINGSON, D. S. 1999 The fringe region technique and the Fourier method used in the direct numerical simulation of spatially evolving viscous flows. SIAM J. Sci. Comp. 20 (4), 1365–1393.
- REDDY, S. C., SCHMID, P. J., BAGGETT, J. S. & HENNINGSON, D. S. 1998. On stability of streamwise streaks and transition thresholds in plane channel flows. *J. Fluid Mech.*, **365**, 269-303
- Schmid, P. J. & Henningson, D. S. 2001. Stability and transition in shear flows. Springer
- SRITHARAN, S. S. 1998  $Optimal\ control\ of\ viscous\ flows.$  (S. S. SRITHARAN ed. ) SIAM.

# Paper 3

3

# Spatially localized convolution kernels for decentralized control and estimation of plane channel flow

By Markus Högberg\* and Thomas R. Bewley<sup>†</sup>

Effective physical-space convolution kernels are determined for the control and estimation of incompressible plane channel flow. The kernels are derived directly from the linearized 3D Navier-Stokes equation and a mathematical statement of the control objective. As a canonical example of the channel-flow control problem, a continuous distribution of blowing and suction on the walls is used as the control and a continuous distribution of skin friction sensing on the walls is used as the measurement. An  $\mathcal{H}_2$  control design is first accomplished for the linearized Navier-Stokes system (in the form of the Orr-Sommerfeld/Squire equations) for an array of wavenumber pairs  $\{k_x,k_z\}$ , then the resulting set of feedback gains are inverse-transformed to the physical domain. The optimal physical-space convolution kernels so determined exhibit localized spatial support with exponential decay, thus facilitating truncation and application in an approximate fashion with spatially compact feedback rules in a completely decentralized setting on a massive array of identical, interconnected MEMS tiles integrating sensing, actuation, and the control logic.

The compact feedback control convolution kernels so computed are then implemented in constant-mass-flux direct numerical simulations of the nonlinear Navier-Stokes equation. For initially laminar flows at  $Re_c=2000$  with both random and oblique-wave initial flow perturbations, the ability of the constant-gain linear control feedback to stabilize the nonlinear flow system is demonstrated for initial flow perturbations with magnitudes well above the threshold which induces transition to turbulence in the uncontrolled system. When the linear control feedback is applied to fully turbulent flows at  $Re_{\tau}=100$ , via a gain scheduling approach which tunes the linear feedback gains to the instantaneous mean flow profile, complete relaminarization of the turbulent flow is attained.

#### 1. Introduction

The process of transition of a laminar flow to turbulence is only partially understood. Recent reviews of this active research topic can be found in Trefethen

<sup>\*</sup>Department of Mechanics, Royal Institute of Technology (KTH), SE-100 44 Stockholm, Sweden

<sup>&</sup>lt;sup>†</sup>Dynamic Systems & Control Group, Dept. of MAE, UC San Diego, La Jolla, CA 92093, USA

et al. (1993), Berlin, Wiegel, & Henningson (1999), and Schmid & Henningson (2001). Feedback control strategies designed to delay or eliminate transition which have been based on this limited physical understanding have been largely unfruitful. The present work is one in a series of several investigations to derive transition control strategies directly from first principles, bypassing phenomenological descriptions of transition which are still incomplete. Other investigations in this vein include Joshi, Speyer, & Kim (1997), Cortelezzi & Speyer (1998), Cortelezzi, Lee, Kim, & Speyer (1998), and Bamieh & Dahleh (2000); a recent survey of research in this area is given in Bewley (2001).

After the introduction (§1), the three main chapters of this paper outline the three main contributions of the present work:

- §2: Demonstration that optimal control theory applied to the linearized partial differential equations governing fluid flow in a plane channel, when solved in Fourier space and then inverse-transformed to physical space, can indeed yield feedback kernels with localized support and exponential decay. Care must be taken both in the numerical discretization and in the formulation of the control problem itself in order to achieve this result. The physical structure, extent, and symmetries of the resulting convolution kernels coincide with intuition derived from reasonable hypotheses about the dynamics of the flow structures.
- §3: Demonstration of the effectiveness of linear full-state feedback with fixed, spatially compact feedback kernels (given by truncation of the localized structures computed in §2) for the prevention of transition to turbulence in perturbed laminar channel flows at  $Re_c = 2000$ . It is shown that the linear control feedback prevents transition in perturbed laminar flows that would otherwise quickly become turbulent due to nonlinearities in the system. Both random and oblique-wave initial perturbations to the laminar flow are considered, per the cases of particular physical significance enumerated by Reddy *et al.* (1998).
- $\S 4$ : Demonstration of the effectiveness of linear full-state feedback with scheduled controller gains (with a novel gain-scheduling strategy based on the fullness of the mean flow profile) for the problem of minimizing a weighted energy measure of fully developed, constant-mass-flux turbulent channel flow at  $Re_{\tau}=100$ . It is shown that fully developed turbulent flow can be completely relaminarized if the gains are scheduled appropriately, though only modest drag and TKE reductions are achieved with fixed-gain linear feedback.

In the concluding discussion (§5), an approach is presented for the implementation of the compensation rules derived in the present work on a massive array of identical, interconnected Micro-Electro-Mechanical-Systems (MEMS) tiles, each of which integrating the functions of sensing, actuation, and the decentralized control logic. Further implications of the spatial localization achieved in the present work are also discussed.

For space considerations, extension of the present work to higher Reynolds numbers and numerical implementation and testing of the estimation kernels and the LQG compensator which combines the estimator and the full-state controller will be deferred to a separate article (Högberg, Bewley, & Henningson 2001).

#### 1.1. Model system: spatially periodic plane channel flow

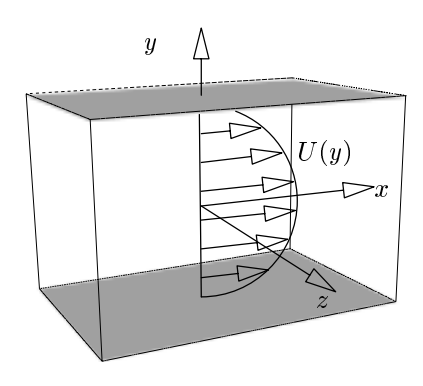


FIGURE 1. Geometry of flow domain.

Small perturbations to an incompressible laminar flow in a channel (Figure 1) are governed by the Orr-Sommerfeld/Squire equations. These equations are derived from the Fourier transform (in the streamwise and spanwise directions, x and z) of the Navier-Stokes equation linearized about some mean flow profile U(y), and may be written at each wavenumber pair  $\{k_x, k_z\}$  as

$$\hat{\Delta}\,\dot{\hat{v}} = \{-i\,k_x\,U\,\hat{\Delta} + i\,k_x\,U'' + \nu\hat{\Delta}(\hat{\Delta})\}\,\,\hat{v} \tag{1a}$$

$$\dot{\hat{\omega}} = \{-i k_z U'\} \hat{v} + \{-i k_x U + \nu \hat{\Delta}\} \hat{\omega},$$
(1b)

where  $\hat{v}$  is the Fourier transform of the velocity component normal to the walls,  $\hat{\omega}$  is the Fourier transform of the vorticity component normal to the walls, and  $\hat{\Delta} \triangleq \partial^2/\partial y^2 - k_x^2 - k_z^2$ . In the present work,  $\delta$  is the channel half width,  $\rho$  is the density, and  $\nu = \mu/\rho$  is the kinematic viscosity. Lengths are scaled such that the upper and lower walls are located at  $y = \pm 1$  (i.e.,  $\delta = 1$ ). All variables associated with the Fourier representation of the system will be distinguished with hats (^).

Control is applied via time-varying boundary conditions on  $\hat{v}$  on the walls. A "no-slip" condition is also enforced, which implies homogeneous boundary conditions on  $\hat{\omega}$  on the walls. The no-slip condition together with the continuity equation further imply homogeneous boundary conditions on  $\partial \hat{v}/\partial y$  on the walls. The  $k_x = k_z = 0$  component of  $\hat{v}$  is constrained to be zero at each wall.

For the purpose of computational simplicity, periodic boundary conditions are assumed on v and  $\omega$  (the inverse Fourier transforms of  $\hat{v}$  and  $\hat{\omega}$ ) in the x and z directions when computing the feedback kernels. The implications of this modeling assumption can be both significant and nonphysical. Spatially-localized feedback kernels, obtained directly from the equations governing fluid

motion for the first time in the present work, are uniquely positioned to effectively relax this nonphysical assumption, as discussed in some depth in §5.

The extent of the computational domain in the x and z directions, denoted  $L_x$  and  $L_z$ , is chosen to be significantly larger than the size of the resulting localized convolution kernels. Adequate streamwise and spanwise extent of the computational domain is verified a posteriori.

Note the spatially-invariant structure of the geometry depicted in Figure 1; statistically speaking, every point on each wall is identical to every other point on that wall. Canonical problems with this sort of spatially-invariant structure in one or more directions form the backbone of much of the literature on flow transition and turbulence.

#### 1.2. Parameterization characterizing channel-flow system

The Reynolds number parameterizes present problem. There are primarily three definitions of the Reynolds number which are relevant for channel flow:

- The centerline Reynolds number  $Re_c \triangleq \bar{u}_c \delta/\nu$  based on the mean centerline velocity  $\bar{u}_c$  (averaged in x and z and, when the flow is statistically stationary, time). The Reynolds number so defined is commonly used to characterize laminar flows.
- The skin-friction Reynolds number  $Re_{\tau} \triangleq \bar{u}_{\tau}\delta/\nu$  based on the mean "skin-friction velocity"  $\bar{u}_{\tau} \triangleq \sqrt{\bar{\tau}_w/\rho}$ , where  $\bar{\tau}_w \triangleq \mu(\partial \bar{u}/\partial y)_{\text{wall}}$  is the mean skin friction on the walls (averaged in x and z and, when the flow is statistically stationary, time). The Reynolds number so defined is commonly used to characterize turbulent flows.
- The bulk Reynolds number  $Re_B \triangleq u_B \delta/\nu$  based on the "bulk" velocity  $u_B \triangleq \frac{1}{V} \int_{\Omega} u_1 \, dV$ , where  $V = 2 L_x L_z$ . The Reynolds number so defined is useful in characterizing flows which are not statistically stationary, as it is the only one of the three Reynolds numbers discussed here that remains exactly constant as the full nonlinear constant-mass-flux channel flow system evolves in time.

Uncontrolled turbulent flow at  $Re_{\tau} \approx 100$ , such as that considered in the present work, corresponds to a bulk Reynolds number of  $Re_{B} \approx 1430$  and a centerline Reynolds number of  $Re_{c} \approx 1710$ ; once relaminarized by the action of control feedback, such a flow has a centerline Reynolds number of  $Re_{c} \approx 2140$  and a skin friction Reynolds number of  $Re_{\tau} \approx 65$ . Note that the laminar and turbulent flows considered in the present work have nearly the same bulk Reynolds number; to facilitate comparison with other work in both transition control and turbulence control, we have picked round numbers for  $Re_{c}(=2000)$  in the transition control simulations and round numbers for  $Re_{\tau}(=100)$  in the turbulence control simulations.

Constant-mass-flux turbulent channel flow at  $Re_{\tau} \approx 100$  is a standard benchmark problem in low-Reynolds number turbulent channel flow simulations for the development and testing of control strategies for wall-bounded turbulence, and is considered in numerous recent references on this topic. See,

e.g., Choi, Moin, & Kim (1994), Lee  $et\ al.$  (1997), and Bewley, Moin, & Temam (2001) for further discussion of the flow physics which relate to the present problem.

#### 1.3. Prior work leading to the present

The present work builds directly, though with certain important modifications, on the methodology laid out by Bewley & Liu (1998), hereafter referred to as BL98. This article describes the Fourier-space representation of the present problem. Spatial localization of the convolution kernels given by inverse Fourier transform of BL98-type control strategies (computed in Fourier space) was anticipated at the outset of this effort based on physical arguments. Specifically:

- a) The controller feedback kernels relating the state estimate inside the domain to the control forcing at some point on the wall should decay quickly as a function of distance, as the control authority of any blowing/suction hole drilled into the wall on the surrounding flow decays rapidly with distance in a distributed viscous system.
- b) Similarly, the estimator feedback kernels relating measurement error at some point on the wall to the estimator forcing on the system model inside the domain should decay quickly as a function of distance, as the correlation of any two flow perturbation variables are known to decay rapidly with distance in a distributed viscous system.

The work of Bamieh, Paganini, & Dahleh (2001) established analytically that spatial localization with exponential decay far from the origin should be expected for  $\mathcal{H}_2/\mathcal{H}_{\infty}$  control and estimation kernels for a broad class of distributed parameter systems with spatially-invariant structure. This work lays an important theoretical foundation for the present study, which is a focused application of  $\mathcal{H}_2$  control theory to a distributed parameter system with this type of spatially-invariant structure.

Several fundamental questions remained unanswered, however, by previous numerical and analytical efforts. Careful numerical investigations such as the present promise to shed light on several of these open questions, including:

- 1) the spatial extent and structure of the localized feedback gains necessary to effectively estimate and control the important dynamics of the channel flow system,
- 2) the effectiveness of the resulting feedback gains when applied to the nonlinear Navier-Stokes equation (both for inhibiting transition and for mitigating the effects of turbulence), and
- 3) the specific requirements on the formulation of the control problem itself necessary to achieve both localization of the kernels (*i.e.*, the proper behavior of the gains at low wavenumbers) and to prevent "ringing" (*i.e.*, to achieve adequate roll-off of the gains at the high wavenumbers).

Due to the complexity of the governing equation and the high dimension of the problem at hand, obtaining effective, well behaved, spatially-localized kernels is not as straightforward as it might seem, and does not follow directly from all controller formulations and numerical discretizations (Bamieh & Miller, private communication, 1999). §2 of the present paper describes both the careful numerical treatment and the reformulation of the control problem from that presented in BL98 which were found to be effective in these regards in the present work.

As documented by BL98 in a closely related controller formulation, the feedback computed in the present work is effective at minimizing both transient energy growth and the relevant input-output transfer function norms in the controlled linear system representing small perturbations to a laminar channel flow. Note that the linear problem is best studied in Fourier space due to the complete decoupling of the control problem at distinct wavenumber pairs when the control problem is formulated correctly, as noted by Bewley & Agarwal (1996) and discussed in detail in BL98. When nonlinearities are introduced, the system dynamics at all wavenumber pairs are coupled, and analysis is more difficult; the present article characterizes the behavior of the linearly-controlled nonlinear system by direct numerical simulation (DNS) of the nonlinear equation governing the controlled flow.

In subcritical flows which are linearly stable, the non-self-adjoint nature of the linear operator governing the evolution of small perturbations to the laminar flow leads to highly nonorthogonal system eigenvectors and, thereby, linear mechanisms for very large transient energy growth (Gustavsson 1991; Butler & Farrell 1992; Reddy & Henningson 1993) and disturbance amplification (Farrell & Ioannou 1993; BL98; Bamieh & Dahleh 2000). These linear phenomena can lead to nonlinear instability even for fairly small initial flow perturbations or external system disturbances. In this paper, we show how such nonlinear instability may be inhibited by the application of decentralized linear feedback control in the physical domain.

The mechanisms for energy growth in the uncontrolled system are strictly linear, as the nonlinear terms in the equation governing the system only redistribute the energy between different modes of flow perturbations. It was demonstrated in BL98 that a notable feature of closed-loop systems with effective control feedback applied is that the closed-loop system eigenvectors are made closer to orthogonal by the application of the control, thereby weakening the linear mechanisms for transient energy growth and disturbance amplification in the controlled system. This observation motivates the application of linear control feedback to the finite but small perturbations leading to nonlinear instability in transitional flows; if the linear control feedback alters the closed-loop system eigenmodes in the correct way, linear transient energy growth and disturbance amplification are reduced, and thus both large flow perturbations and nonlinear instability may be avoided. Indeed, this expected result is obtained in the present work (see §3).

The observation that energy growth is explained strictly by linear mechanisms in this system has also motivated some researchers to speculate about the

possible application of blowing/suction controls computed with linear feedback rules to subdue the large-amplitude flow perturbations present in turbulent flows (Farrell & Ioannou 1996; Kim & Lim 2000). Indeed, when applied correctly (see §4), linear control feedback is found to be remarkably effective on low Reynolds number turbulent channel flow in the present work. A warning about possible shortcomings of linear controllers for application to nonlinear chaotic fluid systems is given in Bewley (1999); such shortcomings might become significant when attempting to apply the present strategy at greater feedback magnitudes or at higher Reynolds numbers.

# 2. Derivation of convolution kernels

# 2.1. Objective: reduce energy of flow perturbations

The objective of the present study is to minimize the flow perturbation energy in a channel flow which is excited by both external disturbances and initial conditions of possibly deleterious structure, while accounting for a finite amount of noise in the flow measurements. To simplify the present study, all disturbances acting on the system are assumed to be zero-mean white Gaussian processes, and the feedback is computed in the  $\mathcal{H}_2$  framework; the extension to unstructured disturbances and the robust  $(\mathcal{H}_{\infty})$  control of channel flows driven by such disturbances is straightforward, as discussed in BL98. Loop Transfer Recovery (LTR), an alternative strategy for achieving closed-loop system robustness, is applied in a related (2D) controller formulation by Cortelezzi, Lee, Kim, & Speyer (1998); further comments about the suitability of LTR for highly nonnormal systems, such as the channel flow problem considered here, are deferred to Bewley (2001).

The energy density of the flow perturbation at any instant is measured by the integral of the square of the velocities over the flow domain  $\Omega$  (in physical space) divided by the volume of the domain V. In the present work, we generalize this quantity a bit and define a weighted measure which scales the energy density by a function f(y), which may be selected as part of the control design. Rewriting this weighted energy measure in  $\hat{v} - \hat{\omega}$  form and incorporating Parseval's theorem leads to

$$\mathcal{E} = \frac{1}{2V} \int_{\Omega} f(y)(u^2 + v^2 + w^2) \, dV =$$

$$\sum_{k_x, k_z} \frac{1}{8k^2} \int_{-1}^{1} f(y) \left( k^2 |\hat{v}|^2 + \left| \frac{\partial \hat{v}}{\partial y} \right|^2 + |\hat{\omega}|^2 \right) \, dy \triangleq \sum_{k_x, k_z} \hat{E},$$
(2)

where  $k^2 = k_x^2 + k_z^2$ . The objective function for the present work is defined as the integral in time of a linear combination of the weighted energy measure of the flow perturbation, defined above, and some measure of the "control effort".

In the present paper, we define this objective function as

$$\mathcal{J} = \int_{0}^{\infty} \left[ \mathcal{E} + \ell^{2} \int_{\Gamma_{2}^{\pm}} \left( \frac{\partial v}{\partial t} \right)^{2} dS \right] dt \triangleq \sum_{k_{x}, k_{z}} \hat{J}, \tag{3}$$

where  $\Gamma_2^{\pm}$  denotes the upper and lower walls. Note that  $\ell^2$  is used as an adjustable parameter to scale the control feedback via a penalty on the "control effort" in the objective function, and that this penalty term is a function of  $(\partial v/\partial t)^2$  on the walls in the present formulation. Excursions of  $v^2$  on the walls are penalized naturally in the term of the cost function related to  $\mathcal{E}$ , as the flow velocities near the wall are continuous and smoothly varying; no additional penalty on the integral of the boundary value of  $v^2$  was found to be necessary in the present work in order to keep this quantity small.

The kernels plotted later in this chapter and applied to the transition problem in §3 take f(y) = 1. This choice is natural, as the transition control problem generally targets system perturbations which fill the entire width of the channel. However, the kernels which we found to be most effective in the turbulence control problem of §4 used a weighting function of  $f(y) = (1 - y^2)^{-1/2}$  (which so happens to be the weighting w(y) in the Sturm-Liouville problem that leads to the Chebyshev polynomials). This choice is also natural, as it places extra emphasis in the control formulation on flow perturbations near the wall, which are known to be of important dynamical significance for sustaining the turbulence cascade (see, e.g., Jimenez 1999). Other choices for f(y) (of those which we tested) were not as effective; specifically, the choice f(y) = 1 failed to relaminarize the turbulent flow in all cases tested.

# 2.2. Transformation of control problem to state-space form

A state vector at each wavenumber pair  $\{k_x,k_z\}$  may be defined by discretization of the wall-normal velocity  $\hat{v}$  and the wall-normal verticity  $\hat{\omega}$  on several gridpoints in the y direction. A Chebyshev collocation technique is used in the y direction with differentiation matrices obtained from the Matlab Differentiation Matrix Suite of Weideman & Reddy (1999). Boundary conditions are handled in the construction of the differentiation matrices in such a way that spurious eigenvalues are eliminated, as suggested by Huang & Sloan (1993), thereby overcoming the chief numerical difficulty reported by BL98. Invocation of the homogeneous boundary conditions on  $\partial \hat{v}/\partial y$  allows inversion of the Laplacian on the LHS of (1a) and expression of (1) in matrix form:

$$\underbrace{\begin{pmatrix} \dot{\hat{\mathbf{v}}} \\ \dot{\hat{\boldsymbol{\omega}}} \end{pmatrix}}_{\hat{\hat{\mathbf{x}}}} = \underbrace{\begin{pmatrix} \hat{\mathcal{L}} & 0 \\ \hat{\mathcal{C}} & \hat{\mathcal{S}} \end{pmatrix}}_{\hat{N}} \underbrace{\begin{pmatrix} \hat{\mathbf{v}} \\ \hat{\boldsymbol{\omega}} \end{pmatrix}}_{\hat{\mathbf{x}}}, \tag{4}$$

where boldface is used to distinguish discretized vectors from their corresponding continuous (non-boldfaced) counterparts. The control is applied via the

time-varying boundary conditions on  $\hat{v}$ . A lifting technique is used to account for these boundary controls in the discretization of the system in the standard state-space form. To accomplish this, the flow perturbation is decomposed such that

$$\hat{\mathbf{x}} = \hat{\mathbf{x}}_i + \hat{\mathbf{x}}_h. \tag{5}$$

The inhomogeneous part  $\hat{\mathbf{x}}_i$  is taken at each instant to satisfy the nonzero boundary conditions on  $\hat{v}_i$ , homogeneous boundary conditions on  $\partial \hat{v}_i/\partial y$  and  $\hat{\omega}_i$ , and a numerically convenient equation on the interior of the domain; in the present case, we define the lifting via the equation  $\hat{N}\hat{\mathbf{x}}_i = 0$  on the interior of  $\Omega$ . Assembling the controls (*i.e.*, the values of the  $\hat{v}$  at the upper and lower walls) into a control vector  $\hat{\boldsymbol{\phi}}$ , this system may easily be solved for arbitrary  $\hat{\boldsymbol{\phi}} = \hat{\boldsymbol{\phi}}(t)$  and written as

$$\hat{\mathbf{x}}_i = \hat{Z}\hat{\boldsymbol{\phi}}, \quad \text{where} \quad \hat{\boldsymbol{\phi}} = \begin{pmatrix} \hat{v}(+1) \\ \hat{v}(-1) \end{pmatrix} \quad \text{and} \quad \begin{pmatrix} \hat{\boldsymbol{\phi}} = \hat{\boldsymbol{\phi}}(t), \\ \hat{\mathbf{x}}_i = \hat{\mathbf{x}}_i(t), \end{pmatrix}$$
 (6)

and  $\hat{Z}$  is a constant matrix relating the blowing/suction distribution  $\hat{\phi}$  to the lifting  $\hat{\mathbf{x}}_i$  at each instant. The equation governing  $\hat{\mathbf{x}}_h$  may therefore be found by substitution of (5) into (4) and imposing homogeneous boundary conditions on  $\hat{v}_h$ ,  $\partial \hat{v}_h/\partial y$ , and  $\hat{\omega}_h$ . Noting (6), the result may be written in standard state-space form:

$$\underbrace{\begin{pmatrix} \hat{\mathbf{x}}_h \\ \hat{\boldsymbol{\phi}} \end{pmatrix}}_{\hat{\mathbf{x}}_c} = \underbrace{\begin{pmatrix} \hat{N} & \hat{N}\hat{Z} \\ 0 & 0 \end{pmatrix}}_{\hat{A}} \underbrace{\begin{pmatrix} \hat{\mathbf{x}}_h \\ \hat{\boldsymbol{\phi}} \end{pmatrix}}_{\hat{\mathbf{x}}_s} + \underbrace{\begin{pmatrix} -\hat{Z} \\ I \end{pmatrix}}_{\hat{B}_2} \dot{\hat{\boldsymbol{\phi}}}. \tag{7}$$

Note that the control  $\hat{\boldsymbol{\phi}}$  is the *time derivative* of the normal velocity on the walls, and the state vector  $\hat{\mathbf{x}}_s$  includes the normal velocity on the upper and lower walls,  $\hat{\boldsymbol{\phi}}$ , appended to the homogeneous vector  $\hat{\mathbf{x}}_h$ . Note also that, for the convenient lifting we have defined and used here, we may take  $\hat{N}\hat{Z}=0$  in the above expression, since  $\hat{N}\hat{\mathbf{x}}_i=\hat{N}\hat{Z}\hat{\boldsymbol{\phi}}=0$ .

The contribution to the weighted energy measure coming from each wavenumber pair (see (2)) is easily written in matrix form as  $\hat{E} = \hat{\mathbf{x}}^* \, \hat{Q} \, \hat{\mathbf{x}}$ , where  $\hat{Q}$  is defined as in BL98 to account for numerical integration over the stretched grid used in the Chebyshev discretization. Note by (2) that the total weighted energy measure of the flow perturbation,  $\mathcal{E}$ , may be minimized by minimizing the weighted energy measure of each (decoupled) Fourier mode,  $\hat{E}$ , separately. Noting the decomposition (5) and the definition of  $\hat{\mathbf{x}}_s$  in (7),  $\hat{E}$  may be written in terms of the state vector  $\hat{\mathbf{x}}_s$  as

$$\hat{E} = \hat{\mathbf{x}}_s^* \begin{pmatrix} \hat{Q} & \hat{Q}\hat{Z} \\ \hat{Z}^*\hat{Q} & \hat{Z}^*\hat{Q}\hat{Z} \end{pmatrix} \hat{\mathbf{x}}_s \triangleq \hat{\mathbf{x}}_s^* \hat{\mathcal{Q}} \hat{\mathbf{x}}_s.$$

#### 2.3. Control strategy

Recall the standard state-space form (7) of the discretized equation governing the Fourier-space representation of flow perturbations in our system. We now seek the feedback control rule  $\dot{\hat{\phi}} = \hat{\mathcal{K}}\hat{\mathbf{x}}_s$  at each wavenumber pair  $\{k_x, k_z\}$  which, with limited control effort, minimizes the weighted flow perturbation energy at that wavenumber pair,  $\hat{E}$ , on  $t \in [0, \infty)$ . This is a standard optimal control problem. Defining the objective function  $\mathcal{J}$  in physical space as in (3), it is seen that the control problem decouples into several constituent linear quadratic minimization problems at each wavenumber pair independently. The cost function to be minimized at each wavenumber pair is given in matrix form by

$$\hat{J} = \int_{0}^{\infty} (\hat{\mathbf{x}}_{s}^{*} \hat{\mathcal{Q}} \hat{\mathbf{x}}_{s} + \ell^{2} \dot{\hat{\boldsymbol{\phi}}}^{*} \dot{\hat{\boldsymbol{\phi}}}) dt \triangleq \int_{0}^{\infty} (\hat{\mathbf{x}}_{s}^{*} \hat{C}_{1}^{*} \hat{C}_{1} \hat{\mathbf{x}}_{s} + \dot{\hat{\boldsymbol{\phi}}}^{*} \hat{D}_{12}^{*} \hat{D}_{12} \dot{\hat{\boldsymbol{\phi}}}) dt,$$

where

$$\hat{C}_1 \triangleq \begin{pmatrix} \hat{\mathcal{Q}}^{1/2} \\ 0 \end{pmatrix}$$
 and  $\hat{D}_{12} \triangleq \begin{pmatrix} 0 \\ \ell I \end{pmatrix}$ .

The feedback control rule  $\dot{\hat{\phi}} = \hat{\mathcal{K}}\hat{\mathbf{x}}_s$  which minimizes  $\hat{J}$  is given by

$$\hat{\mathcal{K}} = -\frac{1}{\ell^2} \hat{B}_2^* \hat{X}, \quad \text{where} \quad \hat{X} = \text{Ric} \begin{pmatrix} \hat{A} & -\frac{1}{\ell^2} \hat{B}_2 \hat{B}_2^* \\ -\hat{C}_1^* \hat{C}_1 & -\hat{A}^* \end{pmatrix}$$

and  $\mathrm{Ric}(\cdot)$  denotes the solution of the associated algebraic Riccati equation (Laub 1991), in accordance with standard linear optimal control theory applied to the complex system (7) at each wavenumber pair  $\{k_x,k_z\}$ . Note that  $\ell^2$ , which scales the penalty on the control effort in the cost function, is used as an adjustable parameter to scale the control feedback.

Decomposing  $\dot{\hat{\phi}} = \hat{\mathcal{K}}\hat{\mathbf{x}}_s$  and  $\hat{\mathbf{x}}_i = \hat{Z}\hat{\boldsymbol{\phi}}$  according to

$$\begin{pmatrix} \dot{\hat{v}}(+1) \\ \dot{\hat{v}}(-1) \end{pmatrix} = \begin{pmatrix} \hat{\mathcal{K}}_{+1,\hat{\mathbf{v}}_h} & \hat{\mathcal{K}}_{+1,\hat{\boldsymbol{\omega}}_h} & \hat{\mathcal{K}}_{+1,\hat{v}(+1)} & \hat{\mathcal{K}}_{+1,\hat{v}(-1)} \\ \hat{\mathcal{K}}_{-1,\hat{\mathbf{v}}_h} & \hat{\mathcal{K}}_{-1,\hat{\boldsymbol{\omega}}_h} & \hat{\mathcal{K}}_{-1,\hat{v}(+1)} & \hat{\mathcal{K}}_{-1,\hat{v}(-1)} \end{pmatrix} \begin{pmatrix} \hat{\mathbf{v}}_h \\ \hat{\boldsymbol{\omega}}_h \\ \hat{v}(+1) \\ \hat{v}(-1) \end{pmatrix},$$

$$\begin{pmatrix} \hat{\mathbf{v}}_i \\ \hat{\boldsymbol{\omega}}_i \end{pmatrix} = \begin{pmatrix} \hat{Z}_{\hat{\mathbf{v}}_i,\hat{v}(+1)} & \hat{Z}_{\hat{\mathbf{v}}_i,\hat{v}(-1)} \\ \hat{Z}_{\hat{\boldsymbol{\omega}}_i,\hat{v}(+1)} & \hat{Z}_{\hat{\boldsymbol{\omega}}_i,\hat{v}(-1)} \end{pmatrix} \begin{pmatrix} \hat{v}(+1) \\ \hat{v}(-1) \end{pmatrix},$$

it is convenient to rearrange the gain matrix  $\hat{\mathcal{K}}$  into a form  $\hat{K}$  with which the simple control feedback rule  $\dot{\hat{\phi}} = \hat{K}\hat{\mathbf{x}}$  may be employed. Decomposing this new feedback rule such that

$$\begin{pmatrix} \dot{\hat{v}}(+1) \\ \dot{\hat{v}}(-1) \end{pmatrix} = \begin{pmatrix} \hat{\mathsf{K}}_{+1,\hat{\mathbf{v}}} & \hat{\mathsf{K}}_{+1,\hat{\boldsymbol{\omega}}} \\ \hat{\mathsf{K}}_{-1,\hat{\mathbf{v}}} & \hat{\mathsf{K}}_{-1,\hat{\boldsymbol{\omega}}} \end{pmatrix} \begin{pmatrix} \hat{\mathbf{v}} \\ \hat{\boldsymbol{\omega}} \end{pmatrix}$$
 (8)

and defining

$$\begin{split} \hat{\mathsf{K}}_{\pm 1,\hat{v}(+1)} &= \hat{\mathcal{K}}_{\pm 1,\hat{v}(+1)} - \hat{\mathcal{K}}_{\pm 1,\hat{\mathbf{v}}_h} \hat{Z}_{\hat{\mathbf{v}}_i,\hat{v}(+1)} - \hat{\mathcal{K}}_{\pm 1,\hat{\boldsymbol{\omega}}_h} \hat{Z}_{\hat{\boldsymbol{\omega}}_i,\hat{v}(+1)} \\ \hat{\mathsf{K}}_{\pm 1,\hat{v}(-1)} &= \hat{\mathcal{K}}_{\pm 1,\hat{v}(-1)} - \hat{\mathcal{K}}_{\pm 1,\hat{\mathbf{v}}_h} \hat{Z}_{\hat{\mathbf{v}}_i,\hat{v}(-1)} - \hat{\mathcal{K}}_{\pm 1,\hat{\boldsymbol{\omega}}_h} \hat{Z}_{\hat{\boldsymbol{\omega}}_i,\hat{v}(-1)}, \end{split}$$

it follows that

$$\begin{split} \hat{\mathsf{K}}_{\pm 1, \hat{\mathbf{v}}} &= \begin{pmatrix} \hat{\mathsf{K}}_{\pm 1, \hat{v}(+1)} & \hat{\mathcal{K}}_{\pm 1, \hat{\mathbf{v}}_h} & \hat{\mathsf{K}}_{\pm 1, \hat{v}(-1)} \end{pmatrix} \\ \hat{\mathsf{K}}_{\pm 1, \hat{\boldsymbol{\omega}}} &= \begin{pmatrix} 0 & \mathcal{K}_{\pm 1, \hat{\boldsymbol{\omega}}_h} & 0 \end{pmatrix}. \end{split}$$

The feedback control rule  $\dot{\hat{\phi}} = \hat{K}\hat{\mathbf{x}}$  effectively performs a discrete integration in y across the channel, with the gains  $\hat{K}_{\pm 1,\hat{\mathbf{v}}}$  and  $\hat{K}_{\pm 1,\hat{\mathbf{\omega}}}$  as weights. As a cosine stretching function is used for the distribution of gridpoints in the y direction in this formulation (see BL98), it is necessary to scale the control gains appropriately (by the inverse of the cosine stretching function) in order to convert the gain  $\hat{K}$  in (8) to a grid-independent weighting function  $\hat{K}$  on a continuous integral of the form

$$\dot{\hat{v}}(y = \pm 1) = \int_{-1}^{1} [\hat{K}_{\pm 1,\hat{v}}(\bar{y})\hat{v}(\bar{y}) + \hat{K}_{\pm 1,\hat{\omega}}(\bar{y})\hat{\omega}(\bar{y})]d\bar{y}$$
(9)

at each wavenumber pair  $\{k_x, k_z\}$ . We denote the necessary (and straightforward) transformation symbolically as  $\hat{K} = \Xi^{-1}\hat{K}$ . Incorporation of the weights  $\hat{K}$  into a nonlinear DNS code, in turn, requires scaling of the control gains by the grid stretching function used in the nonlinear simulation code in a similar fashion.

The optimal control problem described above has been derived for each wavenumber pair  $\{k_x, k_z\}$  independently. The inverse Fourier transform of the Fourier-space control feedback rule (9) is given by the following convolution sum in physical space:

$$\dot{v}(x,y=\pm 1,z,t) = \int_{\Omega} \left( K_{\pm 1,v}(x-\bar{x},\bar{y},z-\bar{z}) \, v(\bar{x},\bar{y},\bar{z},t) + K_{\pm 1,\omega}(x-\bar{x},\bar{y},z-\bar{z}) \, \omega(\bar{x},\bar{y},\bar{z},t) \right) d\bar{x} \, d\bar{y} \, d\bar{z},$$

where  $K_{\pm 1,v}(x,y,z)$  and  $K_{\pm 1,\omega}(x,y,z)$  are the inverse Fourier transforms of  $\hat{K}_{\pm 1,\hat{v}}(k_x,y,k_z)$  and  $\hat{K}_{\pm 1,\hat{\omega}}(k_x,y,k_z)$  respectively. Physical-space interpretation of the structure of K is straightforward when one considers the above expression for x=z=0. In this setting, one sees directly how the kernel weights the velocity field as a function of  $(\bar{x},\bar{y},\bar{z})$  in order to give the control input  $\dot{v}(x=0,y=-1,z=0)$ , as shown in Figures 2 and 3.

#### 2.4. Estimation strategy

We now seek the estimator feedback at each wavenumber pair  $\{k_x, k_z\}$  which, while accounting for both state disturbances and measurement noise, minimizes

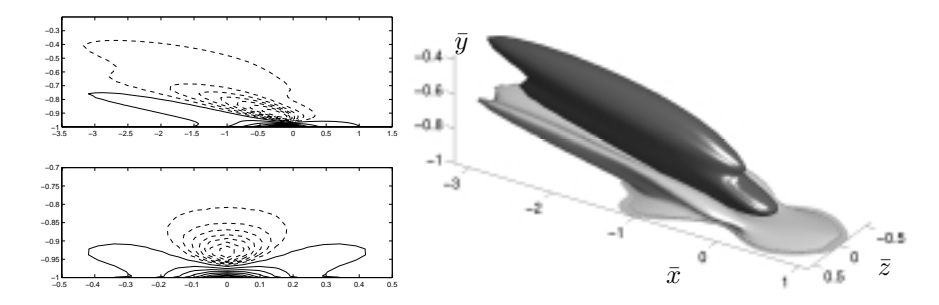


FIGURE 2. Controller gain  $K_{-1,v}$  relating the state v inside the domain to the control forcing term  $\dot{v}(x=0,y=-1,z=0)$  on the wall. Contours in an  $\bar{x}\bar{y}$  plane at  $\bar{z}=0$  (top) and a  $\bar{z}\bar{y}$  plane at  $\bar{x}=0$  (bottom) are shown on the left, and two isosurfaces (one positive and one negative) of the convolution kernel are shown on the right. Gains computed with  $\ell=1$  and a mean-flow profile of  $U(y)=1-y^2$  at  $Re_c=2000$  for a  $2\pi\times 2\times 2\pi$  box at a resolution of  $128\times 72\times 128$  Fourier, Chebyshev, Fourier modes in  $\bar{x},\bar{y},\bar{z}$  respectively.

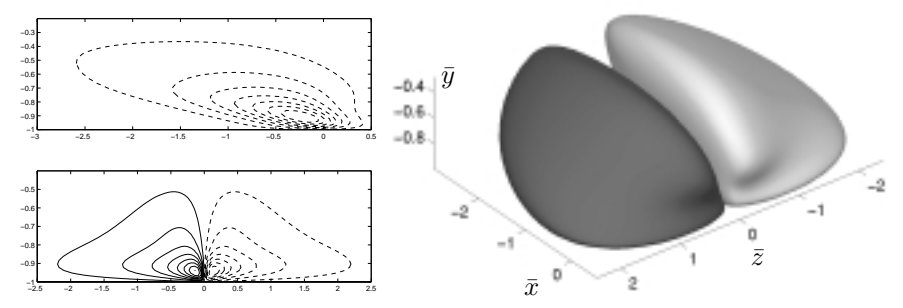


FIGURE 3. Controller gain  $K_{-1,\omega}$  relating the state  $\omega$  inside the domain to the control forcing term  $\dot{v}(x=0,y=-1,z=0)$  on the wall. Contours in an  $\bar{x}\bar{y}$  plane at  $\bar{z}=-0.24$  (top) and a  $\bar{z}\bar{y}$  plane at  $\bar{x}=0$  (bottom) are shown on the left, and two isosurfaces of the convolution kernel are shown on the right.

the energy of the state estimation error on  $t \in [0, \infty)$ . This is a standard Kalman filter problem.

In order to develop the Kalman filter for the present problem, we must first model the disturbances to the state equation and the noise in the available measurements. Following Bewley (2001), we now model the state equation (7) and the skin-friction measurements of our system as disturbed by a random (zero-mean white Gaussian) process  $\hat{\mathbf{w}}$  such that

$$\dot{\hat{\mathbf{x}}}_h = \hat{N}\,\hat{\mathbf{x}}_h + \hat{B}_1\,\hat{\mathbf{w}} - \hat{Z}\dot{\hat{\boldsymbol{\phi}}}$$
$$\hat{\mathbf{y}}_h = \hat{C}_2\hat{\mathbf{x}}_h + \hat{D}_{21}\hat{\mathbf{w}},$$

where

$$\hat{B}_1 = (\hat{G}_1 \quad 0), \quad \hat{C}_2 \hat{\mathbf{x}}_h = \frac{\hat{G}_2^{-1}}{Re} \begin{pmatrix} \frac{\partial \hat{\omega}_h}{\partial y} \\ \frac{\partial \hat{\omega}_h}{\partial y} \end{pmatrix}_{y=-1}, \quad \text{and} \quad \hat{D}_{21} = \begin{pmatrix} 0 & \alpha I \end{pmatrix},$$

where  $\hat{G}_1$  is defined as the square root of the expected covariance of the state disturbances and  $\alpha \hat{G}_2$  is defined as the square root of the expected covariance of the measurement noise. We assume that these covariances are time invariant and that the covariance of the measurement noise is nonsingular. The problem is scaled such that  $\bar{\sigma}(\hat{G}_1^2) = 1$ , and  $\alpha$  is selected such that  $\bar{\sigma}(\hat{G}_2^2) = 1$ . Any known structure of the disturbance covariances entering the problem should thus be accounted for in the selection of the matrices  $\hat{G}_1$  and  $\hat{G}_2$  (both with unity maximum singular value) during the compensator design, retaining the quantity  $\alpha$  to reflect the balance between the magnitude of the measurement noise and the magnitude of the state disturbances. This scaling of the disturbances is particularly convenient, and is a natural choice for problems of this sort because it retains the dual structure of the control and estimation problems. The scalar knob  $\alpha$  on the estimation problem, analogous to the scalar knob  $\ell$  on the control problem, affords a sufficient but not excessive degree of flexibility in the compensator design. This is important when working with high-dimensional discretizations of infinite-dimensional systems, as it is not feasible when designing dynamic compensators for such systems to conduct a parametric variation on the individual elements of  $\hat{G}_1$  and  $\hat{G}_2$ .

Given that the blowing/suction distribution  $\hat{\phi}$  and the lifting function  $\hat{Z}$  are known, the (noisy) measurements  $\hat{\mathbf{y}}_h$  of the quantity  $\hat{C}_2\hat{\mathbf{x}}_h$  may easily be extracted from the available (noisy) wall measurements of the streamwise or spanwise drag, via (5) and (6). Only the field  $\hat{\mathbf{x}}_h$  needs to be estimated in order to construct an estimate of the complete state vector  $\hat{\mathbf{x}}_s$  (or, indeed, to estimate  $\hat{\mathbf{x}}$  itself); we will denote our estimate of  $\hat{\mathbf{x}}_h$  as  $\hat{\mathbf{x}}_e$ , and our estimate of  $\hat{\mathbf{y}}_h$  as  $\hat{\mathbf{y}}_e$ . The model of the system which we will use in our estimator is

$$\dot{\hat{\mathbf{x}}}_e = \hat{N}\hat{\mathbf{x}}_e - \hat{Z}\dot{\hat{\boldsymbol{\phi}}} - \hat{\boldsymbol{\psi}}, 
\dot{\hat{\mathbf{y}}}_e = \hat{C}_2\hat{\mathbf{x}}_e, 
\hat{\boldsymbol{\psi}} = \hat{L}\Delta\hat{\mathbf{y}} \triangleq \hat{\mathbf{L}}(\hat{\mathbf{y}}_h - \hat{\mathbf{y}}_e).$$
(10)

Note that the (unknown) effects of the disturbances  $\hat{\mathbf{w}}$  are not included in the estimator model. The estimator feedback rule  $\hat{\boldsymbol{\psi}} = \hat{\mathsf{L}}\Delta\hat{\mathbf{y}}$  minimizing the expected value of the  $L^2$ -norm of the estimation error is given by

$$\hat{\mathsf{L}} = -\frac{1}{\alpha^2} \, \hat{Y} \, \hat{C}_2^*, \qquad \text{where} \qquad \hat{Y} = \mathrm{Ric} \begin{pmatrix} \hat{N}^* & -\frac{1}{\alpha^2} \, \hat{C}_2^* \, \hat{C}_2 \\ -\hat{B}_1 \, \hat{B}_1^* & -\hat{N} \end{pmatrix},$$

in accordance with standard Kalman filter theory. Note that  $\alpha^2$ , which models the assumed quality of the measurements, is used as an adjustable parameter to scale the estimator feedback. Note that the estimator feedback rule  $\hat{\psi} = \hat{\mathsf{L}} \Delta \hat{\mathbf{y}}$  decomposes according to

$$\begin{pmatrix} \hat{\psi}_{\hat{\mathbf{v}}_e} \\ \hat{\psi}_{\hat{\boldsymbol{\omega}}_e} \end{pmatrix} = \begin{pmatrix} \hat{\mathsf{L}}_{\hat{\mathbf{v}}_e,+1} & \mathsf{L}_{\hat{\mathbf{v}}_e,-1} \\ \hat{\mathsf{L}}_{\hat{\boldsymbol{\omega}}_e,+1} & \mathsf{L}_{\hat{\boldsymbol{\omega}}_e,-1} \end{pmatrix} \begin{pmatrix} \Delta \hat{y}(+1) \\ \Delta \hat{y}(-1) \end{pmatrix}.$$

Unlike the control feedback  $\hat{K}$ , the estimator feedback  $\hat{L}$  represents the estimator model forcing per unit length in the y direction. Thus, simple interpolation of the discrete quantity  $\hat{L}$  is sufficient to determine a continuous weighting function  $\hat{L}$  by which a continuous analog of the discrete estimator (10) may be forced via feedback of the form

$$\hat{\psi}_{\hat{v}_e}(y) = \hat{L}_{\hat{v}_e,+1}(y)\Delta\hat{y}(+1) + \hat{L}_{\hat{v}_e,-1}(y)\Delta\hat{y}(-1)] 
\hat{\psi}_{\hat{\omega}_e}(y) = \hat{L}_{\hat{\omega}_e,+1}(y)\Delta\hat{y}(+1) + \hat{L}_{\hat{\omega}_e,-1}(y)\Delta\hat{y}(-1)].$$
(11)

The Kalman filter problem described above has been derived for each wavenumber pair  $\{k_x, k_z\}$  independently. The inverse Fourier transform of the Fourier-space estimator feedback rule (11) is given by the following convolution sums in physical space:

$$\psi_{v_e}(x, y, z, t) = \int [L_{v_e, +1}(x - \bar{x}, y, z - \bar{z}) \Delta y(\bar{x}, +1, \bar{z}, t) + L_{v_e, -1}(x - \bar{x}, y, z - \bar{z}) \Delta y(\bar{x}, -1, \bar{z}, t)] d\bar{x} d\bar{z}$$

$$\psi_{\omega_e}(x, y, z, t) = \int [L_{\omega_e, +1}(x - \bar{x}, y, z - \bar{z}) \Delta y(\bar{x}, +1, \bar{z}, t) + L_{\omega_e, -1}(x - \bar{x}, y, z - \bar{z}) \Delta y(\bar{x}, -1, \bar{z}, t)] d\bar{x} d\bar{z}$$

where  $L_{v_e,\pm 1}(x,y,z)$  and  $L_{\omega_e,\pm 1}(x,y,z)$  are the inverse Fourier transforms of  $\hat{L}_{\hat{\nu}_e,\pm 1}(k_x,y,k_z)$  and  $\hat{L}_{\hat{\omega}_e,\pm 1}(k_x,y,k_z)$  respectively. The structure of L represents the forcing of the model equation in the estimator as a function of a measurement error at a single point. Using  $\Delta y(\bar{x},-1,\bar{z})=\Delta y_o\delta(\bar{x})\delta(\bar{z})$  in the convolution integral results in  $\psi_{v_e}(x,y,z)=L_{v_e,-1}(x,y,z)\cdot\Delta y_o$  and  $\psi_{\omega_e}(x,y,z)=L_{\omega_e,-1}(x,y,z)\cdot\Delta y_o$ , which facilitates this interpretation. Typical kernels are shown in Figures 4 and 5.

The LQG compensator for boundary control of transition via feedback of wall skin-friction measurements is constructed by combining the full-state LQR feedback of §2.3 with the Kalman filter of §2.4 in the standard fashion. The fact that the usual separation rule of LQG applies in the present case may be seen immediately in the physical-space representation of the present problem (*i.e.*, the system shown in Figure 1, governed by the linearized spatially periodic Navier-Stokes equation, together with the quadratic objective function (3)). This problem is a completely standard LQG problem to which the separation principle applies directly, though numerical discretizations of this control problem have such high dimension that they are computationally intractable. Thus,

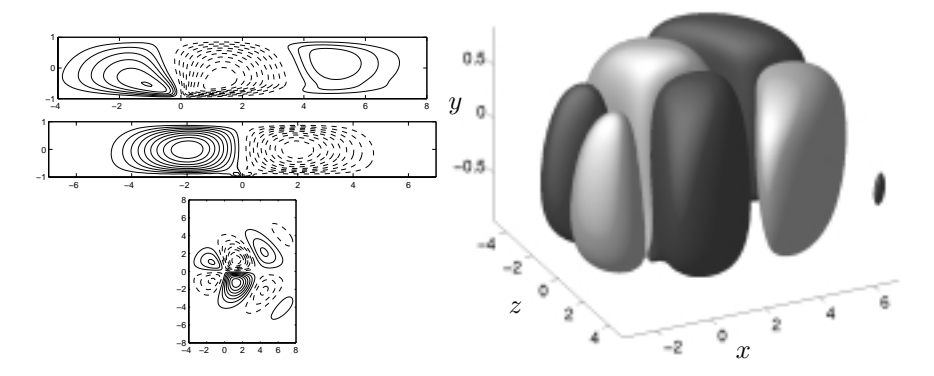


FIGURE 4. Estimation gain  $L_{v_e,-1}$  relating the wall measurement  $\Delta y(x=0,y=-1,z=0)$  to the forcing term  $\psi_{v_e}$  inside the domain. Contours in an xy plane at z=0.45 (top), a zy plane at x=0 (middle), and an xz plane at y=-0.56 (bottom) are shown on the left, and two isosurfaces of the convolution kernel are shown on the right. Gains computed with  $\alpha=100$ ,  $\hat{G}_1=C_1/|C_1|$ ,  $(\alpha^{-1}\hat{G}_2)=I$ , and a mean flow profile of  $U(y)=1-y^2$  at  $Re_c=2000$  for a  $8\pi \times 2 \times 6\pi$  box at a resolution of  $170 \times 70 \times 84$  modes.

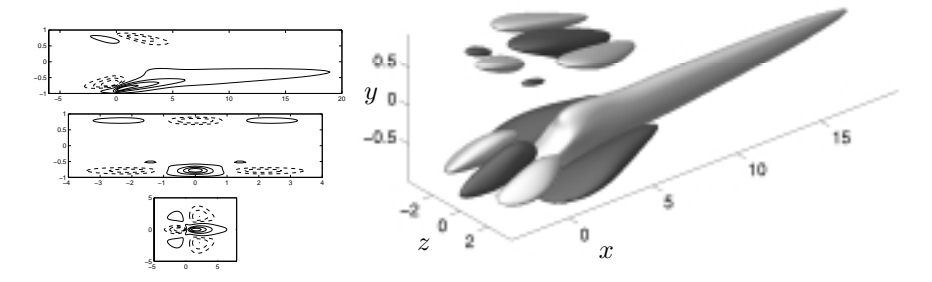


FIGURE 5. Estimation gain  $L_{\omega_e,-1}$  relating the wall measurement  $\Delta y(x=0,y=-1,z=0)$  to the forcing term  $\psi_{\omega_e}$  inside the domain. Contours in an xy plane at z=0 (top), a zy plane at x=1.47 (middle), and an xz plane at y=-0.76 (bottom) are shown on the left, and two isosurfaces of the convolution kernel are shown on the right. Note that the aspect ratio of the xy contour plot is scaled to better reveal its structure.

in this work, the decoupled control and estimation problems are transformed to Fourier space and solved there, where further decoupling (of each Fourier mode) may be leveraged. Finally, the resulting feedback gains are transformed back to physical space for further analysis and implementation.

## 2.5. Spatial localization of convolution kernels

As shown in Figures 2 through 5, the feedback convolution kernels for both the control and estimation problems, as derived above, are spatially localized. The

kernels so computed are independent of the box size in which they were computed, so long as the computational box is sufficiently large. Further, the feedback gains in the present work are well behaved at high spatial wavenumbers; the physical-space convolution kernels are well resolved on a computational grid which is appropriate for the simulation of the physical system of interest. As the feedback convolution kernels have localized spatial support, they can be truncated with a prescribed degree of accuracy at a finite distance from each sensor and actuator, arriving at spatially compact feedback rules that can be computed and applied in a decentralized fashion on arbitrarily large arrays of sensors and actuators, as discussed further in §5.

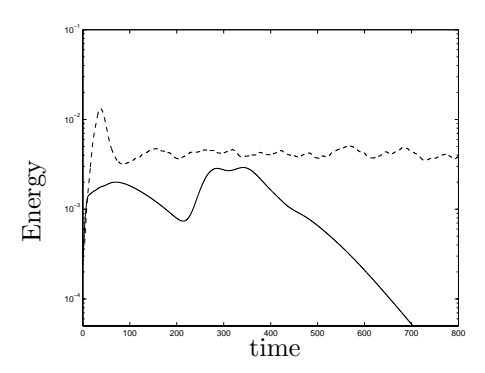
Note that the control convolution kernels angle away from the wall in the upstream direction. Coupled with the mean flow profile indicated in Figure 1, this accounts for the convective delay required to anticipate flow perturbations on the interior of the domain with actuation at the wall somewhere downstream. The estimation gains, on the other hand, extend well *downstream* of the measurement point, accounting for the convective delay between the motion of flow structures on the interior of the domain and their eventual influence on the drag profile on the wall; during this time delay, the flow structures responsible for these motions convect downstream. For space considerations, further analysis of these kernels in a fluid-mechanical context will be deferred to a future paper (Högberg, Bewley, & Henningson 2001).

#### 3. State feedback control of transition

Direct numerical simulations of the nonlinear Navier–Stokes equation (using the code benchmarked by Bewley, Moin, & Temam 2001) were first used to confirm the results from linear analysis, showing good agreement in terms of the reduction of the maximum transient energy growth for infinitesimal initial perturbations in the controlled linear system. For the "random" and "oblique-wave" initial conditions of particular physical significance enumerated by Reddy et al. (1998), hereafter referred to as RSBH98, at perturbation energy densities well above the transition thresholds reported by RSBH98, the controller prevents transition and brings the flow back to the laminar state, as shown in Figure 6. The simulations reported here have been performed at  $Re_c = 2000$  subject to the following:

- a. The perturbation energy density of the initial conditions in the "oblique-wave" perturbation case is  $2.4 \cdot 10^{-4}$  plus 1% in random noise, which is  $102 \times$  the threshold value reported by RSBH98 which leads to transition in the uncontrolled flow for initial perturbations of this structure.
- b. The perturbation energy density of the initial conditions in the "random" perturbation case is  $5 \cdot 10^{-4}$ , which is  $7 \times$  the threshold value reported by RSBH98 which leads to transition in the uncontrolled flow for initial perturbations of this structure.

The box size used is  $2\pi \times 2 \times 2\pi$  with sufficient resolution – the same as that used to compute the transition thresholds by RSBH98 – to resolve the flows



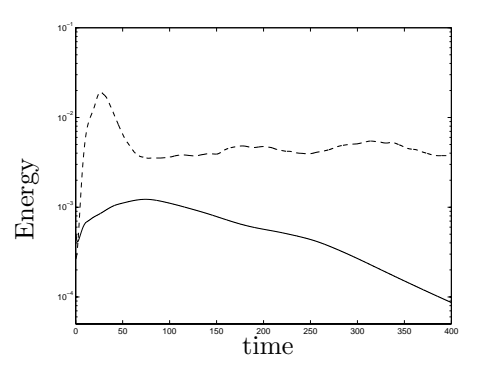


FIGURE 6. Evolution of oblique waves (left) and an initially random flow perturbation (right) added to a laminar flow at  $Re_c=2000$ , with and without decentralized linear control feedback. The magnitude of the initial flow perturbations in these simulations greatly exceed the thresholds reported by Reddy et al. (1998) that lead to transition to turbulence in an uncontrolled flow (by a factor of 102 for the oblique waves and by a factor of 7 for the random initial perturbation). Solid lines indicate the energy evolution in the controlled case, dashed lines indicate the energy evolution in the uncontrolled case. Both of the uncontrolled systems lead quickly to transition to turbulence whereas both of the controlled systems relaminarize. For the controlled cases, initial perturbations with greater energy fail to relaminarize, whereas initial perturbations with less energy relaminarize earlier.

under consideration. In the uncontrolled simulations with initial perturbations at these relatively high perturbation energy densities, system non-normality quickly leads to energetic flow perturbations and transition to turbulence, whereas in the controlled simulations the flows are driven back to the laminar state.

# 4. State feedback control of turbulence

When designing controllers based on the linearized equation (1), it is necessary to select a base flow profile U(y) about which to linearize the equations. However, during both the latter stages of transition and the relaminarization of a fully turbulent flow, there is a significant evolution of the mean flow profile. Using information about the instantaneous mean-flow profile  $\bar{u}(y)$  (averaged in x and z only) to tune the controller gains via a gain scheduling approach is thus warranted. By choosing a set of suitable test profiles  $U_i(y)$  covering the range between the laminar and turbulent flows (Figure 7), and computing the corresponding feedback convolution kernels for each such profile, we can select the gains that most closely correspond to those appropriate for the particular mean flow profile  $\bar{u}(y)$  at each instant.

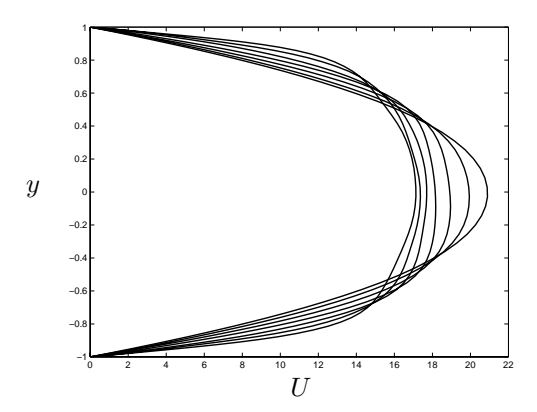


FIGURE 7. Test profiles  $U_i(y)$  used for the scheduling of the gains, computed via a constant-mass-flux 1D flow simulation of a fully-developed turbulent mean flow profile relaxing to the parabolic laminar flow profile.

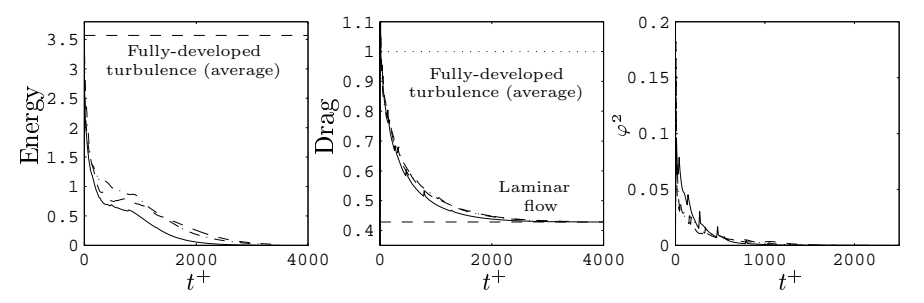


FIGURE 8. Evolution of initially fully-developed turbulence at  $Re_{\tau}=100$  with three different controller realizations. Left: energy of flow perturbation. Center: drag. Right: mean-square value of the control  $\phi$ . Note that application of the gain-scheduled linear feedback causes the fully turbulent 3D flows to relaminarize in all three cases.

The gains were scheduled in the present work simply by selecting at each timestep those gains which were computed from the mean profile  $U_i(y)$  in Figure 7 which most closely matched (in the  $L^2$  sense) the instantaneous mean flow profile  $\bar{u}(y)$  in the simulation. More sophisticated scheduling approaches were also investigated, such as performing a least-squares fit of the instantaneous mean flow profile with the test profiles, and then using the coefficients of this fit to perform a weighted linear combination of the feedback gains determined for each test profile. The performance obtained with this more sophisticated approach was comparable with the simpler approach of simply selecting the precomputed feedback gains computed from the nearest mean flow profile.

The same DNS code as that used in §3 was then used to test the linear control feedback applied to a turbulent flow at  $Re_{\tau} = 100$ , using the gain scheduling approach described above. As shown in Figure 8, this resulted in relaminarization of the turbulent flow. The DNS code, resolution, and initial conditions used in this test were those benchmarked by Bewley, Moin, & Temam (2000).

It is notable that fixed feedback gains, computed either for the laminar profile or for the uncontrolled mean turbulent profile, were much less effective than the gain scheduling approach described above, and failed to relaminarize the flow, achieving at best 15% drag reduction. Thus, adjusting the linear feedback gains to compensate for the evolving mean flow profile is identified to be a crucial step in the successful application of the linear compensators computed herein to the fully nonlinear problem of turbulent channel flow.

#### 5. Discussion

# 5.1. Localized kernels naturally relax nonphysical assumptions

Transition phenomena in physical systems, such as boundary layers and plane channels, are not spatially periodic, though it is often useful to characterize the response of such systems with Fourier modes. Application of Fourier-space controllers which assume spatial periodicity in their formulation to physical systems which are not spatially periodic, as proposed by Cortelezzi & Speyer (1998), will be corrupted by Gibbs phenomenon, the well-known effect in which a Fourier transform is spoiled across all frequencies when the data one is transforming is not itself spatially periodic. In order to correct for this phenomenon in formulations which are based on Fourier-space computations of the control, windowing functions such as the Hanning window are appropriate. Windowing functions filter the measured signals such that they are driven to zero near the edges of the physical domain under consideration, thus artificially imposing spatial periodicity on the non-spatially periodic measurement vector. In essence, such windowing functions impose a degree of spatial localization (of a width equal to some fraction of the full width of the spatial domain under consideration) on control feedback rules which are not themselves naturally spatially localized.

As noted previously, the spatially localized (once truncated, spatially compact) convolution kernels computed in the present work are independent of the box size in which they were computed, so long as this computational box is sufficiently large. The feedback kernels computed here for finite, spatially periodic computational domains are unchanged when the size of the computational box in which these kernels were determined is increased. Thus, the box size may (hypothetically) be extended to infinity in the x and z directions. Such an extension models the physical situation of spatially-evolving flow perturbations in a spatially invariant geometry and mean flow. Spatial localization of the kernels thus relaxes the nonphysical assumption of spatial periodicity

of the computational domain used in the their derivation, and facilitates implementation of these kernels in physical systems with spatially evolving flow perturbations.

# 5.2. Localized kernels facilitate decentralized control

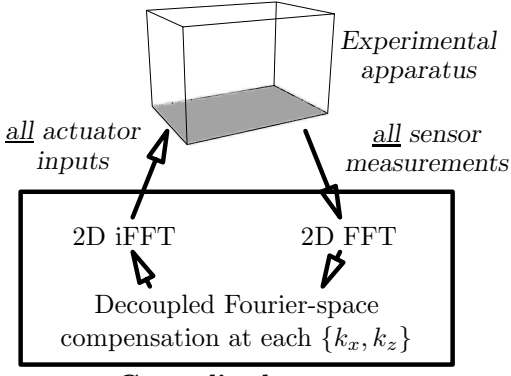
Though the windowing approach suggested above somewhat alleviates the corruption due to Gibbs phenomenon in the application of Fourier-space feedback control to non-spatially periodic systems, application of such control strategies (via on-line FFTs of the complete measurement vector and inverse FFTs of the complete control vector) still require centralized computations. For massive arrays of sensors and actuators in distributed spatially-invariant systems, it is highly desirable to localize the computation of the estimator feedback to functions of nearby measurements only, and to localize the computation of the control feedback to functions of nearby state variables only, rather than requiring centralized coordination of the entire system. Physical-space convolution kernels with compact spatial support lend themselves naturally to decentralized control. Fourier-space feedback computations, which require on-line FFTs and inverse FFTs, do not.

Figures 9 and 10 illustrate the important distinction between the centralized and decentralized methods of implementing control strategies for the distributed flow system. The main bottleneck suffered by the centralized approach when extended to a massive array of sensors and actuators is the communication of the signals to and from the centralized signal processing equipment. The decentralized approach does not suffer from this bottleneck.

In the decentralized approach, several MEMS tiles are fabricated, each with sensors, actuators, and an identical logic circuit (for a review of MEMS fabrication issues, see Ho & Tai 1998). The computations on each tile are limited in spatial extent, with the individual logic circuit on each tile responsible for the (physical-space) computation of the state estimate only in the volume immediately above that tile. Each tile communicates its local measurements and state estimates with its immediate neighbors, with the number of tiles over which such information propagates in each direction depending on the tile size and spatial extent of the truncated convolution kernels. By replication, we can extend such an approach to arbitrarily large arrays of sensors and actuators. Though additional truncation of the kernels will disrupt the effectiveness of this control strategy near the edges of the array, such edge effects are limited to the edges in this case (unlike Gibbs phenomenon), and should become insignificant as the array size is increased.

#### 5.3. Conclusions

Spatially-compact convolution kernels for the decentralized feedback control and estimation of transitional flows have been determined. These kernels have been found via inverse Fourier transformation and truncation of a set



# Centralized computer coordinating entire system

FIGURE 9. Centralized approach to the control of plane channel flow in Fourier space.

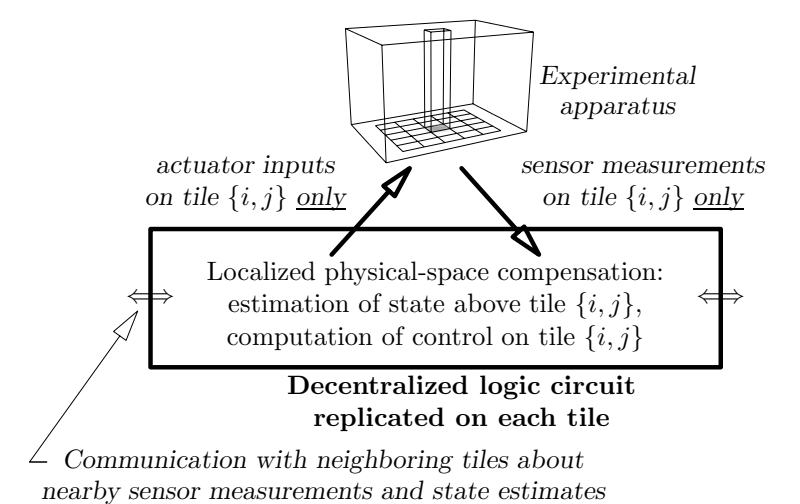


FIGURE 10. Decentralized approach to the control of plane channel flow in physical space.

of optimal control and estimation feedback matrices determined for the Orr-Sommerfeld/Squire system on an array of wavenumber pairs  $\{k_x,k_z\}$ . The full-state feedback control kernels have been shown to effectively prevent transition in 3D direct numerical simulations of the nonlinear Navier-Stokes equation at  $Re_c=2000$  for initial conditions which rapidly lead to transition to turbulence when feedback control is not applied. Using a novel gain scheduling approach, the full-state feedback control kernels have also been shown to effectively subdue perturbations in a fully turbulent 3D channel flow at  $Re_\tau=100$ , completely relaminarizing the turbulent flow.

The importance of the spatial localization (or, upon truncation, the spatial compactness) of the present kernels can not be over-emphasized. This is the critical link which connects feedback controllers designed for artificial, spatially-periodic model systems to implementation-ready feedback strategies appropriate for the decentralized control of physical systems with spatially-evolving flow perturbations via tiled arrays of MEMS devices.

The derivation of control and estimation schemes utilizing more practical actuation and measurement strategies should follow from this work as a straightforward extension. It is hoped that this research, in addition to providing direct information about how the processes of transition and turbulence may be effectively estimated and controlled, will also provide indirect evidence about the fundamental nature of these physical phenomenon by identifying the fluid motions targeted by effective control strategies. Analysis of the structure of the resulting convolution kernels should provide a powerful new method of analysis of these classical but only partially understood problems in fluid mechanics.

### Acknowledgments

The authors thank Bassam Bamieh, Dan Henningson, and Scott Miller for useful discussions related to this work, and Satish Reddy for providing the initial conditions for the transition simulations.

#### References

- Bamieh, B., Paganini, F., & Dahleh, M. 2000 Distributed Control of Spatially-Invariant Systems. *IEEE Trans. Auto. Control*, to appear.
- Bamieh, B., & Dahleh, M. 2000 Energy amplification in channel flows with stochastic excitation. *Phys. Fluids*, submitted.
- Bewley, T.R. 1999 Linear control and estimation of nonlinear chaotic convection: harnessing the butterfly effect. *Phys. Fluids* **11**, 1169-1186.
- Bewley, T.R. 2001 Flow control: new challenges for a new Renaissance  $Progress\ in$   $Aerospace\ Sciences\ 37,\ 21-58.$
- Bewley, T.R., & Agarwal, R. 1996 Optimal and robust control of transition. Center for Turbulence Research, Proceedings of the summer program 1996, 405–432.
- Bewley, T.R., & Liu, S. 1998 Optimal and robust control and estimation of linear paths to transition. *J. Fluid Mech.* **365**, 305-349.
- Bewley, T.R., Moin, P., & Temam, R. 2001 DNS-based predictive control of turbulence: an optimal benchmark for feedback algorithms. *J. Fluid Mech.* 477, 179–225.
- Berlin, S., Wiegel, M., & Henningson, D.S. 1999 Numerical and experimental investigations of oblique boundary layer transition. *J. Fluid Mech.*, **393**, 23-57.
- Butler, K.M., & Farrell, B.F. 1992 Three-dimensional optimal perturbations in viscous shear flows. *Phys. Fluids* A **4**, 1637-1650.

- CHOI, H., MOIN, P., & KIM, J. 1994 Active turbulence control for drag reduction in wall-bounded flows. J. Fluid Mech. 262, 75-110.
- CORTELEZZI, L., & SPEYER, J.L. 1998 Robust reduced-order controller of laminar boundary layer transitions. *Physical Review* E **58**, 1906-1910.
- CORTELEZZI, L., LEE, K.H., KIM, J., & SPEYER, J.L. Skin-friction drag reduction via robust reduced-order linear feedback control. *Int. J. Comp. Fluid Dyn.* 11, 79-95.
- Farrell, B.F., & Ioannou, P.J. 1993 Stochastic forcing of the linearized Navier–Stokes equation. *Phys. Fluids* A **5**, 2600-2609.
- FARRELL, B.F., & IOANNOU, P.J. 1996 Turbulence suppression by active control *Phys. Fluids* A **8** (5), 1257–1268.
- Gustavsson, L.H. 1991 Energy growth of three-dimensional disturbances in plane Poiseuille flow. *J. Fluid Mech.*, **224**, 241-260.
- Ho, C.-M., & Tai, Y.-C. 1998 Micro-electro-mechanical systems (MEMS) and fluid flows Ann. Rev. Fluid Mech. 30, 579-612.
- HUANG, W., & SLOAN, D.M. 1993 The pseudo-spectral method for solving differential eigenvalue problems. J. Comput. Phys. 111, 399-409.
- HÖGBERG, M., BEWLEY, T.R., & HENNINGSON, D. S. 2001 Decentralized feedback control and estimation of transition in plane channel flow. Submitted to J. Fluid Mech.
- JIMENEZ, J. 1999 The physics of wall turbulence. Physica A 263, 252-262.
- JOSHI, S.S., SPEYER, J.L., & KIM, J. 1997 A systems theory approach to the feedback stabilization of infinitesimal and finite-amplitude disturbances in plane Poiseuille flow. J. Fluid Mech. 332, 157-184.
- Kim, J., & Lim, J. 2000 A linear process in wall-bounded turbulent shear flows. *Phys. Fluids* **12** (8), 1885-1888
- LAUB, A.J. 1991 Invariant subspace methods for the numerical solution of Riccati equations. In *The Riccati Equation* (ed. Bittaini, Laub, & Willems) 163-196. Springer.
- LEE, C., KIM, J., BABCOCK, D., & GOODMAN, R. 1997 Application of neural network to turbulence control for drag reduction. *Phys. Fluids*, **9**, 1740-7.
- REDDY, S.C., & HENNINGSON, D.S. 1993 Energy growth in viscous channel flows. J. Fluid Mech. **252**, 209-238.
- REDDY, S.C., SCHMID, P.J., BAGGETT, J.S., & HENNINGSON, D.S. 1998 On stability of streamwise streaks and transition thresholds in plane channel flows. *J. Fluid Mech.* **365**, 269-303.
- Schmid, P.J., & Henningson, D.S. 2001 Stability and transition in shear flows. Springer.
- Trefethen, L.N., Trefethen, A.E., Reddy, S.C., & Driscoll, T.A. 1993 Hydrodynamic stability without eigenvalues *Science* **261**, 578-584.
- Weideman, J.A.C., & Reddy S.C. 1999 A Matlab Differentiation Matrix Suite. ACM Transactions of Mathematical Software 26 (4), 465–519.

Paper 4

4

# Decentralized feedback control and estimation of transition in plane channel flow

By Markus Högberg\*, Thomas R. Bewley $^{\ddagger}$  and Dan S. Henningson\*, $^{\dagger}$ 

Modern linear control theory has recently been established as a viable tool for developing effective, spatially localized convolution kernels for feedback control and estimation of linearized Navier-Stokes systems. In the present work, the localized kernels computed with this approach are shown to eventually decay exponentially with distance, facilitating physical-space truncation and implementation in a decentralized setting. It is demonstrated that such truncation to spatially compact kernels with finite support does not significantly degrade the effectiveness of this approach.

The effectiveness of these kernels for significantly expanding the domain of stability of the nonlinear channel flow system is quantified using direct numerical simulations. This quantification is done in terms of transition thresholds which is proposed as a relevant performance measure for transition control schemes. Initial flow perturbations with streamwise vortices, oblique waves, and random excitations over an array of several Fourier modes are considered over a range of Reynolds numbers ( $Re_{cl}=2000,\,3000,\,$  and 5000). It is shown that the minimum amplitude of these initial flow perturbations which is sufficient to excite nonlinear instability, and thereby promote transition to turbulence, is significantly increased by application of the localized linear control.

Exponential convergence of a decentralized physical-space state estimator with wall measurements is demonstrated. In addition we combine the estimator and the full-state feedback controller to obtain a wall-information-based linear compensator. The compensator performance is also quantified, and key issues related to improving the performance of this compensator, which is degraded as compared with the full-state feedback controller, are discussed.

<sup>\*</sup>Department of Mechanics, Royal Institute of Technology (KTH), SE-100 44 Stockholm, Sweden

 $<sup>^\</sup>dagger \text{The Swedish Defence Research Agency ( FOI ), Aeronautics Division, SE-172 90 Stockholm, Sweden$ 

 $<sup>^{\</sup>ddagger}$  Dynamic Systems & Control Group, Dept. of MAE, UC San Diego, La Jolla, CA 92093,USA

#### 1. Introduction

### 1.1. Stability and transition in shear flows

The process of laminar-turbulent transition is of importance in many engineering applications as well as an active research area within the field of fundamental flow physics. Laminar flows typically exhibit much less drag, mixing, and heat transfer than their turbulent counterparts, and are often more prone to separate in the presence of an adverse pressure gradient. Understanding the process of laminar-turbulent transition is therefore a key issue when prediction and control of drag, mixing, heat transfer, and/or separation is of interest, and effective strategies both to delay and to accelerate the transition process are needed.

The transition process most often starts with the growth of small disturbances on a laminar base flow. It can therefore be characterized, at least in its initial stages, by solutions of the linearized Navier-Stokes equation.

Traditionally, such solutions have been characterized in terms of the exponential growth or decay rates of its individual eigenmodes. In particular, for boundary-layer and channel flows, the Fourier-transformed linearized Navier-Stokes equations may easily be manipulated into the Orr-Sommerfeld and Squire equations. The least stable eigenmodes of this system of equations vary in the streamwise direction only, and are referred to as Tollmien-Schlichting (TS) waves. For laminar base flows without inflection points, these waves are two-dimensional and grow on a viscous time scale. In the past, the Reynolds number at which one of these waves becomes linearly unstable, the so-called critical Reynolds number, has been a key feature. The calculation of exponential growth rates and critical Reynolds numbers for a wide variety of flows has been the object of numerous efforts by researchers investigating flow stability over the last century; key results are compiled in Drazin & Reid (1981). One common path to transition is the exponential growth of two-dimensional TSwaves, followed by a secondary instability of these finite-amplitude waves to small-amplitude three-dimensional disturbances and the rapid evolution of the flow towards a fully turbulent state (see, e.g., Herbert (1988)).

In many shear flows, disturbance growth ensues and transition takes place well below the critical Reynolds number predicted by linear theory. During the last decade, several researchers have investigated the mechanisms responsible for such subcritical transition. It has been shown that the key feature responsible is the non-orthogonality of the eigenmodes of the Orr–Sommerfeld/Squire operator (Butler & Farrell (1992); Reddy & Henningson (1993); Henningson & Reddy (1994)). The subcritical growth in the solution to the linearized equations is associated with a superposition of non-orthogonal, decaying modes; as the individual decay rates of the several superposed modes are different, destructive interference of the various modes can decrease as time evolves, leading to the possibility for transient energy growth which is sometimes quite

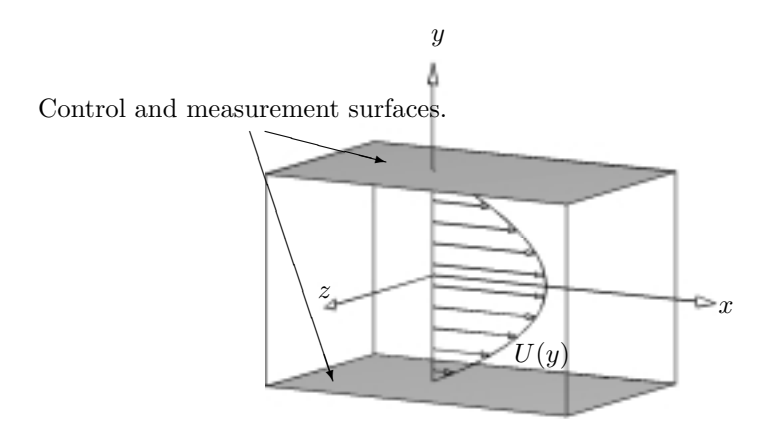


FIGURE 1. Geometry of flow domain and coordinate system used.

large. Such "non-modal growth" is often easily excited by external disturbances (Trefethen et al. (1993)). The disturbances that grow the most, which we label as "worst-case" disturbances, are disturbances which vary in the spanwise direction only, initially appearing as streamwise vortices and eventually evolving into streamwise streaks. These disturbances are fundamentally different than Tollmien-Schlichting waves, which vary in the streamwise direction only. Worst-case disturbances, sometimes labeled "optimal" disturbances (depending on one's viewpoint), were, for boundary layer and channel flows, first calculated by Butler & Farrell (1992). Several transition scenarios initiated by disturbances experiencing non-modal growth have been investigated; for a recent review of subcritical transition scenarios, see Schmid & Henningson (2001). In the present paper, we will discuss the application of modern flow control techniques to the problem of subcritical transition in plane channel flow; to set the stage, we first describe in greater detail some relevant background on the subcritical transition process.

# 1.2. Canonical subcritical transition problem: plane channel flow

Small perturbations  $\{u, v, w\}$  to a laminar flow U(y) in a channel (Figure 1) are governed by the Orr-Sommerfeld/Squire equations. These equations are derived from the Fourier transform (in the x and z directions) of the Navier-Stokes equation linearized about a mean flow profile U(y), and may be written at each wavenumber pair  $\{k_x, k_z\}$  as

$$\hat{\Delta} \dot{\hat{v}} = \{ -i k_x U \hat{\Delta} + i k_x U'' + \hat{\Delta} (\hat{\Delta} / Re_{cl}) \} \hat{v}$$
(1a)

$$\dot{\hat{\omega}} = \{-i \, k_z \, U'\} \, \hat{v} + \{-i \, k_x \, U + \hat{\Delta}/Re_{cl}\} \, \hat{\omega},$$
 (1b)

where  $\hat{\omega}$  is the wall-normal vorticity,  $\hat{\Delta} \equiv \partial^2/\partial y^2 - k_x^2 - k_z^2$ , hats (^) denote Fourier coefficients, and primes (') denote wall-normal derivatives. The Reynolds number  $Re_{cl} = U_c h/\nu$  parameterizes the problem, where h is the

half-width of the channel,  $U_c$  is the centerline velocity, and  $\nu$  is the kinematic viscosity of the fluid. Without loss of generality, we assume the walls are located at  $y = \pm 1$ .

Assuming modes with exponential time dependence, the above system becomes an eigenvalue problem with two distinct solution families. The first family of solutions contains the Orr–Sommerfeld modes, which involves eigensolutions of the equation for the wall-normal velocity. The least stable Orr–Sommerfeld mode is the Tollmien-Schlichting wave mentioned earlier. For the plane channel-flow problem under consideration here, there are no exponentially growing solutions for Reynolds numbers  $Re_{cl} < 5772$  (Orszag (1971)). The second family of solutions contains the Squire modes and have zero wall-normal velocity. It can be shown that the Squire modes are always stable.

Transition experiments show that plane channel flows typically undergo transition to turbulence at Reynolds numbers as low as  $Re_{cl} = 1000$  (Patel & Head (1969); Carlson, Widnall & Peeters (1982)). The discrepancy between the critical Reynolds number for linear instability and the Reynolds number at which transition is actually observed is a direct consequence of the nonnormality of the Orr–Sommerfeld/Squire operator for the plane channel flow problem, as mentioned previously. As a result, there is a possibility for transient disturbance energy growth, which scales as  $O(Re_{cl}^2)$  and has a maximum magnitude of about a factor of 200 at  $Re_{cl} = 1000$  (Reddy & Henningson (1993)). In addition, there is an enhanced sensitivity of such a system to external disturbance forcing: the response of the output energy can be up to  $O(Re_{cl}^4)$  greater than the input disturbance energy (Trefethen et al. (1993)). This heightened system sensitivity is mainly associated with the evolution of streamwise vortices into streamwise streaks.

# 1.3. Characterizing nonlinear instability: transition thresholds

Two transition scenarios starting with disturbances experiencing non-modal growth have been investigated by Reddy et al. (1998), and involve the growth of primarily streamwise structures to finite amplitude followed by their subsequent secondary instability. These scenarios are initialized with a) a pair of superimposed oblique waves, and b) streamwise vortices with an antisymmetric v component across y=0, as illustrated in Figures 2a and b. Notice that 1%random noise is added to all transition scenarios tested in order to break the symmetries. Note also that the streamwise vortices with maximum transient growth actually have a v component which is symmetric across y = 0; however, similar transition scenarios starting with symmetric streamwise vortices have higher threshold energies for transition (Reddy et al. (1998)). The energy evolution in various wavenumber components of the flow are exemplified in Figures 3a and b for these transition scenarios. We see in Figure 3(a) that the oblique waves induce streamwise vortices that efficiently generate streamwise streaks. In Figure 3(b) the scenario is similar, but the streamwise vortices are introduced directly without the presence of the oblique waves. The streamwise

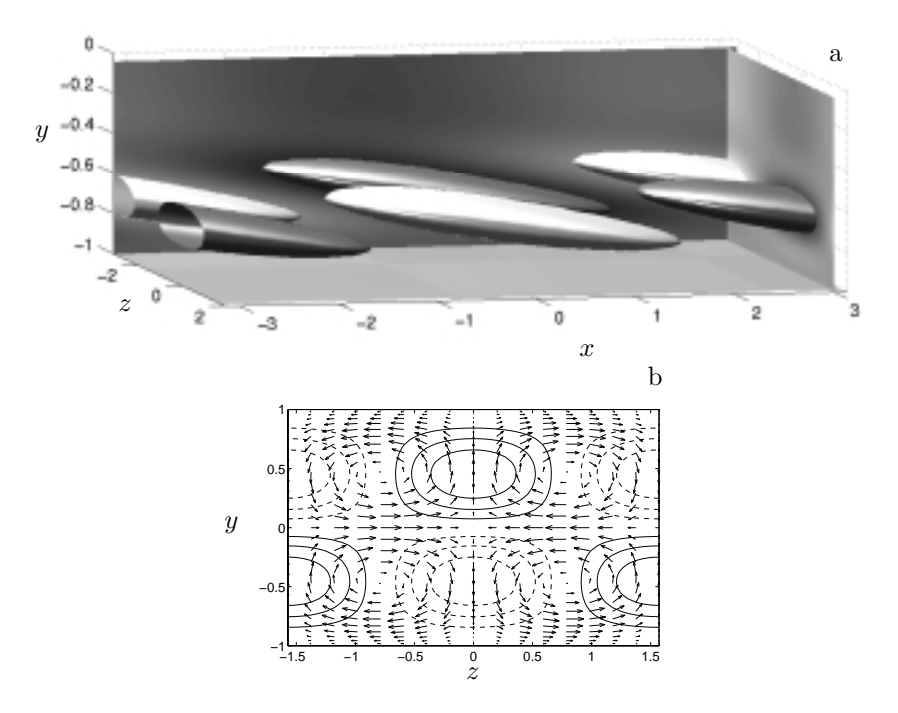


FIGURE 2. Velocity fields for initial conditions: a) Oblique waves showing isosurfaces at half the maximum value of the normal velocity (light) and at half the minimum value (dark). The slices show the distribution of normal velocity where light is positive and dark is negative. b) Streamwise vortices showing contours of v, solid contours for positive velocity and dashed for negative, and velocity vectors of v, w in a z-y plane at x=0.

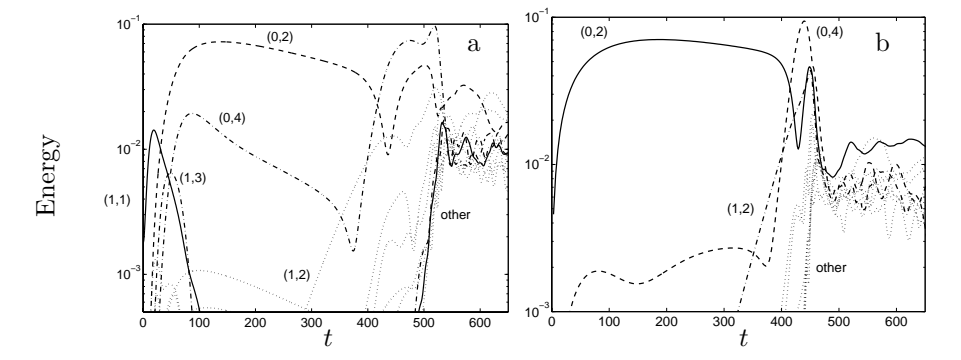


FIGURE 3. Energy evolution in different  $(k_x, k_z)$  modes for a) the oblique wave transition scenario b) the streamwise vortex transition scenario.

streaks grow to finite amplitudes and eventually secondary instabilities cause the breakdown to turbulence.

To quantify the transition process, Reddy et al. (1998) defined a transition time and determined the dependence of this time with respect to the energy of the initial perturbation. The transition time T is given as the time by which the friction coefficient  $c_f$  reaches its mean value, i.e.

$$c_f(T) = \frac{1}{2} (c_{f \max} + c_{f \min}).$$

If the turbulent state is never reached, we define T to be infinite. The lowest perturbation energy density resulting in a finite value of T is defined to be the transition threshold for that perturbation.

Figure 4 shows the threshold energy for transition in plane Poiseuille flow for the two scenarios described above as well as for Tollmien-Schlichting waves and "random" perturbations introduced into the lowest wavenumbers of the flow. The symbols represent results from direct numerical simulations, and the lines represent a least-squares fit to the data points. For Reynolds numbers below the data points, the flow relaminarizes, and for Reynolds numbers above the data points, the flow becomes turbulent. As is evident in the figure, the transition scenario based on Tollmien-Schlichting waves requires a much larger initial energy density to result in the onset of turbulence than the three other transition scenarios. Such transition thresholds can be viewed as indicators of how sensitive the nonlinear evolution of the flow is to different initial flow perturbations, and therefore provide an excellent means of quantifying the nonlinear performance of a transition control strategy. In this paper, we will develop and test full-state-feedback controllers as well as wall-informationbased compensators in order to stabilize the nonlinear flow system. We will quantify the effectiveness of these control strategies in terms of how well they can increase these transition thresholds.

## 1.4. Flow control background

Using linear control theory for controlling flow instabilities is a fairly new concept. Early work on controlling instabilities in laminar flows has been mostly devoted to using the wave superposition principle for anti-phase modal suppression. The paper by Thomas (1990) reviews the early efforts on the control of Tollmien-Schlichting (TS) waves using an anti-phase control strategy. A brief review is given also by Metcalfe (1994). Other reviews on flow control can be found in e.g. Moin & Bewley (1994), Gad-el-Hak (1996), Lumley & Blossey (1998) and Bewley (2001). Here we briefly review earlier work related to the present paper.

Much of the focus of flow control has been on the problem of turbulence control and drag reduction. One of the most popular control strategies for numerical control of turbulence is *opposition* control introduced by Choi, Moin & Kim (1994). A detection plane for the velocity was introduced in the flow at a distance  $y^+ \approx 10$  from the walls in a channel. The detected velocity was

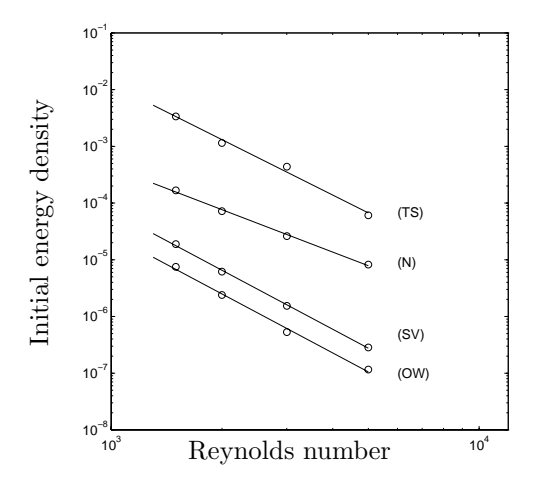


FIGURE 4. Transition threshold energy versus Reynolds number (based on centerline velocity and channel half-height) for plane Poiseuille flow. Shown are four curves obtained from direct numerical simulations starting with various initial conditions: optimal streamwise vortices, a pair of optimal oblique waves, Tollmien-Schlichting waves, and divergence-free lowwavenumber noise. Adapted from Reddy et al. (1998).

then phase shifted by 180° and applied as a boundary condition on the wall. With this method the drag in a turbulent channel was reduced by as much as 25% using the normal velocity and by 30% using the spanwise velocity. The control strategy was also evaluated by Farrell & Ioannou (1996) by application to a linear system, studying the linear dynamics of the closed loop system with opposition control finding that the variance of their parameterized turbulence could be reduced as much as by 70% near the wall.

The physical mechanism behind the success of opposition control is related to manipulation of near-wall streamwise vortices. An alternative way of treating the near wall vortices is used in Koumoutsakos (1999) resulting in a drag reduction of about 40% in a turbulent channel flow at  $Re_{\tau} = 180$ . This feedback control scheme only relies on measurements of the spanwise vorticity flux at the wall. Lee et al. (1997) used a neural network to find adaptively a feedback law for the local wall shear stress achieving about 20% drag reduction, also with a simple control scheme deduced from the results of the neural network.

Possible applications of gradient based optimal control techniques were identified and analyzed by Abergel & Temam (1990) and much of the current efforts on optimal flow control can be traced back to that particular paper. Choi et al. (1993) introduced the concept of suboptimal control and this methodology was applied to a turbulent channel flow at  $Re_{\tau} = 100$  by Bewley & Moin (1994) resulting in a 17% drag reduction. The suboptimal control of Lee, Kim & Choi (1998) also uses this idea to derive the optimal boundary conditions for minimizing a carefully designed objective function based on wall pressure fluctuations or wall shear stress, resulting in a skin friction drag reduction of up to 22%. Receding horizon optimization means that a large time interval is divided into smaller parts, and then the control is optimized over these parts successively. It is possible with this method to completely relaminarize the flow in a channel with turbulent initial conditions at  $Re_{\tau} = 100$ , and this has been done using direct numerical simulations (DNS) by Bewley, Moin, & Temam (2001) and using large eddy simulations (LES) by Collis *et al.* (2000).

In many applications turbulence can be avoided initially but eventually there is transition to turbulence. By trying to control the transition process the need for turbulence control can be avoided at least to some extent. Since energy growth in a fluid flow is a linear process it makes sense that linear equations could be used to control transition. Based on the findings reported by e.g. Henningson (1996); Farrell & Ioannou (1996); Kim & Lim (2000), the importance of linear mechanisms for sustaining turbulence, especially the coupling between normal velocity and vorticity, indicate that linear controllers could also be used to control turbulence. Using the linearized equations for flow control was investigated by Hu & Bau (1994), where they used proportional control based on wall shear measurements to stabilize a laminar plane channel flow through heating or cooling at the walls in order to change the viscosity of the flow. They also suggested that the influence of the applied control on the domain of attraction for the laminar flow should be quantified, and this is similar to what is attempted in the present work for more advanced controllers. In the paper by Joshi, Speyer, & Kim (1997), classical linear control theory is applied to stabilize the flow in a two dimensional channel using blowing and suction on the channel walls with measurements of wall shear. The control problem was formulated using a streamfunction approach suitable for two dimensional problems. Extension of this work using modern control theory and employing model reduction for the compensator is presented in Joshi, Speyer, & Kim (1999), and the corresponding multi wavenumber case is treated in Cortelezzi et al. (1998). In Lee et al. (2001) extension of the two dimensional controller to a three dimensional one by augmenting an ad hoc scheme in the third direction is suggested and tested in a turbulent flow. The streamfunction formulation was also used by Baramov, Tutty & Rogers (2000) to apply robust  $(\mathcal{H}_{\infty})$  control to the two dimensional fluid system with multi-wavenumber control, accounting for effects of localized actuation and sensing. A problem formulation for proper treatment of three dimensional perturbations is presented in Bewley & Liu (1998) and in Kang et al. (1999).

The present paper builds on the work by Bewley & Liu where both optimal  $(\mathcal{H}_2)$  and robust  $(\mathcal{H}_{\infty})$  control strategies were applied to isolated wavenumber pairs in a linearized channel flow with three-dimensional perturbations. The  $\mathcal{H}_2$  problem was extended, using a slightly modified formulation of the problem,

to handle multiple wavenumbers by Högberg & Bewley  $(2000^{a,b})$  resulting in a control law localized in physical space. It was shown that these controllers can, with a slightly modified objective function, be used in a simple gain scheduling scheme to relaminarize turbulence at  $Re_{\tau} = 100$  in a channel. Application of these linear controllers to instabilities in spatial boundary layer flows is performed in Högberg & Henningson (2001) for stationary as well as time varying perturbations in Blasius and Falkner–Skan–Cooke boundary layers.

In the current paper the ability of these linear controllers, without gain scheduling, to prevent transition in channel flow is investigated and quantified. Transition thresholds are proposed as a relevant performance measure that allows for qualitative comparisons of different control schemes in terms of how well they work in the presence of nonlinearities.

We also introduce a state estimator in the form of an extended Kalman filter that can be used to reconstruct the flow field from wall measurements with exponential convergence. The state estimator is combined with the controller, and the ability of the resulting compensator to prevent transition in channel flow is also quantified using the transition thresholds.

# 1.5. Outline of paper

The remainder of this paper is organized as follows. In section 2, the governing equations and the formulation of the control and estimation problem is reviewed. Properties of the resulting control and estimation kernels are discussed and a short description of the numerical methods used is given. In section 3, the results of the many simulations required to determine transition thresholds are presented for both the full-state-feedback and the wall-measurement-based feedback control strategies. An effort is also made to try to explain the action of the control and its response to certain perturbations. Section 4 contains a discussion of the results and also outlines possible extensions of the approach from the perspectives of both fluid mechanics and control theory.

# 2. Approach

The initial stages of transition are accurately described by the linearized Navier-Stokes equations. Straightforward manipulation of these equations results in the Orr-Sommerfeld/Squire equations for small perturbations to a mean flow. These equations can be transformed into Fourier space, where the equations for different wavenumber pairs completely decouple and can be treated separately, (equations (1a) and (1b)). Bewley & Liu (1998) suggested to compute optimal control rules and estimator feedback rules for each wavenumber pair separately in Fourier space, and then to combine them in an inverse Fourier transform, resulting in physical space convolution kernels describing the control and estimation feedback rules. It was predicted by Bamieh, Paganini, & Dahleh (2000) that such kernels should be spatially localized with exponentially decaying tails. Truncation results in truly compact kernels, relaxing the assumption of spatial periodicity imposed by utilizing the Fourier representation. In practice this enables the convolution kernels so computed to be used in physical, non-spatially-periodic flows. In section 2.3.2 it is demonstrated that the current approach indeed yields such localized kernels with exponential decay. The issue of controlling and estimating infinite dimensional systems based on a finite dimensional model is discussed in e.g. Ito & Morris (1998) where details on the mathematical properties of the Riccati equations are also presented.

# 2.1. Abbreviated summary of linear compensation

In this section, we give an abbreviated summary of the derivation of the control and estimation problem; for further details, the reader is referred to Högberg & Bewley  $(2000^b)$  and Högberg & Henningson (2001). As a first step, the governing equations need to be put in a form suitable for application of standard control theory. The Orr–Sommerfeld/Squire equations (1a) and (1b) are usually written with a Laplacian operator on the left hand side. Fortunately, this Laplacian operator can, with care, be inverted if the boundary conditions are taken into account properly, thus resulting in the desired form of the governing equations:

$$\dot{\hat{v}} = \underbrace{\hat{\Delta}^{-1} \{ -i \, k_x \, U \, \hat{\Delta} + i \, k_x \, U'' + \hat{\Delta} (\hat{\Delta} / Re_{cl}) \}}_{\hat{L}_{OS}} \, \hat{v}$$
 (2a)

$$\dot{\hat{\omega}} = \underbrace{\{-i\,k_z\,U'\}}_{\hat{L}_C} \hat{v} + \underbrace{\{-i\,k_x\,U + \hat{\Delta}/Re_{cl}\}}_{\hat{L}_{SO}} \hat{\omega}. \tag{2b}$$

Writing these equations in operator form, we get

$$\dot{\hat{\mathbf{x}}}_f = \hat{N}\hat{\mathbf{x}}_f,\tag{3}$$

where

$$\hat{N} = \begin{pmatrix} \hat{L}_{OS} & 0 \\ \hat{L}_{C} & \hat{L}_{SQ} \end{pmatrix} \quad \text{and} \quad \hat{\mathbf{x}}_{f} = \begin{pmatrix} \hat{v} \\ \hat{\omega} \end{pmatrix}.$$

In order to formulate an objective function we need an expression for the energy E of the flow perturbations.

$$E = \frac{1}{2V} \int_{\Omega} (u^2 + v^2 + w^2) \, dV =$$

$$\sum_{k_x, k_z} \frac{1}{8k^2} \int_{-1}^{1} \left( k^2 |\hat{v}|^2 + \left| \frac{\partial \hat{v}}{\partial y} \right|^2 + |\hat{\omega}|^2 \right) \, dy \triangleq \sum_{k_x, k_z} \hat{E}.$$

$$(4)$$

For each wave number pair,  $\hat{E}$  can be written as  $\hat{\mathbf{x}}_f^* \hat{Q} \hat{\mathbf{x}}_f$  where  $\hat{Q}$  is an operator containing the operators needed to describe the energy measure. Due to the separation principle of optimal control theory, see e.g. Skelton (1988) p. 411,

the estimation and control problems can be treated separately in the derivation that follows.

# 2.1.1. Control strategy

In order to obtain the standard state-space form for the boundary control of the Orr-Sommerfeld/Squire equations, the non-homogeneous boundary conditions need to be treated properly. By lifting the boundary conditions they can be represented as a volume forcing in the homogeneous equations. Using the principle of superposition the non-homogeneous boundary conditions can be represented by a particular solution to the non-homogeneous equations  $\hat{v}$  $\hat{v}_h + \hat{v}_i$  and similarly for  $\omega$  such that  $\hat{\mathbf{x}}_f = \hat{\mathbf{x}}_h + \hat{\mathbf{x}}_i$ . This particular solution is then parameterized such that it has only one degree of freedom represented by the normal velocity on the wall. Since there are two walls in a channel two particular solutions are used. The resulting form of the system of equation is

$$\dot{\hat{\mathbf{x}}} = \hat{A}\hat{\mathbf{x}} + \hat{B}\hat{\mathbf{u}}$$

where

$$\hat{A} = \begin{pmatrix} \hat{N} & \hat{N}\hat{Z} \\ 0 & 0 \end{pmatrix}, \quad \hat{B} = \begin{pmatrix} -\hat{Z} \\ I \end{pmatrix}, \quad \hat{\mathbf{x}} = \begin{pmatrix} \hat{v}_h \\ \hat{\omega}_h \\ \hat{\phi} \end{pmatrix} = \begin{pmatrix} \hat{\mathbf{x}}_h \\ \hat{\phi} \end{pmatrix}$$

and  $\hat{Z}$  is the representation of the particular solutions and **u** contains the time derivative of the normal velocity on the walls  $(\hat{\phi})$ . The particular solutions can be chosen such that  $\hat{N}\hat{Z}=0$ , which results in a simple structure. The energy measure is now

$$\hat{E} = \hat{\mathbf{x}}^* \begin{pmatrix} \hat{Q} & \hat{Q}\hat{Z} \\ \hat{Z}^*\hat{Q} & \hat{Z}^*\hat{Q}\hat{Z} \end{pmatrix} \hat{\mathbf{x}} \triangleq \hat{\mathbf{x}}^*\hat{\mathcal{Q}}\hat{\mathbf{x}}.$$

Defining an objective function,

$$\hat{J} = \int_{0}^{\infty} (\hat{\mathbf{x}}^* \hat{\mathcal{Q}} \hat{\mathbf{x}} + \ell^2 \hat{\mathbf{u}}^* \hat{\mathbf{u}}) \, \mathrm{d}t,$$

the control  $\hat{\mathbf{u}}$  minimizing  $\hat{J}$  is according to standard control theory given by,

$$\hat{\mathbf{u}} = \hat{K}\hat{\mathbf{x}}, \text{ where } \hat{K} = -\frac{1}{\ell^2}\hat{B}^*\hat{X}$$

and where  $\hat{X}$  is the positive self-adjoint solution to the operator Riccati equation,

$$\left(\hat{A}\hat{X} + \hat{X}\hat{A}^* - \hat{X}\hat{B}\frac{1}{\ell^2}\hat{B}^*\hat{X} + \hat{Q}\right)\hat{\mathbf{x}} = 0, \quad \forall \text{ admissible } \hat{\mathbf{x}}.$$
 (5)

Notice that  $\ell^2$  is an adjustable parameter regulating a penalty on the integral of the square of the time derivative of the control velocity at the walls. The integral of the square of the control velocity itself is naturally penalized through the lifting terms in  $\hat{Q}$ ; though additional control penalties on this term could be imposed, this was not found to be necessary in the present work. The feedback rule  $\hat{K}(k_x, k_z)$  obtained is for feedback of the homogeneous part of the flow only. By modifying  $\hat{K}(k_x, k_z)$  to incorporate the effect of the feedback of the inhomogeneous part of the flow, kernels for the total flow are obtained. Feedback rules are computed for an array of wavenumber pairs and then inverse Fourier transformed to physical space to give the feedback law as a convolution integral of the form,

$$\dot{v}(x,y=\pm 1,z) = \int_{\Omega} \left( K_{\pm 1,v}(x-\bar{x},\bar{y},z-\bar{z})v(\bar{x},\bar{y},\bar{z}) + K_{\pm 1,\omega}(x-\bar{x},\bar{y},z-\bar{z})\omega(\bar{x},\bar{y},\bar{z}) \right) d\bar{x} d\bar{y} d\bar{z},$$

$$(6)$$

where  $K_{\pm 1,*}$  denotes the physical space feedback convolution kernel for the upper and lower walls of the wall-normal velocity or wall-normal vorticity respectively. The integral representation in the y direction is obtained by normalizing the gains with respect to the particular integration weights of the Chebyshev discretization used in the computation. Typical control kernels are shown in Figure 5. For kernels computed for the Falkner–Skan–Cooke boundary layer profiles see Högberg & Henningson (2001).

# 2.1.2. Estimator strategy

Estimating the state of the flow based on measurements at the wall is a dual problem to that of controlling the flow with wall actuation in the sense that the same procedure is used to solve the problems. In this case an equation for the error of the state estimate is formulated and a volume forcing feeding back the measurement error minimizing the integral of the state error is sought. The non-homogeneous terms cancel, since they are identical in the state equations and the estimator equations; thus, in the equation for the error of the state, only the homogeneous equations need to be considered. An estimator of this type is known as a Kalman filter, and is a standard problem. The single wavenumber case was considered in Bewley & Liu (1998) with a problem formulation similar to the one used in the present paper. Following Högberg & Bewley (2000<sup>b</sup>), we now model the state equation (3) and the skin-friction measurements of our system as disturbed by a random (zero-mean white Gaussian) process  $\hat{\mathbf{w}}$  such that

$$\dot{\hat{\mathbf{x}}}_h = \hat{N}\,\hat{\mathbf{x}}_h + \hat{B}_1\,\hat{\mathbf{w}} - \hat{Z}\dot{\hat{\phi}} \tag{7}$$

$$\hat{\mathbf{y}}_h = \hat{C}_2 \hat{\mathbf{x}}_h + \hat{D}_{21} \hat{\mathbf{w}},\tag{8}$$

where

$$\hat{B}_{1} = \begin{pmatrix} \hat{G}_{1} & 0 \end{pmatrix}, \quad \hat{C}_{2}\hat{\mathbf{x}}_{h} = \frac{\hat{G}_{2}^{-1}}{Re_{cl}} \begin{pmatrix} \frac{\partial \hat{\omega}_{h}}{\partial y} \\ \frac{\partial \hat{\omega}_{h}}{\partial y} |_{y=-1} \end{pmatrix}, \quad \text{and} \quad \hat{D}_{21} = \begin{pmatrix} 0 & \alpha I \end{pmatrix},$$

where  $\hat{G}_1$  is defined as the square root of the expected covariance of the state disturbances and  $\alpha \hat{G}_2$  is defined as the square root of the expected covariance of the measurement noise. We assume that these covariances are time invariant and that the covariance of the measurement noise is nonsingular. The problem is scaled such that  $\bar{\sigma}(\hat{G}_1^2) = 1$ , and  $\alpha$  is selected such that  $\bar{\sigma}(\hat{G}_2^2) = 1$ . Any known structure of the disturbance covariances entering the problem should thus be accounted for in the selection of the characteristics of  $\hat{G}_1$  and  $\hat{G}_2$ (both with unity maximum singular value) during the compensator design, retaining the quantity  $\alpha$  to reflect the balance between the magnitude of the measurement noise and the magnitude of the state disturbances. Given that the blowing/suction distribution  $\hat{\phi}$  and the lifting function  $\hat{Z}$  are known, the (noisy) measurements  $\hat{\mathbf{y}}_h$  of the quantity  $\hat{C}_2\hat{\mathbf{x}}_h$  may easily be extracted from the available (noisy) wall measurements of the streamwise or spanwise drag. Only the field  $\hat{\mathbf{x}}_h$  needs to be estimated in order to construct an estimate of the complete state vector  $\hat{\mathbf{x}}_s$  (or, indeed, to estimate  $\hat{\mathbf{x}}$  itself); we will denote our estimate of  $\hat{\mathbf{x}}_h$  as  $\hat{\mathbf{x}}_e$ , and our estimate of  $\hat{\mathbf{y}}_h$  as  $\hat{\mathbf{y}}_e$ . The model of the system which we will use in our estimator is

$$\dot{\hat{\mathbf{x}}}_e = \hat{N}\hat{\mathbf{x}}_e - \hat{Z}\dot{\hat{\phi}} - \hat{\psi}, 
\hat{\mathbf{y}}_e = \hat{C}_2\hat{\mathbf{x}}_e, 
\hat{\psi} = \hat{L}\Delta\hat{\mathbf{y}} \triangleq \hat{L}(\hat{\mathbf{y}}_h - \hat{\mathbf{y}}_e).$$
(9)

Note that the (unknown) effects of the disturbances  $\hat{\mathbf{w}}$  are not included in the estimator model. The estimator feedback rule  $\hat{\psi} = \hat{L}\Delta\hat{\mathbf{y}}$  minimizing the expected value of the  $L^2$ -norm of the estimation error is given by

$$\hat{L} = -\frac{1}{\alpha^2} \, \hat{Y} \, \hat{C}_2^*,$$

where  $\hat{Y}$  is the positive self-adjoint solution to the Riccati equation,

$$\left(\hat{N}^*\hat{Y} + \hat{Y}\hat{N} - \hat{Y}\hat{C}_2^* \frac{1}{\alpha^2}\hat{C}_2\hat{Y} + \hat{B}_1\hat{B}_1^*\right)\hat{\mathbf{x}}_e = 0, \quad \forall \text{ admissible } \hat{\mathbf{x}}_e$$

in accordance with standard Kalman filter theory. Note that  $\alpha^2$ , which models the assumed quality of the measurements, is used as an adjustable parameter to scale the estimator feedback. The Kalman filter problem described earlier has been derived for each wavenumber pair  $\{k_x, k_z\}$  independently. The inverse Fourier transform of the Fourier-space estimator feedback rule is given by the following convolution sums in physical space:

$$\psi_{v_e}(x,y,z) = \int \left( \mathbf{L}_{v_e,+1}(x-\bar{x},y,z-\bar{z}) \, \Delta y(\bar{x},+1,\bar{z}) + \right.$$

$$\left. \mathbf{L}_{v_e,-1}(x-\bar{x},y,z-\bar{z}) \, \Delta y(\bar{x},-1,\bar{z}) \right) \mathrm{d}\bar{x} \, \mathrm{d}\bar{z}$$

$$\psi_{\omega_e}(x,y,z) = \int \left( \mathbf{L}_{\omega_e,+1}(x-\bar{x},y,z-\bar{z}) \, \Delta y(\bar{x},+1,\bar{z}) + \right.$$

$$\left. \mathbf{L}_{\omega_e,-1}(x-\bar{x},y,z-\bar{z}) \, \Delta y(\bar{x},-1,\bar{z}) \right) \mathrm{d}\bar{x} \, \mathrm{d}\bar{z}$$

where the estimator forcing kernels  $\mathbf{L}_{v_e,\pm 1}(x,y,z)$  and  $\mathbf{L}_{\omega_e,\pm 1}(x,y,z)$  are the inverse Fourier transforms of  $\hat{L}_{\hat{v}_e,\pm 1}(k_x,y,k_z)$  and  $\hat{L}_{\hat{\omega}_e,\pm 1}(k_x,y,k_z)$  respectively. The structure of L represents the forcing of the model equation in the estimator as a function of a measurement error at a single point. Using  $\Delta y(\bar{x},-1,\bar{z})=\Delta y_o\delta(\bar{x})\delta(\bar{z})$  in the convolution integral results in  $\psi_{v_e}(x,y,z)=L_{v_e,-1}(x,y,z)\cdot\Delta y_o$  and  $\psi_{\omega_e}(x,y,z)=L_{\omega_e,-1}(x,y,z)\cdot\Delta y_o$ , which facilitates this interpretation. Typical estimator forcing kernels are shown in Figure 6.

### 2.2. Computation of linear feedback kernels

The control and estimator feedback for each wavenumber pair is computed using Matlab. The Orr–Sommerfeld/Squire system is discretized in the normal direction using Chebyshev collocation such that,

$$\bar{f} = [f(y_1), ..., f(y_N)]^T, \quad f(y_i) = \sum_{n=1}^N \tilde{f}_n T_n(y_i), \quad y_i = \cos \frac{i \pi}{N},$$

where  $\{T_n(y)\}_{n=1}^N$  are the Chebyshev polynomials. The Differentiation Matrix Suite by Weideman & Reddy (2000) is used to create the differentiation matrices and then the matrix operators for the equation are compiled. Since a lifting technique is used the matrices for the homogeneous problem can be used utilizing the clamped boundary conditions suggested by Huang & Sloan (1993). The problem with spurious eigenvalues and eigenvectors is then avoided. The integration weights  $W(y_j)$  for the Chebyshev grid with the Gauss-Lobatto collocation points is computed using an algorithm from Hanifi, Schmid & Henningson (1996),

$$\int_{-1}^{1} f(y) \, \mathrm{d}y = \sum_{j=0}^{N} f(y_j) W(y_j), \quad W(y_j) = \frac{b_j}{N} \left\{ 2 + \sum_{n=2}^{N} c_n \frac{1 + (-1)^n}{1 - n^2} \cos(\frac{n \, j \, \pi}{N}) \right\},$$

where  $b_j$  and  $c_n$  are found from,

$$f(y) = \sum_{n=0}^{N} c_n T_n(y) \sum_{j=0}^{N} \frac{b_j}{N} f(y_j) T_n(y_j).$$

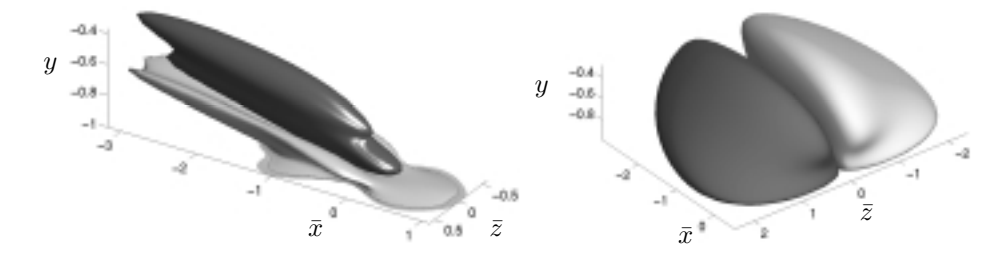


FIGURE 5. Localized controller gains relating the state x inside the domain to the control forcing **u** at the point  $\{x =$ 0, y = -1, z = 0} on the wall: visualized are a positive (light) and negative (dark) isosurface of the convolution kernels for (left) the wall-normal component of velocity and (right) the wall-normal component of vorticity. (Högberg & Bewley  $2000^{b}$ )

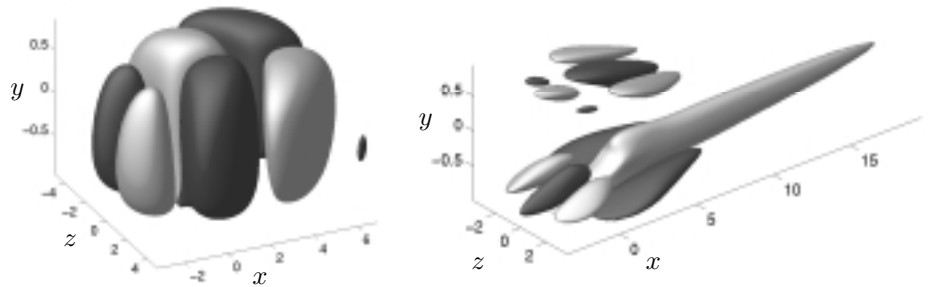


FIGURE 6. Localized estimator gains relating the measurement error  $(\mathbf{y} - \hat{\mathbf{y}})$  at the point  $\{x = 0, y = -1, z = 0\}$  on the wall to the estimator forcing terms  $\mathbf{v}$  inside the domain: visualized are a positive (light) and negative (dark) isosurface of the convolution kernels for (left) the wall-normal component of velocity and (right) the wall-normal component of vorticity. (Högberg & Bewley  $2000^b$ )

These weights provide spectral accuracy of the integration and are used to assemble the energy measure matrix Q. The Riccati equation (5) is solved using an algorithm from Skelton (1988) p. 350 which mainly involves computation of eigenvectors. More efficient methods for solving Riccati equation can be found in e.g. Laub (1991). The kernel computations are performed on an ordinary workstation and take about 2-3 hours for the kernels presented here.

# 2.3. Localized convolution kernels

## 2.3.1. Kernel structure

The convolution kernels computed using the approach described above are depicted in Figures 5 and 6. The control convolution kernels shown in Figure 5 angle away from the wall in the *upstream* direction. Considering the shape of the mean flow profile indicated in Figure 1, this accounts for the convective delay which requires us to anticipate flow perturbations on the interior of the domain with actuation on the wall somewhere downstream. The estimation convolution kernels shown in Figure 6, on the other hand, extend well downstream of the measurement point. This accounts for the delay between the motions of the convecting flow structures on the interior of the domain and the eventual influence of these motions on the local drag profile on the wall; during this time delay, the flow structures responsible for these motions convect downstream. Note that the upstream bias of the control kernels and the downstream bias of the estimation kernels, though physically tenable, were not prescribed in the problem formulation. A posteriori study of the streamwise, spanwise, and wall-normal extent, the symmetry, and the detailed shape of such control and estimation kernels provides us with a powerful new tool with which the fundamental physics of this distributed fluid-mechanical system may be characterized.

The localized convolution kernels illustrated in Figures 5 and 6 are approximately independent of computational box size in which they were computed, so long as this box is sufficiently large. Thus, when implementing these kernels, we may effectively assume that they were derived in an *infinite*-sized box, relaxing the non-physical assumption of spatial periodicity used in the problem formulation and modeling the physical situation of spatially-evolving flow perturbations in a spatially-invariant geometry and mean flow.

The localized convolution kernels illustrated in Figures 5 and 6 are also approximately independent of the computational mesh resolution with which they were computed, so long as this computational mesh is sufficiently fine. Indeed, a computational mesh which is sufficient to resolve the flow under consideration also adequately resolves these convolution kernels.

# 2.3.2. Exponential decay

The kernels have a structure with exponential decay at a finite distance away from the origin. In order to illustrate this decay, control kernels for the normal velocity have been computed for  $Re_{cl}=2000$  and  $\ell=1$  with high resolution for four different sizes of the computational box. This is a representative case for showing the behavior of the kernels at a distance from the origin, and the other kernels show a similar behavior. The squared value of the kernels is first integrated in the y direction to obtain a representation of the kernel weights in the xz plane. This planar representation is then integrated in z to show the behavior as a function of z, and integrated in z to show the behavior as a function of z. The results are normalized with the maximum value of the result from the smallest box and shown in Figure 7.

Due to the imposed periodicity, the exponential decay of the kernels is interrupted for small box sizes. However, by increasing the size of the computational box, we clearly see that the decay of the magnitude of the tails is

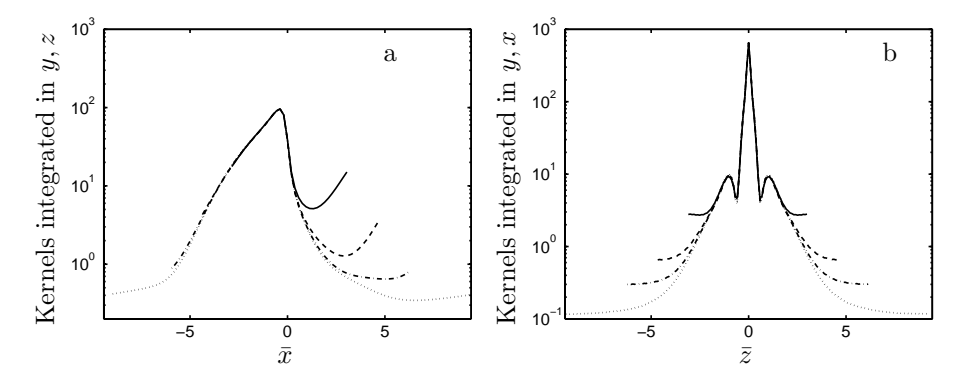


FIGURE 7. Illustration of exponential decay of control convolution kernel for normal velocity. a: As a function of x b: As a function of z. solid lines: box size  $2\pi \times 2\pi$  with resolution  $32 \times 64$  in  $x \times z$ , dashed lines box size  $3\pi \times 3\pi$  with resolution  $48 \times 96$  in  $x \times z$ , dash-dot is box size  $4\pi \times 4\pi$  with resolution  $64 \times 128$  in  $x \times z$  and dotted is box size  $6\pi \times 6\pi$  with resolution  $96 \times 192$  in  $x \times z$ . In all cases  $\ell = 1$ ,  $Re_{cl} = 2000$  and the number of gridpoints in y was 70.

significantly extended, while the shape of the kernel in the vicinity of the origin remains unchanged. In a sufficiently large box, we should see decay of the kernel magnitude over several orders of magnitude as we move away from the origin. However, computation of the kernel over such a large domain is difficult, as it is computationally expensive. Plots such as Figure 7 are sufficient to illustrate that the kernels we seek are converged in the region of interest near the origin. Motivated by the apparent exponential decay of these kernels away from the origin, we can perform truncation in the physical domain, thus obtaining spatially compact control and estimation kernels with support only over a finite region.

# 3. Simulations

# 3.1. Simulation of nonlinear system

The direct numerical simulation code used in Bewley, Moin, & Temam (2001) is used to perform the simulations of temporal channel flow with constant massflux. The code uses Fourier series with 3/2 dealiasing in the spanwise and streamwise directions and second order accurate finite differences in the wallnormal direction. The treatment of the derivatives in the wall-normal direction is implicit to enhance stability of the code when blowing and suction boundary conditions are applied. (An explicit treatment would result in extremely small timesteps required for stability of the simulation when blowing/suction controls are applied due to the clustering of gridpoints near the walls). Time advancement is performed with a third-order accurate Runge-Kutta method

Scenario	$Re_{cl}$	$\operatorname{Grid}$	Lower	Upper
(SV)	2000	$16 \times 81 \times 64$	$6.32 \times 10^{-6}$	$6.64 \times 10^{-6}$
,	3000	$16 \times 81 \times 64$	$1.46 \times 10^{-6}$	$1.52\times10^{-6}$
	5000	$16\times81\times64$	$2.56\times10^{-7}$	$2.65\times10^{-7}$
(OW)	2000	$16 \times 81 \times 64$	$2.33 \times 10^{-6}$	$2.43 \times 10^{-6}$
, ,	3000	$16 \times 81 \times 64$	$5.03 \times 10^{-7}$	$5.53 \times 10^{-7}$
	5000	$16\times81\times64$	$1.14 \times 10^{-7}$	$1.19\times10^{-7}$
(N)	2000	$32 \times 81 \times 64$	$7.00 \times 10^{-5}$	$7.50 \times 10^{-5}$
. ,	3000	$32 \times 81 \times 64$	$2.50\times10^{-5}$	$2.75\times10^{-5}$
	5000	$40\times97\times80$	$8.50\times10^{-6}$	$8.75\times10^{-6}$

Table 1. Transition thresholds for streamwise vortices (SV), oblique waves (OW) and random noise (N) determined by Reddy *et al.* using a Fourier, Chebyshev, Fourier discretization.

by Aksevoll & Moin (1995). A fractional step method is used to update the pressure and to enforce a divergence free flow. The transition thresholds for the uncontrolled flow are verified for the present code using the same routines as in Reddy *et al.* (1998) to generate initial conditions. More details about the simulation code can be found in Bewley, Moin, & Temam (2001).

To make comparisons easier the thresholds obtained by Reddy et al. (1998) are tabulated in Table 1. The initial conditions for oblique waves and streamwise vortices used are such that they have the optimal shape in the y direction that maximizes their transient growth and are contained in the lowest wavenumbers in the simulations. In addition, random noise in the form of Stokes modes with 1% of the energy of the primary perturbation is added distributed over all combinations of the wavenumbers  $k_x = (0, \pm 1, \pm 2) k_{x0}$  and  $k_z = (0, \pm 1, \pm 2) k_{z0}$ . In the random noise case all the energy is distributed over these wavenumbers. The box size in the streamwise vortex case is  $2\pi \times 2 \times \pi$ in  $x \times y \times z$  with the fundamental wavenumbers  $k_{x0} = 1$  and  $k_{z0} = 2$ . For both the oblique wave and random noise cases the box size is  $2\pi \times 2 \times 2\pi$  in  $x \times y \times z$ having the fundamental wavenumbers  $k_{x0} = 1$  and  $k_{z0} = 1$ . The threshold values are found by starting with a large interval containing the threshold and then this interval is successively shortened until it is acceptably small. The final values are then verified using a different resolution. This requires many simulations and a condensed presentation of the results such as is Table 2 has required many hundreds of hours of computer time.

Ful	ll-state	feed	hack

Scenario	$Re_{cl}$	Grid	Lower	Upper	Improvement Factor
(SV)	2000 3000 5000	$16 \times 128 \times 64$ $16 \times 128 \times 64$ $16 \times 128 \times 64$	$1.50\times10^{-5}$	$6.55 \times 10^{-5}$ $1.55 \times 10^{-5}$ $3.10 \times 10^{-6}$	10 9.6 11.5
( OW )	2000 3000 5000	$16 \times 128 \times 64$ $16 \times 128 \times 64$ $16 \times 128 \times 64$	$2.38 \times 10^{-4}$ $6.50 \times 10^{-5}$	$2.50 \times 10^{-4}$ $7.00 \times 10^{-5}$	102 109 122
( N )	2000 3000 5000	$32 \times 128 \times 64$ $32 \times 128 \times 64$ $32 \times 128 \times 64$	$1.80\times10^{-4}$		7 6.8 5.7

Table 2. Controlled transition thresholds using a Fourier, Finite difference, Fourier discretization. Verified using lower resolution  $12 \times 128 \times 42$  and  $28 \times 128 \times 58$ 

# 3.2. Modification of transition thresholds with full state feedback

Direct numerical simulations of the fully nonlinear Navier-Stokes equations with linear feedback control are performed at three different subcritical Reynolds numbers,  $Re_{cl} = 2000$ , 3000 and 5000. Control kernels are computed using the same resolution and box size as in the simulations with  $\ell = 0.1$  in all cases. Through an iterative procedure the transition thresholds have been determined for the three different perturbations, streamwise vortices, oblique waves and random noise, as reported in Table 2 and Figure 8. The "Improvement Factor" column in Table 2 shows the relation between the average of the upper and lower threshold for the controlled and the uncontrolled cases. If this Factor is two, it means that the initial energy density threshold value is approximately two times higher in the controlled case than in the uncontrolled case. The transition threshold for the streamwise vortex perturbation is increased up to 11.5 times the uncontrolled value, corresponding to more than a threefold increase in perturbation amplitude. Oblique wave perturbations, which in the uncontrolled case have the lowest threshold energy, appear to be the easiest to control since the threshold energy is increased up to 122 times the uncontrolled value. One reason for this might be that the control of the linear growth of the oblique waves efficiently prevents the nonlinear generation of strong streamwise vortices, which in turn has an effect on the generation of streamwise streaks. In the controlled case the streamwise vortex perturbations have the lowest values of the transition thresholds, about one order of magnitude lower than the two other perturbations, suggesting that the underlying transition mechanism

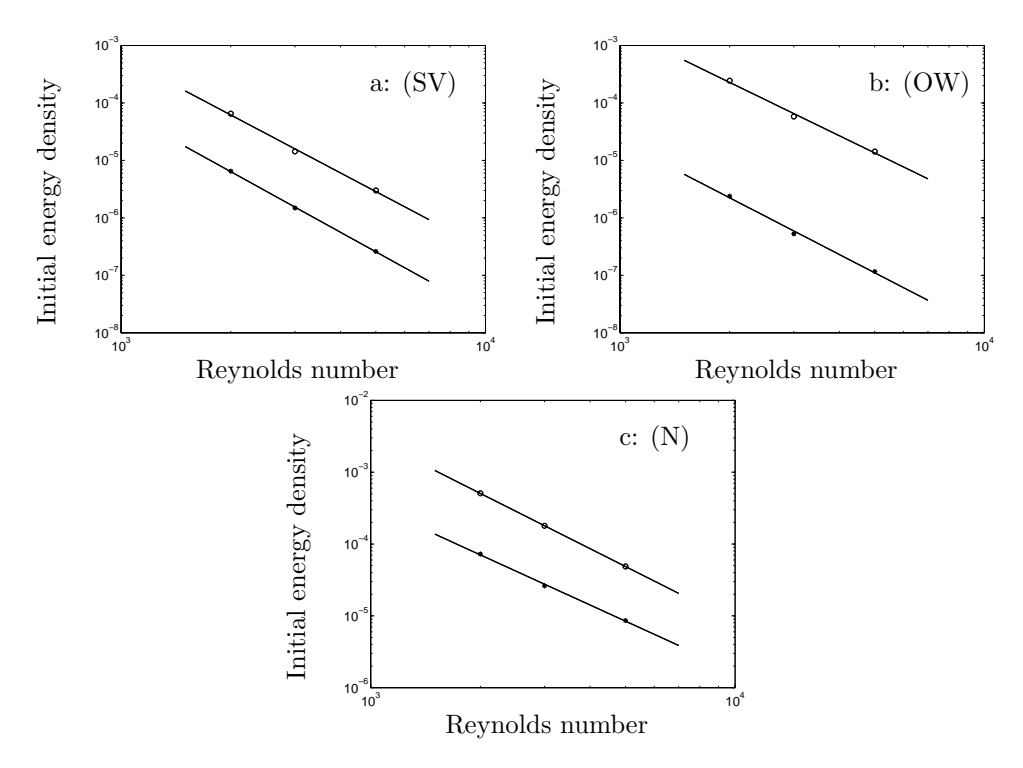


FIGURE 8. Transition threshold energy versus Reynolds number for feedback controlled plane Poiseuille flow. Shown are the curves obtained from direct numerical simulations with control compared with the uncontrolled cases. One plot for each case starting with various initial conditions: a) optimal streamwise vortices, b) a pair of optimal oblique waves, and c) divergence-free low-wavenumber noise. The open circles are the values obtained with full information state feedback control and the stars are the values for the uncontrolled case computed by Reddy et al. (1998). The solid lines are least square fits to the data.

in the streamwise vortex scenario is the most powerful one in the controlled flow. The smallest factor for the increase in transition threshold is obtained for the random perturbation and is approximately 7 times the uncontrolled value. This indicates that the random noise transition scenario is the most difficult to control, meaning that the effect of the controller is smallest. In summary the controller increases the transition threshold by roughly one order of magnitude for streamwise vortices, a little bit less for random noise and about two orders of magnitude for oblique waves.

# 3.3. Effectiveness of truncated kernels

Performing truncation of the kernels by setting their values to zero at a certain distance away from the origin (smaller than the box size in which they were computed) results in truly compact kernels. To test the effectiveness of a truncated kernel, the kernel used for the threshold computations was truncated by setting it to zero outside a box with the limits  $\bar{x} \in (-3, 1)$  and  $\bar{z} \in (-2.5, 2.5)$  using a smoothed step function. Compare with Figure 7 to see approximately how much of the kernel information is ignored through this operation. The method of truncation might seem rather abrupt, but more sophisticated schemes for performing the truncation were not found to be necessary. Applying such a truncated kernel in the direct numerical simulation of a random noise perturbation at  $Re_{cl} = 2000$  reproduces the interval for the threshold values as for the untruncated kernels in Table 2. This interval is fairly tight and this shows that the truncation did not significantly degrade the performance of the control despite the significant reduction in the kernel extent resulting from the truncation.

# 3.4. Analysis of feedback structure

In order to try to understand how the controller acts, the oblique wave and streamwise vortex cases with control are studied in some more detail. In Figure 9 the velocity fields, a short time after the full information control is applied, are shown for the oblique wave (a) and streamwise vortex (b) cases. The action of the control has be studied with the help of animations in order to understand how the control acts on the perturbations. In the oblique wave case the isosurfaces in Figure 9a are elongated in the streamwise direction, compare with Figure 2a, and move down to the wall where they shrink again. New, almost stationary, oblique waves are formed in the center of the channel and these are then controlled in an out-of-phase fashion while accelerating. There is then a rapid reduction of the perturbation amplitude and only a streaky perturbation remains. Even with the help of animations it is difficult to explain the action of the control in detail. The process is complicated and non-intuitive, and the advantage of using control theory, which does not require a priori knowledge of the "dominant mechanisms" of the transition process, is readily apparent. It is clear that the growth of the oblique wave is efficiently lowered by the control by comparing Figure 10 and Figure 3a. It is interesting to note that the control energy is shifted from one set of wavenumbers to another set of wavenumbers as the flow evolves in time, as shown in Figure 11. Initially the oblique wave mode is the focus of the control effort, but when this mode has decayed to a level lower than the streak modes, the control focuses its effort on the streak modes instead. It should be noted that the contour levels are not the same in the different frames in Figure 11. The largest energy is used initially before the oblique wave mode has its maximum and then it rapidly decays. Thereby the streaks are not forced so efficiently by the oblique waves and the streak amplitude is much lower than in the case without control. When the oblique

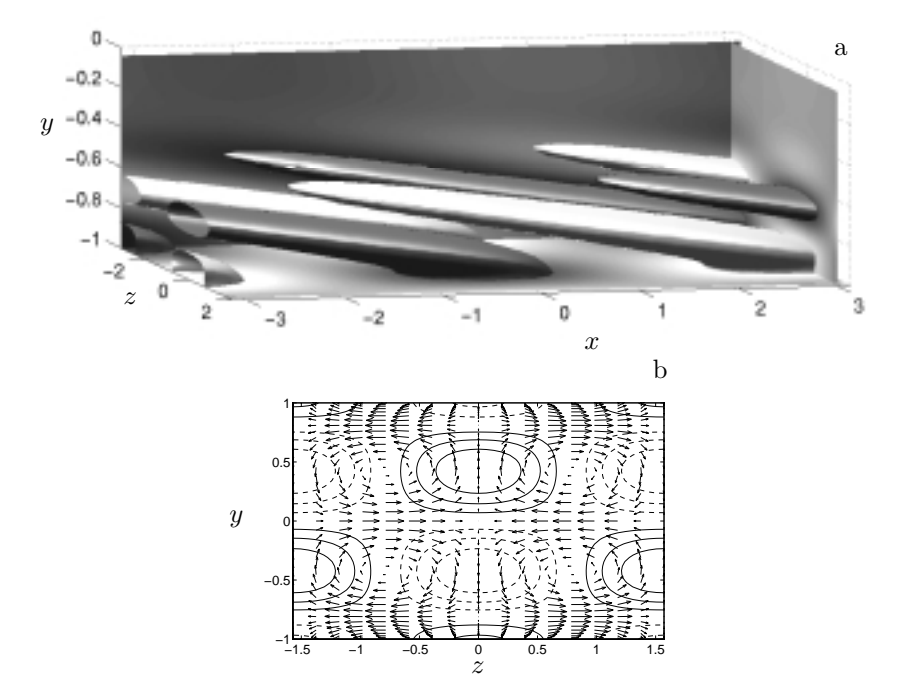


FIGURE 9. Velocity field showing the reaction of the control to the initial conditions in Figure 2: a) Control of oblique waves showing isosurfaces at half the maximum value of the normal velocity (light) and at half the minimum value (dark). The slices show the distribution of normal velocity where light is positive and dark is negative. b) Control of streamwise vortices showing contours of v, solid contours for positive velocity and dashed for negative, and velocity vectors of v, w in a z-y plane at x=0.

waves have decayed a streaky structure appears and then the control acts in a way similar to the streamwise vortex control case.

In the streamwise vortex case the wall normal velocity is of opposition type. Figure 9b shows the reaction of the control to the streamwise vortex initial condition. Where the flow is going towards the wall blowing is applied and vice versa. In the animation one can see that the vortices are pushed away from the wall by buffer vortices created by the blowing and suction and virtual walls, using the terminology of Hammond et al. (1998), are created near the center of the channel. Streamwise streaks rapidly develop in the regions between the real walls and the virtual walls as a result of the blowing and suction applied. The virtual walls then move slowly towards the real walls as the blowing and suction decrease, and the vortices reappear between the virtual walls in the center of the channel. The streaks in the near-wall region decay as

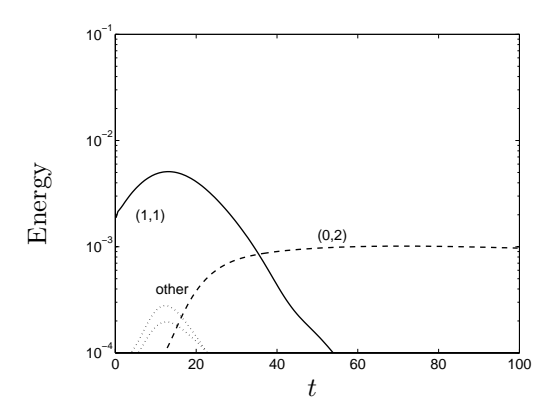


FIGURE 10. Energy evolution in different modes for control of oblique waves. The (0,2) mode slowly decays to zero after t = 100.

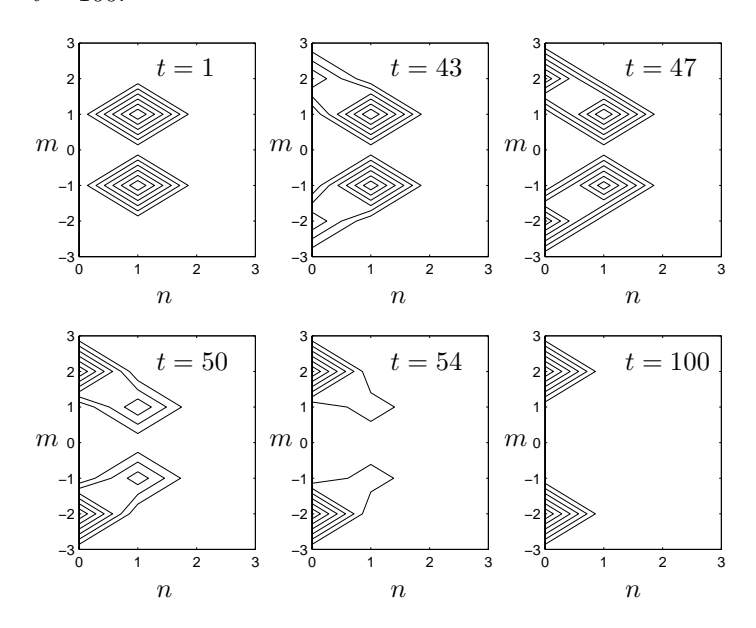


Figure 11. Contour plot of  $\phi^2(k_x, k_z)$  for control of oblique waves at t = [1, 43, 47, 50, 54, 100]. where  $k_x = n k_{x0}$  and  $k_z =$  $m k_{z0}$ . Notice that the contour levels are not equal in the different plots but decreases with time.

the blowing and suction weaken, and since a low-speed streak is located where the vortices in the center of the channel move momentum from the inner part of the channel towards the virtual wall a high speed streak is created above the low speed streak, and vice versa for the high speed streak. These streaks in the interior of the channel merge slowly, probably through diffusion, with the

ones directly above or below resulting in streaks that fill the whole region in between the virtual walls. These streaks then decay slowly and the blowing and suction on the walls decreases at the same time. The virtual walls slowly move towards the center of the channel again as the streaks decrease and eventually disappear.

### 3.5. Convergence of estimator with feedback from measurements

Estimating the state of the flow from available measurements is a crucial step towards practical implementation of this type of controller. Possible measurements are, e.g., the components of the shear stress and pressure fluctuations on the wall. Many different independent measurements give more information about the state of the flow. In the present study we have focused on the use of a measurement of the wall normal derivative of the wall-normal vorticity component. This appears to be sufficient to get exponential convergence of the state estimate, but it is rather slow. The estimator forcing kernels are computed as described in section 2.1.1 with  $\alpha = 0.1$  and then used to force the flow in a fully nonlinear simulation. This is known as an extended Kalman filter. Estimation of a nonlinear system using a linear estimator is discussed in, e.g., Bewley (1999). The initial state in the estimator is an unperturbed laminar flow at the same Reynolds number as the measured flow in all cases presented here. In Figure 12 the energy of the difference between the state in the measured flow and in the estimator is plotted versus time. The initial state in the unknown flow is a random perturbation at an energy level below the transition threshold. The initial guess in the estimator is an unperturbed laminar flow at  $Re_{cl} = 3000$ . Estimator forcing kernels are computed for both  $\hat{G}_1\hat{G}_1^* = \hat{Q}$  and  $\hat{G}_1\hat{G}_1^* = I$ . Using either estimator, there is an initial transient increase in the error after which it decays at an exponential rate. The transient is due to the fact that it is not possible to get uniform decay of the state error using only the current measurements, as the system representing the estimator error is non-normal, just like the controlled closed loop system. For more discussion about the closed loop properties of the linear system see Bewley & Liu (1998). Using  $\hat{G}_1\hat{G}_1^* = \hat{Q}$  gives a small transient during a long time whereas using  $\hat{G}_1\hat{G}_1^*=I$  gives a larger transient for a shorter time. Since both the initial behavior and the convergence are important issues there is no intuitive reason why one would be better than the other. The amplitude of the initial transient could be of importance when the perturbation energies are large and nonlinear effects are strong. If the estimator state undergoes transition due to this transient the compensator cannot be expected to work particularly well. For this reason the estimator with  $\hat{G}_1\hat{G}_1^* = \hat{Q}$  that has a lower amplitude of the transient is the primary choice for the estimator-based control studies that follow.

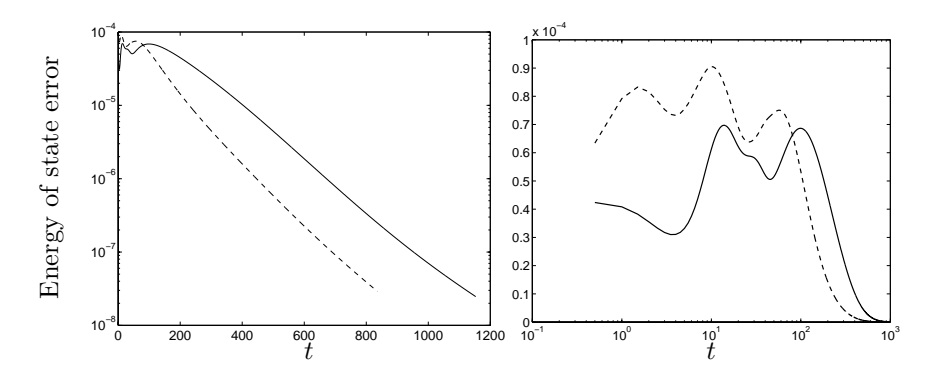


FIGURE 12. Convergence of estimator computed with  $\alpha =$ 0.1 for a random perturbation with an energy just below the transition threshold at  $Re_{cl} = 3000$ . Solid with  $\hat{G}_1\hat{G}_1^* = \hat{Q}$ and dashed with  $\hat{G}_1\hat{G}_1^* = I$ . Left: logarithmic in vertical axis, right: logarithmic in horizontal axis.

#### 3.6. Modification of transition thresholds with estimator-based control

In the case of measurement based control we run two different nonlinear direct numerical simulations simultaneously. One with the initial perturbation we wish to control and one estimator with no initial perturbation. Measurements are taken in both simulations and the difference between the two is used to force the estimator using the forcing kernels. The state in the estimator, which as shown in the previous section for the uncontrolled case converges exponentially to the correct state, is then used to compute the update of the control which is then applied in both simulations simultaneously. This combination of estimator and controller is called a measurement-based dynamic compensator. The control kernels are the same as used for the full information case and the estimation kernels are computed with the same box size and resolution as the simulations with  $\alpha = 0.1$ .

The compensator was first tested for an oblique wave at  $Re_{cl} = 2000$  and a comparison of the perturbation energy with the full information controller and for the uncontrolled flow is plotted in Figure 13. In this case the initial energy density was  $1.25 \times 10^{-5}$  but the perturbation did not have the optimal shape in y and no additional random noise was added. The total energy reduction for the full information controller and the compensator appears to be of the same order. The compensator performance was even closer to that of the full information controller if a good initial guess for the state in the estimator was provided. This demonstrates that the compensator is successful in reducing the energy growth of an oblique wave perturbation, but the question is what happens when the amplitude of the perturbations are large and noise is present. In order to test the compensator performance the "worst-case" situation when the initial state in the estimator is an unperturbed flow is considered.

(N)

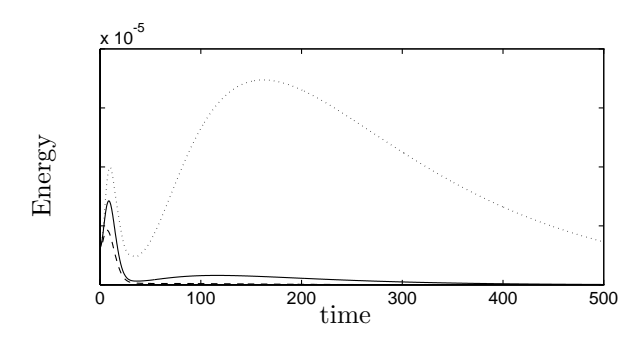


FIGURE 13. Performance of full information linear controller (dashed) and compensator using  $\hat{G}_1\hat{G}_1^* = \hat{Q}$  (solid) compared to the uncontrolled (dotted) energy evolution.

Measurement feedback

#### Improvement Scenario Lower Upper $Re_{cl}$ Grid Factor $\hat{G}_1\hat{G}_1^* = \hat{Q}$ $16 \times 128 \times 64 \quad 1.75 \times 10^{-5}$ $2.00\times10^{-5}$ (SV) 2.9 $1.25 \times 10^{-5}$ $16 \times 128 \times 64$ $1.50 \times 10^{-5}$ (OW) 2000 5.8 $16 \times 128 \times 64 \quad 9.00 \times 10^{-5}$ $1.00 \times 10^{-4}$ 1.31 $16\times128\times32\quad 3.25\times10^{-5}$ $3.50\times10^{-5}$ (N) 3000 1.28 $16 \times 128 \times 32 \quad 1.00 \times 10^{-5}$ $1.25 \times 10^{-5}$ 50001.30 $\hat{G}_1\hat{G}_1^* = I$

TABLE 3. Compensator controlled transition thresholds using a Fourier, Finite difference, Fourier discretization, for the initial perturbations: (SV)–Streamwise vortex, (OW)– Oblique wave and (N)– Random perturbation. Upper part of table with  $\hat{G}_1\hat{G}_1^*=\hat{Q}$  and lower part with  $\hat{G}_1\hat{G}_1^*=I$ .

1.48

 $2000 \quad 16 \times 128 \times 64 \quad 1.05 \times 10^{-4} \quad 1.10 \times 10^{-4}$ 

Simulations are performed at Reynolds number 2000 for all three types of initial perturbations; Table 3 contains the resulting transition thresholds from these simulations. With  $\hat{G}_1\hat{G}_1^*=I$  only one case at  $Re_{cl}=2000$  with random noise is considered. The transition threshold for the streamwise vortex

perturbation is increased 2.9 times the uncontrolled value. Oblique wave perturbations appear to be the easiest to control using the compensator (as with the full-state feedback controller), and the threshold energy is increased 5.8 times the uncontrolled value. In the compensator-controlled case the oblique wave perturbations, as opposed to streamwise vortices in the full information control cases, have the lowest values of the transition threshold. This is just as in the uncontrolled case but the transition threshold energies in the compensator controlled case are approximately of the same order for the streamwise and oblique wave perturbations and about one order higher for the random noise.

As for the full information case the smallest factor for the increase in transition threshold is obtained for the random perturbation and is only 1.3. For the case with  $G_1G_1^* = I$  the initial transient in the estimator is larger but the improvement factor is increased to 1.48 with the corresponding compensator. The conjecture that the large transient in the estimator would degrade the performance of the compensator was thus not correct. The choice of  $G_1$  is a delicate issue and further research is needed to find the optimal choice for transition control. Remember also that the results can be improved by providing a good initial guess in the estimator, suggesting an alternative route to better performance. The small increase in threshold values for the random noise also in the compensator case further suggests that this is the most difficult perturbation to control. For the random noise perturbation simulations at the higher Reynolds numbers 3000 and 5000 are performed at to verify that the factor is kept approximately constant also in the compensator case as seen in Table 3.

#### 4. Discussion

The effectiveness of the strategy for control and estimation of transitional flows from Högberg & Bewley  $(2000^b)$  has been quantified for three significant types of perturbations in subcritical channel flow studied in Reddy et al. (1998). A large number of direct numerical simulations have been performed in order to determine the transition threshold energies for the controlled flows both in the full information and measurement based settings. The localization of the kernels with exponentially decaying tails and the small effect on their efficiency from truncation compared to the untruncated kernels has been demonstrated.

In the full information control case, we have shown that the controller can increase the threshold energies for transition as much as 122 times the uncontrolled value for oblique wave perturbations and approximately 10 and 7 times for the streamwise vortex and random noise perturbations respectively. The lowest threshold value is obtained for the streamwise vortices in the controlled case indicating that the transition mechanism involved in this scenario is the most powerful one. The factor of increase in the threshold energies is approximately constant for different Reynolds numbers for all types of perturbations considered. This results in lower threshold values for higher Reynolds numbers.

The measurement based state estimator was implemented as an extended Kalman filter and shown to give exponential convergence of the estimated state to the measured state. This convergence was found to be rather slow and further research is necessary in order to improve the results. Additional independent measurements such as pressure fluctuations and spanwise and streamwise drag can perhaps be used to speed up the convergence. Another way of getting faster convergence is to try to construct a good initial guess for the estimator. It should be noted that for the estimator, as well as the compensator cases, the box size used in the simulation are not large enough to fit the estimation kernels depicted in Figure 6. This is however not a problem here since truncated estimation kernels are not used, but future studies should test the estimation in a sufficiently large box in order to motivate the use of this type of estimator in a decentralized scheme. The box sizes used in the present studies was motivated by allowing for comparison with the results of Reddy et al. (1998).

In the compensator case we have not quantified the performance to the same extent as in the full information case. The reason is that the results were not as good as expected with the current approach due to the slow convergence of the estimator, and also because these simulations are twice as costly compared to the full information case since two flow fields have to be marched in time simultaneously. A rule of thumb when designing compensators is that the estimator should converge faster than the controller in order to achieve good and robust performance. Incorporation of the existing knowledge about the physics and the mechanisms of transition and turbulence could also be beneficial for the compensator design. The development of more efficient estimators is needed and hopefully such estimators will provide means to raise these threshold values for the compensator to levels close to those obtained with the full information controller. The results are however of interest since we can draw the conclusion that the most difficult problem to control is the one with random noise perturbations, and that the reason in the compensator case is mainly the slow convergence of the estimator, and this will help in focusing the future efforts.

Since the problem we are studying in this paper is highly idealized it should be clarified how these results will lead to practical feedback compensators to be used in engineering applications. The advantage of the current approach is that truncation in physical space results in kernels that have compact spatial support with maintained performance and this facilitates a convenient strategy for decentralized physical space implementation. For a thorough discussion about the implication of this property of the kernels and practical implementation issues the reader is deferred to Bewley (2001).

#### 4.1. Extensions

#### 4.1.1. $\mathcal{H}_{\infty}$ control

In more realistic situations, where we cannot assume perfect measurements and precise actuation, robustness is necessary. The present formulation can with

small modifications also be used to compute robust  $(\mathcal{H}_{\infty})$  compensators. In the case of  $\mathcal{H}_{\infty}$  control the problems of control and estimation are coupled and the separation principle no longer applies. This is described in detail in Doyle et al. (1989). In Bewley & Liu (1998)  $\mathcal{H}_{\infty}$  compensation was performed for one wavenumber pair and shown to have some different characteristics than the optimal  $\mathcal{H}_2$  compensator. A similar approach was also used in the recent paper by Baramov, Tutty & Rogers (2000). Robustification with respect to changes in the mean flow profile is motivated by the success of the gain scheduling technique in Högberg & Bewley  $(2000^b)$ , and robustness to the nonlinearities not included in the Orr-Sommerfeld/Squire equations could also improve the present results.

#### 4.1.2. Spatially-developing flows

The extension to spatially evolving flows is straightforward. The modification necessary is to include the base flow from Blasius, Falkner-Skan or Falkner-Skan-Cooke flows and then proceed as described in the present paper to compute the control and estimation kernels. Assuming that the flow is locally parallel, a number of kernels computed using the Orr-Sommerfeld/Squire equations with the local mean flow profiles can then be applied at different streamwise positions to cover a large control domain. This is done using one control kernel in one streamwise interval in Högberg & Henningson (2001) for stationary as well as time varying perturbations. Application of measurement based control in this case is a natural next step.

#### 4.1.3. Reduced order compensation

The current system has very large dimensions and could be difficult to realize in real time applications. One solution to this problem is to do model reduction of the closed loop system and achieve a low dimensional compensator. Model reduction for robust control of transition in two dimensional channel flow is evaluated in e.g. Cortelezzi & Speyer (1998) and Joshi, Speyer, & Kim (1999), and the three dimensional problem is discussed in Kang et al. (1999). This is an active are of research and many possibilities remain to explored.

# Acknowledgments

The authors thank Bassam Bamieh and Scott Miller for useful discussions related to this work, and Satish Reddy for providing the initial conditions for the transition simulations.

# References

Abergel, F. & Temam, R. 1990 On some control problems in fluid mechanics. Theoret. Comput. Fluid Dyn. 1, 303-325.

- AKSEVOLL, K. & Moin, P. 1995. Large eddy simulation of turbulent confined coannular jets and turbulent flow over a backward facing step. *Report TF-63*, Thermosciences Division, Dept. of Mech. Eng. Stanford University.
- Bamieh, B., Paganini, F., & Dahleh, M. 2000 Distributed Control of Spatially-Invariant Systems. *IEEE Trans. Automat. Contr.*, to appear.
- BARAMOV, L., TUTTY, O. R. & ROGERS, E. 2000 Robust control of plane Poiseuille flow. AIAA Fluid 2000 Conference, 19-22 June 2000, Denver, CO, Paper AIAA-2000-2684
- Bewley, T. R. 2001 Flow control: new challenges for a new Renaissance *Progress in Aerospace Sciences* 37, 21-58.
- Bewley, T. R. 1999 Linear control and estimation of nonlinear chaotic convection: harnessing the butterfly effect. *Phys. Fluids* **11**, 1169-1186.
- Bewley, T. R., & Liu, S. 1998 Optimal and robust control and estimation of linear paths to transition. *J. Fluid Mech.* **365**, 305-349.
- Bewley, T. R. & Moin, P. 1994 Optimal control of turbulent channel flow for reduction of pressure fluctuations. In *Active Control of Vibration and Noise* (K. W. Wang *et al.*eds.) ASME DE, **75**.
- Bewley, T. R., Moin, P., & Temam, R. 2001 DNS-based predictive control of turbulence: an optimal benchmark for feedback algorithms. *J. Fluid Mech.* 477, 179–225.
- Butler, K. M., & Farrell, B. F. 1992 Three-dimensional optimal perturbations in viscous shear flows. *Phys. Fluids* A **4**, 1637-1650.
- Carlson, D. R., Widnall, S. E. & Peeters, M. F. 1982 A flow visualization study of transition in plane Poiseuille flow. *J. Fluid Mech.* **121**, 487-505.
- Choi, H., Moin, P. & Kim, J. 1994 Active turbulence control for drag reduction in wall-bounded flows. *J. Fluid Mech.* **262**, 75–110.
- Choi, H., Temam, R., Moin, P. & Kim, J. 1993 Feedback control for unsteady flow and its application to the stochastic Burgers equation. J. Fluid Mech. 253, 509–543.
- COLLIS, S. S., CHANG, Y., KELLOG, S. & PRABHU, R. D. 2000 Large eddy simulation and turbulence control AIAA-paper 2000–2564.
- CORTELEZZI, L., & SPEYER, J. L. 1998 Robust reduced-order controller of laminar boundary layer transitions. *Physical Review* E **58**, 1906-1910.
- CORTELEZZI, L., SPEYER, J. L., LEE, K. H. & KIM, J. 1998 Robust reduced-order control of turbulent channel flows via distributed sensors and actuators. *Proc.* 37th IEEE Conf. on Decision and Control 2, 1906–1911.
- DOYLE, J. C., GLOVER, K., KHARGONEKAR, P. P. & FRANCIS, B. A. 1989 State-space solutions to standard  $\mathcal{H}_2$  and  $\mathcal{H}_{\infty}$  control problems. *IEEE Trans. Automat. Contr.*, **34** (8), 831–847.
- Drazin, P. G. & Reid, W. H. 1981 *Hydrodynamic Stability*, Cambridge University Press
- FARRELL, B. F., & IOANNOU, P. J. 1996 Turbulence suppression by active control *Phys. Fluids* 8 (5), 1257–1268.
- GAD-EL-HAK, M. 1996 Modern developments in flow control. Appl. Mech. Rev. 49 (7), 364–379.
- HAMMOND, E. P., BEWLEY, T. R. & MOIN, P. 1998 Observed mechanisms for

- turbulence attenuation and enhancement in opposition-controlled wall-bounded flows. Phys. Fluids 10, 2421–2423
- HANIFI, A., SCHMID P. J. & HENNINGSON D. S. 1996 Transient growth in compressible boundary layer flow. Phys. Fluids, 8, (3), 826–836.
- HENNINGSON, D. S. 1996 Comment on "Transition in shear flows. Nonlinear normality versus non-normal linearity" [Phys. Fluids 7, 3060 (1995)] Phys. Fluids 8, (8), 2257 - 2258.
- Henningson, D. S. & Reddy, S. C. 1994 On the role of linear mechanisms in transition to turbulence. Phys. Fluids, 6, 1396-1398.
- HERBERT, T. 1988 Secondary Instability of boundary layers. Ann. Rev. Fluid Mech. **20**, 487-526.
- Hu, H. H. & Bau, H. H. 1994 Feedback control to delay or advance linear loss of stability in planar Poiseuille flow. Proc. Royal Soc. London Ser. A 447, (1930),
- Huang, W., & Sloan, D. M. 1993 The pseudo-spectral method for solving differential eigenvalue problems. J. Comput. Phys. 111, 399-409.
- HÖGBERG, M. & BEWLEY, T. R. 2000<sup>a</sup> Spatially localized convolution kernels for feedback control of transitional flows. In Proc. 39th IEEE Conf. on Decision and Control 4, 3278-3283
- HÖGBERG, M. & BEWLEY, T. R. 2000<sup>b</sup> Spatially-compact convolution kernels for decentralized control and estimation of plane channel flow. Submitted to it Automatica
- HÖGBERG, M. & HENNINGSON, D. S. 2001 Linear optimal control applied to instabilities in spatial boundary layers. Submitted to J. Fluid Mech.
- Ito, K. & Morris, K. A. 1998 An approximation theory of solutions to operator Riccati equations for  $\mathcal{H}^{\infty}$  control. SIAM J. Control optim. **36** (1), 82–99.
- JOSHI, S. S., SPEYER, J. L., & KIM, J. 1997 A systems theory approach to the feedback stabilization of infinitesimal and finite-amplitude disturbances in plane Poiseuille flow. J. Fluid Mech. 332, 157-184.
- Joshi, S. S., Speyer, J. L., & Kim, J. 1999 Finite-dimensional optimal control of Poiseuille flow. J. Guidance, Control, and Dynamics 22 No. 2, 340–348.
- KANG, S. M., RYDER, V., CORTELEZZI, L.& SPEYER, J. L. 1999 State-space formulation and controller design for three-dimensional channel flows Proc. American Control Conference 3, 1627–1631.
- Kim, J. & Lim, J. 2000 A linear process in wall-bounded turbulent shear flows *Phys.* Fluids **12** (8), 1885–1888.
- Koumoutsakos, P. 1997 Active control of vortex-wall interactions. Phys. Fluids 9 (12), 3808-3816.
- KOUMOUTSAKOS, P. 1999 Vorticity flux control for a turbulent channel flow. Phys. Fluids 11 (2), 248–250.
- Laub, A. J. 1991 Invariant subspace methods for the numerical solution of Riccati equations. In The Riccati Equation (ed. Bittaini, Laub, & Willems) 163-196. Springer.
- Lee, K. H., Cortelezzi, L., Kim, J. & Speyer, J. L. 2001 Application of Robust Reduced-Order Controller to Turbulent Flows for Drag Reduction. Phys. Fluids **13** (5), 1321–1330.

- Lee, C., Kim, J., Babcock, D., & Goodman, R. 1997 Application of neural network to turbulence control for drag reduction. *Phys. Fluids* **9** (6), 1740-1747.
- Lee, C., Kim, J. & Choi, H. 1998 Suboptimal control of turbulent channel flow for drag reduction. J. Fluid Mech. 358, 245–258.
- Lumely, J. & Blossey, P. 1998 Control of turbulence. Ann. Rev. Fluid Mech. 30, 311–327.
- METCALFE, R. W. 1994 Boundary layer control: A brief review. In *Computational Fluid Dynamics '94*, *Invited lectures of the Second European CFD Conference; Stuttgart, Germany.* (ed. S. Wagner, J. Periaux, E. Hirschel.), 52–60, John Wiley & Sons.
- Moin, P. & Bewley, T. R. 1994 Feedback control of turbulence. *Appl. Mech. Rev.* 47 (6), part 2, S3-S13.
- Orszag, S. A. 1971 Accurate solution of the Orr–Sommerfeld equation. *J. Fluid Mech.* **50**, 689-703.
- PATEL, V. C. & HEAD, R. 1969 Some observations on skin friction and velocity profiles in fully developed pipe and channel flows. *J. Fluid Mech.* 38, 181-201.
- Rebbeck, H. & Choi, K.-S. 2001 Opposition control of near-wall turbulence with a piston type actuator. *Phys. Fluids* **13** (8), 2142–2145.
- REDDY, S. C., & HENNINGSON, D. S. 1993 Energy growth in viscous channel flows. J. Fluid Mech. 252, 209-238.
- Reddy, S. C., Schmid, P. J., Baggett, J. S., & Henningson, D. S. 1998 On stability of streamwise streaks and transition thresholds in plane channel flows. *J. Fluid Mech.* **365**, 269-303.
- Schmid, P. J., & Henningson, D. S. 2001 Stability and transition in shear flows. Springer.
- Skelton, R. E. 1988 Dynamic Systems Control, Linear Systems Analysis and Synthesis John Wiley & Sons
- Thomas, A. S. W. 1990 Active wave control of boundary-layer transition. In *Viscous Drag Reduction in Boundary Layers* (Bushnell, D. M. & Hefner, J. N., editors). American Institute of Aeronautics and Astronautics, Washington, D.C. Vol. 123 in *Progress in Astronautics and Aeronautics*.
- TREFETHEN, L. N., TREFETHEN, A. E., REDDY, S. C., & DRISCOLL, T. A. 1993 Hydrodynamic stability without eigenvalues *Science* **261**, 578-584.
- Weideman, J. A. C., & Reddy S. C. 2000 A Matlab Differentiation Matrix Suite. ACM Transactions of Mathematical Software 26 (4), 465–519

Paper 5

5

# Optimal control of transition initiated by oblique waves in channel flow

By Markus Högberg\*, Thomas R. Bewley<sup>†</sup>, Martin Berggren<sup>‡§</sup>, and D. S. Henningson\*<sup>‡</sup>

Using two different approaches to optimal control in channel flow an effort is made to try to identify differences and similarities. One approach is to use the Navier-Stokes equations and apply a gradient based optimization technique to find the optimal control. The other approach is to make use of the linearized equations known as the Orr-Sommerfeld-Squire equations to compute the optimal control. Limiting ourselves to look only at oblique wave perturbations we compare the resulting energy evolution from application of the respective control strategies. Qualitatively the performance of the two approaches are similar, at least when they work under comparable conditions. The non-linear control can be more aggressive initially since there is no direct limitation on the time derivative of the control even though the discretization implicitly enforces some degree of penalty. Adjusting the parameters properly we can show that the control from the two approaches are very similar. Also we try to quantify the performance of the estimator based control, or compensation, using only measurements on the wall, compared to the full-state information control. The performance of the compensator is found to be good for small perturbations, especially if a good initial guess can be provided.

## 1. Introduction

The goal of this work is to develop methods to prevent transition to turbulence. We determine how to do control in the optimal way given the method of controlling the flow, and an objective function describing the features of the flow to be controlled. The method of actuation chosen here is blowing and suction at the walls, since it is a fairly simple way of acting on the flow, and also because it is a technique that is widely used. Blowing and suction has successfully been used for similar problems, namely control of turbulence, where complete relaminarization was obtained in Bewley et al.(2001). The blowing and suction is applied to flow in a channel, where we can find many of the

<sup>\*</sup>Department of Mechanics, Royal Institute of Technology (KTH), SE-100 44 Stockholm, Sweden

<sup>&</sup>lt;sup>†</sup>Dynamic Systems & Control Group, Dept. of MAE, UC San Diego, La Jolla, CA 92093,USA

 $<sup>^{\</sup>ddagger} \text{The Swedish Defence Research Agency ( FOI ), SE-172 90 Stockholm, Sweden$ 

<sup>§</sup>Department of Scientific Computing, Uppsala University

interesting bypass transition scenarios. We use two different approaches to optimal control, one based on the non-linear Navier–Stokes equations and one on the 3D Orr–Sommerfeld–Squire equations.

In the non-linear case, we use the adjoint equation to compute objective function gradients. It is an efficient method in the sense that only two computations are required for each optimization iteration independent of the number of degrees of freedom of the control. First the state equation (Navier–Stokes) is solved and then this solution is used as input to the adjoint equation that is solved next and gives the gradient of the objective function. Optimization is performed with a limited memory quasi Newton method described in Byrd et al.(1994). The resulting control will be optimal for the specific perturbation and time domain studied.

In the linear case, optimal  $(\mathcal{H}_2)$  controllers and estimators are developed for the 3D Orr-Sommerfeld–Squire equations at a large array of wavenumber pairs  $\{k_x, k_z\}$ , using a technique closely related to that described by Bewley & Liu (1998), and transformed to the physical domain. The feedback gains for both the control and estimation problems are shown to be represented by well-resolved, spatially-localized convolution kernels, see Högberg and Bewley (2001). The resulting control kernels represent the optimal feedback strategy for an arbitrary perturbation to minimize the energy over the infinite time domain. The physical-space controller, estimator, and compensator which combines them are then applied in (nonlinear) direct numerical simulations of flow in a channel with oblique wave perturbations. The different transition scenarios in channel flow have been bench-marked by Reddy et al. (1998).

# 2. Control problem

An adjoint direct numerical simulation (DNS) code has been developed based on an existing spectral channel flow code by Lundbladh et al. (1992) to perform the non-linear as well as the linear control computations. Temporal DNS are performed. Fourier modes are used for the span-wise and stream-wise directions and Chebyshev collocation in the wall normal direction. The modification necessary to solve the adjoint equations involves a change in what corresponds to the non-linear terms for the Navier–Stokes solver to forcing terms depending on the choice of objective function. Solution of the adjoint equation requires full information about the solution of the Navier–Stokes equation in space and time. Based on previous findings we have used a discretization of the continuous equations instead of an exact discrete adjoint, see Högberg & Berggren (2000). For simulation with an estimator or compensator a similar code bench-marked by Bewley et al. (2001) with finite differences in the wall normal direction is used.

The flow geometry is the one in figure 1 with blowing and suction applied at both walls of the channel and periodic boundary conditions on the streamwise and span-wise directions. For the non-linear optimization the objective

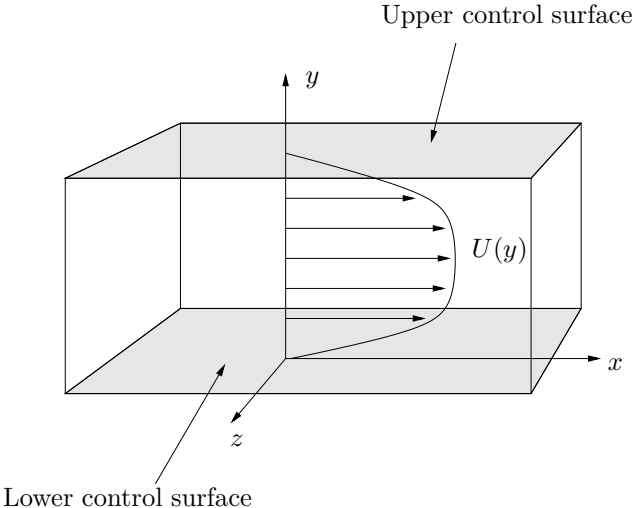


FIGURE 1. Geometry for control of channel flow.

function  $J_{nl}$  is,

$$J_{nl} = \frac{\varepsilon}{2} \int_{T_{C0}}^{T_{CF}} \varphi^2(x, z, t) d\Gamma + \frac{1}{2} \int_{T_{E0}}^{T_{EF}} (u(x, y, z, t) - u_{\text{lam}}(y))^2 d\Omega$$

where the control  $\varphi$  is applied from time  $t = T_{C0}$  to  $T_{CF}$  on the boundary  $\Gamma$ and the energy of the deviation from the laminar profile  $u_{lam}$  is measured from time  $t = T_{E0}$  to  $T_{EF}$  in the computational domain  $\Omega$ . The spatial resolution of the control is the same as for the simulation and temporally the control is linearly interpolated in time. In the linear case the objective function  $J_l$  is,

$$J_{l} = \frac{\varepsilon}{2} \int_{0}^{\infty} \frac{\partial \varphi(x, z, t)}{\partial t}^{2} d\Gamma + \frac{1}{2} \int_{0}^{\infty} (u(x, y, z, t))^{2} d\Omega$$

and the controllers are computed by solving an optimal control problem for each wavenumber pair separately. In short a Riccati equation containing the Orr-Sommerfeld-Squire matrices, the energy measure matrix and the forcing matrix is solved to find the optimal controller. For further details see Högberg and Bewley (2001). The estimator used is an extended Kalman filter and is computed in a way similar to that of the linear controller. The objective function in this case measures the energy of the state error and of the forcing used. The penalty parameter for the forcing is denoted  $\alpha$ . A low value of alpha should be used when the measurements are expected to be free from noise and a high value for noisy measurement data. Notice that the linear controllers and estimators are computed off-line once and for all and then applied online in the simulations.

#### 3. Simulations, results and discussion

All simulations are performed at  $Re = U_c h/\nu = 2000$  where the Reynolds number is based on the half channel height h and the centerline velocity  $U_c$ . The resolution is  $8 \times 65 \times 8$  Fourier  $\times$  Chebyshev  $\times$  Fourier modes in  $x \times 8$  $y \times z$  respectively. For the code with finite differences in the wall normal direction 81 points are used. In all simulations the same particular oblique wave perturbation is used as initial condition at t=0. Control is applied in all Fourier modes on both the upper and lower wall of the channel, and for the estimator case measurements are done in all Fourier modes at both walls. The control is parameterized in the non-linear case to a specific number of degrees of freedom with equispaced distance  $\Delta t$  while in the linear case it is free to change arbitrarily at every time step. For the non-linear optimal control computations about 200 velocity fields are saved during the solution of the flow, and these are then linearly interpolated when used in the solution of the adjoint equations. The penalty parameter  $\varepsilon$  is zero in the non-linear computations since the corresponding objective function for the linear controller does not add extra penalty on the control velocity.

#### 3.1. Non-linear control

We have computed linear controls and corresponding non-linear controls for comparison in terms of performance to investigate how close the optimal linear control is to the optimal non-linear control, with a similar objective function. To allow for comparison between the two different controls we need to make sure that the time interval is long enough to be considered as infinite by the non-linear controller. We also need to adjust the time resolution of the control to get a comparable penalty on the time-derivative. Even if we adjust the parameters to give similar objective functions the non-linear controller still has the advantage of being able to adjust to the particular perturbation and make use of non-linear effects. In figure 2 the energy evolution of the perturbation is plotted for different values of the penalty on the time-derivative of the linear control. A similar restriction can be put on the non-linear controller by changing the time resolution of the control. In figure 3 the effect of changing this resolution for the non-linear controller is plotted. One can say that there is a qualitative correspondence between the penalty on the time-derivative in the linear case and the time-resolution of the control in the non-linear case. Notice that the resolution of the controller in time is not related to the time step in the simulations. Two cases, one with linear control and one with non-linear, with similar behavior initially are compared in terms of the energy evolution if figure 4. Except for the small difference initially it is hard to distinguish one curve from the other. It seems as the linear controller does an almost as good job as the non-linear one in this case. Evaluating the objective functions gives a 2% higher value for the linear controller in this case. A quantitative agreement is obtained by inserting the linear control solution into the nonlinear optimization and computing the gradient norm for this solution. In this case

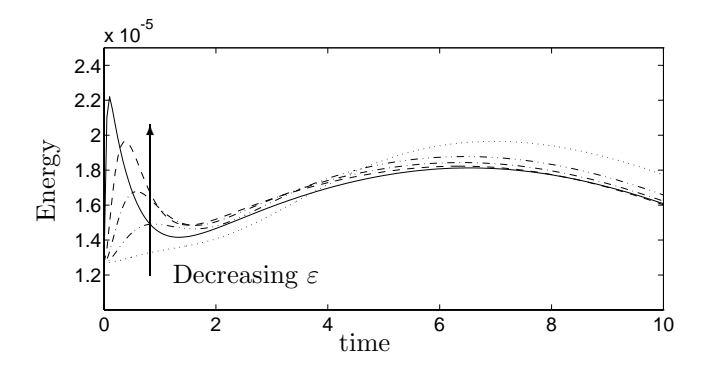


FIGURE 2. Energy evolution of controlled cases with linear control for different values of the penalty parameter  $\varepsilon = 0.01, 0.05, 0.1, 0.2, 0.5$  as solid, dash, dash-dot, dash-dot, dot respectively.

the gradient norm is close to zero and satisfies the optimization criteria for the nonlinear optimization.

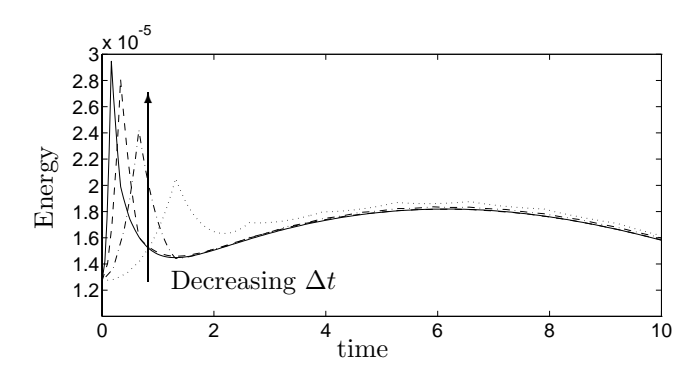


FIGURE 3. Energy evolution of optimally controlled cases with non-linear control for different time resolution of the control. Using 300,150,75,37 degrees of freedom in time as solid, dash, dash-dot, dot respectively.

# 3.2. Linear control

In the linear case we have pre-computed convolution kernels that are applied online in the DNS. The controller, utilizing full information of the flow-field, can prevent transition at perturbation levels well above the uncontrolled transition thresholds computed by Reddy et al.(1998), see Högberg and Bewley (2001). The estimator converges exponentially to the correct state of the flow as shown in figure 5. Unfortunately the rate of this convergence is somewhat low, and there was no way of speeding it up further using the present formulation of the

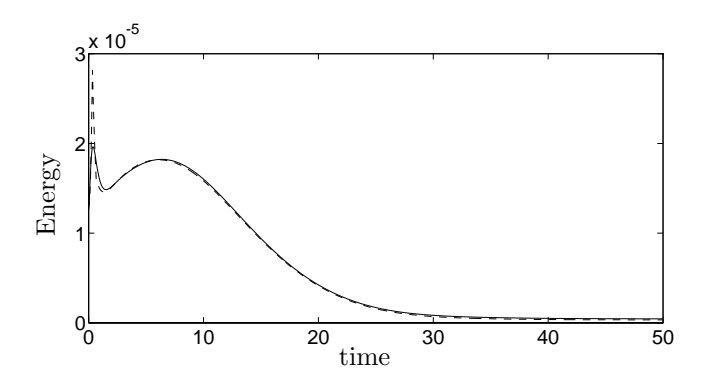


FIGURE 4. Energy evolution of optimal linear control case with  $\varepsilon=0.05$  ( solid ) and optimal non-linear control with 150 degrees of freedom in time ( dash ).

estimation problem. In figure 6 the effect of changing the penalty parameter  $\alpha$  is shown. It turns out that it is favorable to decrease it to obtain speedup of the convergence, but only up to a certain limit. Estimation of the oblique wave perturbation with  $\alpha=0.01$  is illustrated in figure 7. There is a time lag in the energy evolution of the estimator compared to the true state, but eventually the estimator gets closer and closer.

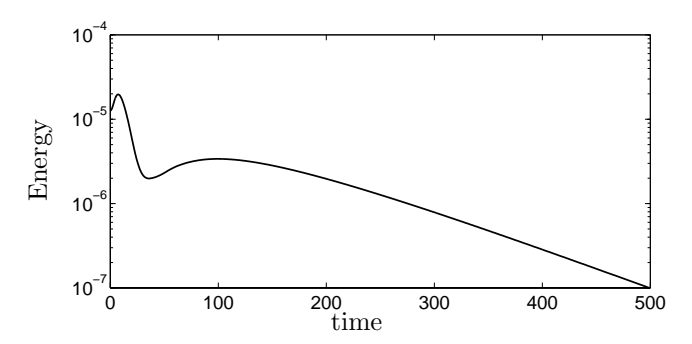


Figure 5. Energy of state error in estimation for  $\alpha = 0.01$ .

Combining the estimator and controller into a compensator where the flow is controlled based only on wall measurements is the next step. With perfect initial data for the estimator the performance would be the same as for full information control. Starting with an unperturbed flow in the estimator is more of a challenge, and the result from this is plotted in figure 8. The compensator is able to lower the energy growth substantially but not as much as the full information controller. In a spatial case one could imagine having the estimator upstream of the controller. Here that would correspond to giving the estimator a head start before applying control. Estimating the flow until t=50 and then applying the compensator and comparing it to the full information controller

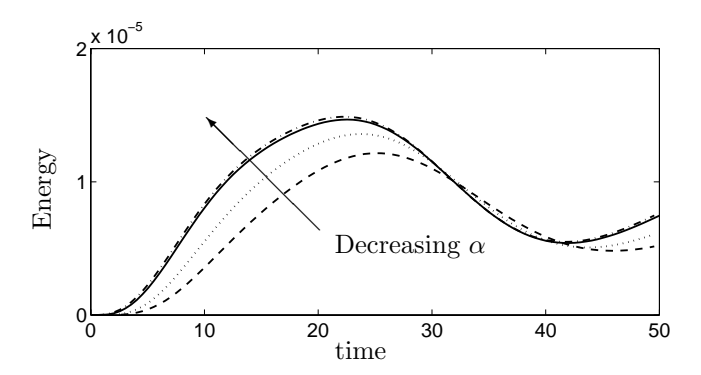


FIGURE 6. Energy evolution in estimator with different values on the penalty parameter  $\alpha$ = 0.001, 0.01, 0.05, 0.1, as dashdot, solid, dotted, dashed respectively.

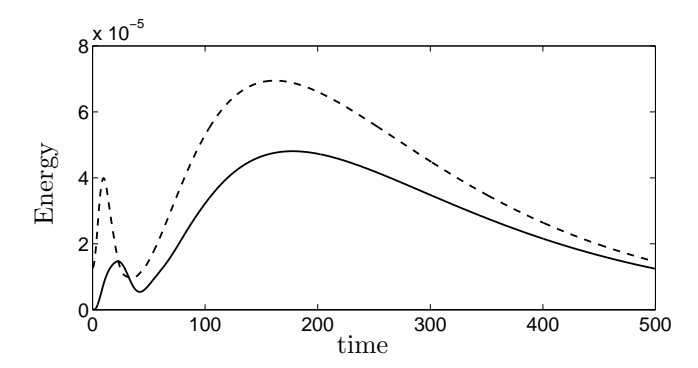


FIGURE 7. Energy evolution of the estimator with  $\alpha=0.01$  (solid ) and the true uncontrolled state ( dash ).

applied at t=50 shows that the compensator performance is now close to that of the full information controller. In figure 9 the energy evolution for the full information control case is compared to that of the "head started" compensator and the regular compensator with zero perturbation as initial guess at t=50.

# 3.3. Conclusions

The action of the optimal linear controller is very similar to that of the optimal non-linear control. A comparison with a nonlinear optimal controller, based on iterative adjoint computations, shows only small differences to the controllers based on the linearized equations. The perturbation evolution can be reproduced from wall measurements online, using an estimator with exponential convergence rate after some initial transients. When basing the control on wall measurements only the performance is not as good, but still energy growth is reduced. Giving the compensator a better initial guess improves the

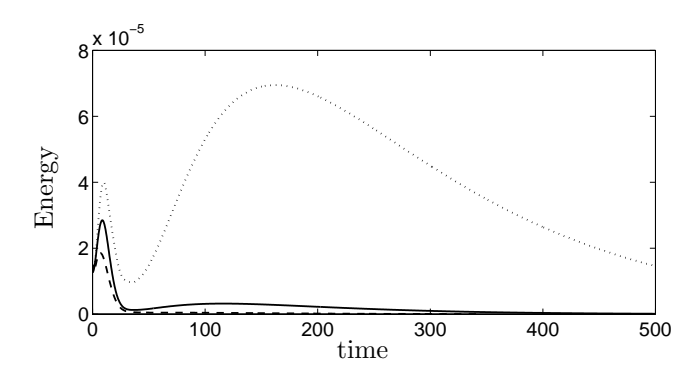


FIGURE 8. Full information linear controller ( dashed ) and compensator ( solid ) performance compared to the uncontrolled ( dotted ) energy evolution.

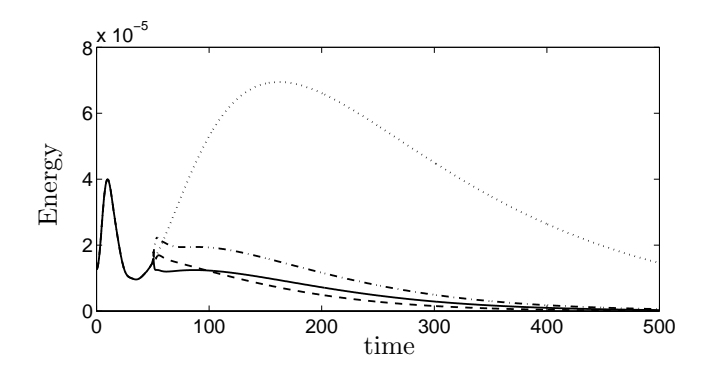


FIGURE 9. Full information controller ( dash ) and "head started" compensator ( solid ) and regular compensator (dashdot ) performance compared to the uncontrolled ( dot) energy evolution.

performance substantially. One future focus for linear compensation should be development of better estimators with fast convergence.

# References

Bewley, T. R., Moin, P. & Temam, R. 2001 DNS-based predictive control of turbulence: an optimal target for feedback algorithms. *J. Fluid Mech.* 477, 179–225.

Bewley, T. R. & Liu, S. 1998 Optimal and robust control and estimation of linear paths to transition *J. Fluid Mech.* **365**, 305-349

Byrd, R. H., Peihuang, L., Nocedal, J. & Zhu, C. 1994 A limited memory

- algorithm for bound constrained optimization *Technical Report NAM-08* Northwestern University.
- Högberg, M. & Bewley, T. R. 2001 Spatially localized convolution kernels for decentralized control and estimation of transition in plane channel flow. Submitted to Automatica
- HÖGBERG, M. & BERGGREN, M. 2000 Numerical approaches to optimal control of a model equation for shear flow instabilities. *Journal of Flow, Turbulence and Combustion* **65**, (3/4), 273–298.
- Lundbladh, A., Henningson, D. S. & Johansson A. V. 1992 An Efficient Spectral Integration Method for the Solution of the Navier-Stokes Equations. FFA TN 1992-28
- REDDY, S. C., SCHMID, P. J., BAGGETT, J. S. & HENNINGSON, D. S. 1998 On stability of streamwise streaks and transition thresholds in plane channel flows. *J. Fluid Mech.* **365**, 269-303

Paper 6

# Secondary instability of cross-flow vortices in Falkner-Skan-Cooke boundary layers

By Markus Högberg\* and Dan Henningson\*†

Linear eigenvalue calculations and spatial direct numerical simulations (DNS) of disturbance growth in Falkner-Skan-Cooke (FSC) boundary layers have been performed. The growth rates of the small amplitude disturbances obtained from the DNS calculations show differences compared to linear local theory, i.e. non-parallel effects are present. With higher amplitude initial disturbances in the DNS calculations, saturated cross-flow vortices are obtained. In these vortices strong shear layers appear. When a small random disturbance is added to a saturated cross-flow vortex, a low frequency mode is found located at the bottom shear layer of the cross-flow vortex and a high frequency secondary instability is found at the upper shear layer of the cross-flow vortex. The growth rates of the secondary instabilities are found from detailed analysis of simulations of single frequency disturbances. The low frequency disturbance is amplified throughout the domain, but with a lower growth rate than the high frequency disturbance, which is amplified only once the cross-flow vortices have started to saturate. The high frequency disturbance has a growth rate that is considerably higher than the growth rates for the primary instabilities, and it is conjectured that the onset of the high-frequency instability is well correlated with the start of transition.

#### 1. Introduction

A disturbance in an unstable laminar flow often results in transition to a turbulent state, but in some cases it takes the flow into another laminar more complicated state. If the disturbances are small, compared to the base flow, the analysis can be simplified by using linearized equations for the disturbance evolution. If the disturbances reach a higher level, nonlinear effects become important. Traditionally, transition prediction in two-dimensional flows has been based on the study of the evolution of so called Tollmien-Schlichting (T-S) waves. The growth of these waves is governed by the Orr-Sommerfeld equation. For flows where this exponential instability is weak, recent work by Butler & Farrell (1992); Reddy & Henningson (1993); Trefethen et al. (1993) have shown the importance of transiently growing three-dimensional disturbances .

<sup>\*</sup>Department of Mechanics, Royal Institute of Technology (KTH), SE-100 44 Stockholm, Sweden

<sup>&</sup>lt;sup>†</sup>The Swedish Defence Research Agency (FOI), SE-172 90 Stockholm, Sweden

Typically, this growth results in streaky structures rather than two-dimensional waves. For an overview of results regarding transient growth, see Henningson (1995).

In three-dimensional boundary layer flows, there are additional processes that can lead to transition. Examples of such flows are, flow over swept wings, rotating discs, cones and spheres and cones at an angle of attack. More about these flows can be read in Reed & Saric (1989). In a three-dimensional flow the direction of the base flow is a function of the normal coordinate, and the velocity profile usually has an inflection point. This means that there usually exists an inviscid inflectional instability, see e.g. Gregory, Stuart, & Walker (1955). This primary instability may result in amplification of oblique traveling waves and of stationary vortices. Local linear stability theory predicts nonstationary modes to be more amplified than stationary modes. However in most experiments the stationary ones are preferred Reed & Saric (1989). The reason may be that the effective receptivity of stationary cross-flow modes to surface roughness is stronger than that for traveling waves to free-stream fluctuations, see Choudhari (1994), Morkovin (1969) and Morkovin (1977) for receptivity issues. Another reason may be related to phase averaging in the experimental measuring techniques. Only recently has measurements been made where the traveling modes have been introduced in three-dimensional boundary layer flow in a repeatable manner, see e.g. Lingwood (1996), Lerche (1997).

Effects of transient growth have also been seen in three-dimensional boundary layers, see Breuer & Kuraishi (1994), although it may here be of less importance due to the large growth rates of the primary exponential instabilities present.

In addition to the convective instabilities discussed so far, there is evidence that three-dimensional boundary layers may experience so called absolute instabilities. These are instabilities which grow at a fixed location, without being swept downstream by the base flow. In a rotating disc boundary layer a true absolute instability has been found by Lingwood (1995), whereas in for infinite swept plate boundary layers a chordwise absolute instability has been found, see Lingwood (1997). The disturbances associated with the latter absolute instability are still swept away in the spanwise direction and it is not clear that they would have any greater chance of causing transition than traditional convective instabilities.

When stationary cross-flow modes are initiated they grow according to linear theory until nonlinear effects cause saturation, and strong so called cross-flow vortices develop. There are two types of secondary instability of stationary cross-flow vortices that have been observed in simulations and experiments by Kohama, Saric & Hoos (1991); Malik, Li & Chang (1994); Deyhle & Bippes (1996) and reported in a thesis of Lerche (1997), one low frequency and one high frequency instability. The low frequency oscillations appear earlier in the breakdown process than the high frequency one. The high frequency oscillations

have been detected just prior to breakdown. At this point, the strong cross-flow vortices contain sharp shear layers that appear to be inflectionally unstable, see Malik, Li & Chang (1994).

A slightly different scenario has been found by e.g. Müller & Bippes (1988), who found that is was the traveling modes which dominated the transition process. The reason this occurred is the higher level of free-stream turbulence that was present in their experiment, which caused a stronger forcing of timedependent disturbances. Although the amplitude of the stationary modes was smaller in this scenario, compared to flows with lower free-stream turbulence, the transition occurred earlier.

In this investigation we use direct numerical simulations (DNS) to obtain a physical understanding of the breakdown process of stationary cross-flow vortices. Direct numerical simulations have been used previously to study the stability and transition associated with cross-flow vortices, e.g. Müller, Bestek & Fasel (1993); Spalart, Crouch & Ng (1994); Wintergerste & Kleiser (1996). However, none have concentrated on the secondary instability of cross-flow vortices, which is the main aim of the present investigation. In a computational environment it is straight forward to generate a base flow including strong crossflow vortices, and then add a desired disturbance. We use a base flow from an experiment made at DLR, Göttingen by Bippes (1991), that is suitable for investigations of cross-flow vortices and their stability features. Linear stability calculations are made as well as DNS, and the results are analyzed and compared. In addition results of secondary instability of cross-flow vortices are also reported.

#### 2. Background

## 2.1. Falkner-Skan-Cooke Profiles

We consider an infinite swept flat plate where  $\frac{\partial}{\partial z} = 0$ . For this case the dimensional boundary layer equations according to Schlichting (1979) become:

$$u^* \frac{\partial u^*}{\partial x^*} + v^* \frac{\partial w^*}{\partial y^*} = U_{\infty}^* \frac{\mathrm{d}U_{\infty}^*}{\mathrm{d}x^*} + \nu \frac{\partial^2 u^*}{\partial y^{*2}}$$
 (1)

$$u^* \frac{\partial w^*}{\partial x^*} + v^* \frac{\partial w^*}{\partial y^*} = \nu \frac{\partial^2 w^*}{\partial y^{*2}}$$
 (2)

$$\frac{\partial u^*}{\partial x^*} + \frac{\partial v^*}{\partial y^*} = 0 \tag{3}$$

with the boundary conditions:

$$u^* = v^* = w^* = 0 \quad at \quad y^* = 0 \tag{4}$$

$$u^* \to U_{\infty}^*, w^* \to W_{\infty}^* \quad as \quad y^* \to \infty$$
 (5)

where  $u^*, v^*, w^*$  are the chordwise (x), normal (y) and spanwise (z) velocity components, respectively, and \* denotes dimensional quantities. See figure 1 for a definition of the coordinate system. We assume that the chordwise base flow at the boundary layer edge obeys a power law according to,  $U_{\infty}^* = U_0^* (x^*/x_0^*)^m$  and that  $W_{\infty}^* = \text{constant}$ . A self-similar solution may be found if we select

$$\eta = \{ (m+1)U_{\infty}^*/2\nu x^* \}^{1/2} y^* \tag{6}$$

Introducing the stream-function

$$\Psi^* = (2U^*\nu x^*/m + 1)^{1/2} f(\eta) \tag{7}$$

with  $u^*=\partial\Psi^*/\partial y^*$  and  $v^*=-\partial\Psi^*/\partial x^*$  and  $w^*=W_\infty^*g(\eta)$  reduces the boundary layer equations to a function of the single variable  $\eta$ , we have

$$f''' + ff'' + \beta_H (1 - f'^2) = 0 (8)$$

$$g'' + fg' = 0 (9)$$

where the Hartree parameter is  $\beta_H = 2m/(m+1)$  and the boundary conditions are

$$f = f' = g = 0 \quad if \quad \eta = 0 \tag{10}$$

$$f' \to 1, g \to 1 \quad as \quad \eta \to \infty$$
 (11)

f' and g can then be combined into the Falkner-Skan-Cooke velocity profiles, see Cooke (1950), as

$$U(y) = f'[\eta(y)] \tag{12}$$

$$W(y) = \frac{W_{\infty}^*}{U_{\infty}^*} g[\eta(y)]. \tag{13}$$

with  $y = y^*/\delta_0^*$ . Note that

$$\delta^* = \{ (m+1)U_{\infty}^* / 2\nu x^* \}^{-1/2} \int_{0}^{\infty} (1-f') d\eta$$
 (14)

which implies that

$$\delta_0^* = \{(m+1)U_0^*/2\nu x_0^*\}^{-1/2}C\tag{15}$$

where

$$C = \int_{0}^{\infty} (1 - f') \mathrm{d}\eta \tag{16}$$

Then we have

$$\eta = C \left\{ \frac{U_{\infty}^* x_0^*}{U_0^* x^*} \right\}^{1/2} y \tag{17}$$

where  $x_0^*$  is a fixed position. The profiles (12) and (13) will be used as a base flow in the stability investigations and as initial conditions in the direct numerical simulations presented.

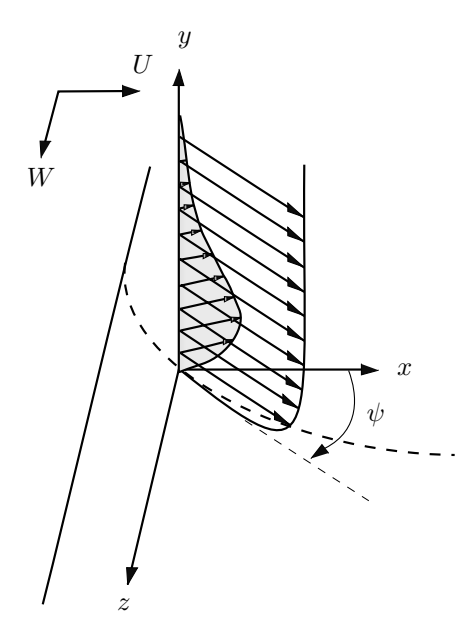


FIGURE 1. Coordinate system used in this report.  $\psi$  is the angle to the streamline of the flow in the free-stream, U is the chordwise component and W is the spanwise component. The dotted line is the streamline of the flow in the freestream over a flat plate with a pressure gradient in the x direction

# 2.2. Linear Theory

The most common way of investigating the stability of a flow to small disturbances, is to assume that the flow can be divided into two parts,

$$(u, v, w) = (U, 0, W) + (u', v', w')$$
(18)

where U and W are the base flow components in the chordwise and spanwise directions, respectively. It is here assumed that the parallel flow assumption holds, i.e. the base flow components only varies with the normal coordinate. The primed quantities represent a small perturbation. We also assume wavelike disturbance of the form

$$u' = \hat{u}e^{i(\alpha x + \beta z - \omega t)} \tag{19}$$

where  $\alpha$  and  $\beta$  are the x and z components of the wave number vector and  $\omega$  is the frequency and  $\hat{u}$  is the complex amplitude function for the chordwise velocity. Inserting these assumptions into the Navier-Stokes equations and linearizing, we find the resulting disturbance equations that can be reduced to the following set of two coupled equations

$$[D^2 - (\alpha^2 + \beta^2)]^2 \hat{v} = iR[(\alpha U + \beta W - \omega)[D^2 - (\alpha^2 + \beta^2)] -$$

x	$R_{\delta^*}$	$\psi$ (deg.)
0	337.9	55.3
20.59	351.2	54.7
209.5	461.6	50.9
220.0	467.3	50.7
261.9	490.0	50.0
500	694.1	44.98

TABLE 1. Relations between different parameters at different locations on the flat plate.  $R_{\delta^*}$  is the Reynolds number based on the displacement thickness and the local free-stream velocity and  $\psi$  is the angle of the external streamline.

$$(\alpha D^2 U + \beta D^2 W)]\hat{v} \tag{20}$$

$$(\alpha DW - \beta DU)\hat{v} = \left[\frac{1}{R}(D^2 - (\alpha^2 + \beta^2)) - i(\alpha U + \beta W - \omega)\right]\hat{\eta} \quad (21)$$

where  $\hat{v}$  and  $\hat{\eta} = i(\beta \hat{u} - \alpha \hat{w})$  are the amplitude functions for the normal velocity and the normal verticity, respectively. D stands for the differential operator in the wall-normal direction. The boundary conditions are

$$\hat{v}(0) = 0 , \, D\hat{v}(0) = 0 , \, \hat{\eta}(0) = 0$$
 (22)

$$\hat{v}(y) \to 0, \ D\hat{v}(y) \to 0, \ \hat{\eta}(y) \to 0 \text{ as } y \to \infty$$
 (23)

Here R is the Reynolds number based on the velocity scale  $U_{\infty}$  and the displacement thickness  $\delta^*$ , both taken at the streamwise location  $x_0$ .

Equation (20) is referred to as the Orr-Sommerfeld equation, and the equation (21) is known as the Squire equation. The base flow used in this investigation is found from the Falkner-Skan-Cooke (FSC) velocity profiles given in the previous section. The equations, considered as a spatial eigenvalue problem, are solved using a spectral collocation technique with Chebyshev polynomials in the normal direction, and a companion matrix technique. The technique is explained e.g. in Lundbladh et al. (1994).

Results from the spatial eigenvalue problem will be compared to results from the Parabolic Stability Equations (PSE). This extended approximation offers an effective way to take non-parallel effects into account using an advanced multiple scales technique, first developed by Bertolotti, Herbert & Spalart (1992). In this paper we present results by Hanifi (private communication) as a check on the direct numerical simulation results. The PSE code used is described in Hanifi et al. (1994).

The computations model an experiment made by Bippes (1991) at DLR in Göttingen, where the flow over a swept flat plate has been designed to approximate Falkner-Skan-Cooke flow. In the experiment small discs were placed periodically close to the front of the plate, in order to excite well defined cross-flow vortices. Their spanwise spacing was chosen to be approximately the same as that of the most growing stationary cross-flow disturbance. We will use the flow conditions of this experiment as the laminar base flow in the present investigation.

It is important to note that we are not primarily concerned with the details of the numerical modeling of the experiment. For us it suffices to know that we have chosen a test case which is of practical interest and can be realized in an experiment. In addition, the previous investigations of Bippes (1991) did not address the secondary instability of the cross-flow vortices, which are the emphasis of the present paper, but rather their interaction with traveling waves. Unfortunately, the later work dealing with the high-frequency secondary instability by Lerche (1997), a student of Hans Bippes, was done at slightly different flow conditions. Thus a detailed quantitative comparison of the present results with that of Lerche (1997) cannot be made, and we have to be content to compare the qualitative features.

In all of the simulations presented here the inflow position in the computational domain will be at x=0, corresponding to a Reynolds number of R=337.9. Unless otherwise stated, the calculations presented will be scaled with the displacement thickness and the free-stream velocity at this position. With this scaling the distance from the leading edge to the start of the computational box can be found using equation (15) and is found to be

$$x_0 = \frac{m+1}{2C^2}R = 354.0, (24)$$

and the distance between the small discs generating the cross-flow vortices are about 25.14, corresponding to a spanwise wavenumber of about  $\pm 0.25$ . The outflow position in the computations is located 500 initial displacement thicknesses downstream, which corresponds to  $R_{\delta^*}=694.1$ . Note that when  $R_{\delta^*}$  rather than R is used, we assume that the Reynolds number is based on the local displacement thickness and free-stream velocity. The base velocity at the boundary layer edge in the experiment by Bippes (1991) can now be written

$$U_{\infty} = \left(\frac{x}{x_0} + 1\right)^{0.34207} \tag{25}$$

$$W_{\infty} = 1.442 \tag{26}$$

See Högberg & Henningson (1996) for a further discussion of issues relating to the computational modeling of the experiment and table 1 for the relationships between the coordinates used in the computational box, the Reynolds number and the angle of the external streamline of the Falkner-Skan-Cooke flow.

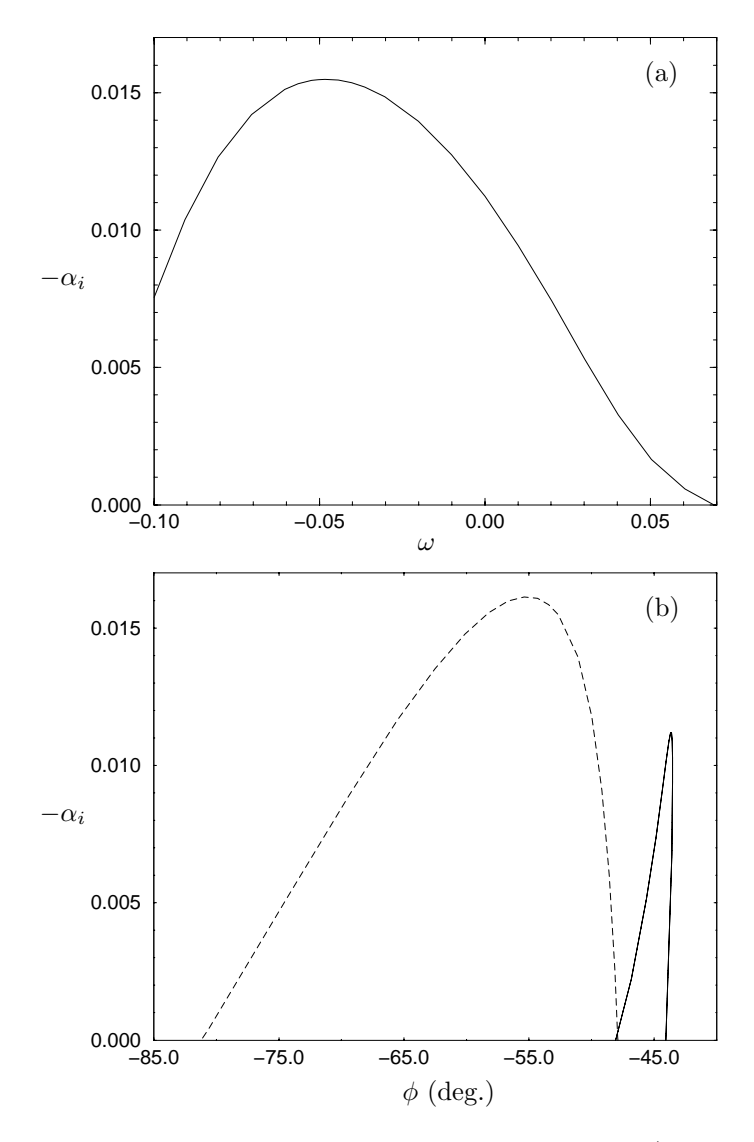


FIGURE 2. Growth rates for  $\beta=0.25$  at x=261.9. a) Growth rate v/s. frequency. b) Growth rate v/s. angle of wave number vector. Solid line:  $\omega=0.0$ ; dashed:  $\omega=-0.04835$ 

# 2.4. Linear stability characteristics of the base flow

In figures 2 (a,b) the behavior of the unstable modes with a wavenumber  $\beta = -0.25$  is shown at a chordwise position x = 261.9, corresponding to  $R_{\delta^*} = 490.0$ . This chordwise position is about halfway between the inflow and the outflow of the computational domain used in the numerical simulations, and should thus give a good idea of the typical behavior of the unstable

modes expected in the calculations. The results are found by use of the Orr-Sommerfeld and Squire equations derived in section 2.2.

Figure 2(a) shows the growth rate vs. the frequency, and it is clear that traveling modes are more unstable than the stationary one. In figure 2(b) the growth rates of the stationary mode and the traveling mode with largest growth rate ( $\omega = -0.04835$ ) is shown vs. the angle of the wavenumber vector. It is seen that the traveling modes are unstable for a broad range of angles, whereas the stationary mode is only unstable for waves with a wave angle of about 45°. This implies that the phase lines of the unstable stationary modes, and thus the direction of the resulting cross-flow vortices are about 45°. This angle is close to the angle of the Falkner-Skan-Cooke free-stream velocity vector at that chordwise position.

#### 2.5. Direct Numerical Simulations

The incompressible Navier-Stokes equations, for flow over a flat plate, are discretized using a spectral method. For spatial simulations, a fringe region technique is used to allow a streamwise inflow and outflow of the computational domain, retaining the periodic boundary conditions. At a constant distance from the flat plate an artificial boundary is introduced and a free-stream boundary condition applied. The horizontal directions are discretized using Fourier series and the normal direction using Chebyshev series. Time integration is performed using a third order Runge-Kutta method for the advective and forcing terms and a Crank-Nicolson for the viscous terms. More about the code can be found in Lundbladh, Henningson & Johansson (1992); Lundbladh et al. (1994). The disturbances in the flow field are generated using localized volume forces,

$$\frac{\partial \mathbf{u}}{\partial t} = NS(\mathbf{u}) + \lambda(x)(\mathbf{u} - \mathbf{u}_{\lambda}) + F, \tag{27}$$

where  $\mathbf{u} = (u, v, w)$ . The term  $\lambda(x)(\mathbf{u} - \mathbf{u}_{\lambda})$  is the fringe forcing, where  $\mathbf{u}_{\lambda}$  is the desired flow solution in the fringe and  $\lambda(x)$  is a non-negative fringe function which is non-zero only in the fringe region. The localized disturbance forcing is given by the vector  $F = (F_1, F_2, F_3)$ . It is possible to generate different kinds of disturbances, both random and harmonic.

The random forcing is constructed by randomly distributing the amplitude among a given number of spanwise Fourier components at each time interval. The random forcing, which is directed normal to the wall, has the form

$$F_2 = F_{rand} = e^{(-((x-x_0)/x_{scale})^2 - (y/y_{scale})^2)} f(z,t)$$
(28)

where

$$f(z,t) = t_{amps}g(z) + t_{ampt}[(1 - b(t))h^{i}(z) + b(t)h^{i+1}(z)]$$
(29)

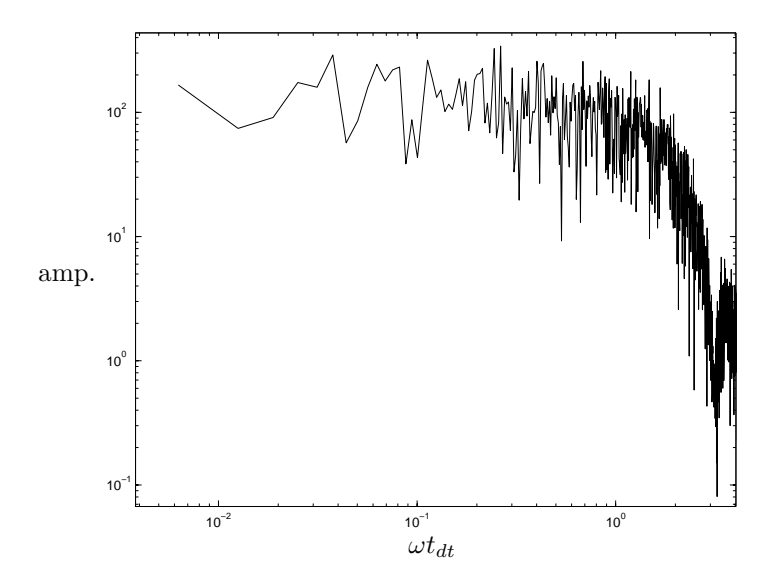


FIGURE 3. Frequency spectrum for the random part of the local forcing.

and

$$i = \inf(t/t_{dt}) \tag{30}$$

$$i = \inf(t/t_{dt})$$
 (30)  
 $b(t) = 3p^2 - 2p^3$  (31)  
 $p = t/t_{dt} - i$  (32)

$$p = t/t_{dt} - i (32)$$

g(z) and  $h^{i}(z)$  are Fourier series of unit amplitude with random coefficients, and  $t_{ampt}$ ,  $t_{amps}$  is the time dependent and the stationary disturbance amplitude, respectively. The number of random coefficients in each Fourier series is given by a parameter named  $n_{modes}$ . Random values are generated for  $h^{i}(z)$  with the spacing  $t_{dt}$  in time and then the ramp function b(t) is used to interpolate this to a smooth forcing. The frequency spectrum for the random part of the forcing is almost constant in the range  $\omega = 0$  to  $\omega = 1/t_{dt}$  and then decays quickly to zero outside, see figure 3.

The harmonic disturbance is constructed as an exponentially decaying function centered at y=0 and  $x=x_{loc0}$ . It is also possible to give a relationship between the x and z component of the disturbance to align the disturbance to a streamline. The harmonic forcing has the form

$$F_2 = F_{harm} = amp_y e^{(-(y/y_{scale})^2)} g(x, z) f(t) h_1(t)$$
 (33)

where

$$g(x,z) = \cos(2\pi(z - xl_{skew})/z_{scale})e^{-[(x-x_{loc0})/x_{scale}]^2}$$
 (34)

			Stationary forcing		Time-dependent forcing			_	
Case	Box	Resolution	Pos.	Type	$t_{ m amps}$	Pos.	Type	$t_{ m ampt}$	$\omega$
1	A	$384 \times 49 \times 4$	20.59	A	$10^{-5}$				
2	A	$384 \times 49 \times 4$				20.59	$^{\rm C}$	$5*10^{-6}$	0.04835
3	В	$192\times49\times48$	20.59	В	$10^{-3}$				
4	В	$192 \times 49 \times 48$				20.59	D	$10^{-3}$	
5	A	$384 \times 49 \times 16$	20.59	A	$3.6 \times 10^{-3}$				
6	A	$576 \times 65 \times 24$	20.59	A	$3.6 \times 10^{-3}$				
7	A	$576 \times 49 \times 24$	20.59	A	$3.6 \times 10^{-3}$	20.59	D	$10^{-5}$	
8	A	$576 \times 65 \times 24$	20.59	A	$3.6 \times 10^{-3}$	209.5	D	$10^{-4}$	
9	A	$768 \times 65 \times 24$	20.59	A	$3.6 \times 10^{-3}$	209.5	D	$10^{-4}$	
10	A	$768 \times 65 \times 24$	20.59	A	$3.6 \times 10^{-3}$	20.59	$^{\rm C}$	$10^{-6}$	0.0957
11	A	$768 \times 65 \times 24$	20.59	A	$3.6 \times 10^{-3}$	220.0	$^{\rm C}$	$10^{-3}$	0.957

Table 2. Summary of the different simulations where Box A denotes  $500 \times 8 \times 25.14$  and Box B denotes  $500 \times 8 \times 251.4$ . Lower table shows the type of forcing.

and

$$f(t) = S(-t/t_{scale}) \tag{35}$$

where

$$S(x) = \begin{cases} 0 & x \le 0\\ 1/[1 + e^{\frac{1}{x-1} + \frac{1}{x}}] & 0 < x < 1\\ 1 & x \ge 1 \end{cases}$$

and

$$h_1(t) = \cos(\omega_h t) \tag{36}$$

The function f(t) must be used to give a smooth turn on of the forcing to avoid problems with transients that may grow and cause transition in the flow. For stationary disturbances  $\omega_h$  is chosen as zero, otherwise it is the  $\omega$  given in table 2. In the simulations presented in this paper  $amp_y$  is designated  $t_{amps}$  for stationary disturbances or  $t_{ampt}$  for time-dependent (oscillating) disturbances.

Table 2 contains information about the different flow cases that have been simulated. Cases 1–4 have small enough amplitudes such that the disturbance evolution is linear, with the latter two simulations having a computational box width ten times the former and a random disturbance generation. Cases 5–11 all have the smaller spanwise box size and have disturbances for which nonlinear effects are significant. The resolution has been checked in several ways. Comparing the results from cases 5 and 6, 8 and 9, and 7 and 10 confirmed that the resolution is sufficient in our simulations. The growth rate curves from cases 5 and 6 were the same, and so were they for cases 8 and 9.

## 3. Results

#### 3.1. Comparison between Linear Theory and DNS

As a check on the numerics we start with a comparison between results of linear stability theory, PSE and direct numerical simulations. We consider the exponential amplification of disturbances in a spatially growing boundary layer. First a start field is generated, using the FSC profiles, and then a stationary or time-dependent disturbance is generated using a volume force at  $x=20.95, R_{\delta^*}=351.2$  see Table 2, to obtain the cross-flow vortices or the traveling waves. The Navier-Stokes equations are then solved until a stationary or periodic state is achieved.

First we will verify that the spanwise spacing of the disturbance generators in the experiments corresponds to a mode of maximum growth rate. We use a computational domain in the spanwise direction which is ten times greater than that associated with a single mode and introduce random stationary disturbances along a line parallel to the leading edge. In figure 4, which is labeled as case 3 in table 2, the normal velocity associated with the cross-flow eigenmode is shown viewed from below. The disturbances grow downstream and appear to be inclined at about 45 degrees. This corresponds to the most unstable direction in figure 2(b) for the zero-frequency disturbance. At the end of the box in figure 4 there are ten vortices, corresponding to a wave length in the zdirection that is equivalent to the width of the computational box used in the rest of the direct numerical simulations presented. Thus, the spacing of the roughness elements used in the experiments by Bippes (1991) to generate the vortices is indeed close to the wavelength of the most unstable zero-frequency mode. In case 4, a small amplitude random disturbance was introduced at the same location as in case 3. This disturbance gave oblique, unsteady, traveling waves similar to what Müller & Bippes (1988) found in a study with higher free-stream forcing. In their case the transition process was dominated by the traveling modes.

The growth rate is the complex part of the chordwise wave number,  $-\alpha_i$ . In figure 5 this is compared to the chordwise derivative of the disturbance magnitude and results from cases 1,2,6 shown. Here the disturbance is generated with a stationary or time-dependent (harmonic) forcing. Note that due to the

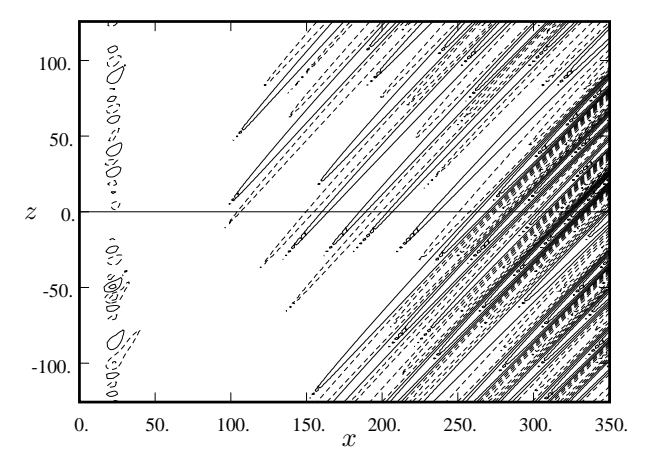


FIGURE 4. Contour lines of the disturbance velocity in the normal direction at y=0.5. The spacing between the contours is 0.00005; The vortices are generated by random stationary disturbances at x=20.95.

presence of non-parallel effects the correspondence is poor between linear theory and DNS. This is also true for the non-stationary disturbance which is chosen to correspond to the one with maximum spatial growth rate. The good agreement between PSE results and DNS is a verification of the validity of the DNS results. The dips in the growth rate curves obtained from the DNS results from the fact that the local forcing does not input pure eigenmodes.

#### 3.2. Base Flow - Saturated Vortices

When the amplitude of the initial disturbance in the DNS is increased, the cross-flow vortices reach a saturated state, where the exponential disturbance growth is suppressed by nonlinear effects. For the flow with saturated vortices we have to increase the number of spectral modes as has been done in cases 5 and 6. The saturation can be seen in the decrease of the spatial growth rate of the stationary higher amplitude disturbance, also shown in figure 5. Contours of the chordwise velocity in an x-y plane is shown in figure 6(a), where the strong saturated vortices can be clearly seen.

As a starting point of the investigations of the interaction between traveling and stationary cross-flow modes a base flow with saturated cross-flow vortices can be used. To this base flow it is possible to add disturbances at different locations and with different structures. The saturated vortices contain strong shear layers, as seen in figure 6(a), which can be expected to support secondary instabilities. The shear layer at the bottom of the vortex is a result of fluid moving at a high velocity coming down with the vortex towards the wall into a region with a lower velocity. The layer on the side and at the top of the vortex

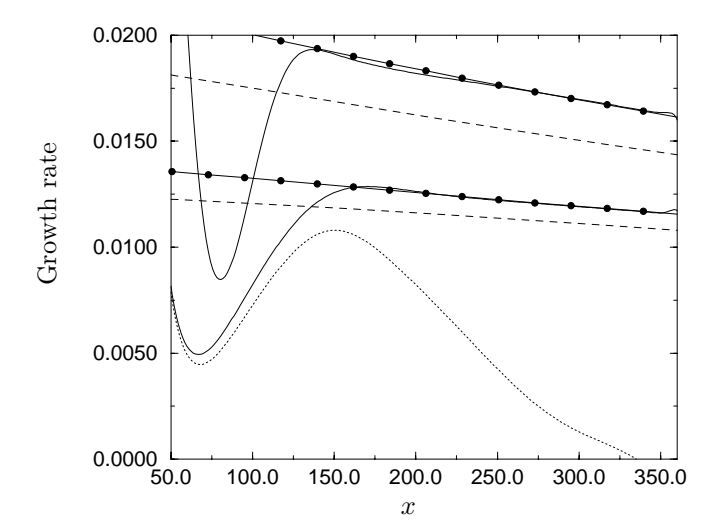


FIGURE 5. Growth rates v/s. x. Solid lines: Results from DNS calculations  $\omega=0$  (lower) and  $\omega=-0.04835$  (upper); dashed: results of local eigenvalue computation for the same frequencies; dotted: DNS calculation for flow with saturated cross-flow vortices; filled circle: results from nonlocal PSE calculations (A. Hanifi, private communication)

is the result of that low velocity fluid is carried by the vortex into a region with fluid moving at a higher velocity.

#### 3.3. Secondary instabilities

Figures 6(b,c) shows the response of the vortex to time-dependent random forcing at two different positions. These results will be described in some detail in the next two sections.

# 3.3.1. Low Frequency Mode

When a random time-dependent disturbance is located at the same x value as the stationary disturbance, a low frequency oscillation develops downstream in the box. In figure 6(b) the rms values of the flow in the vortices are shown. It seems that the disturbance growth is supported mainly in the shear layer at the bottom of the vortex.

Figure 7 shows the instantaneous chordwise disturbance velocity in a field where the stationary time averaged mean flow,  $u_{mean}$ , is subtracted. The levels of the disturbance are low compared to the vortex. In the frequency spectrum from case 7 in figure 8, taken in the center of one of the vortex rms contours  $(x=337,\ y=2.5\ {\rm and}\ z=0)$ , there is a peak at a frequency in the region of the most amplified traveling wave. If we study figure 2(a), we can see that this frequency is unstable from linear analysis, but has a lower growth rate than it

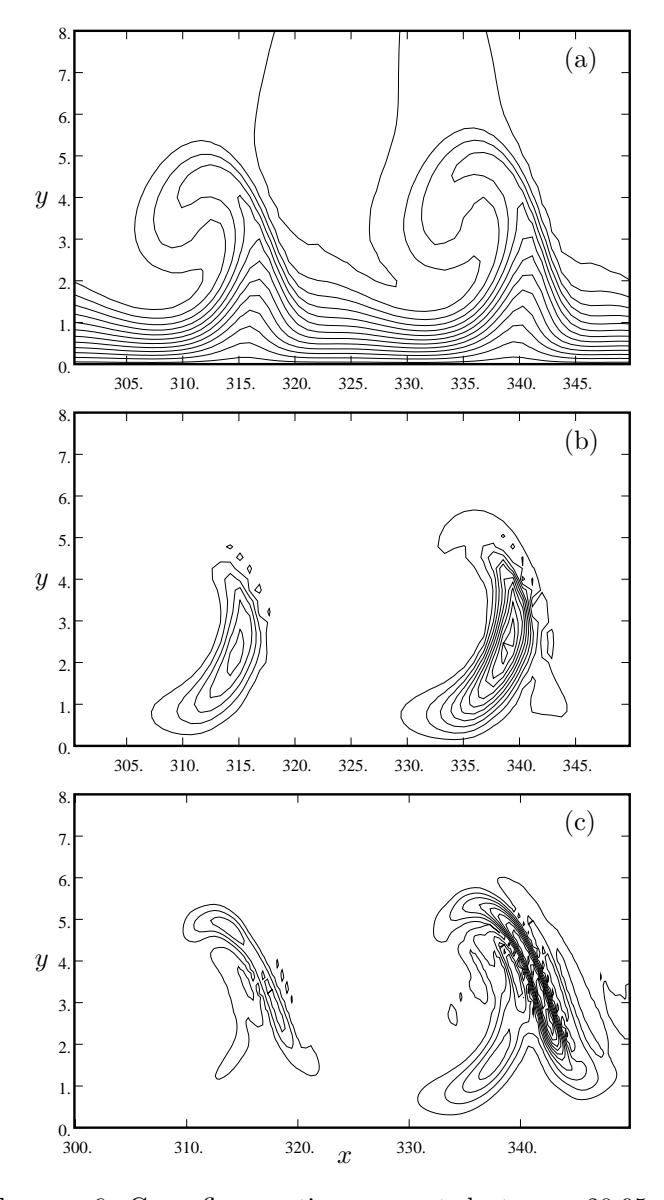


FIGURE 6. Cross-flow vortices generated at x=20.95 and their secondary instability. a) Contours of chordwise velocity at z=0. Contour spacing 0.1. b) Contours of rms of u at z=0, with contour spacing 0.0002; non-stationary random-frequency disturbance generated at x=20.95. c) Contours of rms of u at z=0, with contour spacing 0.001; non-stationary random-frequency disturbance generated at x=20.95.

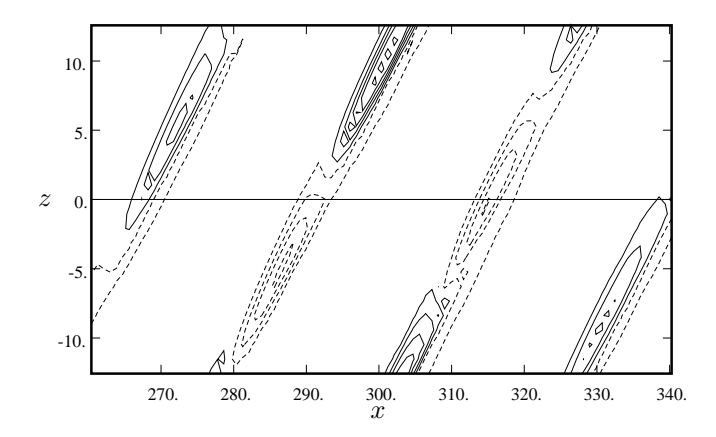


Figure 7. Contours of u- $u_{mean}$  at y = 3, spacing 0.0002

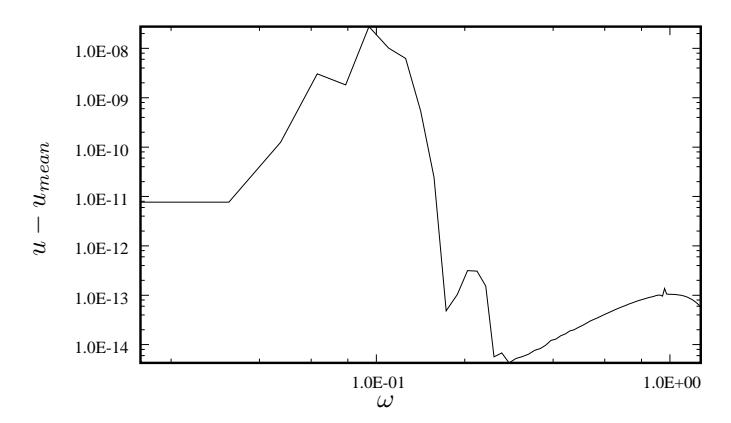


FIGURE 8. Frequency spectrum at  $x=337,\,y=2.5$  and z=0, which is located at the point where the maximum rms of the disturbance occurs.

has in figure 13. If this frequency only is superimposed on the vortex, which is done in the simulations in case 10, we essentially reproduce figures 6(c) and 7. However, by integrating the solution far enough in time we can obtain a periodic solution and easily calculate its growth rate. The growth rate of this low frequency mode is compared to the primary instabilities in figure 13. It is clear that the low frequency mode grows faster than the primary ones if the vortices are strong. To obtain the growth rate for the low frequency secondary instability, smoothing was used on the original data.

These results indicate that the low frequency mode can be viewed as an interaction between the zero-frequency and amplified traveling modes, since the presence of vortices modifies an already existing primary instability into what Fischer & Dallmann (1991) calls a secondary instability. The main changes in the primary traveling mode due to the presence of the finite amplitude

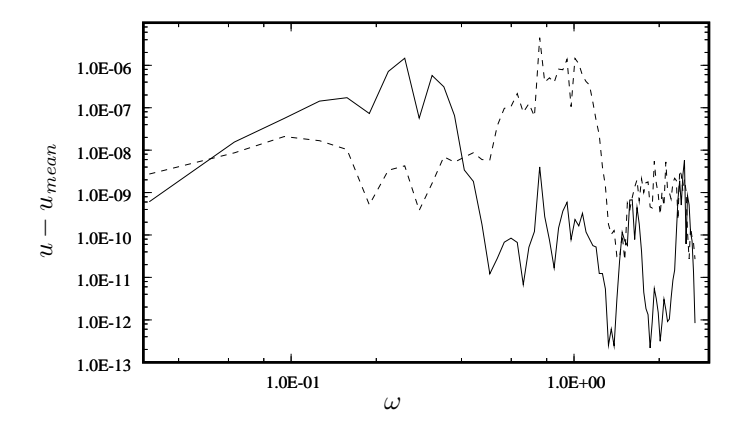


FIGURE 9. Solid: Frequency spectra at x = 335, y = 1.0, z=0 dashed: at x=337, y=5.2, z=0 for cross-flow vortex with random frequency disturbance at x = 209.5

cross-flow vortex, are the increased growth rate and the modification of the eigenfunction to have a local maximum at the lower shear layer of the stationary vortex.

#### 3.3.2. High Frequency Secondary Instability

In experiments by Kohama, Saric & Hoos (1991); Devhle & Bippes (1996), a high frequency instability has been observed just prior to transition. The frequency of this instability has been found to be about one order of magnitude higher than that of the most amplified traveling wave, as was also found in calculations by Malik, Li & Chang (1994).

To trigger this instability in our base flow the random disturbance generation was moved downstream to a position where the vortex was close to saturation. The most unstable frequencies supported by the saturated vortex was found by adding a random disturbance to the base flow at x = 209.5. This disturbance triggered both low and high frequency instabilities. See figure 6(c) for contours of the rms of the chordwise velocity. If this is compared to figure 6(b) it is apparent that the extent of the rms-fluctuations increases when the random disturbance generator is moved downstream, particularly towards the top of the vortex. The frequency spectra in figure 9 show both a peak for a high and for a low frequency at different locations in the cross-flow vortex. The high frequency is found in the upper part of the vortex and the low frequency at the bottom.

From analysis of the frequency spectra it was found that a frequency of about  $\omega = 0.957$  was the most unstable in the upper part of the vortex. In the calculations labeled case 10, a small amplitude harmonic oscillation at this frequency was introduced centered at x = 220. A smooth turn on of the forcing was used to avoid big transients that could lead to a transition in the flow. This

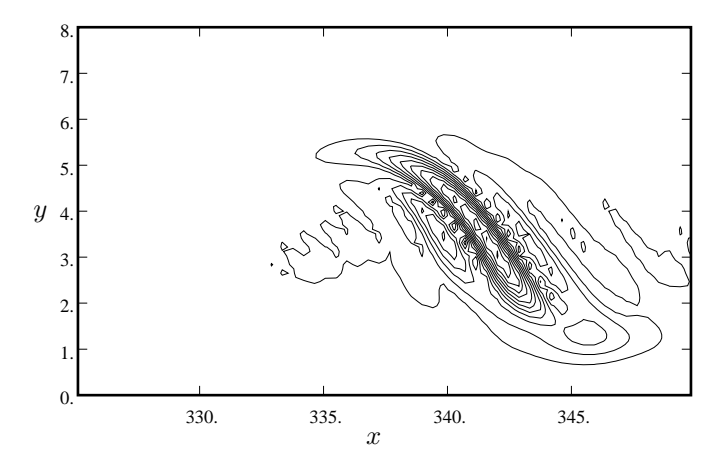


FIGURE 10. Cross-flow vortices generated by a stationary disturbance at x=20.59. Rms of u, with contour spacing 0.00025 non-stationary harmonic high-frequency disturbance generated at x=220

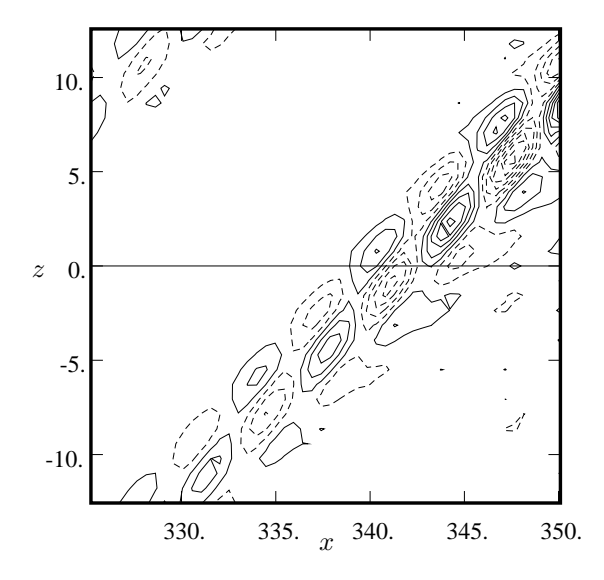


Figure 11. Contours of  $u-u_{mean}$  at y=3 , spacing=0.00005

disturbance grew mainly in the upper shear layer of the cross-flow vortex, see figure 10. In the thesis by Lerche (1997) the location of growing high-frequency disturbances is also found to be in the upper shear layer of the vortex.

Viewed from below in figure 11, where the time averaged flow is subtracted, it is evident that the high frequency oscillation is superimposed on the vortex.

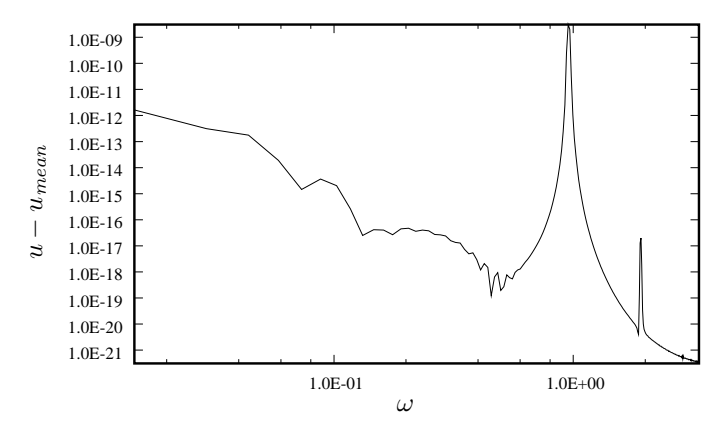


Figure 12. Frequency spectra at x=342 , y=3.0 , z=0for cross-flow vortex with random frequency disturbance

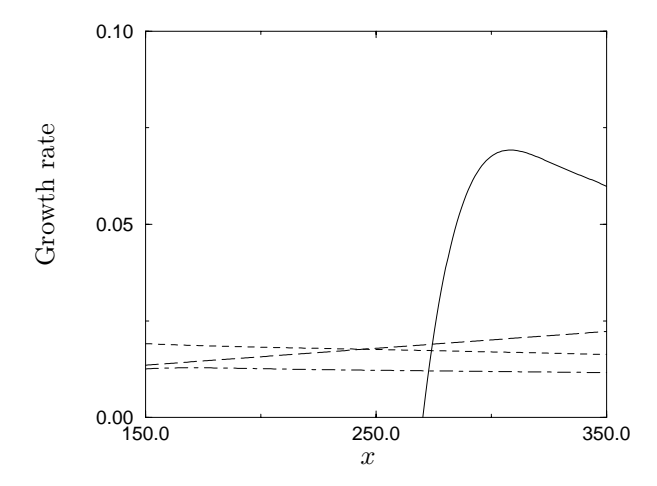


FIGURE 13. Growth rates for the secondary instabilities. Dash dotted line: zero-frequency disturbance, Short dashed: most unstable mode, Long dashed: low-frequency mode, Solid: High-frequency secondary instability.

Note that the wavelength of the disturbance is about one fourth of that corresponding to the low frequency secondary instability seen in figure 7.

The frequency spectra in figure 12 shows a clean peak at the frequency of the generated disturbance. This is clearly a frequency that is highly amplified by the vortex.

The growth rate for this frequency is considerably higher than the growth rates of the primary instabilities, see fig 13. It is also higher than the growth

rate of the low frequency mode. This indicates that the high-frequency secondary instability, when the conditions are favorable, dominate the transition process making it very rapid. One interesting aspect of the high frequency instability is that the neutral point is located quite far downstream (x=270). At that point the cross-flow vortex is almost saturated and the corresponding growth rate is close to zero, see figure 5. Note that to obtain the growth rate of the high frequency secondary instability smoothing was used on the original data.

## 4. Summary and discussion

Linear eigenvalue calculations and direct numerical simulations of the evolution of disturbances in Falkner-Skan-Cooke boundary layers have shown that the non-parallel effects on growth rates are present. This has been confirmed using non-parallel calculations based on the parabolic stability equations. The non-parallel effects are larger for traveling waves compared to stationary disturbances.

When stationary disturbances with higher amplitudes are introduced in the direct numerical simulations, saturated cross-flow vortices are obtained. The secondary instability of these vortices are considered by superimposing small random disturbances on the cross-flow vortices. A low frequency mode is found located at the bottom shear layer of the cross-flow vortex, and a high frequency secondary instability is found at the upper shear layer of the cross-flow vortex. In agreement with the findings of Fischer & Dallmann (1991), the low frequency mode can be viewed as an interaction between the zero-frequency and amplified traveling waves. Introducing a high frequency harmonic disturbance results in a high frequency oscillation in the upper part of the vortex. The high-frequency disturbances appear only once the cross-flow vortices have saturated and have considerably higher growth rates than the low-frequency secondary instability.

The results of the present investigation confirms that the high-frequency oscillations found in the experiments of Deyhle & Bippes (1996); Kohama, Saric & Hoos (1991), Lerche (1997) is a result of a secondary instability of the shear layer located on top of the cross-flow vortex, something also suggested by the results of Malik, Li & Chang (1994). This is the first time that this instability has been seen in direct numerical simulations. In particular it is interesting that both the low and the high-frequency instability appeared as a result of a forcing by random noise. Thus both instabilities can be expected to exist in a real flow situation, and it is the nature of the disturbance environment in the flow of interest which determines which instability will appear. In a low noise environment one may expect the high-frequency instability to cause transition, since it has so much higher growth rate, whereas in a flow with higher levels of free-stream turbulence transition may be caused by the lowfrequency instability, since it has an onset further upstream. The latter scenario was found in an experiment of Müller & Bippes (1988) using a wind tunnel with rather high free-stream turbulence level. The dominant transition route may of course also be determined by the receptivity of the boundary layer to particular frequencies of disturbances in the freestream turbulence.

For flows with low free-stream turbulence levels, the results of the present investigation indicate that the streamwise location of the start of transition should be well correlated with the neutral point of the high-frequency instability, since the turn on of the instability is quite rapid and high values of the growth rate are reached quickly.

We wish to thank Anders Lundbladh who's initial calculations of these flows were used as a guide in the choice of numerical and physical parameter values. We also thank Ardeshir Hanifi for performing the PSE calculations using the DLR/FFA NOLOT/PSE code, and Stellan Berlin for all the help in checking the results.

This work has been performed at the Aeronautical Research Institute of Sweden (FFA) and has been supported by the Swedish National Board for Industrial and Technical Development (NUTEK).

#### References

- Bertolotti, F. P., Herbert, T. & Spalart, P. R. 1992 Linear and nonlinear stability of the Blasius boundary layer. *J. Fluid Mech.* 242, 441–474.
- BIPPES, H. 1991 Experiments on transition in three-dimensional accelerated boundary-layer flows. *Proceedings from the R.A.S. Conference on Boundary layer transition and control, Cambridge, England.*
- Breuer, K. S. & Kuraishi, T. 1994 Transient growth in two- and three-dimensional boundary layers. *Phys. Fluids* **6**, 1983–1993.
- Butler, K. M. & Farrell, B. F. 1992 Three-dimensional optimal perturbations in viscous shear flow. *Phys. Fluids A* 4, 1637–1650.
- Choudhari, M. 1994 Roughness induced generation of crossflow vortices in three-dimensional boundary layers. *Theor. Comput. Fluid Dyn.* 6, 1–30.
- COOKE, J. C. 1950 The boundary layer of a class of infinite yawed cylinders. *Proc. Camb. Phil. Soc.* 46,645–648
- Deyhle, H. & Bippes H. 1996 Disturbance growth in an unstable three-dimensional boundary layer and its dependence on environmental conditions. *J. Fluid Mech.* **316**, 73–113
- FISCHER, T. M. & DALLMANN, U. 1991 Primary and secondary stability analysis of a three-dimensional boundary-layer flow. *Phys. Fluids A* 3, 2378–2391.
- GREGORY, N., STUART, J. T. & WALKER, W. S. 1955 *Phil. Trans. R. Soc. Lond. A* **248**, 155.
- HANIFI, A., HENNINGSON D. S., HEIN, S., BERTOLOTTI, F. P. & SIEMEN, M. 1994. Linear Nonlocal Instability Analysis - the linear NOLOT code. FFA TN 1994-54.
- HENNINGSON D. S. 1995 Bypass transition and linear growth mechanisms. *Advances in Turbulence V* (Ed. R. Benzi), pp 190–204. Kluwer
- HÖGBERG, M. & HENNINGSON, D. S. 1996 Cross-flow vortices and their secondary instability in Falkner-Skan-Cooke boundary layers. FFA TN 1996-60.
- Kohama, Y., Saric W. S. & Hoos J. A. 1991 A high frequency, secondary instability of crossflow vortices that leads to transition. *Proc. R.A.S. Conf. on: Boundary-Layer Transition and Control, Cambridge University April 8-12*
- LERCHE, T. 1997 Experimentelle Untersuchung nichtlinearen Strukturbildung im Transitionsprozeß einer instabilen Grenzschicht Fortscrittberichte, VDI, Reihe 7: Strömungstechnik, Nr. 310.
- LINGWOOD, R. J. 1995 Absolute instability of the boundary layer on a rotating disc. J. Fluid Mech. 299, 17–33.
- LINGWOOD, R. J. 1996 An experimental study of absolute instability of the rotatingdisc boundary-layer flow. J. Fluid Mech. 314, 373–405.
- LINGWOOD, R. J. 1997 On the impulse response for swept boundary-layer flows. J. Fluid Mech. **344**, 317–334.
- Lundbladh A., Henningson D. S. & Johansson A. V. 1992 An Efficient Spectral Integration Method for the Solution of The Navier-Stokes Equations. *FFA TN* 1992-28.
- Lundbladh A., Schmid P. J., Berlin S. & Henningson D. S. 1994 Simulation of bypass transition for spatially evolving disturbances. *AGARD-CP* 551, 18-1, 18-13.

- MALIK, M. R., LI F. & CHANG, C.-L. 1994 Crossflow disturbances in threedimensional boundary layers: nonlinear development, wave interaction and secondary instability. J. Fluid Mech. 268, 1–36.
- MORKOVIN, M. V. 1969 On the many faces of transition. In *Viscous Drag Reduction*, (ed. C. S. Wells), pp. 1–31. Plenum Press.
- Morkovin, M. V. 1977 Instability, transition to turbulence and predictability.  $AGARDograph\ 236.$
- MÜLLER, B., BESTEK, H. & FASEL, H. 1993 Numerical simulation of the spatial disturbance development in transitional boundary layers along a swept plate. In *Near-Wall Turbulent Flows* (Eds. R.M.C. So, C.G. Speziale & B.E. Launder), Elsevier.
- MÜLLER, B. & BIPPES, H. 1988 Experimental study of instability modes in a three-dimensional boundary layer. AGARD-CP 438, No. 18.
- REED H. L. & SARIC W. S. 1989 Stability of three-dimensional boundary layers.

  Ann. Rev. Fluid Mech. 21, 235–84
- REDDY S. C. & HENNINGSON D. S. 1993 Energy growth in viscous channel flows. J. Fluid Mech. 252, 209–238.
- Schlichting, H. 1979 Boundary-Layer Theory, 7th Edn. McGraw-Hill.
- Spalart, P. R., Crouch, J. D. & Ng, L. L. 1994 Numerical study of realistic perturbations in three-dimensional boundary layers. AGARD-CP 551, 30-1–30-10
- TREFETHEN, L. N., TREFETHEN, A. E., REDDY, S. C. & DRISCOLL, T. A. 1993 Hydrodynamic Stability Without Eigenvalues. *Science* **261**, 578–584.
- Wintergerste, T. & Kleiser, L. 1996 Direct numerical simulation of transition in a three-dimensional boundary layer. In *Transitional Boundary Layers in Aeronautics* (R.W.A.M. Henkes & J.L. van Ingen, Eds.), 145–153, North Holland.

## Paper 7

# Linear optimal control applied to instabilities in spatial boundary layers

By Markus Högberg\* and Dan S. Henningson\*†

The work presented extends on previous research on linear controllers in temporal channel flow to spatially evolving boundary layer flow. The flows studied are the ones on an infinite swept wedge described by the Falkner–Skan–Cooke (FSC) velocity profiles, including the special case of the flow over a flat plate. These velocity profiles are used as the base flow in the Orr–Sommerfeld–Squire equations to compute the optimal feedback control through blowing and suction at the wall utilizing linear optimal control theory. The control is applied to a parallel FSC flow with unstable perturbations. Through an eigenvalue analysis and direct numerical simulations (DNS), it is shown that instabilities are stabilized by the controller in the parallel case. The localization of the convolution kernels for control is also shown for the FSC profiles.

Assuming that non-parallel effects are small a technique is developed to apply the same controllers in a DNS of a spatially evolving flow. The performance of these controllers is tested in a Blasius flow with both a Tollmien-Schlichting (TS) wave and an optimal spatial transiently growing perturbation. It is demonstrated that TS waves are stabilized and that transient growth is lowered by the controller. Then the control is also applied to a spatial FSC flow with unstable perturbations leading to saturated cross-flow vortices in the uncontrolled case. It is demonstrated that the linear controller successfully inhibits the growth of the cross-flow vortices to a saturated level and thereby delays the possibility for transition through secondary instabilities. It is also demonstrated that the controller works for relatively high levels of nonlinearity, and for stationary as well as time varying perturbations.

## 1. Introduction

In many fluid-mechanics systems, like boundary-layers undergoing transition to turbulence, dramatic effect on global flow parameters may be achieved by minute local perturbations. Whereas such a fundamental instability property is a problem in many applications, it is the basis for the vision of dramatic performance improvements of fluid-mechanics systems using devices sensing

<sup>\*</sup>Department of Mechanics, Royal Institute of Technology (KTH), SE-100 44 Stockholm, Sweden

 $<sup>^{\</sup>dagger}$ The Swedish Defence Research Agency ( FOI ), SE-172 90 Stockholm, Sweden

and acting only on small parts of the flow with minute energy. Such control devices could be used to obtain drag reduction on bodies, increased lift on wings, increased propulsion efficiency, heat- and mass-transfer reduction or enhancement, control of combustion instabilities, control of vortex shedding and aeroacoustic pressure fluctuations.

Recent advances in computer capacity, sensor development and systems control for fluid dynamics have opened new perspectives for the design and control of flow systems (see for instance the review articles of Gad-el-Hak (1996), Lumley & Blossey (1998) and Bewley (2001)). Internationally this area has seen a strong expansion over the last few years.

Traditionally passive control, i.e. design or flow alteration not dynamically dependent on the state of the flow, has been used to control fluid mechanical systems. Active control of boundary layers is a more recent development, where e.g. transition has been delayed by cancelling TS waves by anti-phase modal suppression. Early work is reviewed by Thomas (1990) and a brief, later review is given by Metcalfe (1994). These studies show that the instabilities may indeed be significantly suppressed, but complete elimination of the primary disturbances are not obtained.

Researchers have only recently attempted to apply optimal-control ideas to flow control problems. A main feature with such an approach is that no a priori knowledge of the functional behavior of an effective control is needed. Also, the method is general; it can be used for such disparate tasks as finding the optimal shapes of wings (Jameson (1989)), minimizing the vorticity of an unsteady internal flow by manipulating the inlets (Berggren (1995)), as well as controlling boundary-layer transition (Joslin et al. (1997)) and turbulence (Bewley, Moin & Temam (2001)). In addition, optimal control based on the linearized equations has shown great success in recent applications to channel flow (see Joshi, Speyer & Kim (1997), Bewley & Liu (1998) and Högberg & Bewley (2000)). In this approach modern linear control theory is used to construct feedback control kernels as well as estimator forcing kernels, which can be used together as an on-line compensator.

Control of transition in boundary layer flows has numerous application areas, and so far there has been little use made of active control strategies in practice. Experimentally control has been applied to boundary layer flows using both passive and active strategies, utilizing many different means of actuation. A complete review is not given here but rather a few examples to give a taste of the activities in this field. Passive strategies include using riblets and surface roughness to modify the flow. A thorough study on the use of riblets to suppress the intensity of streamwise vortices in boundary layers is summarized by Kozlov & Grek (2000). Using passive control, Saric, Carrillo & Reibert (1998) showed that it was possible to use leading edge roughness for transition control in order to delay transition by exploiting the non-linear nature of the flow. To be able to use this method in a general case an actuation method was developed by White & Saric (2000) who introduced a variable surface roughness at the

leading edge of a swept wing to actively control transition initiated by cross-flow vortices. The success of generalizing the passive control scheme into an active relies on a better understanding of the transition process, especially the role of secondary instabilities. The breakdown of a localized disturbance into a turbulent spot in a flat plate boundary layer was successfully delayed using active wall bumps by Breuer, Haritonidis & Landahl (1989). An active strategy to control streamwise vortices and streaks in boundary layers was applied by Jacobson & Reynolds (1998). They developed an actuator that produces a high- and a low-speed streak that was used to delay transition. The use of these active control strategies in a practical feedback control scheme relies, in addition to a good physical understanding of the transition process, on development of accurate sensors and actuators.

As an alternative to experiments, computations can be used to investigate what is possible to achieve under ideal conditions, as well as to test new strategies. Active control of cross-flow vortices related to the aforementioned work by Saric, Carrillo & Reibert (1998) has been studied numerically by Wassermann & Kloker (2000) where an out of phase type control was applied to cross-flow vortex packets using DNS. They found that a modal control, where the phase shift of the control was adjusted individually for different modes was necessary to achieve an effective total amplitude reduction. Cathalifaud & Luchini (2000) applied an optimal control technique to the boundary layer equations to control optimal spatially developing perturbations in the boundary layer on a flat or concave wall. They used the adjoint equations to perform a gradient based optimization with the objective to minimize the perturbation energy in different spatial intervals. Mughal (1998) used the compressible parabolized stability equations (PSE) to investigate the effect of simple feedback boundary conditions for the wall normal velocity to control for example TS-waves and Görtler vortices. In recent work Pralits, Hanifi & Henningson (2001) have developed a method to couple the boundary layer equations and the PSE in order to optimize a steady mean-flow modifying suction in order to minimize growth of perturbations in boundary layer flows. In the paper by Walther, Airiau & Bottaro (2001) the PSE are used to compute the optimal zero mass flux control for a TS wave in a developing boundary layer. A slightly different approach was investigated by Balakumar & Hall (1999) where an optimization problem coupling the boundary layer equations and the linear stability equations was solved with the objective to move the transition point instead of minimizing the perturbation energy. The numerical approaches to flow control many times assumes ideal conditions that are not present in practice. Robust control schemes are vital to be able to take the step from the computers to the experimental setting and to practical applications.

In the present paper the linear control approach from Högberg & Bewley (2000) is applied to spatially evolving boundary layer flows. In section 2 the Falkner–Skan–Cooke (FSC) boundary layer profiles are introduced and then the formulation of the linear control problem is presented in section 3.

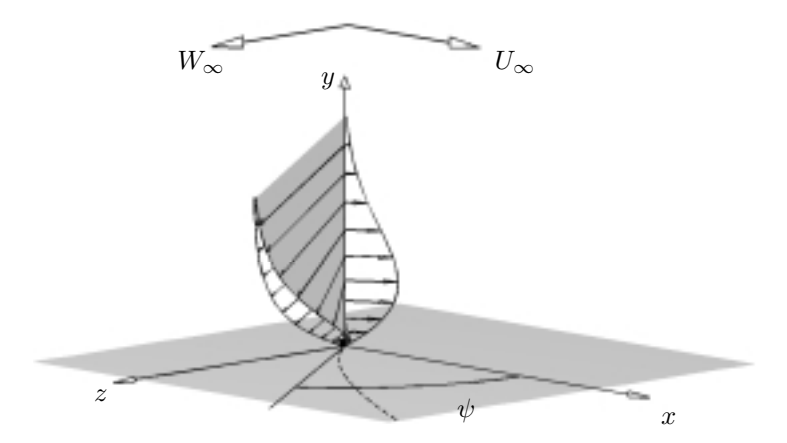


FIGURE 1. Falkner–Skan–Cooke base flow and coordinate system used in this report.  $\psi$  is the angle to the streamline of the flow in the freestream,  $U_{\infty}$  is the chordwise freestream component and  $W_{\infty}$  is the spanwise freestream component. The dashed line is the streamline of the flow in the freestream over a flat plate with a pressure gradient in the x direction

The numerical simulations performed and the methods used is summarized in section 4. In section 5 the linear optimal control is applied in a parallel FSC flow in order to explain some features of the control and then the extension to spatial boundary layers is done in section 6. Results from simulations with and without control in spatial boundary layers is presented in section 7 for the Blasius boundary layer and in section 8 for the FSC boundary layer for non-stationary as well as stationary perturbations. Finally a discussion and conclusions follows in section 9.

## 2. Falkner–Skan–Cooke boundary layers.

The Falkner–Skan-Cooke boundary layer profile family includes a large variety of flows. It includes the Blasius boundary layer as a special case, and the effect of sweep and favorable/adverse pressure gradients can be added. These different flows have been studied previously and are known to exhibit different types of primary instabilities. In order to test the control strategy for different types of instabilities we need to examine its effectiveness in a few different flows.

Consider an infinite swept flat plate where  $\partial/\partial z = 0$ . The dimensional boundary layer equations according to Schlichting (1979) become:

$$u^* \frac{\partial u^*}{\partial x^*} + v^* \frac{\partial w^*}{\partial y^*} = U_{\infty}^* \frac{\mathrm{d}U_{\infty}^*}{\mathrm{d}x^*} + \nu \frac{\partial^2 u^*}{\partial y^{*2}}$$
 (1)

$$u^* \frac{\partial w^*}{\partial x^*} + v^* \frac{\partial w^*}{\partial y^*} = \nu \frac{\partial^2 w^*}{\partial y^{*2}}$$
 (2)

$$\frac{\partial u^*}{\partial x^*} + \frac{\partial v^*}{\partial y^*} = 0 \tag{3}$$

with the boundary conditions:

$$u^* = v^* = w^* = 0 \quad at \quad y^* = 0 \tag{4}$$

$$u^* \to U_\infty^*, w^* \to W_\infty^* \quad as \quad y^* \to \infty$$
 (5)

where  $u^*, v^*, w^*$  are the chordwise (x), normal (y) and spanwise (z) velocity components, respectively, and \* denotes dimensional quantities. See figure 1 for a definition of the coordinate system. We assume that the chordwise base flow at the boundary layer edge obeys a power law according to,  $U_\infty^* = U_0^*(x^*/x_0^*)^m$  and that  $W_\infty^* = \text{constant}$ . A self-similar solution may be found if we select

$$\eta = \{(m+1)U_{\infty}^*/2\nu x^*\}^{1/2}y^* \tag{6}$$

Introducing the stream-function

$$\Psi^* = (2U^*\nu x^*/m + 1)^{1/2} f(\eta) \tag{7}$$

with  $u^* = \partial \Psi^*/\partial y^*$  and  $v^* = -\partial \Psi^*/\partial x^*$  and  $w^* = W_{\infty}^* g(\eta)$  reduces the boundary layer equations to a function of the single variable  $\eta$ , we have

$$f''' + ff'' + \beta_H (1 - f'^2) = 0 (8)$$

$$q'' + fq' = 0 (9)$$

where the Hartree parameter is  $\beta_H = 2m/(m+1)$  and the boundary conditions are

$$f = f' = g = 0 \quad if \quad \eta = 0$$
 (10)

$$f' \to 1, g \to 1 \quad as \quad \eta \to \infty$$
 (11)

f' and g can then be combined into the Falkner-Skan-Cooke velocity profiles, see Cooke (1950), as

$$U(y) = f'[\eta(y)] \tag{12}$$

$$W(y) = \frac{W_{\infty}^*}{U_{\infty}^*} g[\eta(y)]. \tag{13}$$

with  $y = y^*/\delta_0^*$ . Note that

$$\delta^* = \{ (m+1)U_{\infty}^* / 2\nu x^* \}^{-1/2} \int_{0}^{\infty} (1-f') d\eta$$
 (14)

which implies that

$$\delta_0^* = \{ (m+1)U_0^*/2\nu x_0^* \}^{-1/2} C \tag{15}$$

where

$$C = \int_{0}^{\infty} (1 - f') \mathrm{d}\eta \tag{16}$$

Then we have

$$\eta = C \left\{ \frac{U_{\infty}^* x_0^*}{U_0^* x^*} \right\}^{1/2} y \tag{17}$$

where  $x_0^*$  is a fixed position. The profiles (12) and (13) will be used as a base flow in the control computations and as initial conditions in the direct numerical simulations presented.

### 3. Linear control theory.

## 3.1. Problem formulation

To investigate the stability of a flow to small disturbances, one assumes that the flow can be divided into two parts,

$$(u_1, v, w) = (U, 0, W) + (u'_1, v', w')$$
(18)

where U and W are the base flow components in the chordwise and spanwise directions, respectively. It is here assumed that the parallel flow assumption holds, i.e. the base flow components only varies with the normal coordinate. The primed quantities represent a small perturbation. We also assume wavelike disturbance of the form

$$v' = \hat{v}(t)e^{i(\alpha x + \beta z)} \tag{19}$$

where  $\alpha$  and  $\beta$  are the x and z components of the wave number vector and  $\hat{u}(t)$  is the complex amplitude function for the chordwise velocity. Inserting these assumptions into the Navier-Stokes equations and linearizing, we find the resulting disturbance equations that can be reduced to the following set of two coupled equations where appropriate boundary conditions have been included to allow inversion of the Laplacian ( $\Delta = (D^2 - \alpha^2 - \beta^2)$ ).

$$\frac{\mathrm{d}\hat{v}}{\mathrm{d}t} = \underbrace{\Delta^{-1}[-(i\alpha U + i\beta W)\Delta + i\alpha D^2 U + i\beta D^2 W + \frac{1}{R}\Delta^2]}_{\mathcal{L}_{OS}}\hat{v} \quad (20)$$

$$\frac{\mathrm{d}\hat{\eta}}{\mathrm{d}t} = \underbrace{\left[i\,\alpha\,\mathrm{D}W - i\,\beta\,\mathrm{D}U\right]}_{\mathcal{L}_{C}}\,\hat{v} + \underbrace{\left[-i\,(\alpha\,U + \beta\,W) + \frac{1}{R}\Delta\right]}_{\mathcal{L}_{SQ}}\,\hat{\eta} \tag{21}$$

where  $\hat{v}$  and  $\hat{\eta} = i(\beta \hat{u} - \alpha \hat{w})$  are the amplitude functions for the normal velocity and the normal vorticity, respectively. A D denotes the derivative operator the

wall-normal direction. The boundary conditions are

$$\hat{v}(0) = \hat{\varphi} , \, D\hat{v}(0) = 0 , \, \hat{\eta}(0) = 0$$
  
 $\hat{v}(y) \to 0, \, D\hat{v}(y) \to 0, \, \hat{\eta}(y) \to 0 \text{ as } y \to \infty$  (22)

Here R is the Reynolds number based on the velocity scale  $U_{\infty}$  and the displacement thickness  $\delta^*$ , both taken at the stream-wise location  $x_0$ . The normal velocity on the wall  $\hat{\varphi}$  is our control input to the system. To denote the Revnolds number based on local displacement thickness and freestream velocity Rewill be used.

Equation (20) is referred to as the Orr-Sommerfeld equation, and the equation (21) is known as the Squire equation. The U(y) and W(y) profiles used in this investigation is taken from (12) and (13) in the previous section. Since (20) and (21) is a linear system of equations we can divide the solution into two parts one homogeneous  $(\hat{v}_h, \hat{\eta}_h)$  and one inhomogeneous  $(\hat{v}_p, \hat{\eta}_p)$  such that,

$$\hat{v} = \hat{v}_h + \hat{\varphi} \, \hat{v}_p, 
\hat{\eta} = \hat{\eta}_h + \hat{\varphi} \, \hat{\eta}_p,$$
(23)

where the conditions on the particular solution are such that it satisfies (22) with  $\hat{\varphi} = 1$ . Finding a particular solution with non-zero normal velocity on the wall allows us to parameterize the inhomogeneous part of the solution with the time derivative of the wall normal velocity.

$$\frac{\mathrm{d}\hat{v}_{h}}{\mathrm{d}t} = \mathcal{L}_{OS}\left(\hat{v}_{h} + \hat{v}_{p}\,\hat{\varphi}\right) - \hat{v}_{p}\,\dot{\hat{\varphi}} \tag{24}$$

$$\frac{\mathrm{d}\hat{\eta}_{h}}{\mathrm{d}t} = \mathcal{L}_{C}\left(\hat{v}_{h} + \hat{v}_{p}\,\hat{\varphi}\right) + \mathcal{L}_{SQ}\left(\hat{\eta}_{h} + \hat{\eta}_{p}\,\hat{\varphi}\right) - \hat{\eta}_{p}\,\dot{\hat{\varphi}}, \tag{25}$$

$$\frac{\mathrm{d}\hat{\eta}_h}{\mathrm{d}t} = \mathcal{L}_C \left(\hat{v}_h + \hat{v}_p \,\hat{\varphi}\right) + \mathcal{L}_{SQ} \left(\hat{\eta}_h + \hat{\eta}_p \,\hat{\varphi}\right) - \hat{\eta}_p \,\dot{\hat{\varphi}}, \tag{25}$$

with the boundary conditions,

$$\hat{v}_h(0) = 0$$
,  $D\hat{v}_h(0) = 0$ ,  $\hat{\eta}_h(0) = 0$  (26)

$$\hat{v}_h(y) \to 0$$
,  $D\hat{v}_h(y) \to 0$ ,  $\hat{\eta}_h(y) \to 0$  as  $y \to \infty$ . (27)

Now control theory can be used to determine  $\dot{\hat{\varphi}}$  from  $(\hat{v}_h, \hat{\eta}_h)$ . Introducing  $\mathbf{x} = [\hat{v}_h, \, \hat{\eta}_h, \, \hat{\varphi}]^T$  and  $\hat{u} = \dot{\hat{\varphi}}$  we can write,

$$\dot{\mathbf{x}} = A\mathbf{x} + B\hat{u},\tag{28}$$

where

$$A = \begin{bmatrix} \mathcal{L}_{OS} & 0 & \mathcal{L}_{OS}\hat{v}_p \\ \mathcal{L}_C & \mathcal{L}_{SQ} & \mathcal{L}_C\hat{v}_p + \mathcal{L}_{SQ}\hat{\eta}_p \\ 0 & 0 & 0 \end{bmatrix}, \quad B = \begin{bmatrix} -\hat{v}_p \\ -\hat{\eta}_p \\ 1 \end{bmatrix}. \tag{29}$$

Looking for the optimal controller we need to specify an objective function,

$$J = \int_{0}^{\infty} (\mathbf{x}^* Q \mathbf{x} + \ell^2 \hat{u}^* \hat{u}) dt, \tag{30}$$

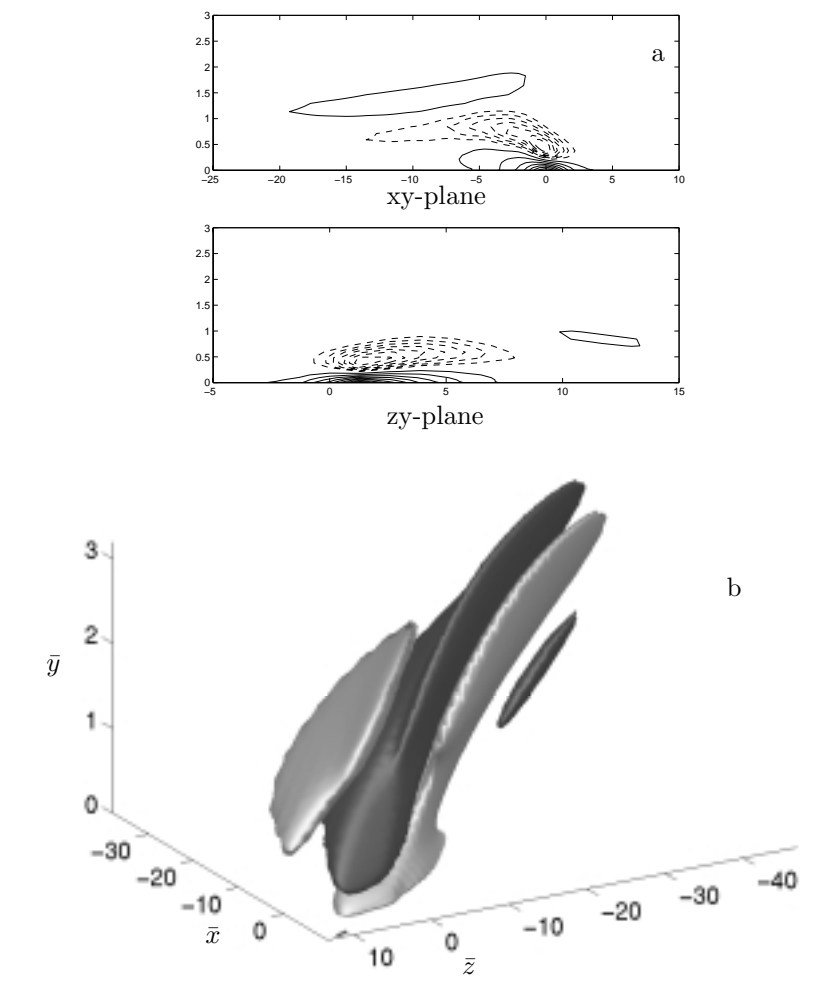


FIGURE 2. Control convolution kernel for the normal velocity computed at R=337.9 with  $\ell=10^2$  and  $r^2=0$  with a resolution of  $192\times65\times96$  Fourier, Chebyshev, Fourier modes in an  $x\times y\times z$  box with the dimensions  $100\times10\times125.7$  respectively. a: Contour plots of xy- and xz-plane. Solid contours are negative values and dashed contours are positive. b: Isosurfaces at 25 (light) and -25 (dark).

where Q is a measure of the energy of the perturbation and  $\ell$  is a parameter penalizing the magnitude of  $\dot{\hat{\varphi}}$ . For each wavenumber pair Q can be written,

$$Q = \begin{bmatrix} \mathcal{Q}_v & 0 & \mathcal{Q}_v \hat{v}_p \\ 0 & \mathcal{Q}_\eta & \mathcal{Q}_\eta \hat{\eta}_p \\ \hat{v}_p^* \mathcal{Q}_v & \hat{\eta}_p^* \mathcal{Q}_\eta & (1+r^2)(\hat{v}_p^* \mathcal{Q}_v \hat{v}_p + \hat{\eta}_p^* \mathcal{Q}_\eta \hat{\eta}_p) \end{bmatrix},$$
(31)

-40

-20

0

20

 $\bar{z}$ 

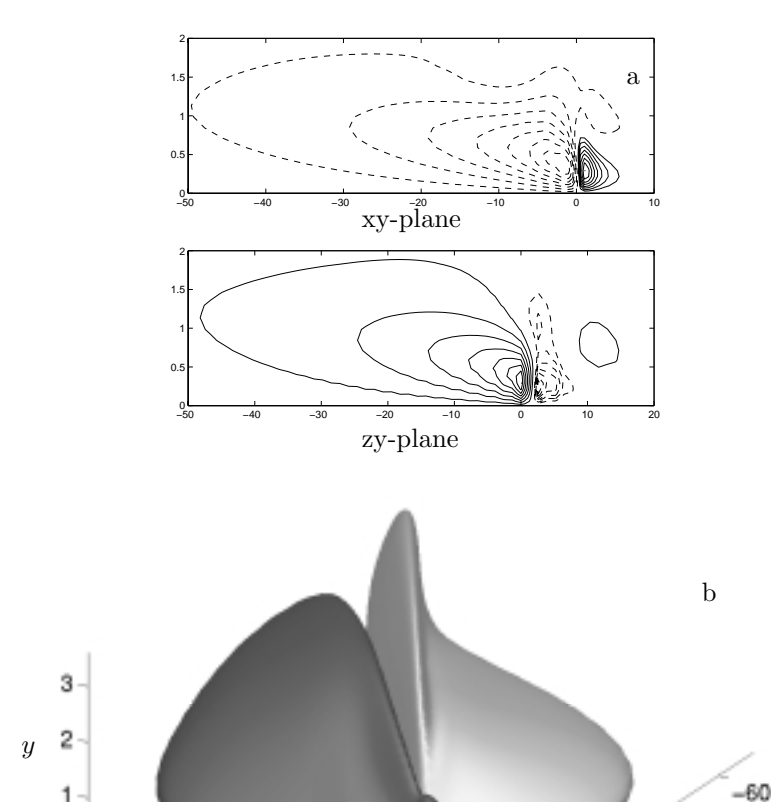


FIGURE 3. Control convolution kernel for the normal vorticity computed at R=337.9 with  $\ell=10^2$  and  $r^2=0$  with a resolution of  $192\times65\times96$  Fourier, Chebyshev, Fourier modes in an  $x\times y\times z$  box with the dimensions  $100\times10\times125.7$  respectively. a: Contour plots of xy- and xz-plane. Solid contours are negative values and dashed contours are positive. b: Isosurfaces at 0.5 (light) and -0.5 (dark).

20

0

 $\bar{x}$ 

where,

-40

-20

$$\hat{v}^* \mathcal{Q}_v \hat{v} = \frac{1}{8} \int_0^{y_\infty} \left( \frac{1}{k^2} \frac{\partial \hat{v}}{\partial y} + \hat{v}^* \hat{v} \right) dy, \quad \hat{\eta}^* \mathcal{Q}_\eta \hat{\eta} = \frac{1}{8} \int_0^{y_\infty} \left( \frac{1}{k^2} \hat{\eta}^* \hat{\eta} \right) dy, \tag{32}$$

with  $k^2 = \alpha^2 + \beta^2$ . The parameter  $r^2$  adds an extra penalty on  $\hat{\varphi}^2$ .

#### 3.2. Discretization and solution procedure

The equations are discretized in y using a Chebyshev collocation technique utilizing the Gauss-Lobatto collocation points such that,

$$\bar{f} = [f(y_1), ..., f(y_N)]^T, \quad f(y_i) = \sum_{n=1}^N \tilde{f}_n T_n(y_i), \quad y_i = \cos \frac{i \pi}{N},$$

where  $\{T_n(y)\}_{n=1}^N$  are the Chebyshev polynomials. The operators mapped to the Chebyshev interval  $-1 \le y \le 1$  and then the discrete operators are compiled using the spectral MATLAB Differentiation Matrix Suite of Weideman & Reddy (2000). The discrete form of the homogeneous evolution equation, ( $\hat{\varphi} = 0$  in (22)), can then be written,

$$\frac{\mathrm{d}}{\mathrm{d}t} \begin{bmatrix} \bar{\hat{v}}_h \\ \bar{\hat{\eta}}_h \end{bmatrix} = \bar{N} \begin{bmatrix} \bar{\hat{v}}_h \\ \bar{\hat{\eta}}_h \end{bmatrix}, \quad \bar{N} = \begin{bmatrix} \bar{\mathcal{L}}_{OS} & 0 \\ \bar{\mathcal{L}}_C & \bar{\mathcal{L}}_{SQ} \end{bmatrix}. \tag{33}$$

The discrete form of (28) is,

$$\dot{\bar{\mathbf{x}}} = \bar{A}\bar{\mathbf{x}} + \bar{B}\hat{u},\tag{34}$$

and analogously the discrete form of Q is denoted  $\bar{Q}$ . The optimal discrete feedback control law  $\hat{u} = \bar{K}\bar{\mathbf{x}}$  can now be found by solving the Riccati equation (see e.g. Skelton (1988)),

$$X\bar{A} + \bar{A}^* X - X\frac{1}{\ell^2}\bar{B}\bar{B}^* X + \bar{Q} = 0,$$
 (35)

where  $\bar{K} = -\frac{1}{\ell^2}\bar{B}^*X$ . Applying this feedback control gives us the closed loop system

$$\dot{\bar{\mathbf{x}}} = \underbrace{(\bar{A} + \bar{B}\bar{K})}_{\bar{A}_{cl}} \bar{\mathbf{x}},\tag{36}$$

where  $\bar{A}_{cl}$  describes the dynamics of the controlled system. Dividing  $\bar{K}$  into three parts such that  $\bar{K}\bar{\mathbf{x}} = \bar{K}_{\bar{v}}\,\bar{v}_h + \bar{K}_{\bar{\eta}}\,\bar{\eta}_h + K_{\hat{\varphi}}\,\hat{\varphi}$ , the contribution from the normal velocity and the normal vorticity can be studied separately. To get the feedback law for the inhomogeneous flow we need to remove the contribution from inhomogeneous part of the flow from the feedback law using a discrete form of (23)

$$\hat{u} = \bar{K}_{\bar{v}} \, \bar{v}_h + \bar{K}_{\bar{\eta}} \, \bar{\eta}_h + K_{\hat{\varphi}} \, \hat{\varphi} = \bar{K}_{\bar{v}} \, \bar{v} + \bar{K}_{\bar{\eta}} \, \bar{\eta} + \underbrace{(K_{\hat{\varphi}} - \bar{K}_{\bar{v}} \, \bar{v}_p - \bar{K}_{\bar{\eta}} \, \bar{\eta}_p)}_{K_{\hat{\varphi}}} \hat{\varphi}. \quad (37)$$

To get a representation of the feedback law as an integral in y instead of a sum the integration weight of the feedback law at each grid-point must be removed since it has been included implicitly in the discrete formulation of the control problem. The integration weights W for the Chebyshev grid with the Gauss—Lobatto collocation points is computed using an algorithm described in the

appendix of Hanifi, Schmid & Henningson (1996),

$$\int_{-1}^{1} f(y) \, dy = \sum_{j=0}^{N} f(y_j) W(y_j), \quad W(y_j) = \frac{b_j}{N} \sum_{n=0}^{N} c_n \cos\left(\frac{n \, j \, \pi}{N}\right) \int_{-1}^{1} T_n(y) \frac{d\hat{y}}{dy} dy,$$

where  $\hat{y}$  is the physical normal coordinate in the boundary layer mapped to the Chebyshev interval  $-1 \le y \le 1$ . The coefficients  $b_i$  and  $c_n$  are found from,

$$f(y) = \sum_{n=0}^{N} \tilde{f}_n T_n(y) = \sum_{n=0}^{N} c_n T_n(y) \sum_{j=0}^{N} \frac{b_j}{N} f(y_j) T_n(y_j).$$

These weights provide spectral accuracy of the integration. We can then introduce the diagonal matrix  $\Theta$  such that,

$$\Theta_{ij} = \delta_{ij} W(y_j),$$

where  $\delta_{ij}$  is the Kronecker delta. We can now define,

$$\hat{K}(\alpha,\beta) = [\bar{\Theta}^{-1}\bar{K}_{\bar{v}},\bar{\Theta}^{-1}\bar{K}_{\bar{\eta}},\mathcal{K}_{\hat{\varphi}}]. \tag{38}$$

By solving for all wave number pairs  $(\alpha, \beta)$  and combining these together we can inverse Fourier transform the combined controllers and get physical space convolution kernels  $k_v$ ,  $k_\eta$  and  $k_\varphi$  describing the feedback law,

$$\dot{\varphi}(x,z,t) = \int_{\Omega} \left( k_v(x-\bar{x},\bar{y},z-\bar{z}) \, v'(\bar{x},\bar{y},\bar{z},t) + k_{\eta}(x-\bar{x},\bar{y},z-\bar{z}) \, \eta'(\bar{x},\bar{y},\bar{z},t) \right) d\bar{x} \, d\bar{y} \, d\bar{z} + \int_{\Gamma} k_{\varphi}(x-\bar{x},z-\bar{z}) \, \varphi(x,z,t) \, d\bar{x} \, d\bar{z},$$
(39)

where  $\Omega$  denotes the inner part of the domain and  $\Gamma$  is the wall. In figure 2b iso surfaces the convolution kernel in physical space for the v velocity can be seen, and in figure 2a there are contour plots of the same kernel. The convolution kernel for  $\eta$  is visualized in figures 3a and 3b. These kernels are computed at x = 50 in a box with the dimensions  $100 \times 10 \times 125.7$  in  $x \times y \times z$  and resolution  $192 \times 65 \times 96$  Fourier; Chebyshev; Fourier modes respectively. The Reynolds number is R = 337.9 with  $\ell = 10^2$  and the cross-flow velocity  $W_{\infty} =$  $1.44232 U_{\infty}(x=0)$  and m=0.34207. These particular kernels were computed, at high resolution, for the purpose of visualization and are not used in the simulations presented here. They are however representative for all the kernels used in terms of their shape and structure. Notice that the kernels show that the control mainly relies on upstream information, and that the convective time delay of the mean flow profiles is taken into account automatically. Turning and twisting the kernel one can see that it is skewed in a way corresponding to the direction of the mean-flow streamline varying with y. Another important property of the kernels is their spatial localization, which is crucial for being able to move on to the spatially developing flow in section 6. To solve the Riccati equations an algorithm based on an eigenvector calculation taken from Skelton (1988) p. 350 was implemented in MATLAB. A study of Riccati equations and methods to find their solutions can be found e.g. in Laub (1991).

#### 4. Direct numerical simulation

A spectral method is used to solve the incompressible Navier-Stokes equations for flow over a flat plate with a pressure gradient. The equation solved is

$$\frac{\partial \mathbf{u}}{\partial t} = NS(\mathbf{u}) + \lambda(x)(\mathbf{u} - \mathbf{u}_{\lambda}) + \mathbf{F},$$

$$\nabla \cdot \mathbf{u} = 0,$$
(40)

where NS represents the Navier-Stokes equations. To retain the periodic boundary conditions and allow a stream-wise inflow and outflow of the computational domain, a fringe region technique ( see e.g. Nordström, Nordin & Henningson (1999) is used in the spatial simulations. This is implemented in the term  $\lambda(x)(\mathbf{u}-\mathbf{u}_{\lambda})$ , where  $\lambda(x)$  is a positive function that is non-zero only in the end of the computational domain and  $\mathbf{u}_{\lambda}$  is the desired solution in this region. The term F represents additional forcing used to introduce perturbations in the flow. An artificial boundary is introduced and a freestream boundary condition applied at a constant distance from the flat plate. In the temporal case the boundary condition Du = Dv = Dw = 0 is used at the upper boundary, in the spatial simulations Du + ku = DU + kU, Dv + kv = DV + kV, Dw = DW + kW is used. The normal direction is discretized using Chebyshev polynomials and in the horizontal directions Fourier series are used. Time integration is performed using a third order Runge-Kutta method for the advective and forcing terms and a Crank-Nicholson for the viscous terms. More about the code can be found in Lundbladh et al. (1999). The disturbances in the flow field are generated by forcing to a particular perturbation in the fringe region or by applying an external volume force. To make sure that changes of forcing and boundary conditions in the x or t directions are smooth a step function is used. It has the form,

$$S(r) = \begin{cases} 0 & r \le 0\\ 1/[1 + e^{\frac{1}{r-1} + \frac{1}{r}}] & 0 < r < 1\\ 1 & r \ge 1 \end{cases}$$
 (41)

where  $r = (x - x_0)/\Delta x$  is used to be able to change the slope, position and the extent of the S function. It is used for example to construct the fringe forcing function  $\lambda(x)$  as well as smooth time varying random perturbations. In table 1 there is an overview of all the simulations reported on in this article.

#### 5. Control in a parallel boundary layer

In order to examine the properties of the computed control, the parallel boundary layer flow is studied. This simple case allows us to illustrate the effect of the control and the parameters of the objective function in terms of temporal

Case	Flow	Perturbation		Con	trol
			$r^2$	$\ell$	$x \in$
1	A	Eigenmode		no	ne
2	A	Eigenmode	0	$10^{5}$	all
3	A	Eigenmode	$10^{5}$	$10^{5}$	all
4	A	Eigenmode	0	$10^{2}$	all
5	В	TS wave		no	ne
6	В	TS wave	0	$10^{2}$	[75, 225]
7	В	Optimal		no	ne
8	В	Optimal	0	$10^{2}$	[75, 225]
9	В	Optimal	0	$10^{2}$	[75, 725]
10	$\mathbf{C}$	Random		no	ne
11	$\mathbf{C}$	Random	0	$10^{2}$	[75, 225]
12	D	Stationary		no	ne
13	$\mathbf{E}$	Stationary	0	$10^{2}$	[25, 175]
14	$\mathbf{E}$	Stationary	0	$10^{2}$	[145, 295]

Letter	Flow	Resolution	Box
A	Temporal FSC	$4 \times 49 \times 4$	$25.14 \times 10 \times 25.14$
В	Spatial Blasius	$576 \times 65 \times 4$	$1128\times20\times12.83$
$\mathbf{C}$	Spatial FSC	$192\times49\times48$	$500 \times 8 \times 251.4$
D	Spatial FSC	$576 \times 65 \times 24$	$500 \times 8 \times 25.14$
$\mathbf{E}$	Spatial FSC	$384 \times 49 \times 16$	$500 \times 8 \times 25.14$

Table 1. Overview of simulations performed. The control kernels are always computed using velocity profiles from the center of the control interval and at the same resolution as the simulation or higher. The rise and fall scale of the control region is  $\Delta x = 5$  in all cases. The Reynolds number is R = 337.9 for the FSC cases and R = 468.34 for the Blasius cases. The fringe region in the spatial simulations starts at x = 1028 in the Blasius cases and at x = 350 for the FSC flows

eigenvalues and eigenvectors. In a boundary layer flow with a three dimensional velocity profile one can always find a direction in which an inviscid instability will exist due to inflection points in the velocity profile. In this direction there will be an unstable eigenvalue with a corresponding eigenmode. We will focus on the flow investigated in Högberg & Henningson (1998) where the Reynolds number was R=337.9 at the beginning of the simulation box with a cross-flow velocity of  $W_{\infty}=1.44232$  and m=0.34207 and the width of the box was  $z_l=25.14$ . This flow was studied in spatial simulations and in section 8 the control will be applied to a few of those cases. A study of the effect on eigen-

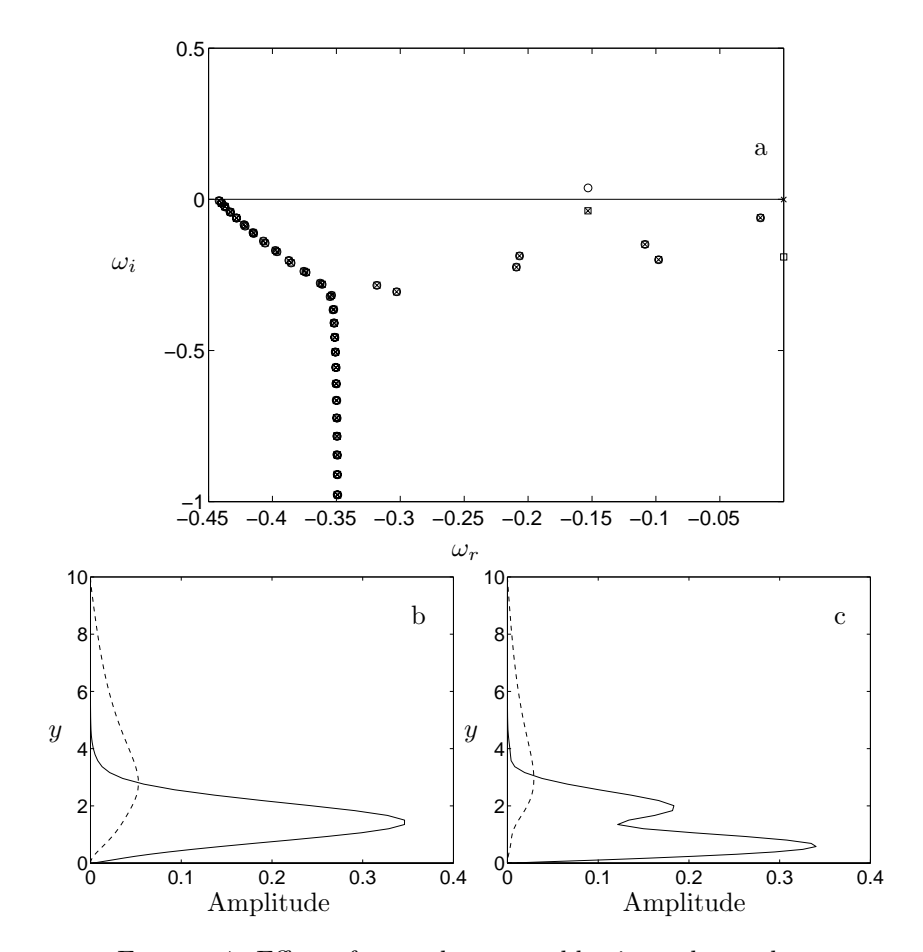


FIGURE 4. Effect of control on unstable eigenvalue and corresponding eigenvector. The parameters are  $\alpha=0.25$ ,  $\beta=-0.25$  with 90 collocation points in y. Uncontrolled eigenvalues and eigenvectors are for  $\bar{N}$  from (33) and controlled ones are for the closed loop system  $\bar{A}_{cl}$  in (36). a: The uncontrolled eigenvalues are represented by the symbol 'o', the controlled ones with 'x' is for  $\ell=10^5$ , r=0 and with ' $\Box$ ' is for  $\ell=10^5$ ,  $r^2=10^5$ . b: The absolute value of the uncontrolled unstable eigenvector, solid is  $\eta$  and dashed v. c: The absolute value of the corresponding controlled eigenvector with  $\ell=10^5$ , solid is  $\eta$  and dashed v. This eigenvector is identical for both values of  $r^2$ .

values and eigenvectors from the control is shown in figure 4. The uncontrolled eigenvalues are those of  $\bar{N}$  in (33) shown with the open circles in figure 4a, and the controlled eigenvalues are those of the closed loop system  $\bar{A}_{cl}$  in (36).

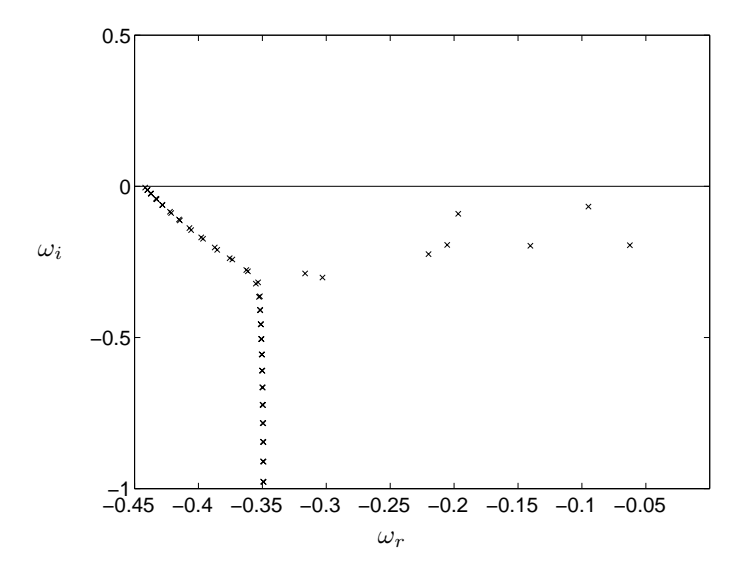


FIGURE 5. Controlled eigenvalues of  $\bar{A}_{cl}$  in (36) for a controller with  $\ell = 10^2$ , r = 0.

The unstable eigenvalue (-0.15315 + i0.037782) is moved by a controller with  $\ell = 10^5$  and r = 0 to (-0.15315 - i0.037783), where the closed loop eigenvalues are plotted using crosses in figure 4a. The corresponding eigenvector also is modified by the control, compare figure 4b and c. The high penalty on the control parameter results in that only the unstable eigenvalue is moved. Actually it is just reflected in the real axis. An additional eigenvalue appears with the value 0.000001 - i0.000602 and is due to the extra degree of freedom introduced to apply the control. This will in fact be the most unstable eigenvalue in the controlled system. Using the extra penalty term  $(r^2)$  on  $\varphi^2$  in the objective function will move this eigenvalue down the imaginary axis. With  $r^2 = 10^5$  this eigenvalue will move to  $(10^{-8} - i0.190367)$ , shown with the closed loop eigenvalues denoted by an open square in figure 4a. With a lower penalty  $\ell$  the unstable eigenvalue would move more and other eigenvalues would also be moved in order to get the system dynamics that minimizes the objective function as shown in figure 5. This is also true for the extra eigenvalue due to the application of control. The movement of eigenvalues and modifications of eigenvectors is discussed in Bewley & Liu (1998) in terms of channel flow. They show that the application of the control makes the eigenvectors 'more orthogonal' and thereby lowers the transient energy growth. Also in the paper by Joshi, Speyer & Kim (1997) the effect of controllers on eigenvalues is studied for channel flow.

In a direct numerical simulation the eigenvector in figure 4b is used as initial perturbation with exponential growth at a low initial energy. Then feedback control is applied first with  $\ell=10^5,\,r^2=0$  and then with  $\ell=10^5,$ 

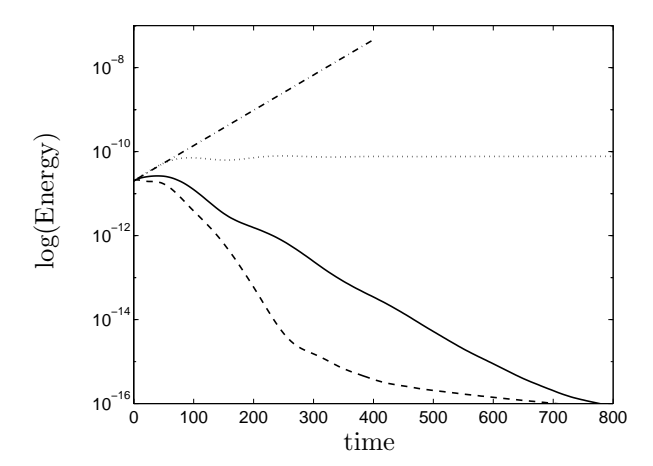


FIGURE 6. Energy growth of uncontrolled unstable eigenvector perturbation and effect of applied controls. dash-dot: uncontrolled energy growth from case 1, dotted: controlled with  $\ell=10^5$  and  $r^2=0$  from case 2, solid: controlled with  $\ell=10^5$  and  $r^2=10^5$  from case 3, dashed: controlled with  $\ell=10^2$  and  $r^2=0$  from case 4.

 $r^2=0$  and finally with  $\ell=10^2,\ r^2=0$ . In figure 6 the energy growth for these different simulations in cases 1-4 in table 1 is shown. The decay of the perturbation after control has been applied is different for the different values of the penalty parameters  $\ell$  and r. The slope in the cases where  $\ell=10^5$  and the uncontrolled case corresponds to the largest eigenvalue of the dynamical system. In summary the application of the linear control strategy to parallel boundary layers show results analogous to those obtained for channel flow in previous studies.

#### 6. Extension to spatial boundary layers

Moving on to a spatial boundary layer flow we need to remember what assumption we make that will allow the controller to work. The key properties necessary for this to work are that the controller only utilizes local information about the flow and that non-parallel effects are small. Assuming that non-parallel effects are small is not really a good assumption for many flows since the growth of the boundary layer can have a substantial effect on the eigenvalues of the system. This can however be of less significance for the application of control since the precise eigenvalues are not as important as the overall dynamics. In the case with cross-flow there is also a change in the direction of the outer streamline in the chordwise direction that is not accounted for with the parallel assumption. Some robustness of the controller performance with respect to a varying mean-flow is expected based on the success in controlling turbulence via a gain scheduling technique in Högberg & Bewley (2000). Only

a few different mean-flow profiles were needed to cover the range from a fully turbulent profile to a laminar one. This indicates that the controller can handle finite deviations of the mean-flow from that for which it was computed. The localization of the convolution kernels implies that only information of the flow field close to the actuation region is used. The property of spatial localization also extends from the channel to the boundary layer flows as demonstrated in figures 2 and 3.

The control kernel is computed in the spatial case in the same way as in the temporal case using a base flow profile at some position where the control will be centered. Then this kernel is used to compute the control over the whole wall of the spatial domain. The resulting control is then filtered with a hat function to act only in a small part of the domain and adjusted to give zero net mass flux. To ensure zero mass flux after the filtering of the control a constant is added to the control,

$$\ddot{\varphi}(x,z) = (\varphi(x,z) + c)H(x) \quad \text{where} \quad c = -\frac{\int_{z} \int_{x} \varphi(x,z) H(x) dx dz}{zl \int_{x} H(x) dx}, \quad (42)$$

and H(x) is a hat function consisting of a combination of two step functions described by equation (41) such that,

$$H(x) = S\left(\frac{x - (x_c - x_l/2)}{\Delta x}\right) - S\left(\frac{x - (x_c + x_l/2)}{\Delta x}\right),\tag{43}$$

where  $x_c$  is the position where the control is computed,  $x_l$  is the length of the control interval and  $\Delta x$  is the rise and fall distance. Since a spectral method is used we can compute the convolution integral as a sum in Fourier space. In the parallel flow only the  $\alpha = \beta = 0$  mode contains the mean flow, but in a spatial simulation the mean flow is contained also in the other  $\beta = 0$  modes, and we must subtract this before we compute the convolution so that only perturbations to the mean flow are reacted upon by the controller. One can expect that the controller will work as well as in the temporal case locally near the position where the mean-flow corresponds to that for which the optimal controller was computed. Further away from this position the computed control is not expected to be as good.

#### 7. Control in a Blasius boundary layer

To test the strategy on a simple case the Blasius boundary layer is studied. One case with a TS wave and one case with the optimal perturbation for spatial transient growth. The Blasius mean flow profile is a special case of the Falkner–Skan profiles with m=0 and no mean-flow component in the z direction. A TS wave is generated by an oscillating two dimensional forcing at the dimensionless frequency F=200, where  $F=2\pi f \nu/U_{\infty}^2\times 10^6$ , in the beginning of the box and allowed to develop downstream. The domain and resolution for the simulation is given in table 1 denoted as case 5. The flow is perturbed just upstream of branch I of the neutral stability curve which is at about Re=507 and the perturbation grows exponentially, shown as the dashed line in figure 7a,

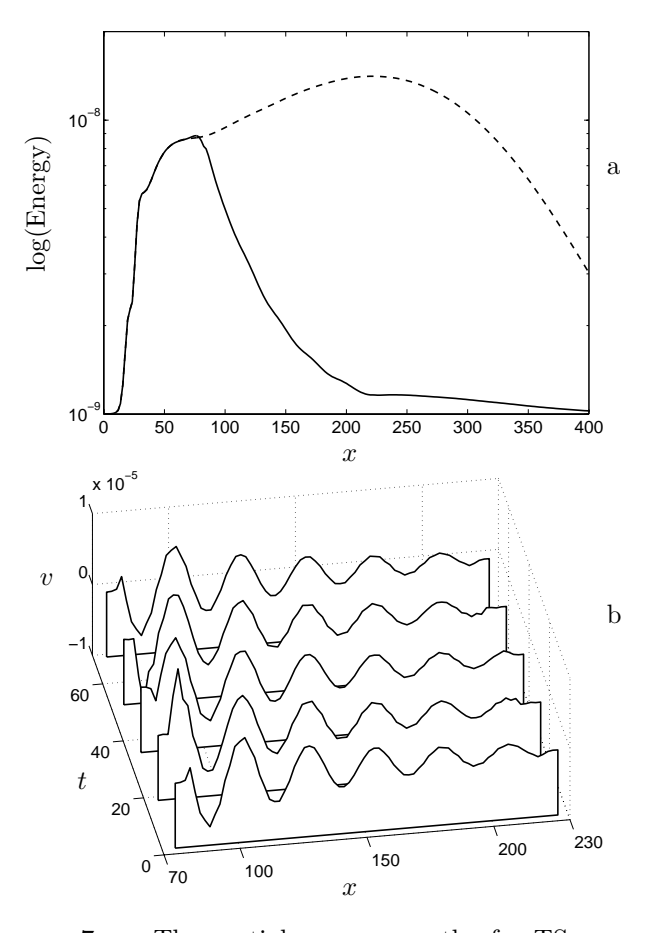


FIGURE 7. a: The spatial energy growth of a TS wave perturbation in a Blasius boundary layer with control from case 6 (solid) and without control from case 5 (dashed). The non-dimensional frequency of the perturbation is F=200. Control is applied in  $x \in [75,225]$ . b: Control signal during one time period of the TS wave.

in the uncontrolled case until it reaches branch II at about Re=723. The small transient in the beginning is due to that we do not force to a pure TS eigenmode. In case 6 in table 1 the controller applied between Re=568.4 and Re=729 corresponding to  $x\in[75,225]$ . The solid line in figure 7a shows that the exponential growth is completely removed by the controller in the control region and instead there is exponential decay. These results are similar to those obtained by Walther, Airiau & Bottaro (2001) where the application of control resulted in exponential decay of the perturbation energy in the unstable region. In figure 7b the control signal on the wall is plotted at different times during a

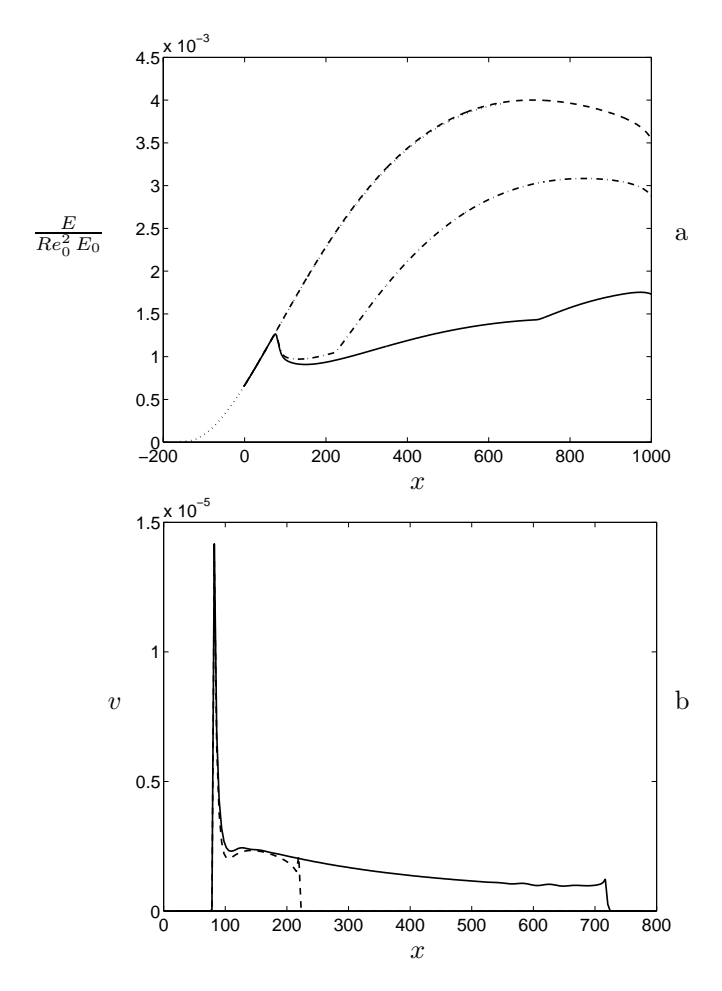


FIGURE 8. a: The spatial energy growth of the optimal spatial perturbation at x=237.24 with R=468.34 in the Blasius boundary layer. Dotted: computed from the boundary layer equations. Dashed: computed with DNS for case 7. Dash-Dotted: With control applied in  $x \in [75, 225]$  from case 8. Solid: With control applied in  $x \in [75, 725]$  from case 9. b: The control (v) distribution at y=z=0 for the streak mode in case 8 with control in  $x \in [75, 725]$  (solid) and case 9 with control in  $x \in [75, 225]$  (dashed).

period of the TS wave. The control signal looks like a TS wave with decaying amplitude and is periodic in time.

Next the performance of the controller for a transiently growing perturbation is studied. The spatial optimal perturbations in a Blasius boundary layer have been computed by Andersson, Berggren & Henningson (1999) and Luchini

(2000). The particular optimal spatial perturbation used here is computed using the technique from Andersson, Berggren & Henningson (1999) introduced at  $Re_0 = 395.4$  and then marched forward using the linear equations to the position where Re = 468.34. The perturbation is optimized to be the one with maximum growth at x = 237.24 in the simulation box. This perturbation is then used in DNS with and without control. The domain and resolution is given in table 1 for case 7 which is the uncontrolled flow. In figure 8a the dotted line shows the energy evolution as the perturbation is marched using the linear equations. The dashed line then shows the result for the uncontrolled perturbation using DNS. The energy measure is defined as,

$$E(\mathbf{u}(x)) = \int_{0}^{2\pi/\beta} \int_{0}^{\infty} (u^2 + v^2 + w^2) \, dy \, dz,$$

and  $E_0$  is the energy of the perturbation at the initial position.

In case 8 the same controller and control interval as in the TS wave case (case 6) is used. In figure 8a the dash dotted line shows the perturbation energy for this case. In this case the simulation is run until a stationary state has been obtained. Immediately when the perturbation reaches the control interval its energy is reduced and then the energy is kept almost constant throughout the control interval. The control velocity for this case is plotted as the dashed line in figure 8b showing an initial peak and then a slowly decaying amplitude. Downstream of the control interval the perturbation grows again, but does not reach the same energy level as in the uncontrolled case.

In case 9 a controller computed further downstream, still with  $l=10^2$  and  $r^2=0$ , is applied in a longer region centered at x=400 and for  $x\in[75,725]$ . There is substantial growth of the boundary layer in this longer interval and the parallel assumption is truly challenged. Even though there is a larger difference in this case between the mean flow used to compute the control kernel and the one at the position where the control interval starts, the solid line in figure 8a shows that the energy decays rapidly and is maintained at a low, slightly increasing, level by the control throughout the control interval. The control signal, solid line in figure 8b, is similar to the one obtained in the shorter interval initially and then there is a slow decay in amplitude in the long interval. Again the perturbation grows downstream of the control interval but now even less than with the short control interval.

In these cases we still have some transient growth where control is applied and downstream, but the total growth is substantially lowered by the control. Comparisons with some of the results of Cathalifaud & Luchini (2000) where optimization is performed to minimize the perturbation energy with control over the whole plate show that the control velocity has a similar distribution and that similar effect on the perturbation energy is obtained. In the cases where they apply control over only a small part of the plate, they found a slightly different shape of the control velocity distribution with a peak also at

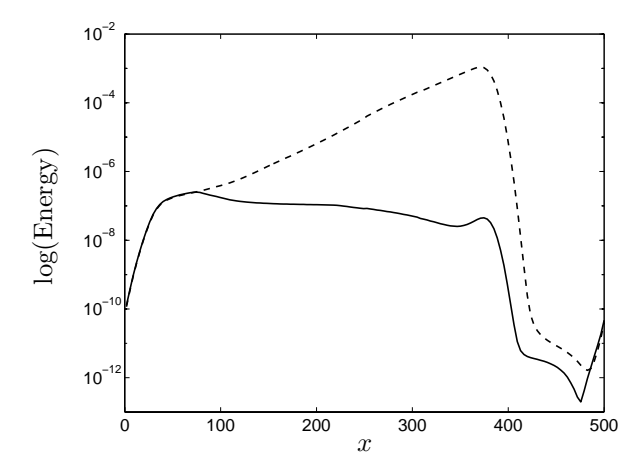


FIGURE 9. Time average of energy integrated in the z direction for uncontrolled (dashed) and controlled (solid) simulations of traveling cross flow vortices from cases 10 and 11 respectively.

the end of the interval. This is probably due to that the optimization problem is slightly different in their case, accounting for the effects of the localization of the control, which is not the case for the optimization problem solved here.

The performance of the control over the longer control interval in case 9 is surprisingly good considering that the change of the mean flow profile is fairly large in this interval. It seems that the controller is indeed robust to finite variations of the mean flow profile and our assumption thereby appear justified.

#### 8. Control in a Falkner-Skan-Cooke flow

## 8.1. Traveling vortices

The flows cases for testing the controller in the FSC flow are taken directly from Högberg & Henningson (1998). Traveling cross-flow vortices appear in experiments with high levels of freestream turbulence for example in Müller & Bippes (1988) and in the simulation of case 10 a perturbation, randomly varying in time and in space, is applied in the beginning of the box. A low amplitude ensures that non-linear effects are small and traveling cross-flow vortices then develop downstream. The box size, resolution and other details are given in table 1. The time average of the perturbation energy, plotted as the dashed line in figure 9, shows the growth of these traveling vortices. The vortices merge and split and form a complicated pattern. A gray-scale image of a snapshot of the normal velocity at y=0.5 is shown in figure 10a where whiter shades indicate positive velocity and darker shades negative velocity. In this case the control will have to react quickly in order to respond to the variation in the perturbation.

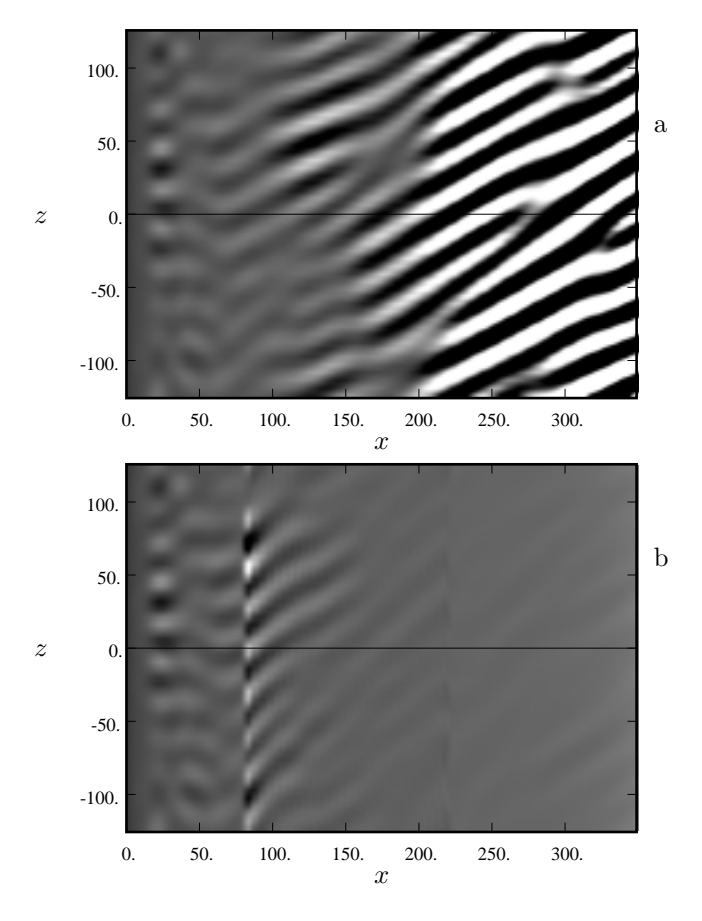


FIGURE 10. Snapshots of the normal velocity v in an xz-plane at y=0.5 for (a) case 10 without control and (b) case 11 with control. Black is  $v \le -4.5 \times 10^{-5}$  and white is  $v \ge 5.5 \times 10^{-5}$ . The control is applied in  $x \in [75, 225]$ .

Control kernels have been computed at the same resolution and box size as in case 10 and 11, given in table 1, with  $\ell=10^2$  and  $r^2=0$  at x=150 where  $\psi=51.96$  degrees and  $\delta^*=1.1232$ . The control is then allowed to act in the interval  $x\in[75,225]$ . The simulation is run long enough to get stationary statistics of the controlled flow and the time average of the energy in the box with control is plotted as the solid line in figure 9. The controller successfully changes the growth into decay of the energy and it is notable that this decay continues even downstream of the control region and all the way to the start of the fringe. The difference between the controlled and uncontrolled perturbation energy where the fringe region starts is about four decades. A snapshot of the normal velocity in case 11 is shown in figure 10b at the same y plane and time as in the uncontrolled case shows that the control action is

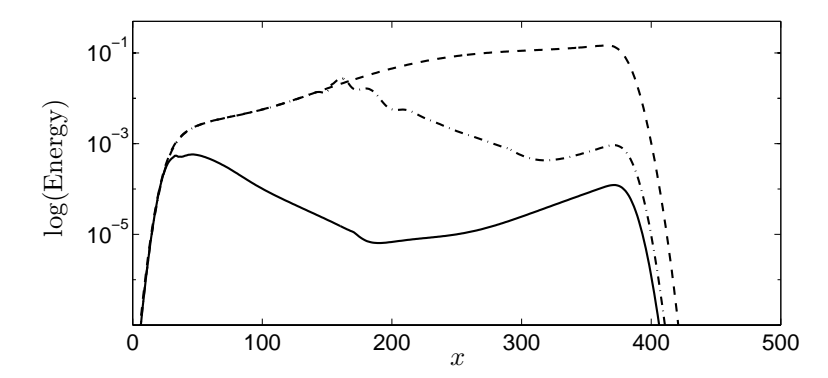


FIGURE 11. Energy growth of uncontrolled perturbation and effect of applied control in spatial DNS for  $\beta=0.25$ . Dashed: case 12 - uncontrolled. Solid: case 13 - controlled with  $\ell=10^2$  and  $r^2=0$  in the interval  $x\in[25,175]$  centered at x=100. Dash-dot: case 14 - controlled with  $\ell=10^2$  and  $r^2=0$  in the interval  $x\in[145,295]$  centered at x=220.

strongest in the beginning of the control region and that the vortices almost completely disappear downstream. Looking closely at figure 10b one can see that a light shade, indicating a positive normal velocity leads to a dark spot in the control region, and vice versa for darker shades, suggesting that the control is of opposition type initially. In the study of Wassermann & Kloker (2000) an opposition type control using blowing and suction in a strip where the optimal phase shift of the control signal was computed for each spanwise mode separately was applied to a cross-flow vortex packet. This strategy was also successful in reducing the perturbation energy, and the importance of the individually computed phase shift for different modes was emphasized. Using the present control strategy the optimal phase shift comes naturally which is a great advantage.

## 8.2. Stationary vortices

If stationary perturbations are introduced in the beginning of the box at an large enough amplitude, stationary non-linearly saturated cross-flow vortices will develop downstream. The instability properties of these vortices have recently been thoroughly studied both experimentally by e.g. Kawakami, Kohama & Okutsu (1999) and Lerche (1997), and numerically by e.g. Högberg & Henningson (1998) and Malik et al. (1999). If we consider stationary perturbations at a finite amplitude applied in the beginning of the box in case 12, box size and resolution is given in table 1, the vortices will reach a saturated level where nonlinearities dominate in the end of the physical region of the box. The energy in the  $\beta=1$  mode, the dashed line in figure 11, grows exponentially initially and then the nonlinear saturation causes the growth rate to decrease

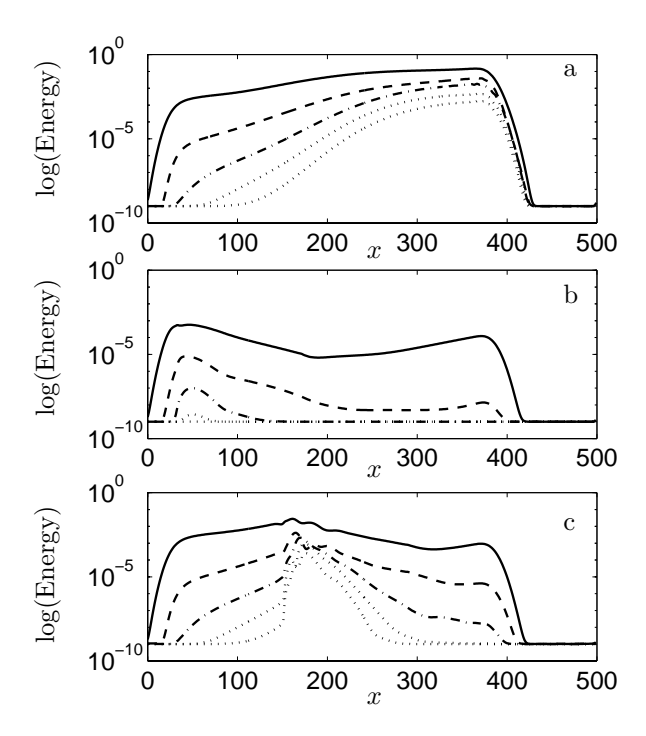


FIGURE 12. The energy in the five lowest  $\beta$  modes from simulations with a strong stationary perturbation for (a) case 12 - uncontrolled, (b) case 13 - control in  $x \in [25, 225]$  and (c) case 14 - with control in  $x \in [145, 295]$ .

and close to the fringe the growth is close to zero. The energy of the five lowest beta modes are shown in figure 12a where one can see that all these modes have similar behavior but the  $\beta = 1$  mode dominates. Control is first applied in case 13 far enough upstream for linear effects to dominate. Kernels have been computed for the mean-flow at x = 100 where  $\psi = 52.95$  degrees and  $\delta^* = 1.085$  with  $\ell = 10^2$ ,  $r^2 = 0$  and with the box size and resolution given in table 1 for case 12. The simulations of the controlled flow are performed at a lower resolution than in the uncontrolled case with  $384 \times 49 \times 16$  and uses kernels with the same resolution. The control is allowed to act in the interval  $x \in [25, 175]$  which starts just downstream of where the perturbations are introduced in the flow. The initial flow field for the simulation was one with fully developed cross-flow vortices where the control was turned on instantaneously and after some transient behavior of the flow and the control a steady state was obtained. The stationary flow is well resolved with the present resolution since the perturbation levels are substantially lower than in the uncontrolled case. The solid line in figure 11 shows the energy in the  $\beta = 1$  mode for this case. The perturbation is efficiently reduced by the control but new cross-flow vortices start to develop downstream of the control region as could be expected for

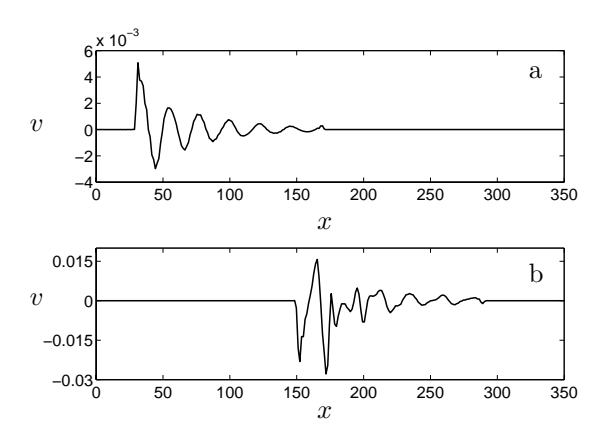


FIGURE 13. The normal velocity on the wall at z=0 in the controlled cases with stationary perturbations. a: Case 13 with control in  $x \in [25, 175]$  using a controller computed with  $\ell=10^2$  and  $r^2=0$  b: Case 14 with control in  $x \in [145, 295]$  using a controller computed with  $\ell=10^2$  and  $r^2=0$ 

this type of inflectional instability. Studying the five lowest  $\beta$  modes in figure 12b shows that the controller efficiently reduces the energy of all these modes. The control velocity on the wall is plotted for one spanwise location at z=0in figure 13a showing a regular sinusoidal signal with a maximum amplitude in the beginning of the control interval. The control region is then, in case 14, moved further downstream centered at x=220 where  $\psi=50.72$  degrees and  $\delta^* = 1.1723$ . The control is allowed to act in the interval  $x \in [145, 295]$ . In the simulation a laminar flow with the stationary perturbation in the beginning of the domain was used as initial flow field. Then when the perturbation reaches the control region the controller reacts to stabilize the flow. This is easier than starting with the fully developed perturbation since the transients when the control is turned on are strong in this case and the time-step in the simulation will be short. At the region where control is applied, the vortices will have reached a higher amplitude than in the previous case and the nonlinear effects are stronger. The simulation is run until a stationary state is obtained and the resulting energy curve is the dash dotted line in figure 11. Despite the nonlinearity the controller reduces the energy of the perturbation within the control interval. The energy curve has some wiggles initially where the perturbation is strongest indicating that nonlinear effects are influencing the control. The normal velocity on the wall is plotted for one spanwise position at z=0also for case 14 in figure 13b. The control signal in this case is distorted and has no apparent deterministic structure which probably is due to the effect of nonlinearities. The maximum amplitude, which is larger than in the upstream interval, of the control appears in the beginning of the control interval and after a few strong oscillations it decays rapidly. The control affects all wave-numbers  $\beta$  and a plot of the effect of the controller on the five lowest values of  $\beta$  in the simulation is shown in figure 12c. In this case the higher modes appear to be amplified in the beginning of the control region before they rapidly decay. The higher energy levels in these modes is related to the shape of the control signal with the nonlinear behavior.

#### 9. Discussion and conclusions

It was expected that the optimal controller could stabilize unstable temporal eigenvalues based on previous work. The changes of eigenvalues and eigenvectors for control applied to TS waves and the effect of controllers on transient growth is studied by for example Bewley & Liu (1998) for channel flow. The main question here was if these methods were transferable to the spatially evolving flow. Even though we have made some assumptions about the physics, we have shown that the controller works very well also in this case. The growth of TS waves could be turned into decay by applying control over the unstable interval also in the spatial case. When we have a spatial optimal perturbation for transient growth in the Blasius boundary layer, the controller could not make the perturbation decay but only lower the growth. In this case it was also shown that the control is effective also over a long spatial interval and not only locally where it is computed. The complicated flow with inflectional instability in the FSC boundary layer was stabilized by the controller for random as well as stationary perturbations. The additional spatial property of a changing direction of the meanflow did not have a significant effect on the effectiveness of the controller in this case. Even higher amplitude perturbations where nonlinear effects are present were stabilized resulting in energy decay in the controlled interval indicating some robustness of the controller to nonlinearities, as well as to changes of the meanflow.

In summary it is demonstrated that the three main mechanisms for energy growth in boundary layers can be controlled, exponential instabilities, non-modal transient energy growth and inflectional instabilities triggered by both stationary and time varying perturbations. It appears that it is sufficient to make use of the Orr-Sommerfeld-Squire equations when designing controllers for most types of primary instability transition scenarios. In fact the importance of linear processes for transition as well as turbulence has been emphasized by several authors investigating these processes see e.g. Henningson (1996); Kim & Lim (2000). The strength and advantage of the present formulation of the control problem is that there is no dependence on what type of perturbation the flow is subject to and transition due to secondary instabilities should not be an issue if one can control the primary ones. One question is how effective the controllers are for preventing transition to turbulence. The present study indicates that the controllers can handle some degree of nonlinearity, and quantification of the controller performance for transition in channel flow is work in progress (Högberg, Bewley & Henningson (2001)). It should be mentioned that there are also important types of instabilities not considered here, namely the absolute and global instabilities. A controller for global instabilities must probably incorporate non-parallel effects since these are crucial for their existence and this can not be obtained using the present formulation of the control problem.

To be able to make use of this type of feedback controller in practice there is need for a good way of estimating the state of the flow based on realizable measurement data. An estimator forcing can be computed from the linear equations as described in Högberg & Bewley (2000) and then applied to force a model of the flow using wall measurements only. The combination of an estimator and a controller is called a compensator, and provides means to control the flow based on these wall measurements. The effectiveness of the estimator and the compensator for transition in channel flow is also studied in ongoing work (Högberg, Bewley & Henningson (2001)), and once this has been done, a natural next step is to extend also these ideas to the spatial boundary layer flows. To be able to obtain a control system usable in practice there might be a need to utilize robust control  $\mathcal{H}_{\infty}$  design to improve the robustness of the compensator. This was studied for the linear system in Bewley & Liu (1998) and showed some different properties compared to the optimal control design which could improve the behavior of the compensator when e.g. nonlinearities are present. In future work this possibility should be explored further and tested also in the nonlinear setting.

The authors wish to thank professor Thomas Bewley for pointing us in the direction of using linear control techniques, and for cooperation in creating the foundation for the present work.

#### References

- Andersson, P., Berggren, M. & Henningson, D. S. 1999 Optimal disturbances and bypass transition in boundary layers. *Phys. Fluids* 11, 134–150.
- Balakumar, P. & Hall, P. 1999 Optimum suction distribution for transition control. *Theoret. Comput. Fluid Dynamics* 13, 1–19.
- Berggren, M. 1995 Optimal Control of Time Evolution Systems: Controllability Investigations and Numerical Algorithms. Ph. D. thesis, Department of Computational and Applied Mathematics, Rice University, Houston, Tx 77251-1892.
- Bewley, T. R. 2001 Flow control: new challenges for a new Renaissance *Prog. Aero. Sci.* 37, 21–58.
- Bewley, T. R. & Liu, S. 1998 Optimal and robust control and estimation of linear paths to transition. *J. Fluid Mech.* **365**, 305-349.
- Bewley, T. R., Moin, P. & Temam, R. 2001 DNS-based predictive control of turbulence: an optimal benchmark for feedback algorithms. *J. Fluid Mech.* 477, 179–225.
- Breuer, K. S., Haritonidis, J. H. & Landahl, M. T. 1989 The control of transient disturbances in a flat plate boundary layer through active wall motion. *Phys. Fluids A* 1, 574–582.

- Cathalifaud, P. & Luchini, P. 2000 Algebraic growth in boundary layers: optimal control by blowing an suction at the wall Eur. J. Mech. B Fluids 19, 469–490.
- COOKE, J. C. 1950 The boundary layer of a class of infinite yawed cylinders. *Proc. Camb. Phil. Soc.* 46, 645–648.
- Gad-el-Hak, M. 1996 Modern developments in flow control. *Appl. Mech. Rev.* 49 (7), 364–379.
- Hanifi, A., Schmid P. J. & Henningson D. S. 1996 Transient growth in compressible boundary layer flow. *Phys. Fluids*, **8**, (3), 826–836.
- HENNINGSON, D.S. 1996 Comment on "Transition in shear flows. Nonlinear normality versus non-normal linearity" [Phys. Fluids 7, 3060 (1995)] Phys. Fluids 8, (8), 2257–2258.
- HÖGBERG, M. & BEWLEY, T. R. 2000 Spatially-compact convolution kernels for decentralized control and estimation of plane channel flow. Submitted to Automatica
- HÖGBERG, M., BEWLEY, T. R. & HENNINGSON, D. S. 2001 Decentralized feedback control and estimation of transition in plane channel flow. in preparation.
- HÖGBERG, M. & HENNINGSON, D. S. 1998 Secondary instability of cross-flow vortices in Falkner-Skan-Cooke boundary layers. J. Fluid Mech. 368, 339–357.
- JACOBSON, S. A. & REYNOLDS, W. C. 1998 Active control of streamwise vortices and streaks in boundary layers. J. Fluid Mech. 360 179–211.
- JAMESON, A. 1989. Computational aerodynamics for aircraft design. Science. 245, 361–371.
- JOSHI, S. S., SPEYER J. L. &KIM, J. 1997 A systems theory approach to the feedback stabilization of infinitesimal and finite-amplitude disturbances in plane Poiseuille flow. J. Fluid Mech. 332, 157–184.
- Joslin, R. D., Gunzburger, M. D., Nicolaides, R. A., Erlebacher, G. & Hussaini, M. Y. 1997 A self-contained, automated methodology for optimal flow control *AIAA Journal* **35**, 816–824.
- KAWAKAMI, M., KOHAMA, Y. & OKUTSU, M. 1999 Stability characteristics of stationary crossflow vortices in three-dimensional boundary layer. AIAA paper 99-0811
- Kim, J., & Lim, J. 2000 A linear process in wall-bounded turbulent shear flows. Phys. Fluids 12 (8), 1885-1888.
- Kozlov, V. V. & Grek, G. R. 2000 Stationary and nonstationary streaky structures and secondary instability of boundary layers. In *Laminar-Turbulent Transition*, *Proc. IUTAM Symposium*, *Sedona*, *Arizona*, *USA* (1999) (FASEL, H. ,SARIC, W., editors). *Springer-Verlag*.
- Laub, A.J. 1991 Invariant subspace methods for the numerical solution of Riccati equations. In *The Riccati Equation* (ed. Bittaini, Laub, & Willems) 163-196. Springer.
- Lerche, T. 1997 Experimentelle Untersuchung nichtlinearen Strukturbildung im Transitionsprozeß einer instabilen Grenzschicht. Fortscrittberichte, VDI, Reihe 7: Strömungstechnik, Nr. 310.
- Luchini, P. 2000 Reynolds-number-independent instability of the boundary layer over a flat surface: optimal perturbations *J. Fluid Mech.* **404** 289–309.
- Lumley, J. & Blossey, P. N. 1998 Control of turbulence. Ann. Rev. Fluid Mech. 30, 311–327.

- Lundbladh A. ,Berlin S.,Skote M.,Hildings C.,Choi J., Kim J. & Henningson D.S. 1999 An efficient spectral method for simulation of incompressible flow over a flat plate. Technical report, Department of Mechanics, KTH, *TRITA-MEK* 1999:11.
- Malik M. R., Li, F., Choudhari M. M. & Chang, C-L 1999 Secondary instability of crossflow vortices and swept-wing boundary-layer transition *J. Fluid Mech.* **399** 86–115.
- METCALFE, R. W. 1994 Boundary layer control: A brief review. In Computational Fluid Dynamics '94, Invited Lectures of the Second European CFD Conference; Stuttgart, Germany (Wagner, S., Periaux, J. & Hirschel, E., editors), 52–60. John Wiley & Sons.
- Mughal, M. S. 1998 Active control of wave instabilities in three-dimensional compressible flows. Theoret. Comput. Fluid Dynamics 12 195–217.
- MÜLLER, B. &BIPPES, H. 1988 Experimental study of instability modes in a three-dimensional boundary layer. AGARD-CP 438, No. 18.
- NORDSTRÖM, J., NORDIN, N. & HENNINGSON, D. S. 1999 The fringe region technique and the fourier method used in the direct numerical simulation of spatially evolving viscous flows. SIAM J. Sci. Comp. 20 (4), 1365–1393.
- Pralits J. O., Hanifi, A. & Henningson D. S. 2001 Adjoint-based optimization of steady suction for disturbance control. Part 1. Incompressible flows. In *Towards optimal design of vehicles with low drag: Applications to sensitivity analysis and optimal control*. Licenciate thesis of Jan Pralits, Department of Mechanics, Royal Institute of Technology, Stockholm, Sweden *TRITA-MEK* 2001:07.
- Schlichting, H. 1979 Boundary-Layer Theory, 7th Edn. McGraw-Hill.
- SARIC, W. S., CARRILLO, R. B. Jr. & Reibert, M. S. 1998 Leading-edge roughness as a transition control mechnism. *AIAA paper 98-0781*.
- Skelton, R. E. 1988 Dynamic Systems Control, Linear Systems Analysis and Synthesis John Wiley & Sons
- Thomas, A. S. W. 1990. Active wave control of boundary-layer transition. In *Viscous Drag Reduction in Boundary Layers* (Bushnell, D. M. & Hefner, J. N., editors). American Institute of Aeronautics and Astronautics, Washington, D.C. Vol. 123 in *Progress in Astronautics and Aeronautics*.
- Walther, S., Airiau, C. & Bottaro, A. 2001 Optimal control of Tollmien–Schlichting waves in a developing boundary layer. *Phys. Fluids*, **13** (7), 2087–2096.
- Wassermann, P., Kloker, M. 2000 DNS-Investigations of the Development and Control of Crossflow Vorticies in a 3D Boundary-Layer Flow. In *Laminar-Turbulent Transition, Proc. IUTAM Symposium, Sedona, Arizona, USA* (1999) (Fasel, H., Saric, W., editors). Springer-Verlag.
- White E. B. & Saric W. S. 2000 Application of variable length leading-edge roughness for transition control on swept wings AIAA 2000-0283.
- Weideman, J. A. C. & Reddy, S. C. 2000 A Matlab Differentiation Matrix Suite. ACM Transaction of Mathematical Software 26 (4), 465–519.